Springer Theses
Recognizing Outstanding Ph.D. Research

Fiona L. Hatton

Hyperbranched Polydendrons

A New Macromolecular Architecture

Springer

Springer Theses

Recognizing Outstanding Ph.D. Research

Aims and Scope

The series “Springer Theses” brings together a selection of the very best Ph.D. theses from around the world and across the physical sciences. Nominated and endorsed by two recognized specialists, each published volume has been selected for its scientific excellence and the high impact of its contents for the pertinent field of research. For greater accessibility to non-specialists, the published versions include an extended introduction, as well as a foreword by the student's supervisor explaining the special relevance of the work for the field. As a whole, the series will provide a valuable resource both for newcomers to the research fields described, and for other scientists seeking detailed background information on special questions. Finally, it provides an accredited documentation of the valuable contributions made by today's younger generation of scientists.

Theses are accepted into the series by invited nomination only and must fulfill all of the following criteria

- They must be written in good English.
- The topic should fall within the confines of Chemistry, Physics, Earth Sciences, Engineering and related interdisciplinary fields such as Materials, Nanoscience, Chemical Engineering, Complex Systems and Biophysics.
- The work reported in the thesis must represent a significant scientific advance.
- If the thesis includes previously published material, permission to reproduce this must be gained from the respective copyright holder.
- They must have been examined and passed during the 12 months prior to nomination.
- Each thesis should include a foreword by the supervisor outlining the significance of its content.
- The theses should have a clearly defined structure including an introduction accessible to scientists not expert in that particular field.

More information about this series at http://www.springer.com/series/8790

Fiona L. Hatton

Hyperbranched Polydendrons

A New Macromolecular Architecture

Doctoral Thesis accepted by
the University of Liverpool, UK

Springer

Author
Dr. Fiona L. Hatton
Fibre and Polymer Technology
KTH Royal Institute of Technology
Stockholm
Sweden

Supervisor
Prof. Steve Rannard
Department of Chemistry
University of Liverpool
Liverpool
UK

ISSN 2190-5053 ISSN 2190-5061 (electronic)
Springer Theses
ISBN 978-3-319-18752-5 ISBN 978-3-319-18753-2 (eBook)
DOI 10.1007/978-3-319-18753-2

Library of Congress Control Number: 2015939159

Springer Cham Heidelberg New York Dordrecht London

Printed on acid-free paper

Springer International Publishing AG Switzerland is part of Springer Science+Business Media (www.springer.com)

Part of this thesis have been published in the following journal articles:

Fiona L. Hatton, Tom O. McDonald, Pierre Chambon, Andrew Owen, Steve P. Rannard, *"Hyperbranched polydendrons: a new controlled macromolecular architecture with self-assembly in water and organic solvents"*, *Chem. Sci.*, **2014**, 5, 1844–1853.

Fiona L. Hatton, Lee M. Tatham, Louise R. Tidbury, Pierre Chambon, Tao He, Andrew Owen and Steve P. Rannard, "*Hyperbranched polydendrons: a new nanomaterials platform with tuneable permeation through model gut epithelium"*, *Chem. Sci.*, **2015**, 6, 326–334.

Supervisor's Foreword

Over the past three decades, polymer chemistry has seen the development of new concepts and experimental techniques that have been increasingly approachable for research groups without access to highly specialised equipment. The advent of highly and ideally branched polymer architectures in the form of hyperbranched polymers and dendrimers heralded a new era for polymer science. Almost concurrently, the introduction of controlled radical polymerisation allowed research groups across the world to develop new chemical strategies towards the formation of ever more complex polymers with placement of functionality, defined chain lengths and tuning of physical properties.

At the overlap of dendrimers and controlled radical polymerisation, a range of polymers termed "linear-dendritic hybrids" have grown in interest and scope. These materials attempt to benefit from both chemistries by taking dendrons, the smaller building blocks of dendrimers, and using them to adorn linear polymers either at the chain ends or as pendant units. In some cases, dendrons have become the linking sections for novel star polymers whilst in other elegant syntheses, dendrons of different chemical types have been linked together to make macromolecules that possess multiple peripherally-initiated linear polymers and numerous functional groups.

This control of architecture comes at some synthetic cost to the chemist. Elaborate strategies to generate uniform macromolecules with defined complexity may also require a large number of chemical stages, each requiring different conditions and purification. The result may be low yielding reactions and, therefore, a subsequent reduction in the breadth of viable application.

The research outlined in this thesis has introduced completely new structures to the field of complex macromolecular architectures. By combining low generation dendrons with controlled radical polymerisation and the concepts from branched vinyl polymerisation, the one-pot synthesis of "hyperbranched-polydendrons" has been achieved. In essence, these materials are linear-dendritic hybrid polymers that are joined along the linear polymer chain to incorporate tens, and sometimes hundreds, of chains on average, each one with a dendron at one chain-end. To

achieve these structures, a level of non-uniformity has been accepted and non-ideal distributions of architecture and molecular weight are present; however, the hyperbranched-polydendrons reported here have been shown to undergo nanoprecipitation to form extremely uniform self-assembled structures whilst requiring relatively simple synthetic strategies and providing a high degree of structural and chemical manipulation.

The importance of such chemistry may not yet be completely clear. Here, the ability of hyperbranched-polydendrons to encapsulate poorly-soluble compounds, and the opportunity to vary the surface functionality and internal environment of their nanoprecipitates, has been utilised in an exploration of their potential in nanomedicine. The role of particulate medicines is growing rapidly and clinics across the world regularly dose nanomedicines for a range of diseases. Administration of nanomedicines to result in circulating nanoparticles is only currently possible through intravenous injection, however, nanoprecipitates derived from hyperbranched-polydendrons have shown some indication that permeation through the gut may be possible if the surface chemistry is accurately controlled. This is uniquely possible through the synthesis of this new material type and future researchers will be presented with opportunities that have been too complex to derive through previous strategies. It may be that nanomedicine is not the ultimate best application of hyperbranched-polydendrons but this thesis opens the door for a wealth of potential application investigations, as early reports of dendrimers, linear-dendritic-hybrids and controlled radical polymerisation all individually did in the past.

Liverpool, UK
February 2015

Prof. Steve Rannard

Abstract

A novel architecture 'hyperbranched polydendrons' (*hyp*-polydendrons) was produced via the synthesis of low generation dendron initiators for ATRP and subsequent copolymerisation of vinyl and divinyl monomers, to give large polymeric macromolecules containing dendron moieties at the end of each primary chain. Subsequent studies of such materials were performed to assess their ability to form nanoparticles via a nanoprecipitation approach, utilising organic solvent and aqueous nanoparticle formation. It was found that the branched polymers were superior to the linear polymer analogues when assessing their nanoprecipitation behaviour.

Mixed initiator *hyp*-polydendrons were also synthesised by the statistical incorporation of different functionality initiators into the reaction mixture. Here, a G2 dendron and different PEG macroinitiators were mixed statistically to produce a series of materials where the primary chain length of the monomer HPMA was also varied. This led to a series of nanoparticles which showed a variation of internal environments when studied using different fluorescent dyes (Nile red and pyrene). Initial pharmacological experiments were promising, however, the initial set of materials did not show prolonged stability in physiologically relevant conditions when using a short PEG macroinitiator (750PEG).

Extending the length of the PEG chain (2000PEG initiator) in the mixed polymerisations produced a range of materials with varying solubilities and, therefore, nanoprecipitation behaviour. Nanoparticles were formed which were stable under physiologically relevant conditions and were studied for their cytotoxicity and transcellular permeability in Caco-2 cells. These materials showed limited toxicity at the concentrations studied and enhanced permeation though the Caco-2 cell monolayer, which is a model of the intestinal epithelial cells.

Further studies of the nanoprecipitation behaviour of different molecular weight fractions of the *hyp*-polydendrons were conducted. This involved separation of molecular weight fractions by dialysis of the *hyp*-polydendrons against two different good solvents, leading to two HMW fractions and two LMW fractions. Analysis of the nanoprecipitation behaviour of these fractions showed that the HMW fractions produced particles with more narrow PdIs, and the mixing of a low

amount of an HMW fraction (1 wt%) with a linear polymer improved the nanoprecipitation behaviour hugely.

Encapsulation of two different guest molecules via nanoprecipitation was assessed using FRET, which can report on the proximity of two fluorophores. Dual loading of the particles with DiO and DiI in a 1:1 ratio gave particles which exhibited a FRET signal, therefore indicating that the two fluorophores were located in the same nanoparticle. Somewhat unexpectedly, it was found that upon mixing of the two singly loaded particles the observed FRET ratio increased over time until it reached a similar value obtained within the dual loaded nanoparticles. This was possibly due to nanoparticle–nanoparticle collisions.

Therefore, *hyp*-polydendrons were produced and utilised to form nanoparticles via a nanoprecipitation approach. Loading of the nanoparticles was achieved and pharmacological benefits were observed for some of the nanoparticle samples, suggesting future benefits for these polymer architectures in nanomedicine applications.

Acknowledgments

I would first like to thank my supervisor, Prof. Steve Rannard for offering me the opportunity to study my Ph.D. and for his constant guidance and support throughout the past 3.5 years. I will miss working with him and the rest of the research group enormously.

I would also like to thank past and present members of the Rannard group for everything; from help with experiments, creating a friendly environment to work in to organising days out and group meals. I would especially like to thank Dr. Pierre Chambon for many discussions which have aided me in my work. I am grateful to Pierre, Hannah and Andy for creating a fun atmosphere in our office.

I would like to thank my friends in the department that I have made throughout my time in Liverpool, in particular, Tamara, Jaclyn, Emily, Rob, Mike, Paul and Ben. Special thanks go to Dr. Ben Alston for help with proofreading some of this work.

With regard to the work presented in this thesis I would like to thank Dr. Lee Tatham and Louise Tidbury who conducted the pharmacological studies in the Department of Molecular and Clinical Pharmacology under the supervision of Prof. Andrew Owen. I am grateful to Lee for help with interpreting the results from these studies and for responding to all of my numerous emails. I would also like to thank Neil Lunt who performed some dialysis experiments discussed in Chap. 5.

Finally I would like to thank my family for all their support and help throughout my studies, for encouraging me and making me believe I could achieve anything if I set my mind to it!

Contents

Abbreviations

ANOVA	Analysis of variance
ATHP-1	Monocyte-derived macrophages
ATP	Adenosine triphosphate
ATRP	Atom transfer radical polymerisation
Caco-2	Human epithelial colorectal adenocarcinoma cell line
CAR	Cellular accumulation ratio
CI	Chemical ionisation
CMC	Critical micelle concentration
CTA	Chain transfer agent
CuAAC	Copper catalysed azide-alkyne click reaction
Đ	Dispersity (GPC)
DLS	Dynamic light scattering
DL_x	Dendritic–$linear_x$
D_n	Number average diameter
DP_n	Degree of polymerisation
Dz	z-Average diameter
ES	Electrospray
FRET	Förster resonance energy transfer
GPC	Gel permeation chromatography
G*x*	Generation *x* dendrimer
HIV	Human immunodeficiency virus
HMW	High molecular weight
HSV	Herpes simplex virus
IgG	Immunoglobulin
LALS	Low angle light scattering
LD	Linear–dendritic
LDL	Dendritic–linear–dendritic
LDL_x	Linear–dendritic–$linear_x$
LMW	Low molecular weight
MALDI-TOF	Matrix assisted laser desorption/ionisation time of flight

M_n	Number average molecular weight
MRI	Magnetic resonance imaging
MTP	Microsomal triglyceride transfer protein
MTT	3-[4,5-dimethylthiazol-2-yl]-2,5 diphenyl tetrazolium bromide
M_w	Weight average molecular weight
MWCO	Molecular weight cut off
NMP	Nitroxide mediated polymerisation
NMR	Nuclear magnetic resonance
P_{app}	Apparent permeability
PdI	Polydispersity index (DLS)
RAFT	Reversible addition-fragmentation chain-transfer
RALS	Right angle light scattering
RI	Refractive index
RLU	Relative luminescence units
ROP	Ring opening polymerisation
SCVP	Self-condensing vinyl polymerisation
SEM	Scanning electron microscopy
TB	Transport buffer
TEER	Transepithelial electrical resistance
TEM	Transmission electron microscopy
*T*g	Glass transition temperature
THP-1	Human monocytic cell line
UV-Vis	Ultraviolet-visible spectroscopy
Φace	Acetone fraction
Φhex	Hexane fraction

Chemical Abbreviations

2000PEG	PEG macroinitiator (2000 $gmol^{-1}$)
750PEG	PEG macroinitiator (750 $gmol^{-1}$)
AIBN	Azobisisobutyronitrile
BAPA	Bis(3-aminopropyl)amine
bis-MPA	2,2-Bis(methylol)propionic acid
bpy	Bipyridyl
CDI	1,1′-Carbonyldiimidazole
DBOP	1,3-Dibenzyloxy-2-propanol
DETA	Diethylenetriamine
DiI	1,1′-Dioctadecyl-3,3,3′,3′-tetramethylindocarbocyanine perchlorate
DiO	3,3′-Dioctadecyloxacarbocyanine perchlorate
DMAP	Dimethylaminopyridine
DMF	Dimethylformamide
DMSO	Dimethylsulphoxide
DOX	Doxorubicin
DVB	Divinylbenzene
EBiB	Ethyl bromo isobutyrate
EGDMA	Ethylene glycol dimethacrylate
EO	Ethylene oxide
FA	Fluoresceinamine
G1	**G1** dendron initiator
G2	**G2** dendron initiator
G2′	**G2′** dendron initiator, using alternative synthesis
HPMA	2-Hydroxypropyl methacrylate
IPA	Isopropyl alcohol
MA	Methyl acrylate
MMA	Methyl methacrylate
PAMAM	Poly(amidoamine)
PBCA	Poly(butyl cyanoacrylate)
PCA	Poly(cyanoacrylate)

PCL	Poly(caprolactone)
PEG	Poly(ethylene glycol)
PGA	Poly(glutamic acid)
PHB	Poly(hydroxybutyrate)
pHPMA	Poly(2-hydroxypropyl methacrylate)
PLA	Poly(lactic acid)
PLGA	Poly(lactic-co-glycolic acid)
pMMA	Poly(methyl methacrylate)
PPI	Polypropylenimine
PS	Polysytrene
PVA	Polyvinyl alcohol
TEA	Triethylamine
THF	Tetrahydrofuran

Chapter 1
Introduction

1.1 Dendrimers

Dendritic shapes are commonly found in nature in forms such as trees, neurons, lightning flashes and snowflakes. In chemical terms a dendrimer is a symmetrical, perfectly branched macromolecule consisting of a core, branching points and surface groups [1]. This general structure of a dendrimer is highlighted in Fig. 1.1 along with one fragment of a dendrimer which can be described as a dendron. The dendritic architecture allows for high surface functionality and therefore the scope of this type of material is huge.

Several well-known dendrimer chemical structures and their corresponding generation number (G*x*) are highlighted in Fig. 1.2. This type of material was first synthesised in the late 1970s and early 1980s by the research groups of Vögtle [2], Tomalia [3] and Newkome [4]. Since then research interest in the area of dendrimer chemistry has increased dramatically, as can be seen by the number of publications each year when searching for "dendrimer" as specified by SciFinder (Jan 2014) in Fig. 1.3.

Dendrimers have proved to be useful in many applications over this time [5], some of which are discussed further below (Sect. 1.1.2). However, the major drawback in the use of dendrimers is due to the lengthy and costly syntheses required to produce them, vide infra.

1.1.1 Dendrimer Synthesis

Dendrimers can either be synthesised via convergent or divergent routes. Each method requires a multi-step synthesis, which becomes more costly and complicated as the generation number increases.

F.L. Hatton, *Hyperbranched Polydendrons*,
Springer Theses, DOI 10.1007/978-3-319-18753-2_1

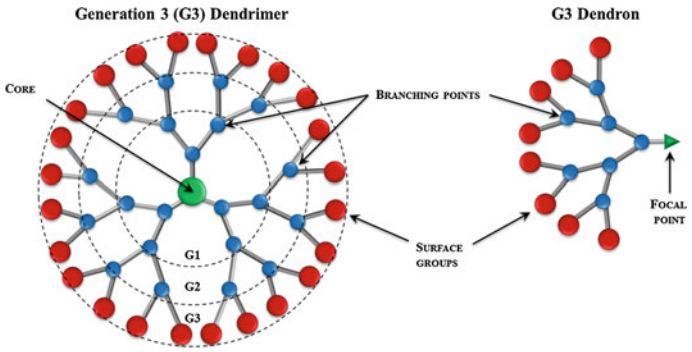

Fig. 1.1 Graphical representation of a generation 3 (G3) dendrimer and corresponding dendron

1.1.1.1 Divergent Synthesis of Dendrimers

Divergent synthesis of dendrimers starts with the core of the molecule and proceeds via sequentially adding branching units (or generations), then finally addition of the surface groups. This is shown in Fig. 1.4. This method of producing dendrimers usually requires protection of functional groups which, after reacting with the core or growing dendrimer, are subsequently deprotected to allow for further reaction and dendrimer growth. Divergent dendrimer synthesis was utilised firstly by Vögtle and coworkers in 1978 [2], but was described as a 'cascade' approach. The first reported description of these materials as 'dendrimers' was in 1985 by Tomalia et al. [3] who produced a series of poly(amidoamine) (PAMAM) dendrimers. The PAMAM dendrimers were synthesised by firstly the exhaustive Michael addition of three molecules of methyl acrylate to a molecule of ammonia, the core, followed by complete amidation of the esters with a large excess of ethylenediamine to give a dendrimer with three primary amine groups at the surface, see Scheme 1.1. This process can be repeated to give dendrimers of higher molecular weights, up to generation 10 (G10), and increased surface functionality. This type of dendrimer has been termed a 'Starburst Dendrimer' and is commercially available.

1.1.1.2 Convergent Synthesis of Dendrimers

Convergent synthesis starts with the surface groups of the resulting dendrimer, coupled together through the branching units and then finally to the core (see Fig. 1.4). Convergent dendrimer synthesis was first reported by Hawker and Fréchet in 1990 [6]. They synthesised aryl ether dendrons up to G6 which were subsequently coupled to a trivalent core to produce the equivalent poly(aryl ether) dendrimers based upon the 'monomer' 3,5-dihydroxy-benzyl alcohol, see

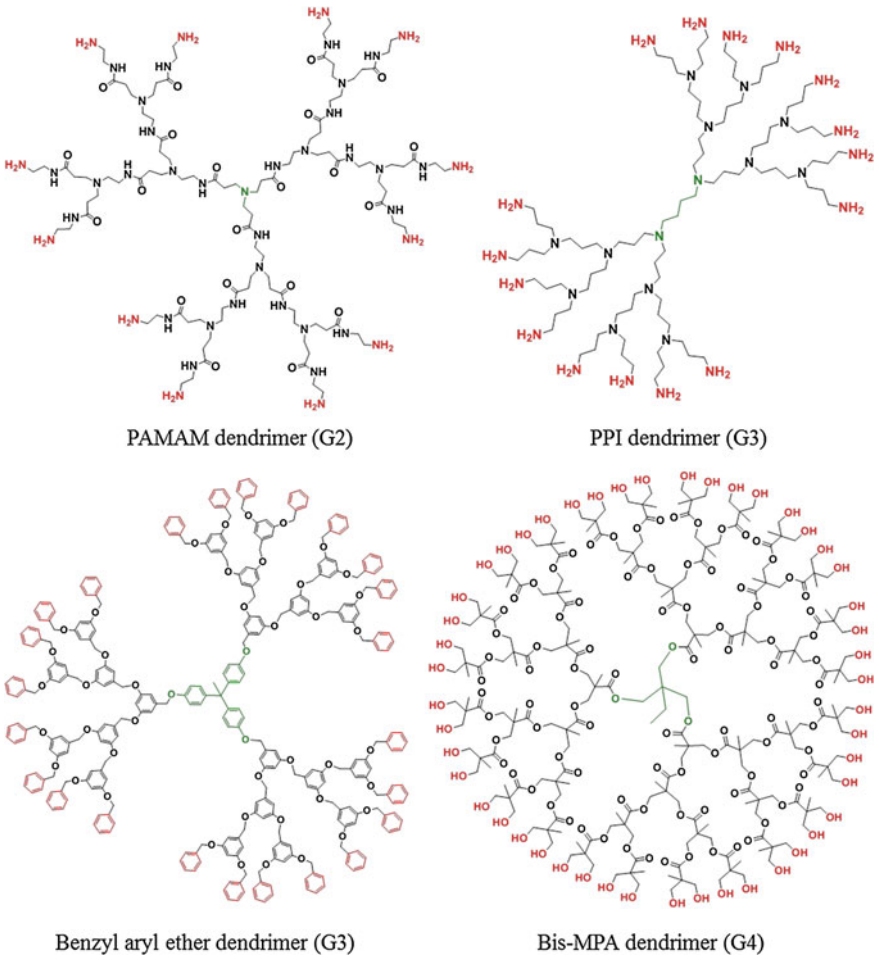

Fig. 1.2 Various types of dendrimer chemical structures, including; poly(amidoamine) (*PAMAM*), polypropylenimine (*PPI*), benzyl aryl ether and 2,2-bis(methylol)propionic acid (*bis-MPA*) based dendrimers. *Red groups* represent the dendrimer surface groups, and *green*, the dendrimer cores

Scheme 1.2. This method showed a greater control over the synthesis of dendrimers, less imperfections arising and without the need for an excess of reagents. However, during the coupling step of the dendrons to the core molecule to form the final dendrimer, the yields declined dramatically with increasing the dendrimer generation achieving 76 and 51 % for the G5 and G6 dendrimers respectively. This reduction in yield was due to steric hindrance of bulky dendron coupling with a small molecule core [6].

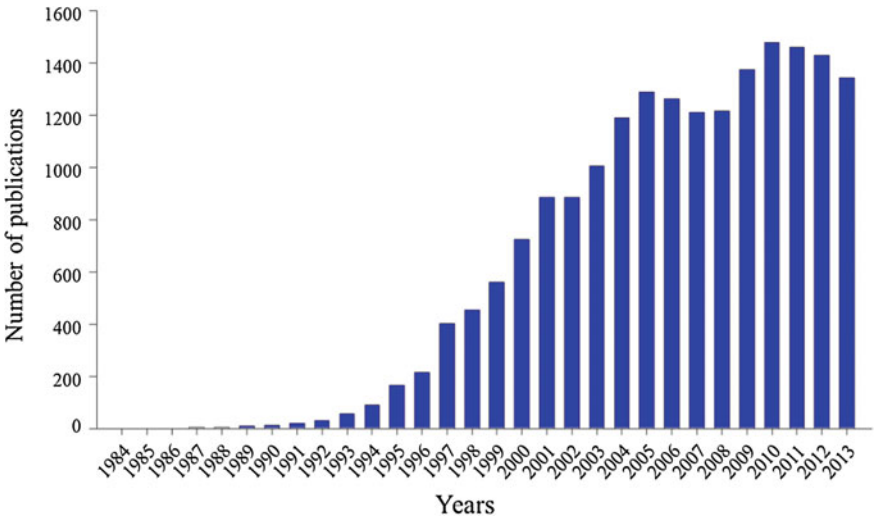

Fig. 1.3 Number of publications, as of January 2014 on SciFinder; search term "dendrimer"

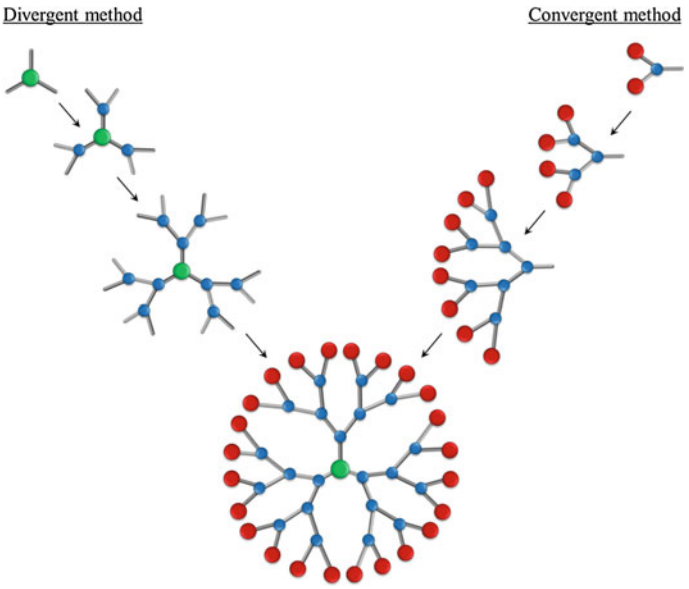

Fig. 1.4 Divergent and convergent methods for dendrimer synthesis

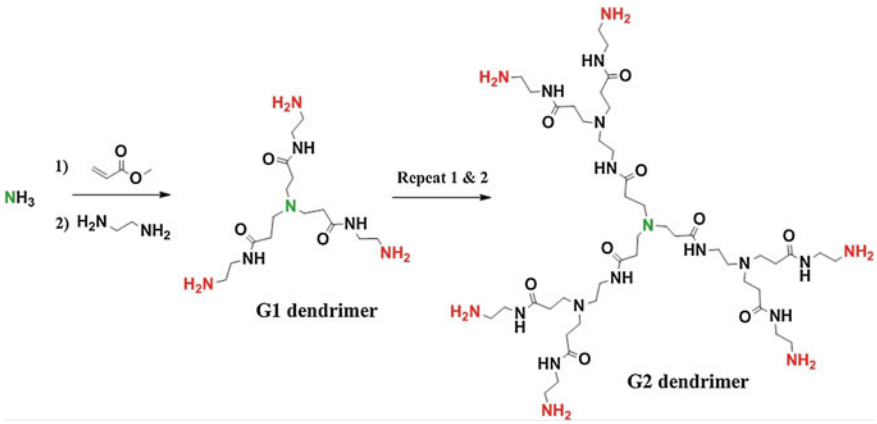

Scheme 1.1 Divergent synthesis of PAMAM dendrimers as described by Tomalia et al. [3]

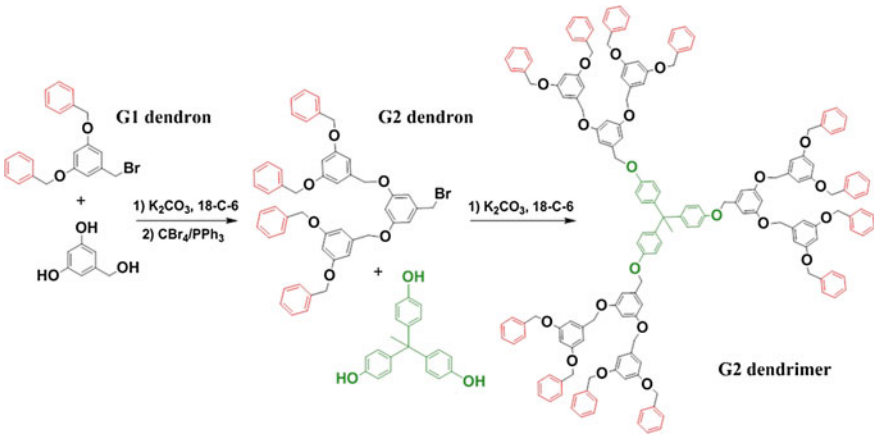

Scheme 1.2 Convergent synthesis of poly(aryl ether) dendrimer as described by Hawker and Fréchet [6]

1.1.1.3 Dendrimer Applications

Dendrimers have been utilised for various applications since their discovery such as; biomedical applications in therapy and diagnostics [7–9], catalysis [10, 11] and optics [12]. Several dendrimers and hyperbranched polymers are commercially available, including PAMAM Starburst dendrimers and 2,2-bis(methylol)propionic acid (bis-MPA) based Boltorn hyperbranched polymers, which has aided greatly the study of these materials for many different research areas.

1.1.2 Dendrimers Towards Biomedical Applications

Easily the largest area for dendrimer application research has been towards biomedical applications. As mentioned briefly this area of research can be characterised as having therapeutic and diagnostic applications.

1.1.2.1 Therapeutic Applications of Dendrimers

The use of dendrimers in therapeutics has been achieved through various methods; drug delivery [5, 13, 14], gene therapy [5, 13, 15], boron neutron capture therapy [5, 16], anti-microbial activity [17] and in some cases the dendrimer itself has been the cause for a therapeutic effect [18, 19].

There are numerous examples of dendrimers being evaluated for drug delivery in the literature [13, 14], which can be distinguished into two categories: physical encapsulation of drug molecules inside the dendrimer or chemical conjugation of the drug molecule to the surface groups of the dendrimer. Examples of each type of drug delivery utilising dendrimer materials are shown in Table 1.1. Dendrimers have been reported functionalised with more than one molecule, for example, Scheme 1.3 shows the synthesis of a PAMAM dendrimer conjugated to poly(ethylene glycol) PEG, folic acid and doxorubicin (DOX), where PEG is a stabilising hydrophilic polymer, folic acid is used as a targeting molecule for the folate receptor (which is overexpressed in cancerous cells) and DOX is an anti-cancer drug [20].

The most active research area in dendrimer-based therapeutics has been towards gene therapy using dendrimers as non-viral transfection agents [13, 15]. Gene therapy involves the use of DNA as a drug to treat a disease, where the DNA is delivered into the cell nucleus to be incorporated into the patient's chromosomes, usually to replace a mutated gene. Cationic dendrimers have been utilised for gene therapy due to the ionic interaction which occurs between the negatively charged DNA (the negative charge from the phosphate groups along the backbone) and the positively charged dendrimer. Dendrimers utilised for gene therapy include PAMAM [21, 22] and polypropylenimine (PPI) [23, 24] dendrimers as they form compact polycations under physiological conditions.

Boron neutron capture therapy is based upon the Boron-10 isotope, which when irradiated by low-energy neutrons emits high energy α-particles and high energy lithium-7 nuclei, therefore causing fatal cell damage. This approach has been used to selectively target cancer cells by using boron containing PAMAM dendrimers [16, 25].

One example of the use of a dendrimer as a therapeutic agent is with relation to prion research [18, 26]. A prion is an infectious agent composed of a misfolded protein. Whilst they are not living organisms, once infecting an individual, prions can induce the misfolding of other proteins into the diseased form. They affect the structure of the brain or other neural tissue and are currently untreatable. It has been shown in preliminary studies that conversion of the normal protein (PrP^C) to the

Table 1.1 Drug delivery utilising dendrimers

	Dendrimer	Drug(s)	Indication	Outcome	References
Encapsulation	Mannosylated PPI dendrimer	Rifampicin	Bactericidal antibiotic	Site-specific delivery to the alveolar macrophages was achieved	[30]
	Dextran conjugated PPI dendrimers	Doxorubicin	Anti-cancer drug	Enhanced uptake was observed in A549 cancer cells when compared to free drug	[31]
	PEGylated G3 and G4 PAMAM dendrimers	Methotrexate, Adriamycin	Anti-cancer drugs	Increasing dendrimer generation and PEG length improved the drug loading capabilities	[32, 33]
	PEGylated G4 PAMAM dendrimer	5-fluorouracil	Anti-cancer drug	PEGylation of the dendrimers lead to a higher drug loading, slower drug release and reduced hemolytic toxicity	[34]
	PEGylated G3 4,4-bis(49-hydroxyphenyl) pentanol core	Indomethacin	Non-steroidal anti-inflammatory drug	An 11 wt% loading of indomethacin was achieved in the G3 dendrimer which also exhibited a sustained release profile	[35]
	G4 PPI dendrimer conjugated with mannose/sialic acid	Zidovudine	Anti-retroviral drug	High loading, sustained release and good biocompatibility were observed. Suggested targeting of zidovudine to HIV reservoirs	[36]
Conjugation	G3-5 PAMAM dendrimer carboxylate surface functional	Cisplatin	Anti-cancer drug	High loading (20–25 wt%) of platinum and selective accumulation in tumour tissue was achieved	[37]
	G1, G2 polyether dendrimers with folate surface functionality	Methotrexate	Anti-cancer drug	Dendrimers bearing folate surface residues were prepared as model drug carriers with potential tumour cell specificity	[38]
	G1-5 1,4,7,10-tetraazacyclododecane core with $-NH_2$ surface groups	5-fluoruracil	Anti-cancer drug	Partial acetylation of the G4 and 5 surface groups lead to improved solubility. The conjugated drug was released slowly	[39]
	G4 PAMAM (–OH) dendrimer	Erythromycin	Antibiotic/anti-inflammatory	High loading ($\sim$16 wt%) of erythromycin, improved solubility and reduced local periprosthetic inflammation in a sustained manner	[40]
	G3-5 PEG-PAMAM dendrimer folate functional	Doxorubicin	Anti-cancer drug	Tumour targeting folate PEG-PAMAM dendrimers with DOX conjugated and super paramagnetic iron oxide	[20]

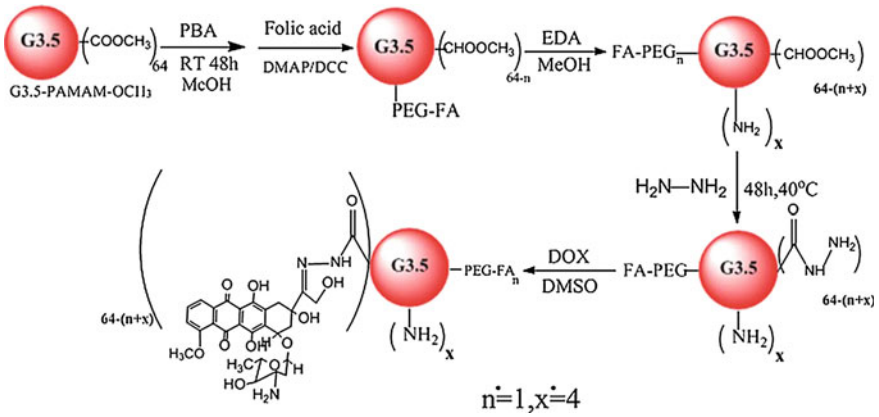

Scheme 1.3 Synthesis of DOX and FA conjugated G3.5 PAMAM dendrimer [20]. Reproduced from Ref. [20] with permission from The Royal Society of Chemistry

infectious misfolded protein (PrP^{Sc}) can be prevented by a PPI dendrimer functionalised with maltose [26]. Another example where the dendrimer itself is the therapeutic agent is the product VivaGel® produced by StarPharma which has been shown to inhibit infection by viruses such as HIV and HSV, and has also been shown to prevent the growth of bacteria. VivaGel® contains the active ingredient SPL7013 which is a dendrimer composed of a divalent core, four successive layers of L-lysine with sodium 1-(carboxymethoxy) naphthalene-3,6-disulfonate groups at the dendrimer surface [19, 27].

Anti-microbial activity has been observed for several different functional dendrimers [17]. Anti-bacterial dendrimers, such as those described by Meyers et al. in 2008 [28], were anionic amphiphilic dendrimer materials (see Fig. 1.5) which possessed Gram positive anti-bacterial activity whilst remaining non-toxic to eukaryotic cells.

Silver-dendrimer complexes have also been utilised as anti-bacterial agents [29]; Balogh et al. describe the activity of various silver-PAMAM dendrimers against

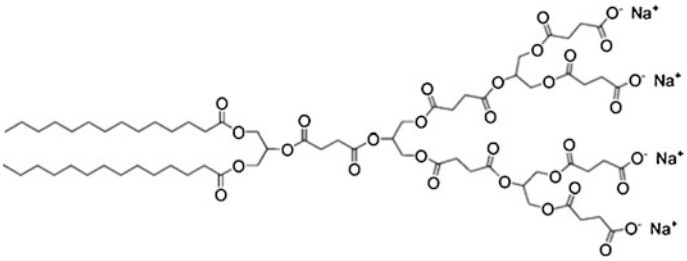

Fig. 1.5 Anionic amphiphilic dendrimer with anti-microbial behaviour, reported by Meyers et al. [28]. Reprinted with permission from [28]. Copyright 2008 American Chemical Society

Staphylococcus aureus, *Pseudomonas aeruginosa*, and *Escherichia coli* bacteria, however the anti-bacterial activity is due to the complexed silver, not directly from the dendrimer.

1.1.2.2 Diagnostic Applications of Dendrimers

The main areas of research for dendrimers in biomedical diagnostics have been as magnetic resonance imaging (MRI) contrast agents and in the detection of DNA [41].

MRI is a powerful medical imaging technique which is used to investigate soft tissue in the human body, for example blood vessels and organs, under healthy and diseased states. MRI is based on the environment sensitive ^{1}H nuclear magnetic resonance (NMR) spectroscopy resonances of water molecules in living systems, which requires a paramagnetic contrast agent to enhance visualisation [42]. The most widely used contrast agents contain Gd^{III} complexes and it is desirable to design MRI contrast agents to have low toxicity, good biocompatibility, stability in physiological conditions as well as good excretion from the body. Dendrimer based Gd^{III} chelates have been shown to exhibit all these properties required, utilising low and high generation PAMAM dendrimers. Depending upon the generation of the dendrimer, and therefore the resulting size of the dendrimer-Gd^{III} chelate, the MRI contrast agents formed could be used for various applications [43].

DNA dendrimers are comprised of DNA strands [44, 45], an example of this type of structure is shown in Fig. 1.6.

DNA dendrimers have been reported that can detect oligonucleotide sequences and, as such, have been developed commercially as 3DNA-technology (Genisphere®) [47]. The 3DNA-technology is currently used in clinical diagnostic tests to improve sensitivity without changing the label or detection reagent. pH responsive, size tunable DNA dendrimers have also been developed [48] to high generations and high yields without purification, towards applications in drug delivery and biosensors.

The Stratus® CS system is an automated clinical diagnostic tool available commercially since 1998. It relies upon a dendrimer-antibody complex which is

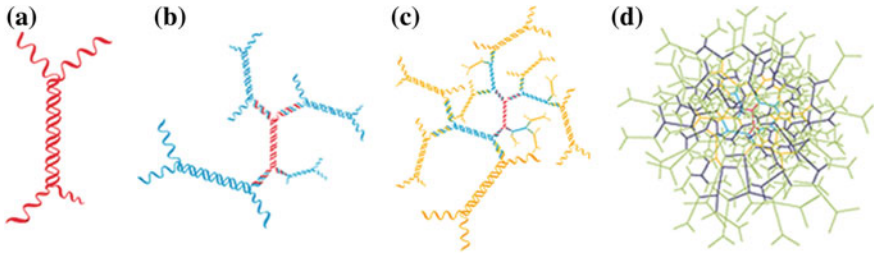

Fig. 1.6 Graphical representation of DNA dendrimers: **a** two complimentary DNS strands; **b** assembly of DNA strands to give a DNA dendrimer; **c** and **d** additional layers of DNA increase the complexity of the DNA dendrimer. Reproduced from the Genisphere® website [46]

used to detect several cardiac markers which can aid in the diagnosis of acute myocardial infarction, deep venous thrombosis, pulmonary embolism, congestive heart failure and inflammatory disorders due to tissue injury and infection [49]. The dendrimer utilised in this technology is based on a Starburst® PAMAM dendrimer coupled to an immunoglobulin (IgG). The use of this dendrimer-antibody complex showed a shorter assay time and improved performance characteristics when compared to the same antibody employed as a double-antibody immune complex.

1.1.3 Limitations in the Use of Dendrimers

Divergent dendrimer growth is generally limited to structures no larger than generation 10, however, the synthesis of a generation 13 dendrimer has recently been reported by Simanek and coworkers [50]. This higher generation is most likely achievable due to the length of the branching unit, which is 18 atoms long, whereas PAMAM dendrimers have branching units that are only 7 atoms long.

The limiting generation can be calculated using Eq. (1.1), where P represents the number of flexible atoms per monomer [51].

$$\text{Limiting generation} = 2.88(\ln P + 1.5) \tag{1.1}$$

This limitation due to steric hindrance is described by de Gennes dense packing [1, 51], whereby as the generation increases, the surface packing of the dendrimer becomes more dense. Therefore if the dendrimer growth remained ideal, a generation would be reached where the surface of the dendrimer is densely packed and prevents further reaction due to steric hindrance. However, in reality as the generation of a dendrimer increases, some of the surface groups are hidden and therefore this leads to defects in the dendrimer structure at earlier generations than predicted.

Another major limitation of dendrimer synthesis is the huge excess of reagents often required to reach complete reaction of each generation layer and high generations. This is particularly relevant for divergent dendrimer synthesis. Convergent dendrimer synthesis struggles to be viable for producing high generation dendrimers as the steric hindrance of coupling large dendrons around a small core molecule becomes over crowded, often leading to incomplete reaction.

1.2 Branched Polymers to Produce Dendrimer-Like Structures

Hyperbranched polymers have created a great deal of interest in academia and industry, as they form large polymeric structures in a one-pot synthesis. Traditionally hyperbranched polymers are synthesised using AB_x monomers, in a polycondensation reaction, which is classified as a step-growth polymerisation.

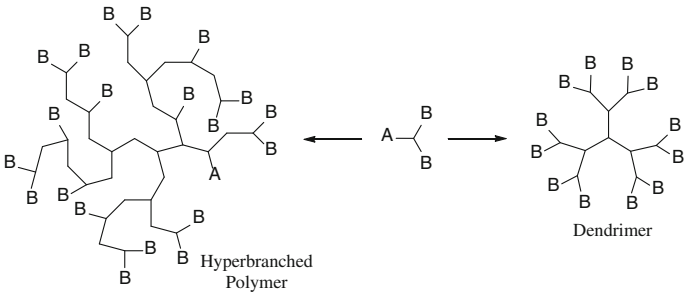

Fig. 1.7 Schematic comparison of a hyperbranched polymer and a dendrimer via an AB_2 monomer

Flory described this type of polymerisation in 1952 [52], however it wasn't given the term 'hyperbranched polymerisation' until 1988 by Kim and Webster [53, 54]. This type of polymerisation affords macromolecules with structures more closely related to networks than dendrimers, see Fig. 1.7.

AB_2, AB_3, AB_4 and AB_6 polycondensations have been reported and applications for hyperbranched polymers include blends and coatings [55, 56].

Hyperbranched or highly-branched polymers can also be synthesised via chain-growth polymerisations, including anionic [57] and radical polymerisation [58]. Anionic polymerisation was first reported in 1956 by Szwarc [59], and is classed as a living polymerisation technique. Anionic polymerisation proceeds with the nucleophilic attack of a double bond by a carbanion which initiates polymerisation. Carbanions that are most commonly used to initiate anionic polymerisation are *n*-butyl, *sec*-butyl or *tert*-butyl anions which are liberated when using the respective alkyl lithium species. Anionic polymerisation is a true living polymerisation technique as the reactive negative charge is almost constantly present at the end of the propagating polymer chain. This technique has been used to synthesise various complex architectures including star polymers, comb polymers and hyperbranched polymers [57].

Free radical polymerisation is a synthetic technique which has become the most widely utilised technique in the production of polymers on an industrial scale. For example, poly(styrene) (PS) is produced via free radical polymerisation and is used to produce common plastic items such as compact disk cases, disposable cutlery, disposable razors and expanded polystyrene for packaging materials. Whilst this method of polymerisation is facile, cost-effective and commonly used it is not an appropriate polymerisation technique when controlled branched polymer architectures are desired. The incorporation of even small amounts of a comonomer which contains two vinyl groups, a divinyl monomer, in a free radical polymerisation can lead to a cross-linked network, macroscopic gelation at high concentrations or microscopic gelation under dilute conditions. The copolymerisation of styrene and divinylbenzene (DVB) by free radical polymerisation was first reported in 1935 by Staudinger and Husemann [60], and further investigations into this copolymerisation have more recently been reported by Antonietti and Rosenauer [61]. In each case the

transition between microscopic and macroscopic gelation was studied. When the DVB content was increased from 5 to 10 %, for example, the corresponding critical weight fraction of the micro/macrogelation transition decreased from 0.120 to 0.102. The production of high molecular weight soluble branched polymers via this method, therefore, requires high dilution which is problematic for producing a scalable method for the production of branched polymers. To produce soluble branched polymers by radical polymerisation techniques, either a chain transfer agent can be included in the reaction or a controlled radical polymerisation method must be employed; this will be discussed in more detail below.

1.2.1 Branched Polymers via Controlled Radical Polymerisation Techniques

Branched vinyl polymerisation is a versatile tool which has been utilised to produce various branched copolymers with varying compositions. Examples of those achieved include; branched homopolymers, branched block copolymers, branched statistical copolymers, branched graft-copolymers and more complex structures such as shaped branched amphiphilic copolymers [58, 62].

The branched radical polymerisation techniques discussed here involve the co-polymerisation of a monofunctional vinyl monomer and a divinyl monomer. This leads to the linking together of two or more linear chains via branching points caused by the inclusion of the divinyl monomer into two different linear chains. The main drawback of this method is that the ratio of divinyl monomer to initiator must be carefully controlled. The theory of gel formation by statistical copolymerisation of vinyl and divinyl monomers was first described by Flory [63–65] and Stockmayer [66–68]. Assuming that no intramolecular cyclisation occurs, and that the reactivities of each vinyl group are the same, gelation will occur when the cross-linking index (number of cross-links per chain) is equal to one. Therefore usually a ratio of 1:0.95 initiator:divinyl monomer or less is used to afford high molecular weight soluble branched polymers [69]. However, in practice other factors can affect this theory; for example, the concentration of monomer in the polymerisation can influence the intermolecular versus intramolecular reaction of the pendant vinyl groups. At high dilutions it has been shown that the intramolecular cyclisation reaction is favoured, whereas the intermolecular reaction is dominant at high monomer concentrations [70, 71]. The effect of diluting these reactions has been followed by ^{1}H NMR [72] and also by modelling [73].

Different polymerisation techniques which can be employed to produce branched polymers include; chain transfer agent mediated free radical polymerisation (Strathclyde approach) [74], atom transfer radical polymerisation (ATRP) [69], reversible addition-fragmentation chain-transfer (RAFT) polymerisation [75] and nitroxide mediated polymerisation (NMP) [76].

One polymerisation technique used to prepare branched polymers whilst avoiding gelation is self-condensing vinyl polymerisation (SCVP). Scheme 1.4

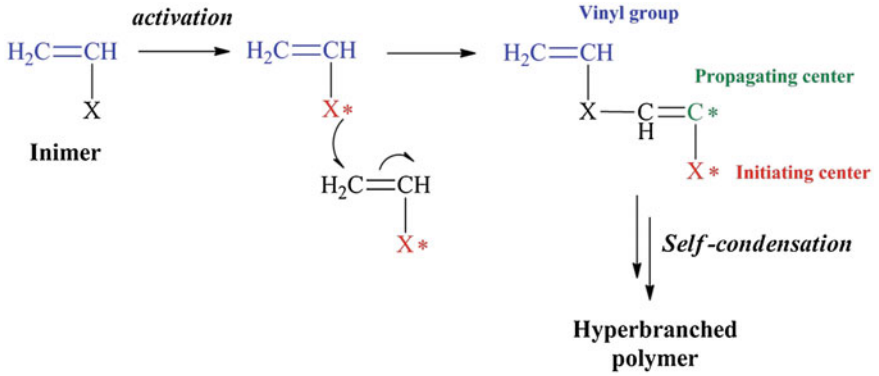

Scheme 1.4 General mechanism of SCVP

highlights the general mechanism of SCVP, which employs an inimer to introduce branching points rather than a divinyl monomer.

An inimer contains a polymerisable group and also a reactive group capable of initiating polymerisation in the same molecule. This method of preparing branched polymers was first reported by Grubbs and coworkers in 1995, where they describe the polymerisation of a styrenic monomer, 3-(1-chloroethyl)-ethenylbenzene, by "living" radical polymerisation [77]. SCVP has also been reported utilising ATRP and RAFT polymerisation techniques, however this technique does not give a polymer with the same functionality at every polymer chain end, and the molecular weight of resulting polymers is generally lower than those obtained utilising different branched polymerisation methods [78]. The structure of polymers produced by SCVP differs greatly from branching polymerisations which utilise a vinyl and divinyl monomer; this is highlighted graphically in Fig. 1.8a.

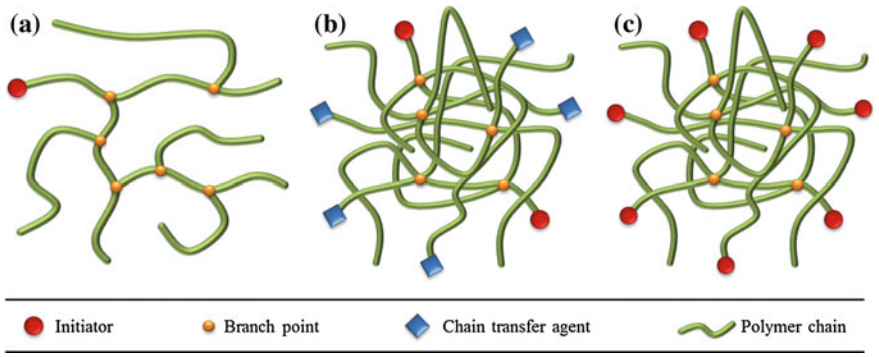

Fig. 1.8 Idealised graphical representation of various hyperbranched polymer architectures produced via radical polymerisation techniques: **a** self-condensing vinyl polymerisation (SCVP); **b** Strathclyde approach; **c** ATRP

1.2.1.1 Branched Polymers via the Strathclyde Method

The copolymerisation of vinyl and divinyl monomers by free radical polymerisation gives rise to insoluble cross-linked polymer networks, as previously described. To overcome this problem in 2000 Sherrington and coworkers developed a method, termed the 'Strathclyde' method, to synthesise soluble branched polymers via the free radical polymerisation of vinyl and divinyl monomers by incorporating a small molecule chain transfer agent (CTA), see Scheme 1.5 [74]. This CTA controls the length of the primary polymer chain to a certain extent which prevents every single chain from bearing a divinyl monomer, therefore avoiding gelation. This method provides branched polymer architectures (Fig. 1.8b) via a relatively facile preparation, however, if functionality is required at the end of the polymer chains, it needs to be incorporated into the CTA, or post-functionalisation is required. Another disadvantage is that a radical initiator is needed to initiate the polymerisation, such as azobisisobutyronitrile (AIBN) for example, therefore some of the polymer chains will bear the radical initiator functionality and some the CTA functionality.

1.2.1.2 Branched Polymers via ATRP

The use of ATRP to produce branched polymers is most relevant to the research presented here and the copolymerisation of a vinyl and divinyl monomer utilising

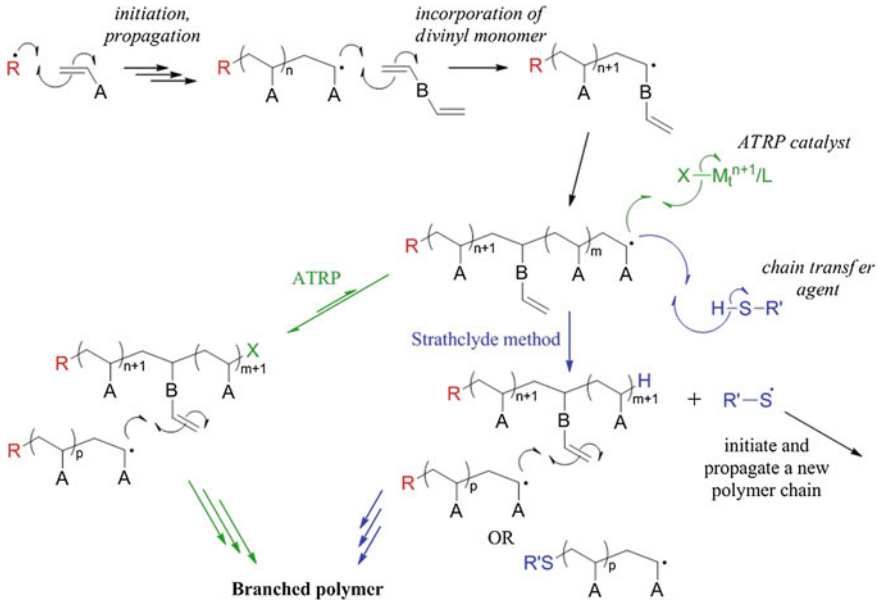

Scheme 1.5 General mechanisms for the formation of branched polymers via both ATRP and the 'Strathclyde' method

ATRP was first reported in 2001 [79]. The authors' purpose in this report was to study the formation of insoluble gels rather than prepare soluble branched polymers. Isaure et al. first reported branched soluble polymers by ATRP in 2004 [69], utilising ethylene glycol dimethacrylate (EGDMA) as the divinyl monomer in the polymerisation of branched poly(methyl methacrylate) (pMMA).

Utilising ATRP for the formation of branched polymers produces architectures similar to those expected via the 'Strathclyde' approach, however, ATRP allows for the incorporation of the initiator functionality at every primary polymer chain end, see Fig. 1.8c. The general mechanisms for the formation for branched polymers via ATRP and the 'Strathclyde' approach are highlighted in Scheme 1.5. There have been various reports utilising ATRP in the formation of branched polymers, including the polymerisation of branched poly(hydroxypropyl methacrylate) (pHPMA) [80] and PS [81].

This method of preparing branched polymers has been utilised to produce different branched polymer architectures, highlighted in Fig. 1.9. The introduction of the branching molecule, divinyl monomer, at various stages of the polymerisation gives rise to these different branched polymer topologies via ATRP. Incorporation of the divinyl monomer within the reaction mixture before the polymerisation is started gives rise to structures similar to that described by Fig. 1.9a. The statistical nature of branching causes links between linear chains (if the amount of divinyl monomer is carefully controlled) to produce branched soluble polymers.

Other methods used to produce branched polymers via the copolymerisation of vinyl and divinyl monomers include the 'arm-first' approach and the 'core-first' approach [82]. The 'arm-first' approach, Fig. 1.9b, begins with the polymerisation of linear polymer chains and the divinyl monomer is added either alone or with a comonomer at high conversion. This forms a highly branched or cross-linked core, with the linear chains forming a shell or corona with the initiator functionality at the periphery. The 'core-first' approach, Fig. 1.9c, proceeds with the polymerisation of divinyl monomer or copolymerisation of vinyl and divinyl monomers to produce a highly branched or cross-linked polymer, which then has more mono-functional vinyl monomer added to propagate linear chains. This gives a similar final structure

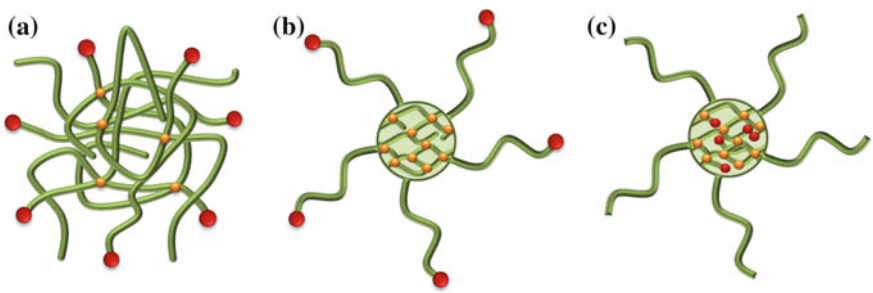

Fig. 1.9 Idealised graphical representation of various branched polymer architectures achieved by copolymerisation of a vinyl and divinyl monomer via ATRP: **a** standard branched polymerisation; **b** the arm-first approach; **c** core-first approach

as the 'arm-first' approach, with a branched core and linear corona, however, in the 'core-first' approach the initiator functionality is located in the branched core.

More complex architectures have been reported such as the synthesis of dumbbell shaped polymeric nanoparticles by He et al. in 2007 [62]. The 'arm-first' approach was adopted, including a small amount of difunctional initiator to cause individual branched polymer cores to be joined to give dumbbell shaped particles after dialysis. This is shown in Fig. 1.10; the hydrophilic 'arms' of the structures stabilise the hydrophobic core of the particles after dialysis.

Due to the statistical nature of ATRP, however, not every difunctional initiator will cause the linking of two branched cores; it is possible for no linking to occur (leading to spherical particles) or the inclusion of multiple difunctional initiators per branched core (leading to clover shaped particles). This approach was also utilised with a tri-functional initiator, where three branched hydrophobic cores were joined, stabilised by the hydrophilic 'arms', to give 'clover-leaf' shaped particles after dialysis [83].

The effect of monomer concentration on the branching mechanism has been studied by Armes and coworkers where they polymerised methyl methacrylate (MMA) via ATRP and RAFT, employing a divinyl monomer which contained a disulphide linkage that allowed cleavage of the branches between linear chains [70]. Utilising ^{1}H NMR they showed it was possible to distinguish between divinyl monomers which had become involved in inter- or intra-molecular reactions (branches or loops, respectively) [72]. They found that the more dilute the polymerisation, more loops were formed during polymerisation, even to the point at which up to 3 equivalents of divinyl monomer to 1 equivalent of initiator could be incorporated (at 10 wt% monomer and via ATRP) without gelation due to the loss of branching points caused by the pendant vinyl groups forming loops.

Matyjaszewski and coworkers have also studied this phenomenon with the co-polymerisation of methyl acrylate (MA) and a diacrylate brancher molecule via ATRP [71]. They found that at a concentration of 0.5–2.4 vol% of monomer that

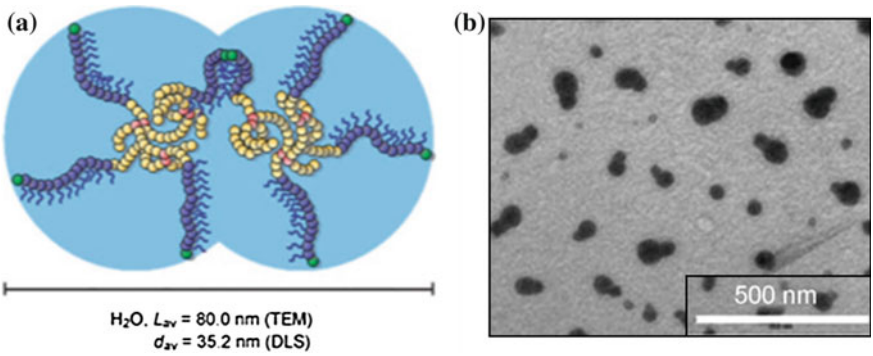

Fig. 1.10 **a** Idealised graphical representation and **b** SEM image of the dumbbell shaped nanoparticles via the 'arm-first' approach [62]. Reproduced from Ref. [62] with permission from John Wiley & Sons, Inc

15 equivalents of di-acrylate could be used without gelation, and at 2.4–5 vol% monomer, 10 equivalents of diacrylate to 1 equivalent of initiator could be introduced without gelation occurring. The copolymerisation at 0.5 vol% led to mostly intramolecular reaction and limited amounts of branched polymers were formed. Whilst they report that the polymerisations achieved high conversions (90 %) it was not reported how long it took to reach these conversions under such dilute conditions.

Branched polymerisation via ATRP has introduced a range of architecturally complex materials, and whilst the synthesis may be facile they do not completely satisfy the structural nature and surface functionality of dendrimers.

1.2.2 Dendritic Hybrid Architectures

Dendritic-polymer hybrids have complex architectures, usually containing linear polymer chains and one or more dendrons. A range of hybrid materials have been reported since the early 1990s with reviews discussing various combinations of polymer and dendritic chemistries [84–87]. The discussion here focuses on the structures highlighted in Fig. 1.11. These include linear-dendritic (LD) hybrids (Fig. 1.11a), dendritic-linear-dendritic (DLD) hybrids (Fig. 1.11b), dendronised linear hybrids (Fig. 1.11c), dendron functional star hybrids (Fig. 1.11d), dendritic-linear$_x$ (DL$_x$) hybrids (Fig. 1.11e) and linear-dendritic-linear$_x$ (LDL$_x$) hybrids (Fig. 1.11f).

The research surrounding LD hybrids began in the early 1990s, since their conception multiple synthetic routes and variations on the linear dendritic structure have been elucidated and reported in the literature. Synthetic routes to such materials have been developed by; (a) growing a linear chain from the dendron focal point, (b) growing a dendron divergently from the end of a linear polymer chain or (c) coupling of a pre-formed dendron and linear polymer chain together [86]. Multiple polymer and dendrimer chemistries have been utilised to produce LD hybrids, and amphiphilic hybrids have shown particular interest due to their solution properties, with abundant biomedical applications. Amphiphilic LD hybrids have been developed that self-assemble into micelle type structures in the size range below 100 nm [88].

DLD hybrids were first reported in 1992 utilising the focal point of hydrophobic G3 and G4 dendrons to couple a dendron at each end of hydrophilic polyethylene glycol (PEG) chains of various lengths [89]. Various DLD hybrids have been reported since and have been utilised in applications such as self-assembly to form aggregates around 200 nm [90], cell internalisation for drug delivery [91] and the formation of isoporous films and 3D networks [92].

Dendronised polymers have received much attention since their development and can be synthesised either via the macromonomer approach or attaching a dendron to a preformed polymer chain [93, 94].

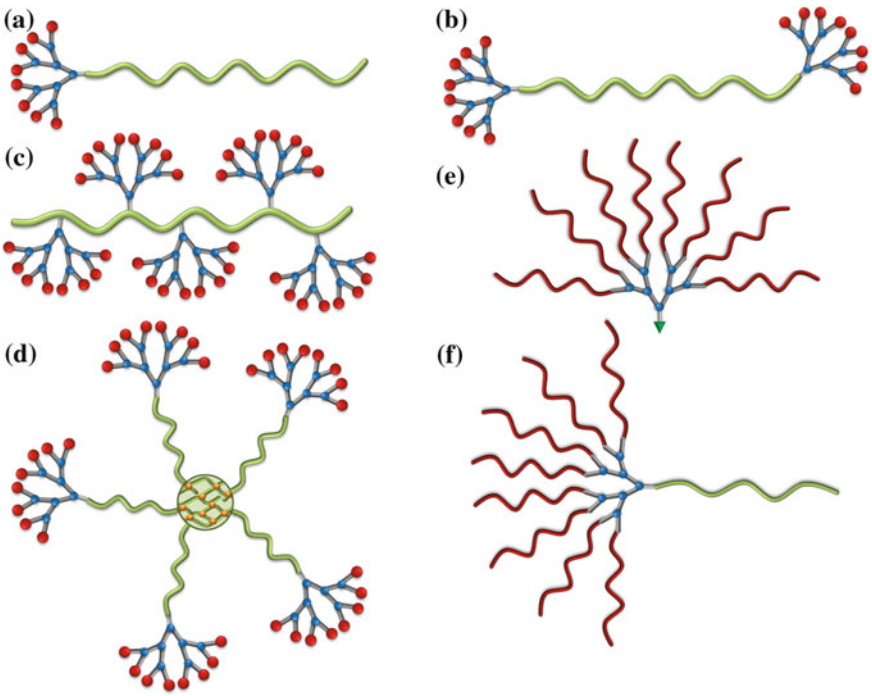

Fig. 1.11 Idealised graphical representation of various dendritic polymer architectures: **a** linear-dendritic (LD) hybrid; **b** DLD hybrid; **c** dendronised linear polymer; **d** dendronised star polymer; **e** DL_x hybrid; **f** LDL_x hybrid

Dendronised functionalised core cross-linked star polymers (Fig. 1.11d) were reported by Hawker and coworkers in 2007 [95]. They utilised bis-MPA based dendrons (G1–G5) with an alkyl halide at the focal point which was capable of initiating an ATRP polymerisation. The dendron initiators were used to polymerise styrene and at high conversion DVB was added therefore forming dendron functional star polymers via the 'arm-first' approach [96].

Similar structures have been synthesised by Hawker and coworkers in 2012, consisting of a hybrid dendritic block copolymers based on a four arm star PEG with cationic G2 or G4 dendrons tethered at each chain end and the corresponding two arm hybrid dendrimers [97]. These hybrid materials showed an enhanced cell internalisation with increasing amino functionality and endosomal escape, and efficient binding to DNA for the four arm dendritic hybrid.

DL_x hybrids refer to dendrons with linear polymers attached to the periphery of the dendron (Fig. 1.11e). An LDL_x hybrid refers to a dendron with linear polymer chains attached to the periphery and focal point of the dendron (Fig. 1.11f). Techniques to synthesise these types of materials include the ring opening polymerisation (ROP) of ε-caprolactone initiated from the dendron (PAMAM) periphery, followed by Cu catalysed azide-alkyne 'click' (CuAAC) reaction of a

PEG to the focal point [98]. The material properties, such as crystallisation properties and self-assembly in micelles or vesicles, were investigated. Bis-MPA based dendrons have also been used to produce LDL hybrids in this manner (i.e. the ROP of ε-caprolactone from the dendron periphery), however, utilising thiol-ene as well as CuAAC 'click' reactions at the dendron focal point [99, 100]. The applications of these bis-MPA based amphiphilic LDL hybrids were subsequently studied; micelles were prepared with successful doxorubicin loading [99], and the formation of various honeycomb films was shown to be affected by the different combinations of hydrophobic/philic blocks [100].

1.3 Atom Transfer Radical Polymerisation (ATRP)

ATRP was first reported independently by Wang and Matyjaszewski [101], and Sawamoto and co-workers [102] in 1995. Since then ATRP has become a well-known polymerisation technique with a huge scope for initiator, monomer, catalyst and ligand chemistries. This polymerisation technique has become extremely useful in the preparation of functional polymers [103–105].

ATRP involves an initiating species bearing a halogen atom, R-X, a transition metal catalyst (e.g. CuCl) and a ligand. The reaction lies in an equilibrium, summarised in Scheme 1.6 and described below.

The transition metal catalyst, M_t^n/L abstracts the halogen from the initiating species, R-X, to form the oxidised species $X\text{-}M_t^{n+1}/L$ and the initiating radical species R•, with a rate constant of activation k_{act}. The initiating radical, R•, reacts with the vinyl group of the monomer to give a radical active centre, which is then available for propagation by further reaction with monomer units with the rate constant of propagation k_p. Termination reactions (k_t) may also occur, usually as coupling or disproportionation, however, they are minimal during the reaction. The polymerisation rate is determined by the equilibrium constant K_{eq} ($K_{eq} = k_{act}/k_{deact}$) in the absence of any side reactions other than radical termination by coupling or disproportionation [106]. The initiation, propagation and termination steps are described individually in Scheme 1.7, using Cu^I as the transition metal.

Control over the polymerisation is maintained as long as, firstly, the initiation rate is fast so as to provide a constant concentration of propagating polymer chains, and secondly, due to the dynamic equilibrium between active and dormant radical species. This equilibrium lies heavily towards the dormant species, therefore reducing

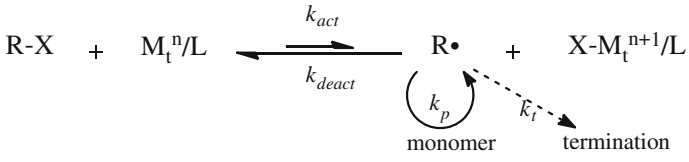

Scheme 1.6 Dynamic equilibrium in ATRP

Initiation

$$R{-}X + Cu^{I}X/Ligand \underset{}{\overset{K_{eq}}{\rightleftharpoons}} R^{\bullet} + Cu^{II}X_2/Ligand$$

$$R^{\bullet} + monomer \xrightarrow{k_p} P_1^{\bullet}$$

Propagation

$$P_n{-}X + Cu^{I}X/Ligand \underset{}{\overset{K_{eq}}{\rightleftharpoons}} P_n^{\bullet} + Cu^{II}X_2/Ligand$$

$$P_n^{\bullet} + monomer \xrightarrow{k_p} P_{n+1}^{\bullet}$$

Termination

$$P_n^{\bullet} + P_m^{\bullet} \xrightarrow{k_t} P_{n+m}$$

Scheme 1.7 Mechanism of ATRP

the number of reactive chain ends present at any one time and so reducing the possibility of unwanted side reactions, which result in higher molecular weights and broader polydispersities. It is the mechanism of the reaction that controls the possible side reactions and allows the synthesis of polymers with narrow dispersity (Đ) whose number average molecular weight depends directly on the amount of initiator used in the reaction. Due to the use of a radical polymerisation technique and transition metal catalyst, care must be taken to ensure no oxygen is present, which would scavange radicals, terminate the polymerisation and oxidise the copper catalyst.

1.3.1 Kinetics for ATRP

Matyjaszewski et al. described the rate laws for ATRP below using the initiation and propagation equations from Scheme 1.7 [107].

$$K_{eq} = \frac{k_{act}}{k_{deact}} = \frac{[P\cdot]\left[Cu^{II}X_2\right]}{\left[Cu^{I}X\right][PX]} \tag{1.2}$$

$$R_p = k_{app}[M] = k_p[P\cdot][M] = k_p K_{eq}[RX]\frac{\left[Cu^{I}X\right]}{\left[Cu^{II}X_2\right]}[M] \tag{1.3}$$

The rate law shown in Eq. (1.3) is valid assuming a fast pre-equilibrium, that the propagation rate (k_p) remains constant, and that termination is negligible. The rate of propagation (R_p) is first order with respect to the monomer concentration [M], initiator concentration [RX] and activator concentration [$Cu^{I}X$].

1.4 Drug Delivery by Encapsulation Using Polymeric Nanomaterials

Drug delivery utilising polymeric nanomaterials is usually employed for either (i) site specific targeting or (ii) improving the pharmacokinetics of a drug [108]. These two approaches for drug delivery utilising nanomedicine are highlighted in Fig. 1.12.

Site specific targeting (Fig. 1.12(i)) is mainly used for the targeting of cancerous tumours in the case for drug delivery. If the anti-cancer drugs can be delivered only to the tumorous tissues specifically, and not accumulate in normal tissues, this would present a much more patient acceptable form of chemotherapy with limited off target toxicity.

Improving drug pharmacokinetics (Fig. 1.12(ii)) is desirable for those drugs that have poor bioavailability and/or rapid clearance, and therefore require high doses to be given to produce the desired therapeutic effect. This can cause the amount of drug in the systemic circulation to become too high and cause toxicity (Fig. 1.12(ii.a)), however, if the dosing is incorrect and too little drug enters the systemic circulation

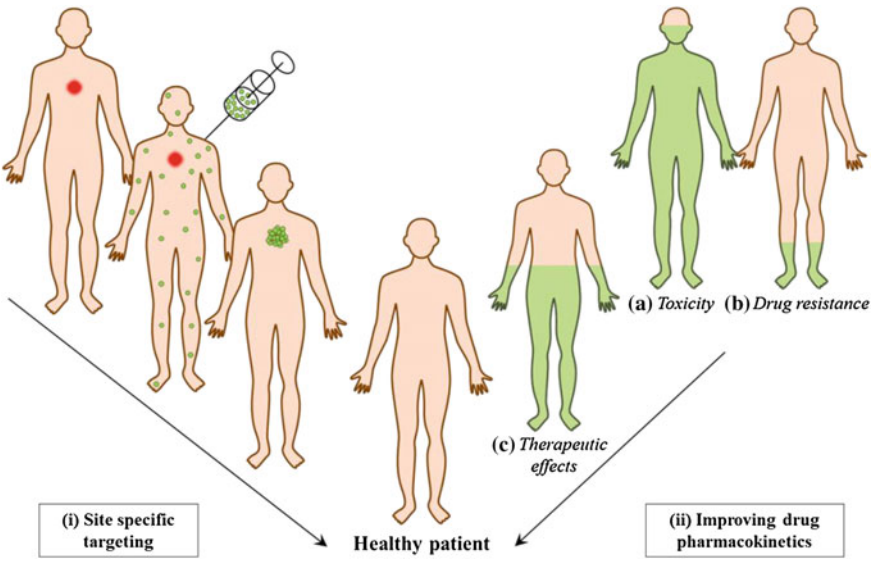

Fig. 1.12 Schematic representing two different approaches for using nanomaterials for drug delivery

drug resistance can occur (Fig. 1.12(ii.b)). This is particularly important when treating HIV as toxicity causes side-effects which leads to patients being non-adherent with their therapy regimens and cessation of drug taking, however, if drug resistance occurs, a new mixture of anti-retroviral drugs needs to be administered to prevent acceleration of the virus. Sustained release over a long period of time would also be highly advantageous to reduce the number of tablets needed to be taken by patients.

Various research groups have investigated the use of polymeric materials for drug delivery, more specifically nanomaterials. Nanomaterials can be described as a material being between 1 and 1000 nm in one dimension [109]. Polymeric nanomaterials which have been reported for drug delivery by encapsulation include micelles, vesicles and nanoparticles (see Fig. 1.13) [109–111]. Some formulations of micelles, vesicles and nanoparticles that have been approved for clinical use or are currently in clinical trials are shown in Table 1.2. Dendrimers are also a different class of nanomaterials which have been utilised for drug delivery by encapsulation, see above (Sect. 1.1.3).

The first requirement of a nanomaterial is that it is biocompatible, therefore the nanomaterial is non-toxic, and if oral delivery is being targeted it must also survive the stomach and small intestine and be absorbed across the gut epithelium to enter the systemic circulation. Biocompatibility is often achieved by incorporating a PEG coating around the nanomaterial [108]. PEG is a well-known biocompatible polymer which has been known to give nanomaterials 'stealth' in the system circulation, preventing the binding of proteins which can cause clearance of materials from the circulation.

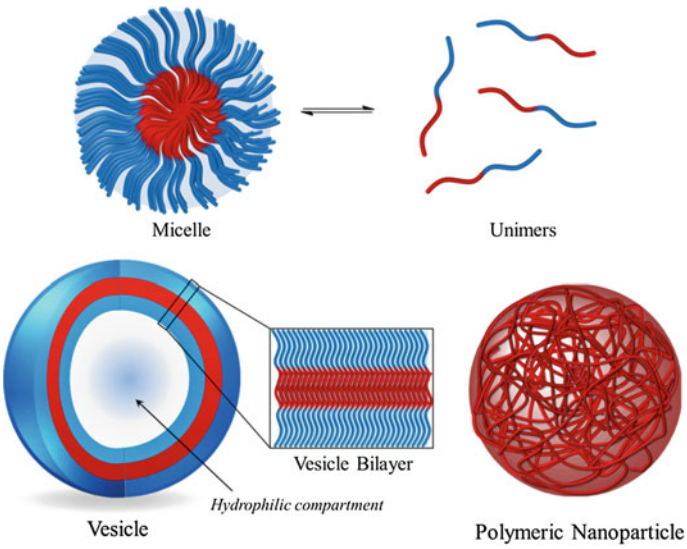

Fig. 1.13 Graphical representation of various types of polymeric nanomaterial utilised in the encapsulation of drugs for drug delivery purposes (not drawn to scale). *Blue sections* represent hydrophilic polymer chains and *red sections* represent hydrophobic polymer chains

Table 1.2 Nanomaterials approved or in clinical trials for various therapies

Nanocarrier type	Name	Drug/nanomaterial	Administration	Indication	Status
Nanoparticles	Abraxane	Paclitaxel bound albumin nanoparticles	Intravenous	Advanced breast cancer, advanced non-small cell lung cancer and advanced pancreatic cancer patients	Approved
	Transdrug	Doxorubicin	Intravenous	Hepatocarcinoma	Approved
	Amphotec	Colloidal suspension of lipid based amphotericin B	Subcutaneous	Invasive aspergillosis patients who are refractory to or intolerant of conventional amphotericin B	Approved
Micelles	Nanoxel	Paclitaxel micelles	Intravenous	Advanced breast cancer	Phase I
	Estrasorb	Estradiol hemihydrate micellar nanoparticles (emulsion)	Transdermal	Reduction in vasomotor symptoms such as hot flushes and night sweats, in menopausal women	Approved
	Genexol-PM	Paclitaxel	Intravenous	Various breast, lung and pancreatic cancer	Phase II-III
	SP1049C	Pluronic block-copolymer doxorubicin micelle	Intravenous	Oesophageal carcinoma	Phase II
Vesicles	Myocet	Vesicle encapsulated doxorubicin-citrate complex	Intravenous	Cardio-protective formulation of doxorubicin used in late stage metastatic breast cancer	Approved
	Doxil	PEGylated doxorubicin HCl vesicles	Intravenous	Metastatic ovarian cancer and AIDS-related Kaposi's sarcoma	Approved
	DaunoXome	Encapsulated-duanorubicin citrate vesicles	Intravenous	Advanced HIV related Kaposi's sarcoma	Approved
	AmBisome	Amphotericin B vesicles	Intravenous	Fungal infections	Approved
	Diprivan	Propofol vesicles	Intravenous	Anaesthetic	Approved

Adapted from Refs. [110, 111]

1.4.1 Polymeric Micelles

Polymeric micelles are self-assembled aggregates of amphiphilic polymers in a colloidal solution, which can be organic or aqueous, however, here only aqueous micelle formulations will be discussed. The critical micelle concentration (CMC) is the concentration of the polymer required for micelle formation; below the CMC the polymers are dissolved in the aqueous phase, usually as unimers and above the CMC they self-assemble into micelles which are in equilibrium with the unimers (see Fig. 1.13). Polymeric micelles are usually formed from the self-assembly of an amphiphilic diblock or triblock copolymer in a core-shell arrangement [112]. The core consists of the hydrophobic segment of the polymer which allows for encapsulation of hydrophobic drugs. The core is stabilised by a corona which is composed of the hydrophilic segment of the polymer.

Polymeric micelles can be used to enhance the solubility of hydrophobic drugs by encapsulation within the hydrophobic core [113]. This is referred to as solubilising the hydrophobic drug and can enhance the bioavailability upon oral administration, reduce adverse effects and enhance permeation across biological membranes, for example the blood-brain barrier when administered intravenously [113].

1.4.2 Vesicles

A vesicle is a spherical structure consisting of a lamellar bilayer and can also be described as liposomes, polymersomes or nanocapsules (see Fig. 1.13) [114]. Vesicles are promising for drug delivery as they have the capability to solubilise hydrophilic and hydrophobic drugs. Hydrophilic drugs can be encapsulated in the internal hydrophilic compartment whilst hydrophobic drugs can be incorporated into the hydrophobic core of the bilayer.

1.4.3 Nanoparticles

Polymeric nanoparticles, sometimes described as nanospheres, are solid colloidal particles (Fig. 1.13) in the range 10–1000 nm. They consist of a hydrophobic core, are static in structure and can be stabilised via charge or steric repulsion [115]. Preparation methods include either dispersion of preformed polymers or polymerisation of monomers in a mini- or micro-emulsion polymerisation [116, 117].

Methods to produce nanoparticle dispersions from preformed polymers include solvent evaporation, nanoprecipitation, salting-out, dialysis and supercritical fluid technology [116]. Nanoprecipitation is the most relevant in the context of this thesis and will be discussed further.

1.4.4 Nanoparticles by Nanoprecipitation

Nanoprecipitation is a solvent exchange method for the dispersion of polymeric nanoparticles utilising preformed polymers and was first described by Fessi et al. in 1989 [118]. The polymer is dissolved in a good solvent (usually a volatile, water miscible solvent which is easily removed after the process, e.g. acetone) and added to an anti-solvent (usually water) whilst undergoing stirring. This process can be reversed; the anti-solvent can be added to the polymer dissolved in the good solvent. Various nanoparticle formulations prepared via nanoprecipitations are shown in Table 1.3. The basic principle behind the technique involves the rapid diffusion of solvent into the anti-solvent phase and subsequent decrease in the interfacial tension between the two phases. This, increases surface area and leads to the formation of small droplets of organic solvent [116]. Lince et al. described the process as being comprised of three stages; nucleation, growth and aggregation [119].

The rate of each of these steps determines the resulting particle size and the driving force of these phenomena is the ratio of polymer concentration over the solubility of the polymer in the solvent mixture. The separation between the nucleation and the growth stages is the key factor for uniform particle formation. Ideally, operating conditions should allow a high nucleation rate strongly dependent on supersaturation and low growth rate.

1.5 Aims of the Project

The aim of this Ph.D. project has been to produce dendrimer-like materials which mimic the surface functionality of a dendrimer with much higher molecular weights and size than conventional dendrimers, whilst maintaining a facile synthesis. These materials have been termed “hyperbranched-polydendrons” (*hyp*-polydendron), a termed coined by the research group. The synthetic aims of this work, subsequent aims with regards to nanoparticle formulations utilising these materials and the assessment of their suitability towards drug delivery applications are discussed below.

1.5.1 Synthetic Aims

The synthetic aims of this work are summarised in Fig. 1.14; as previously discussed the synthesis of dendrimers (Fig. 1.14, **1**) has been reported via various synthetic methodologies. The combination of dendron chemistry and linear polymers to produce hybrid materials is also well studied utilising a dendron as an initiator for the linear polymerisation (Fig. 1.14, **2**). The copolymerisation of mono- and bi-functional monomers to produce high molecular weight soluble branched polymers is also an established phenomenon (Fig. 1.14, **3**). Therefore the

Table 1.3 Nanoparticle formulations produced via the nanoprecipitation approach

Polymer	Guest molecule	Solvent	Non-solvent	Surfactant	Particle diameter (nm)	References
PLGA	Curcumin	Acetone	Water	PVA	95–560	[120]
PLGA	DiI loaded	Acetone/ethanol	Water	Tween 20	63–90	[121]
PLGA	–	Acetone Acetonitrile	Water	–	165 ± 5 164 ± 4	[122]
PLGA-PEG	Docetaxel	Acetone, DMF, Acetonitrile, THF	Water	–	70–250	[123]
PBCA	Chlorambucil	Acetone	Water	Pluronic F 68 Polysorbate 80 Dextran	269 ± 4 210 ± 5 238 ± 5	[124]
Allylic starch	–	Acetone	Water	–	270	[125]
PHB	Nattokinase	Acetone	Water	Tween 80	100–125	[126]
Dextran ester	Conjugated ibuprofen	Acetone	Water	–	77	[127]
PCL diol	Au nano-rods	Chloroform	Water	Pluronic F 127	17.4	[128]
Eudragit L100-55	Tacrolimus	Acetone/ethanol	Water	–	120	[129]
PCA	Gemcitabine	Ethanol/water	Water	–	150	[130]
PLA	–	THF	Water	–	100–300	[131]
PLA	MTP-Chol	Acetone	Water	Epikuron 170	200 ± 50	[132]
PCL	Griseofulvin	Acetone	Water	Span 80/Tween 80	250–400	[133]
PCL	Primidone	Acetone	Water	PE/F68	308–352	[134]
PCL	–	Acetone	Water	–	100–1200	[119]
PHPMA	–	Acetone	Water	–	60–800	[135]
PMMA	Ketoprofen	THF	Water	Cremophor ELP	70–210	[136]
PS	–	THF	Water or water/NaCl	–	50–300	[137]
PS PMMA PCL	–	Acetone	Water	–	105–140 115–210 270–315	[138]

Adapted and edited from Ref. [116]

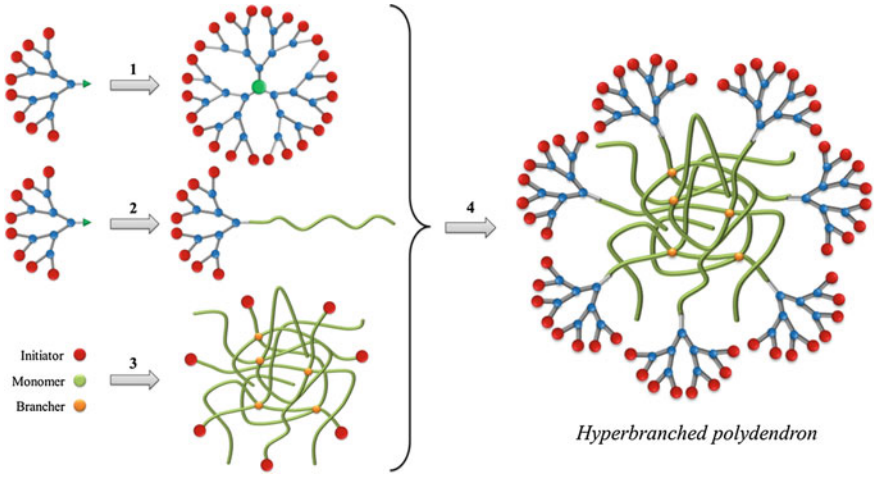

Fig. 1.14 Schematic representation of the synthetic aims of this work; *hyp*-polydendron, shown with idealised structures

combination of these chemistries to produce a high molecular weight branched polymer containing dendron functionality at the end of every polymer chain (Fig. 1.14, **4**) appears feasible.

The impact of varying different features of the *hyp*-polydendrons would then be evaluated, for example using different generation dendron initiators, altering the degree of polymerisation (DP_n) of the primary chains in the *hyp*-polydendron core and the effect of statistically mixing initiators of different functionalities (dendron and non-dendron) in the reaction mixture.

1.5.2 Materials Aims

These *hyp*-polydendrons will be utilised for the formulation of nanoparticles via a nanoprecipitation approach (see Sect. 1.4.4). It was hypothesised that under aqueous conditions the hydrophobic *hyp*-polydendron core would collapse and ultimately precipitate unless stabilising hydrophilic groups were used. Therefore the behaviour of hydrophobic materials in various organic solvents was targeted for initial investigation, tuning the solvents used depending on the solubility of various components of the hydrophobic *hyp*-polydendrons. Nanoprecipitation of *hyp*-polydendrons into water would also be studied, to assess the influence of mixing hydrophilic macroinitiators and hydrophobic dendron initiators.

It was hypothesised that this approach would produce polymeric nanoparticles which contained a hydrophobic core for the encapsulation of hydrophobic guest molecules and dendron moieties to introduce high surface functionality, therefore emulating a dendrimer-like structure on a much larger scale, see Fig. 1.15.

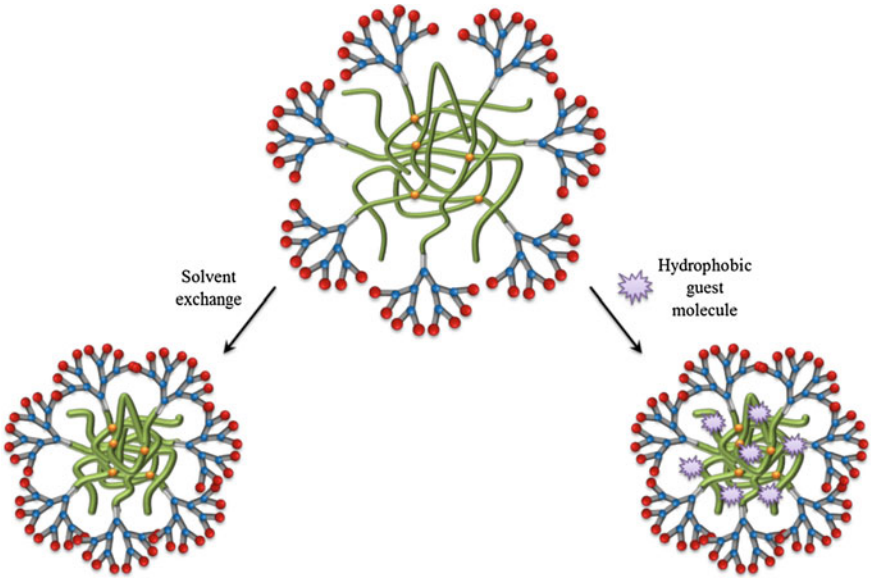

Fig. 1.15 Idealised graphical representation of the materials aims of the project

1.5.3 Overview of Subsequent Experimental Chapters

1.5.3.1 Chapter 2—Synthesis and Characterisation of *Hyp*-polydendron Materials and Subsequent Nanoparticle Formation

Chapter 2 highlights the initial study of novel *hyp*-polydendrons by comparing **G1** and **G2** dendron ATRP initiators with a commercially available initiator, ethyl bromo isobutyrate (**EBiB**), for the homopolymerisation of 2-hydroxypropyl methacrylate (HPMA) to afford linear dendritic and linear polymers with varying degrees of polymerisation (DP_n = 20, 50 and 100). The copolymerisation of HPMA with a divinyl monomer, EGDMA, led to the formation of high molecular weight branched polymers bearing the initiator functionality at the end of each chain, therefore in the case of a dendron initiator, forming *hyp*-polydendrons. The library of polymers synthesised were studied for their self-assembly behaviour in organic solvents (acetone and hexane mixtures) and water via an aqueous nanoprecipitation approach. These two methods lead to the formation of spherical polymeric nanoparticles which had narrow polydispersities when the branched polymers and *hyp*-polydendrons were utilised, when compared with the equivalent linear polymers broader polydispersities were observed.

1.5.3.2 Monomer Choice

It is worth noting that the monomer HPMA was chosen for this project as although it is actually water soluble in the monomeric form, when polymerised pHPMA is more hydrophobic and becomes insoluble in water. The aqueous nanoprecipitation of linear and branched pHPMA has also been previously reported [135], initiated with the commercially available EBiB initiator. Therefore it is hypothesised that the hydrophobic pHPMA would be suitable for the encapsulation of hydrophobic molecules in the core of the nanoparticles.

1.5.3.3 Chapter 3—Mixing Dendron and PEG Initiators for the Polymerisation of Branched pHPMA and Aqueous Nanoparticle Formation

Chapter 3 focuses on the copolymerisation of HPMA and EGDMA using mixed initiator systems, where the statistical incorporation of a **G2** dendron initiator and a PEG macroinitiator at various ratios produced a series of *hyp*-polydendrons with varying amphiphilicity. The aqueous nanoprecipitations performed using these materials showed that generally nanoparticle size increases with the initial and final concentration of polymer used. The series of nanoparticles formed contained varying internal environments, due to the ratio of initiators used, which were probed with two different hydrophobic fluorescent dyes (Nile red and pyrene). These dye loaded particles were also assessed for their cytotoxicity to cells. The particles showed no toxicity to Caco-2 cells, and also showed permeability through a Caco-2 cell transwell plate assay, designed to model the permeability of compounds through the small intestine into the systemic circulation. Further evaluation of these materials was halted due to stability issues in model physiological conditions.

1.5.3.4 Chapter 4—Mixing Dendron and PEG Initiators for the Polymerisation of Branched pHPMA and Formation of Sterically Stabilised Nanoparticles

Chapter 4 also assesses the copolymerisation of HPMA and EGDMA using a mixed initiator system, however, a new G2 dendron initiator was used (now labelled **G2′** due to a different synthetic route) with a longer PEG macroinitiator. The longer PEG macroinitiator was chosen to impart more steric stabilisation upon the nanoparticles formed via nanoprecipitation of these materials. The composition of the *hyp*-polydendrons in this chapter was not only altered by varying the ratio of the two initiators, but also by varying the targeted degree of polymerisation of the HPMA. This altered hydrophobic/hydrophilic content of the *hyp*-polydendrons

quite dramatically and resulted in a variation of results upon aqueous nanoprecipitation. Pharmacological analysis of the *hyp*-polydendrons highlighted specific properties of the nanoparticles required to give a pharmacologically beneficial outcome, i.e. permeability through the intestinal epithelium model experiment. A lead candidate was chosen for further pharmacological assessment, still ongoing at the time of writing.

1.5.3.5 Chapter 5—*Hyp*-polydendrons; Studies of Nanoprecipitation Behaviour

Chapter 5 discusses in further detail the effects of varying the hydrophobic and hydrophilic content of the *hyp*-polydendrons when studying their nanoprecipitation behaviour. Tuning the amount of hydrophobic HPMA to hydrophilic PEG is required to produce the *hyp*-polydendrons with the desired properties upon nanoprecipitations.

This chapter also highlights some fundamental nanoprecipitation experiments where the lower molecular weight fractions of select *hyp*-polydendron samples were removed via dialysis in organic solvents (IPA and MeOH were chosen). The subsequent nanoprecipitation of the high and low molecular weight fractions showed that the high molecular weight fractions produce nanoparticles with more desirable properties (i.e. low polydispersities) than the low molecular weight fractions. The mixing of the equivalent linear dendritic polymer with the high molecular weight fraction revealed that the amount of highly branched material needed to form nanoparticles with these desirable properties is very low (1 wt% or less).

The final piece of experimental work highlighted in this chapter is the encapsulation of two different fluorescent dyes within the nanoparticles analysed by Förster resonance energy transfer (FRET). The two dyes used are described as a FRET pair and one is a donor and the other an acceptor fluorophore. When in close proximity (<10 nm) energy transfer is observed from the donor to the acceptor and this change in fluorescence can determine whether the two fluorophores are indeed encapsulated within the same nanoparticle. Upon mixing the two individually loaded nanoparticle samples an increase in FRET was observed overtime, suggesting the movement of the fluorophores between nanoparticles.

Overall, the research presented within this thesis represents the formation of a new polymeric material class and the subsequent study of the materials within a pharmacological relevant manner. The behaviour of the materials is investigated with respect to the impact of variation within their structural components and the goal is to assess their toxicity to cells and the permeation across the Caco-2 in vitro model of the human small intestinal mucosa to predict the absorption of orally administered drugs or materials. As such, proof-of-concept will be developed for the synthesis and potential application of these novel systems.

References

1. D.A. Tomalia. J.M.J. Fréchet, *Dendrimers and other Dendritic Polymers* (John Wiley & Sons Ltd., UK, 2001)
2. E. Buhleier, W. Wehner, F. Vögtle, Synthesis-Stuttgart **2**, 155–158 (1978)
3. D.A. Tomalia, H. Baker, J. Dewald, M. Hall, G. Kallos, S. Martin, J. Roeck, J. Ryder, P. Smith, Polym. J. **17**, 117–132 (1985)
4. G.R. Newkome, Z.Q. Yao, G.R. Baker, V.K. Gupta, J. Org. Chem. **50**, 2003–2004 (1985)
5. F. Aulenta, W. Hayes, S. Rannard, Eur. Polym. J. **39**, 1741–1771 (2003)
6. C.J. Hawker, J.M.J. Fréchet, J. Am. Chem. Soc. **112**, 7638–7647 (1990)
7. S.E. Stiriba, H. Frey, R. Haag, Angew. Chem. Int. Edit. **41**, 1329–1334 (2002)
8. C.C. Lee, J.A. MacKay, J.M.J. Fréchet, F.C. Szoka, Nat. Biotechnol. **23**, 1517–1526 (2005)
9. M.J. Cloninger, Curr. Opin. Chem. Biol. **6**, 742–748 (2002)
10. D. Astruc, F. Chardac, Chem. Rev. **101**, 2991–3023 (2001)
11. G.E. Oosterom, J.N.H. Reek, P.C.J. Kamer, P.W.N.M. van Leeuwen, Angew. Chem. Int. Edit. **40**, 1828–1849 (2001)
12. A. Adronov, J.M.J. Fréchet, Chem. Commun., 1701–1710 (2000)
13. U. Boas, P.M.H. Heegaard, Chem. Soc. Rev. **33**, 43–63 (2004)
14. E.R. Gillies, J.M.J. Fréchet, Drug Discov. Today **10**, 35–43 (2005)
15. C. Dufes, I.F. Uchegbu, A.G. Schatzlein, Adv. Drug Deliv. Rev. **57**, 2177–2202 (2005)
16. R.F. Barth, D.M. Adams, A.H. Soloway, F. Alam, M.V. Darby, Bioconjug. Chem. **5**, 58–66 (1994)
17. C.Z.S. Chen, S.L. Cooper, Adv. Mater. **12**, 843–846 (2000)
18. S. Supattapone, K. Nishina, J.R. Rees, Biochem. Pharmacol. **63**, 1383–1388 (2002)
19. R. Rupp, S.L. Rosenthal, L.R. Stanberry, Int. J. Nanomed. **2**, 561–566 (2007)
20. Y. Chang, N. Liu, L. Chen, X. Meng, Y. Liu, Y. Li, J. Wang, J. Mater. Chem. **22**, 9594–9601 (2012)
21. G. Navarro, C.T. de ILarduya, Nanomed-Nanotechnol., **5**, 287–297 (2009)
22. J.D. Eichman, A.U. Bielinska, J.F. Kukowska-Latallo, J.R. Baker Jr, Pharm. Sci. Technol. Today **3**, 232–245 (2000)
23. O. Taratula, O.B. Garbuzenko, P. Kirkpatrick, I. Pandya, R. Savla, V.P. Pozharov, H. He, T. Minko, J.Control. Release **140**, 284–293 (2009)
24. Y. Omidi, A.J. Hollins, R.M. Drayton, S. Akhtar, J. Drug Target. **13**, 431–443 (2005)
25. I.J. Majoros, C.R. Williams, J.R. Baker, Curr. Top. Med. Chem. **8**, 1165–1179 (2008)
26. J.M. McCarthy, M. Franke, U.K. Resenberger, S. Waldron, J.C. Simpson, J. Tatzelt, D. Appelhans, M.S. Rogers, PLoS ONE **8**(1), e55282 (2013)
27. T.D. McCarthy, P. Karellas, S.A. Henderson, M. Giannis, D.F. O'Keefe, G. Heery, J.R.A. Paull, B.R. Matthews, G. Holan, Mol. Pharmaceut. **2**, 312–318 (2005)
28. S.R. Meyers, F.S. Juhn, A.P. Griset, N.R. Luman, M.W. Grinstaff, J. Am. Chem. Soc. **130**, 14444–14445 (2008)
29. L. Balogh, D.R. Swanson, D.A. Tomalia, G.L. Hagnauer, A.T. McManus, Nano Lett. **1**, 18–21 (2001)
30. P.V. Kumar, A. Asthana, T. Dutta, N.K. Jain, J. Drug Target. **14**, 546–556 (2006)
31. A. Agarwal, U. Gupta, A. Asthana, N.K. Jain, Biomaterials **30**, 3588–3596 (2009)
32. C. Kojima, K. Kono, K. Maruyama, T. Takagishi, Bioconjug. Chem. **11**, 910–917 (2000)
33. A.K. Patri, J.F. Kukowska-Latallo, J.R. Baker, Adv. Drug Deliv. Rev. **57**, 2203–2214 (2005)
34. D. Bhadra, S. Bhadra, S. Jain, N.K. Jain, Int. J. Pharm. **257**, 111–124 (2003)
35. M.J. Liu, K. Kono, J.M.J. Fréchet, J. Controlled Release **65**, 121–131 (2000)
36. V. Gajbhiye, N. Ganesh, J. Barve, N.K. Jain, Eur. J. Pharm. Sci. **48**, 668–679 (2013)
37. N. Malik, E.G. Evagorou, R. Duncan, Anti-Cancer Drug **10**, 767–776 (1999)
38. K. Kono, M.J. Liu, J.M.J. Fréchet, Bioconjug. Chem. **10**, 1115–1121 (1999)
39. R.X. Zhuo, B. Du, Z.R. Lu, J. Control. Release **57**, 249–257 (1999)

40. A. Bosnjakovic, M.K. Mishra, W.P. Ren, Y.E. Kurtoglu, T. Shi, D.N. Fan, R.M. Kannan, Nanomed-Nanotechnol. **7**, 284–294 (2011)
41. S. Svenson, D.A. Tomalia, Adv. Drug Deliver. Rev. **57**, 2106–2129 (2005)
42. J.A. Peters, J. Huskens, D.J. Raber, Prog. Nucl. Mag. Res. Sp. **28**, 283–350 (1996)
43. H. Kobayashi, M.W. Brechbiel, Adv. Drug Deliver. Rev. **57**, 2271–2286 (2005)
44. R.H.E. Hudson, M.J. Damha, J. Am. Chem. Soc. **115**, 2119–2124 (1993)
45. T.W. Nilsen, J. Grayzel, W. Prensky, J. Theor. Biol. **187**, 273–284 (1997)
46. www.genisphere.com/our-technology
47. J.R. Mora, T.L. Zielinski, B.P. Nelson, R.C. Getts, Biotechniques **44**, 815–818 (2008)
48. T. Zhou, P. Chen, L. Niu, J. Jin, D.H. Liang, Z.B. Li, Z.Q. Yang, D.S. Liu, Angew. Chem. Int. Edit. **51**, 11271–11274 (2012)
49. P. Singh, Biotechnol. Appl. Bioc. **48**, 1–9 (2007)
50. J. Lim, M. Kostiainen, J. Maly, V.C.P. da Costa, O. Annunziata, G.M. Pavan, E.E. Simanek, J. Am. Chem. Soc. **135**, 4660–4663 (2013)
51. P.G. de Gennes, H. Hervet, J. Phys. Lett-Paris **44**, L351–L360 (1983)
52. P.J. Flory, J. Am. Chem. Soc. **74**, 2718–2723 (1952)
53. Y.H. Kim, O.W. Webster, Abstr. Pap. Am. Chem. S, **196**, 104-POLY (1988)
54. Y.H. Kim, O.W. Webster, J. Am. Chem. Soc. **112**, 4592–4593 (1990)
55. Y.H. Kim, J. Polym. Sci. Pol. Chem. **36**, 1685–1698 (1998)
56. S.G. Gaynor, J.S. Wang, K. Matyjaszewski, Macromolecules **28**, 8051–8056 (1995)
57. N. Hadjichristidis, M. Pitsikalis, S. Pispas, H. Iatrou, Chem. Rev. **101**, 3747–3792 (2001)
58. R.M. England, S. Rimmer, Polym. Chem. **1**, 1533–1544 (2010)
59. M. Szwarc, Nature **178**, 1168–1169 (1956)
60. H. Staudinger, E. Husemann, Ber. Dtsch. Chem. Ges. **68**, 1618–1634 (1935)
61. M. Antonietti, C. Rosenauer, Macromolecules **24**, 3434–3442 (1991)
62. T. He, D.J. Adams, M.F. Butler, C.T. Yeoh, A.I. Cooper, S.P. Rannard, Angew. Chem. Int. Edit. **46**, 9243–9247 (2007)
63. P.J. Flory, J. Am. Chem. Soc. **63**, 3096–3100 (1941)
64. P.J. Flory, J. Am. Chem. Soc. **63**, 3091–3096 (1941)
65. P.J. Flory, J. Am. Chem. Soc. **63**, 3083–3090 (1941)
66. W.H. Stockmayer, H. Jacobson, J. Chem. Phys. **11**, 393–393 (1943)
67. W.H. Stockmayer, J. Chem. Phys. **11**, 45–55 (1943)
68. W.H. Stockmayer, J. Chem. Phys. **12**, 125–131 (1944)
69. F. Isaure, P.A.G. Cormack, S. Graham, D.C. Sherrington, S.P. Armes, V. Bütün, Chem. Commun., **9**, 1138–1139 (2004)
70. J. Rosselgong, S.P. Armes, W.R.S. Barton, D. Price, Macromolecules **43**, 2145–2156 (2010)
71. W.W. Li, J.A. Yoon, M.J. Zhong, K. Matyjaszewski, Macromolecules **44**, 3270–3275 (2011)
72. J. Rosselgong, S.P. Armes, Macromolecules **45**, 2731–2737 (2012)
73. P. Polanowski, J.K. Jeszka, W.W. Li, K. Matyjaszewski, Polymer **52**, 5092–5101 (2011)
74. N. O'Brien, A. McKee, D.C. Sherrington, A.T. Slark, A. Titterton, Polymer **41**, 6027–6031 (2000)
75. Z.M. Wang, J.P. He, Y.F. Tao, L. Yang, H.J. Jiang, Y.L. Yang, Macromolecules **36**, 7446–7452 (2003)
76. C.J. Hawker, J.M.J. Fréchet, R.B. Grubbs, J. Dao, J. Am. Chem. Soc. **117**, 10763–10764 (1995)
77. J.M.J. Fréchet, M. Henmi, I. Gitsov, S. Aoshima, M.R. Leduc, R.B. Grubbs, Science **269**, 1080–1083 (1995)
78. C. Gao, D. Yan, Prog. Polym. Sci. **29**, 183–275 (2004)
79. C.F. Jiang, Y.Q. Shen, S.P. Zhu, D. Hunkeler, J. Polym. Sci. Pol. Chem. **39**, 3780–3788 (2001)
80. I. Bannister, N.C. Billingham, S.P. Armes, S.P. Rannard, P. Findlay, Macromolecules **39**, 7483–7492 (2006)
81. W.Y. Huang, H.J. Yang, X.Q. Xue, B.B. Jiang, J.H. Chen, Y. Yang, H.T. Pu, Y. Liu, D.L. Zhang, L.Z. Kong, G.Q. Zhai, Polym. Chem. **4**, 3204–3211 (2013)

82. H.F. Gao, K. Matyjaszewski, Prog. Polym. Sci. **34**, 317–350 (2009)
83. T. He, D.J. Adams, M.F. Butler, A.I. Cooper, S.P. Rannard, J. Am. Chem. Soc. **131**, 1495–1501 (2009)
84. I. Gitsov, J. Polym. Sci. Pol. Chem. **46**, 5295–5314 (2008)
85. A. Carlmark, E. Malmström, M. Malkoch, Chem. Soc. Rev. **42**, 5858–5879 (2013)
86. F. Wurm, H. Frey, Prog. Polym. Sci. **36**, 1–52 (2011)
87. H. Frauenrath, Prog. Polym. Sci. **30**, 325–384 (2005)
88. E.R. Gillies, T.B. Jonsson, J.M.J. Fréchet, J. Am. Chem. Soc. **126**, 11936–11943 (2004)
89. I. Gitsov, K.L. Wooley, J.M.J. Fréchet, Angew. Chem. Int. Edit. **31**, 1200–1202 (1992)
90. Y.Y. Chang, C. Kim, J. Polym. Sci. Pol. Chem. **39**, 918–926 (2001)
91. R.J. Amir, L. Albertazzi, J. Willis, A. Khan, T. Kang, C.J. Hawker, Angew. Chem. Int. Edit. **50**, 3425–3429 (2011)
92. O.C.J. Andren, M.V. Walter, T. Yang, A. Hult, M. Malkoch, Macromolecules **46**, 3726–3736 (2013)
93. A.D. Schluter, J.P. Rabe, Angew. Chem. Int. Edit. **39**, 864–883 (2000)
94. M. Malkoch, A. Carlmark, A. Wodegiorgis, A. Hult, E.E. Malmström, Macromolecules **37**, 322–329 (2004)
95. L.A. Connal, R. Vestberg, C.J. Hawker, G.G. Qiao, Macromolecules **40**, 7855–7863 (2007)
96. L.A. Connal, R. Vestberg, C.J. Hawker, G.G. Qiao, Adv. Funct. Mater. **18**, 3706–3714 (2008)
97. L. Albertazzi, F.M. Mickler, G.M. Pavan, F. Salomone, G. Bardi, M. Panniello, E. Amir, T. Kang, K.L. Killops, C. Brauchle, R.J. Amir, C.J. Hawker, Biomacromolecules **13**, 4089–4097 (2012)
98. C. Hua, S.M. Peng, C.M. Dong, Macromolecules **41**, 6686–6695 (2008)
99. P. Lundberg, M.V. Walter, M.I. Montañez, D. Hult, A. Hult, A. Nyström, M. Malkoch, Polym. Chem. **2**, 394–402 (2011)
100. M.V. Walter, P. Lundberg, D. Hult, A. Hult, M. Malkoch, Polym. Chem. **4**, 2680–2690 (2013)
101. J.S. Wang, K. Matyjaszewski, Macromolecules **28**, 7901–7910 (1995)
102. M. Kato, M. Kamigaito, M. Sawamoto, T. Higashimura, Macromolecules **28**, 1721–1723 (1995)
103. K. Matyjaszewski, J.H. Xia, Chem. Rev. **101**, 2921–2990 (2001)
104. W.A. Braunecker, K. Matyjaszewski, Prog. Polym. Sci. **32**, 93–146 (2007)
105. K. Matyjaszewski, Macromolecules **45**, 4015–4039 (2012)
106. J.H. Xia, S.G. Gaynor, K. Matyjaszewski, Macromolecules **31**, 5958–5959 (1998)
107. K. Matyjaszewski, T.E. Patten, J.H. Xia, J. Am. Chem. Soc. **119**, 674–680 (1997)
108. T.M. Allen, P.R. Cullis, Science **303**, 1818–1822 (2004)
109. R. Duncan, R. Gaspar, Mol. Pharmaceut. **8**, 2101–2141 (2011)
110. L. Zhang, F.X. Gu, J.M. Chan, A.Z. Wang, R.S. Langer, O.C. Farokhzad, Clin. Pharmacol. Ther. **83**, 761–769 (2008)
111. S. Sultana, M.R. Khan, M. Kumar, S. Kumar, M. Ali, J. Drug Target. **21**, 107–125 (2013)
112. G. Riess, Prog. Polym. Sci. **28**, 1107–1170 (2003)
113. V.P. Torchilin, J. Control. Release **73**, 137–172 (2001)
114. M. Antonietti, S. Forster, Adv. Mater. **15**, 1323–1333 (2003)
115. T. Cosgrove, *Colloid Science: Principles, Methods and Applications*, 2nd edn. (John Wiley and Sons Ltd., UK, 2010)
116. J.P. Rao, K.E. Geckeler, Prog. Polym. Sci. **36**, 887–913 (2011)
117. D. Horn, J. Rieger, Angew. Chem. Int. Edit. **40**, 4330–4361 (2001)
118. H. Fessi, F. Puisieux, J.P. Devissaguet, N. Ammoury, S. Benita, Int. J. Pharm. **55**, R1–R4 (1989)
119. F. Lince, D.L. Marchisio, A.A. Barresi, J. Colloid Interf. Sci. **322**, 505–515 (2008)
120. M.M. Yallapu, B.K. Gupta, M. Jaggi, S.C. Chauhan, J. Colloid Interf. Sci. **351**, 19–29 (2010)
121. J. Chang, Y. Jallouli, M. Kroubi, X.B. Yuan, W. Feng, C.S. Kang, P.Y. Pu, D. Betbeder, Int. J. Pharm. **379**, 285–292 (2009)

122. B.J. Nehilla, M. Bergkvist, K.C. Popat, T.A. Desaid, Int. J. Pharm. **348**, 107–114 (2008)
123. J. Cheng, B.A. Teply, I. Sherifi, J. Sung, G. Luther, F.X. Gu, E. Levy-Nissenbaum, A.F. Radovic-Moreno, R. Langer, O.C. Farokhzad, Biomaterials **28**, 869–876 (2007)
124. G.G. Yordanov, C.D. Dushkin, Colloid Polym. Sci. **288**, 1019–1026 (2010)
125. Y. Tan, P.X. Wang, K. Xu, W.B. Li, H.Y. An, L.L. Li, C. Liu, L.S. Dong, Macromol. Mater. Eng. **294**, 855–859 (2009)
126. V. Deepak, S.B.R.K. Pandian, K. Kalishwaralal, S. Gurunathan, Bioresour. Technol. **100**, 6644–6646 (2009)
127. S. Hornig, H. Bunjes, T. Heinze, J. Colloid Interf. Sci. **338**, 56–62 (2009)
128. E. Kim, J. Yang, J. Choi, J.S. Suh, Y.M. Huh, S. Haam, Nanotechnology **20**, 365602 (2009)
129. T. Nassar, A. Rom, A. Nyska, S. Benita, J. Control. Release **133**, 77–84 (2009)
130. B. Stella, S. Arpicco, F. Rocco, V. Marsaud, J.M. Renoir, L. Cattel, P. Couvreur, Int. J. Pharm. **344**, 71–77 (2007)
131. P. Legrand, S. Lesieur, A. Bochot, R. Gref, W. Raatjes, G. Barratt, C. Vauthier, Int. J. Pharm. **344**, 33–43 (2007)
132. I. Seyler, M. Appel, J.P. Devissaguet, P. Legrand, G. Barratt, J. Nanopart. Res. **1**, 91–97 (1999)
133. Z. Zili, S. Sfar, H. Fessi, Int. J. Pharm. **294**, 261–267 (2005)
134. V. Ferranti, H. Marchais, C. Chabenat, A.M. Orecchioni, O. Lafont, Int. J. Pharm. **193**, 107–111 (1999)
135. R.A. Slater, T.O. McDonald, D.J. Adams, E.R. Draper, J.V.M. Weaver, S.P. Rannard, Soft Matter **8**, 9816–9827 (2012)
136. N. Anton, F. Bally, C.A. Serra, A. Ali, Y. Arntz, Y. Mely, M.J. Zhao, E. Marchioni, A. Jakhmola, T.F. Vandamme, Soft Matter **8**, 10628–10635 (2012)
137. C. Zhang, V.J. Pansare, R.K. Prud'homme, R.D. Priestley, Soft Matter **8**, 86–93 (2012)
138. S. Hornig, T. Heinze, C.R. Becer, U.S. Schubert, J. Mater. Chem. **19**, 3838–3840 (2009)

Chapter 2
Synthesis and Characterisation of *Hyp*-polydendron Materials and Subsequent Nanoparticle Formation

2.1 Introduction

The synthesis of high generation dendrimers continues to be a non-cost effective and difficult process, as previously discussed, although the possibility of producing larger materials whilst maintaining such high surface functionality as present in dendrimers is highly desirable.

The aim of this work was to synthesise first and second generation dendron initiators for ATRP, investigate whether these dendron initiators would polymerise under ATRP conditions and to assess how this new functionality might affect the behaviour of branched polymers produced using a simple divinyl monomer incorporation strategy. Three ATRP initiators were chosen for this study, shown in Fig. 2.1. The first and second generation dendron initiators, **G1** and **G2** respectively, were synthesised and compared to a commercially available non-dendron initiator, ethyl bromo isobutyrate, **EBiB**.

These initiators were used to polymerise the monomer 2-hydroxypropyl methacrylate (HPMA) to give linear and branched poly(2-hydroxypropyl methacrylate) (pHPMA), targeting three different number average degrees of polymerisation (DP_n); 20, 50 and 100 monomer units.

The subsequent linear and branched polymers, bearing each initiating group at one end of every polymer chain were to be studied, to assess their behaviour in solvent and aqueous environments to ascertain their ability to form nanoparticles. The ability to form nanoparticles from such materials could give polymeric nanoparticles which contain a high level of functionality introduced via the dendron moieties at one polymer chain end, which has important implications in various applications such as developing biological systems toward drug delivery [1, 2].

Publication arising from this chapter: "Hyperbranched polydendrons: a new controlled macromolecular architecture with self-assembly in water and organic solvents", Fiona L. Hatton, Pierre Chambon, Tom O. McDonald, Andrew Owen and Steven P. Rannard, *Chem. Sci.*, **2014**, *5*, 1844–1853.

F.L. Hatton, *Hyperbranched Polydendrons*,
Springer Theses, DOI 10.1007/978-3-319-18753-2_2

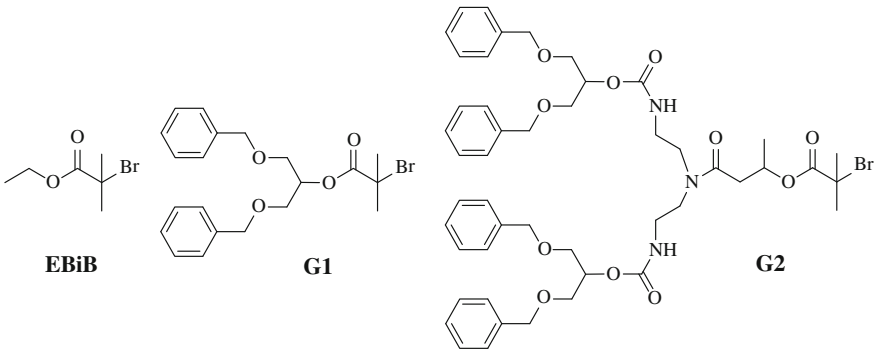

Fig. 2.1 ATRP initiators chosen for the study

2.2 Hydrophobic Dendron Initiator Synthesis

The target surface group for the two dendron initiators was 1,3-dibenzyloxy-2-propanol (DBOP), **1**, shown in Scheme 2.1. This surface group was targeted as it provides a hydrophobic surface functionality which provides a good control for comparison with hydrophilic surface functionalities. The benzyl groups were also useful as they are easily distinguished by ^{1}H NMR spectroscopy as the shifts corresponding to the aromatic protons on the benzyl groups have significantly different chemical shifts to any others present in the targeted polymers.

2.2.1 Generation 1 DBOP Dendron (G1)

Due to the structure of the parent alcohol, **1**, a simple esterification reaction with α-bromoisobutyryl bromide yielded the **G1** dendron initiator, **2**, outlined in Scheme 2.1. This esterification reaction is well reported in the literature for the preparation of various functional initiators for ATRP [3–5].

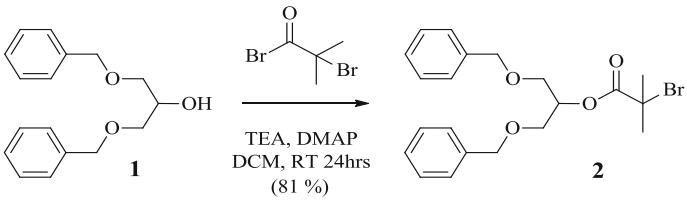

Scheme 2.1 Synthesis of the **G1** DBOP dendron initiator, **2**

The 4-dimethylaminopyridine (DMAP) acted as a catalyst, whereby the nitrogen in the pyridine ring attacks the acyl bromide giving a brief pyridinium intermediate, which is more reactive than the initial acyl bromide therefore aiding the reaction. Triethylamine (TEA) was used to neutralise HBr (a side product of the reaction), this could be seen as a white precipitate which was observed showing formation of the $Et_3NH^+Br^-$ salt, indicative of reaction. The **G1** dendron initiator, **2**, was analysed by ^1H and ^{13}C NMR spectroscopy, electrospray (ES) mass spectrometry and elemental microanalysis, all of which are in agreement with the desired product. Figure 2.2 shows the ^1H NMR spectrum with each peak assigned. The residual solvent peak for $CHCl_3$, which appears at 7.26 ppm, is overlaid by the aromatic proton peaks (7.20–7.35 ppm) present in the molecule therefore the integration for the aromatic protons is slightly higher than expected by theory.

The ^{13}C NMR spectrum is shown in Fig. 2.3 with peaks assigned; the peak corresponding to C9 in the molecule has the same chemical shift as the solvent, and cannot be identified amongst the $CDCl_3$ peaks. The mass spectrum is shown in Fig. 2.4 with important peaks highlighted. It is worth noting that those peaks corresponding to the molecular ion exemplify the isotope pattern expected for bromine perfectly.

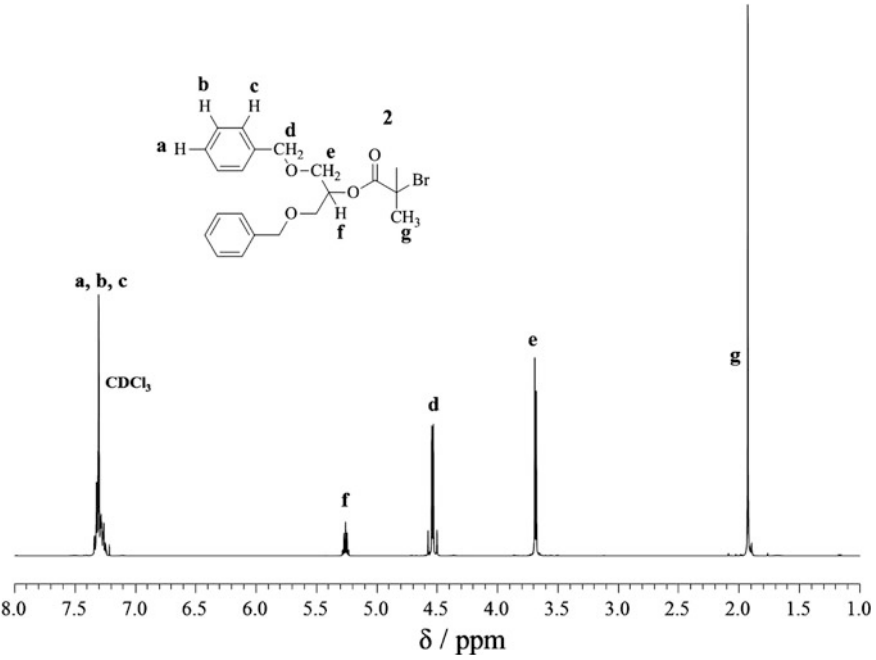

Fig. 2.2 ^1H NMR ($CDCl_3$, 400 MHz) of **G1** DBOP initiator, **2**

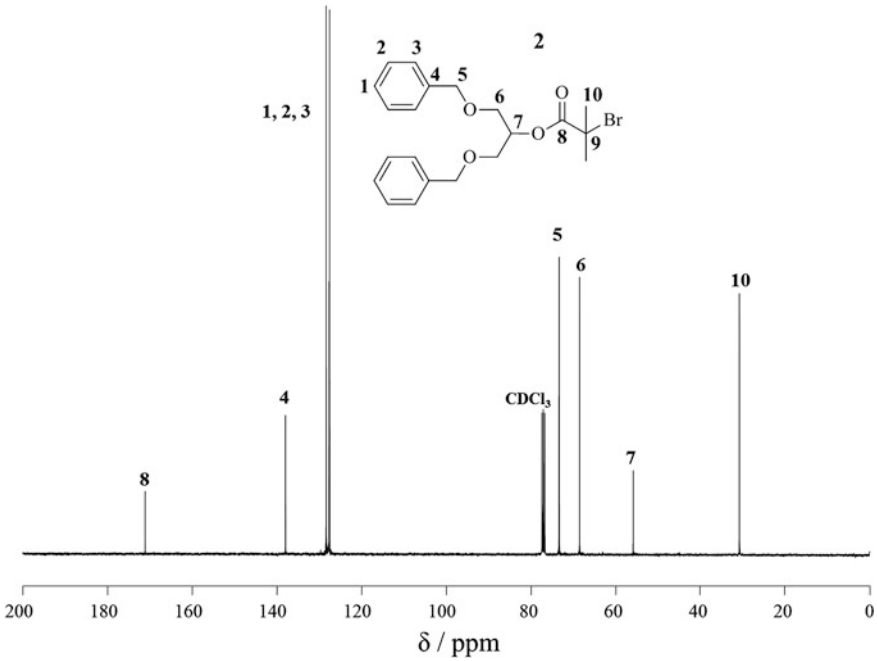

Fig. 2.3 ^{13}C NMR ($CDCl_3$, 100 MHz) of **G1** DBOP initiator, **2**

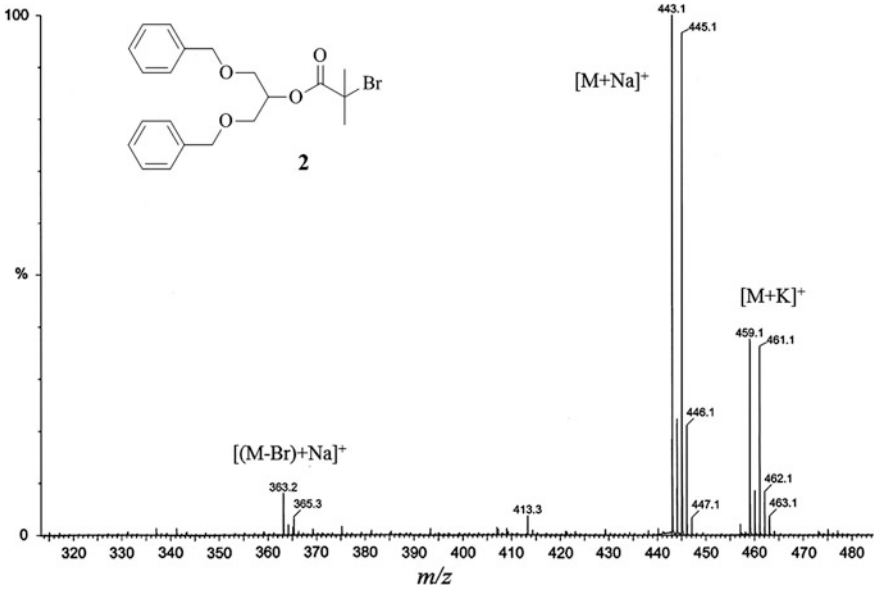

Fig. 2.4 Mass spectrum (ES-MS) of **G1** DBOP initiator, **2**

2.2.2 Generation 2 DBOP Dendron (G2)

The second generation initiator, **6**, was synthesised via a convergent strategy utilising the selectivity of 1,1′-carbonyldiimidazole (CDI) chemistry [6, 7], shown in Scheme 2.2.

The intermediary products from each step (**3**, **4** and **5**) were purified and analysed by ^{1}H and ^{13}C NMR spectroscopy, mass spectrometry and elemental microanalysis (see Appendix, Figs. A.1, A.2, A.3, A.4, A.5. A.6, A.7, A.8 and A.9). The first step involved reaction of the parent alcohol, DBOP, which bears the functionality of the resulting dendron surface group, with CDI. This generated the DBOP imidazole carboxylic ester, **3**, in high yields (97 %). The ^{1}H NMR spectrum of **3** (see Appendix, Fig. A.1) shows clearly that the imidazole ring is present, as 3 resonances were observed for the attached imidazole ring, whereas free imidazole would give only 2 resonances in the aromatic region. The ^{13}C NMR spectrum, see Appendix Fig. A.2, also confirms the correct structure due to the peak at 148.8 ppm, corresponding to the carbonyl carbon (C8) which is not present in the initial alcohol.

This imidazole carboxylic ester intermediate, **3**, was subsequently reacted with diethylenetriamine (DETA) [8]. Due to the selective nature of CDI chemistry only the primary amine functionalities of DETA reacted with **3**, whereas the secondary amine remained intact, leaving a reactive functional group on the molecule allowing for further reaction [6]. This coupling of two 1st generation dendrons, **3**, gave rise

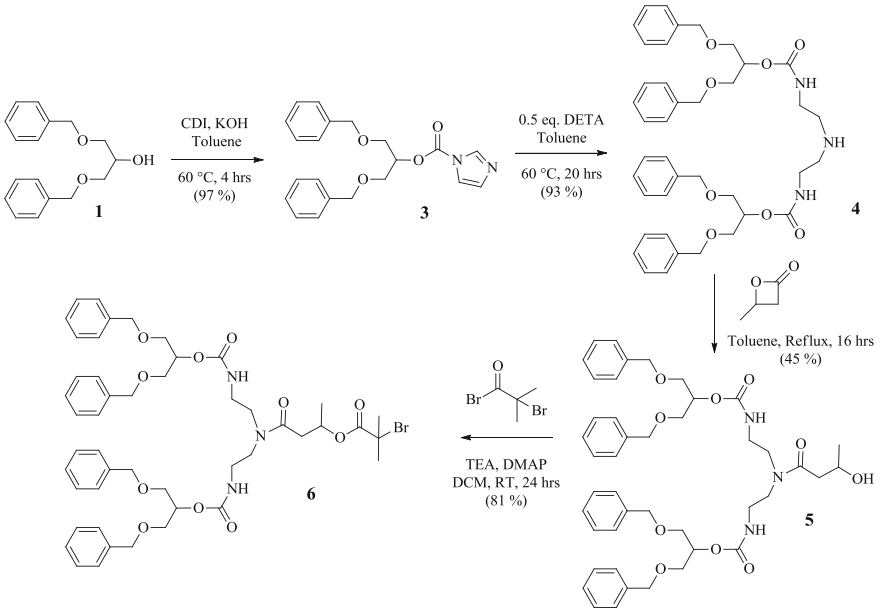

Scheme 2.2 Synthesis of **G2** dendron initiator, **6**

to the second generation dendron or **G2** dendron, **4**. The ^{1}H NMR spectrum (Appendix Fig. A.4) shows new proton environments corresponding to the CH_2s between the urethane bond and secondary amine at 2.60 and 3.15 ppm, with the integrations of the other protons being concordant with the rest of the molecule. ^{13}C NMR spectrum and ES mass spectrometry analysis (Appendix Figs. A.5 and A.6) also confirm the structure of **4**.

The ring-opening reaction of **4** with β-butyrolactone [9] afforded molecule **5** after purification by column chromatography. One side product of the reaction was the ring opening of β-butyrolactone with the urethane nitrogen, which had the same molecular weight as the desired product, **5**, therefore indistinguishable by mass spectrometry, however, the ^{1}H NMR spectroscopy analysis elucidated each structure. The ^{1}H NMR spectrum (Appendix Fig. A.7), ^{13}C NMR spectrum (Appendix Fig. A.8) and ES mass spectrometry analysis (Appendix Fig. A.9) all support the proposed structure of **5**. The yield of **5** was relatively low (45 %) this was believed to be due to the side product formed that reduced the yield of the desired product.

The **G2** dendron, **5**, was converted to the **G2** dendron initiator, **6**, by esterification of the secondary alcohol with α-bromoisobutyryl bromide [3–5], to give the target second generation dendron initiator (**G2** dendron initiator), **6**, in good yields (81 %). The ^{1}H NMR spectrum, shown in Fig. 2.5 with peaks assigned, is strongly indicative of the correct product. It is worth noting however, that as the generation number increases, and therefore the number of protons in the same or similar

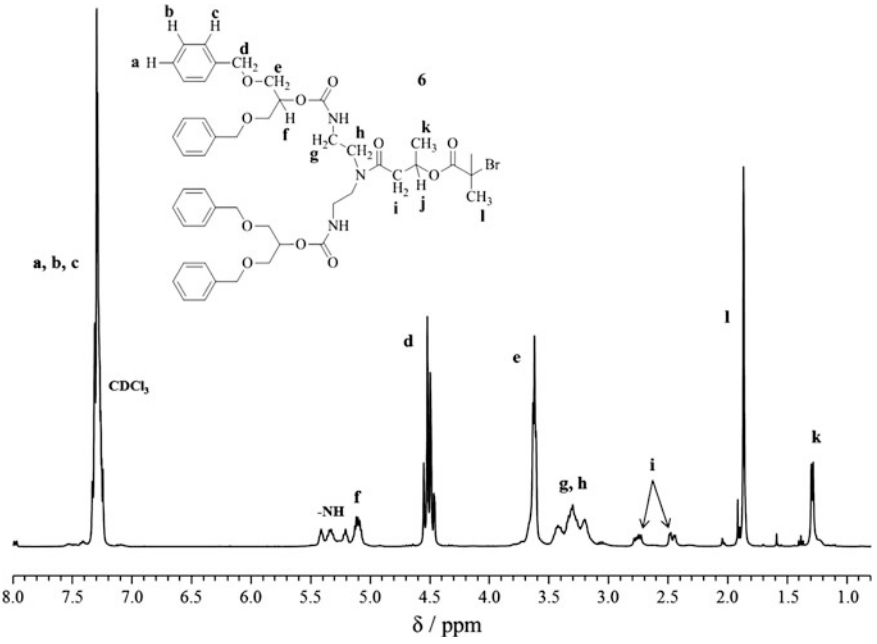

Fig. 2.5 ^{1}H NMR ($CDCl_3$, 400 MHz) of **G2** DBOP initiator, **6**

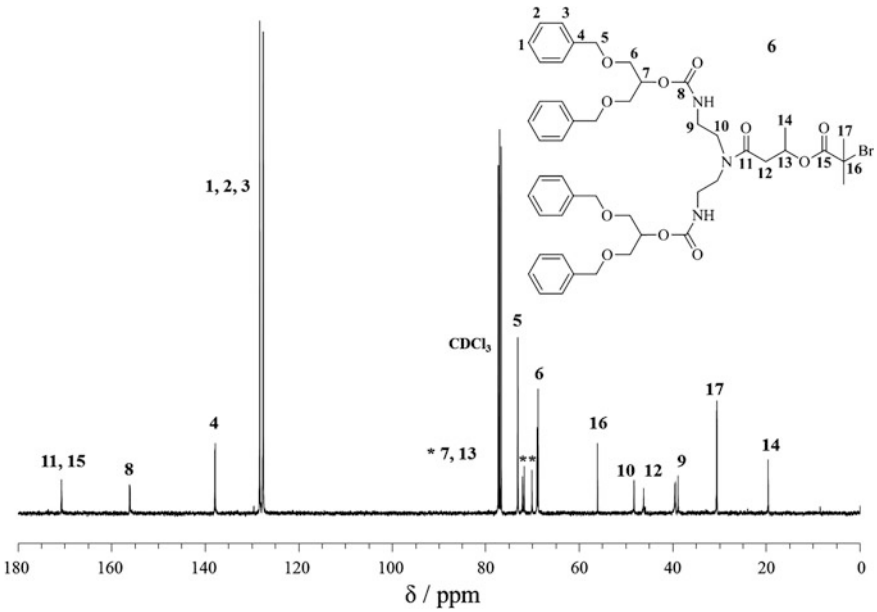

Fig. 2.6 ^{13}C NMR ($CDCl_3$, 100 MHz) of **G2** DBOP initiator, **6**

environment increases, the peaks corresponding to those protons become broader and less well defined. This is due to the peak in the NMR spectrum being a representation of the average of those protons, and so as the number of protons in such environments increases, each of their environments becomes slightly different. This is more evident in higher generation dendrons and dendrimers. ^{13}C NMR spectroscopy (Fig. 2.6) and ES mass spectrometry (Fig. 2.7) also confirm the structure of the **G2** DBOP initiator, **6**. The expected bromine isotope pattern is also observed for this molecule again confirming the correct structure.

2.3 Polymer Synthesis

EBiB, **G1** and **G2** initiators were then used to synthesise either linear or branched pHPMA via ATRP [10, 11]. For the linear polymers, the initiator functionality was present at one chain end. When a divinyl monomer, ethylene glycol dimethacrylate (EGDMA), was introduced highly branched polymer architectures were formed [12–14], as illustrated in Scheme 2.3.

The globular structures of the branched polymers were composed of a core of pHPMA with the initiator decorating the surface and, when a dendron initiator was used, termed a "hyperbranched polydendron"—a *hyp*-polydendron. This term was chosen to represent the hyperbranched structure which contained multiple dendrons in one macromolecule, therefore a polydendron. When the initiator used was a

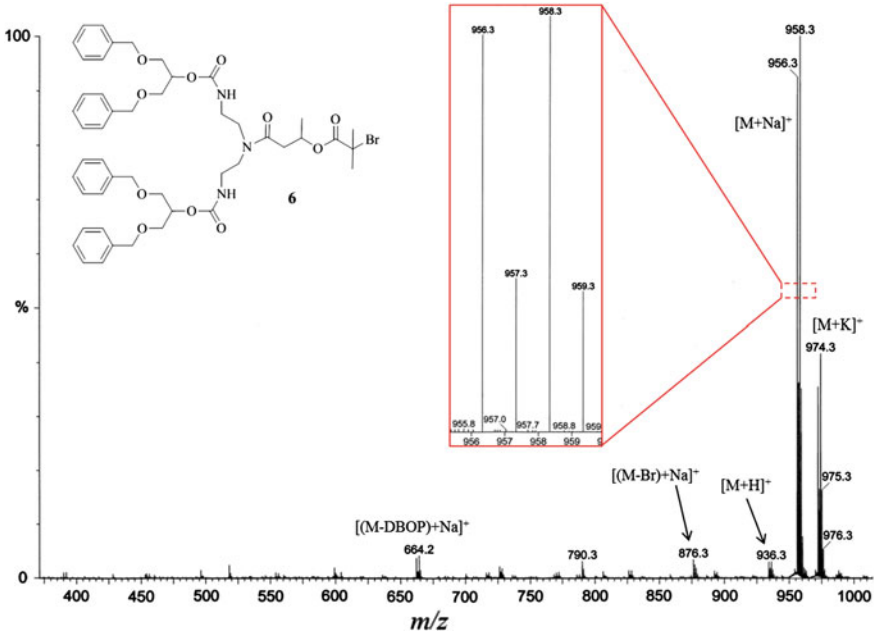

Fig. 2.7 Mass spectrum (ES-MS) of **G2** dendron initiator, **6**, including the $[M + Na]^+$ peak enlarged to see the bromine isotope pattern

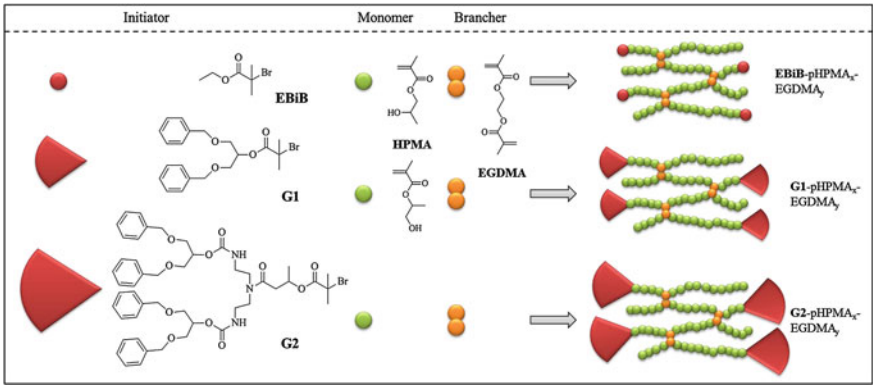

Scheme 2.3 Idealised schematic representation of initiators, monomer and brancher used, and their corresponding branched polymers (both of HPMA's isomers have been depicted)

non-dendron initiator the resulting hyperbranched polymers were termed *hyp*-polymers. Three different number average degrees of polymerisation (DP_n) were targeted (20, 50 and 100 monomer units) for each polymer. Analysis by gel permeation chromatography (GPC) and ^1H NMR spectroscopy analysis for each polymer is collated in Table 2.1.

Table 2.1 ^{1}H NMR and GPC data for all polymers synthesised

Initiator	Target polymer composition	GPC (THF)				^{1}H NMR[b]
		M_n (gmol^{-1})	M_w (gmol^{-1})	Đ	DP_n	DP_n
E	$HPMA_{20}$	5,900[a]	8,000[a]	1.37[a]	39	–
E	$HPMA_{50}$	11,300	14,000	1.24	77	–
E	$HPMA_{100}$	20,700	25,800	1.25	142	–
E	$HPMA_{20}$-$EGDMA_{0.8}$	24,800	165,900	6.70	–	–
E	$HPMA_{50}$-$EGDMA_{0.8}$	147,000	928,500	6.31	–	–
E	$HPMA_{100}$-$EGDMA_{0.8}$	214,200	2,328,000	10.9	–	–
G1	$HPMA_{20}$	5,900	7,800	1.32	38	24
G1	$HPMA_{50}$	9,800	13,000	1.33	65	55
G1	$HPMA_{100}$	20,400	25,600	1.26	138	120
G1	$HPMA_{20}$-$EGDMA_{0.8}$	52,800	545,000	10.3	–	21
G1	$HPMA_{50}$-$EGDMA_{0.8}$	47,200	1,169,000	24.7	–	57
G1	$HPMA_{100}$-$EGDMA_{0.8}$	69,300	1,354,500	19.5	–	119
G2	$HPMA_{20}$	5,700	7,300	1.28	33	21
G2	$HPMA_{50}$	14,400	20,300	1.41	94	49
G2	$HPMA_{100}$	23,300	32,700	1.40	155	101
G2	$HPMA_{20}$-$EGDMA_{0.8}$	153,000	1,565,000	10.2	–	21
G2	$HPMA_{50}$-$EGDMA_{0.8}$	68,400	661,000	9.67	–	55
G2	$HPMA_{100}$-$EGDMA_{0.8}$	164,200	2,227,500	13.6	–	107

[a]Calculated using a different GPC (DMF eluent at 60 °C)
[b]Determined by ^{1}H NMR analysis in d_6-DMSO

2.3.1 Linear Polymers

The polymerisations of HPMA with targeted DP_{20}, DP_{50} and DP_{100} were carried out at 30 °C in methanol with CuCl:bipyridyl (bpy) (1:2), as the catalytic system [15, 16]. Each linear chain bore the functionality of the initiator only once. The DP_n calculated by ^{1}H NMR spectroscopy was less than the value obtained by GPC for all linear polymers. This discrepancy was probably due to the initiator efficiency being less than 100 % for each dendron. The DP_n by ^{1}H NMR includes the unreacted initiator as well as the polymer chain end groups, therefore leading to calculations of polymer chains that are shorter than the GPC analysis, and this effect of reduced initiator efficiency has been previously reported [17, 18]. The DP_n of the **EBiB** initiated polymers could not be calculated as the initiator peaks overlapped with the polymer peaks and could not be adequately distinguished.

In all polymerisations, unreacted initiator remained in the reaction medium after the polymerisations had achieved complete conversion. This could be seen in the refractive index (RI) GPC chromatograms as a small peak corresponding to the initiator eluting just before the solvent front, shown in Fig. 2.8a.

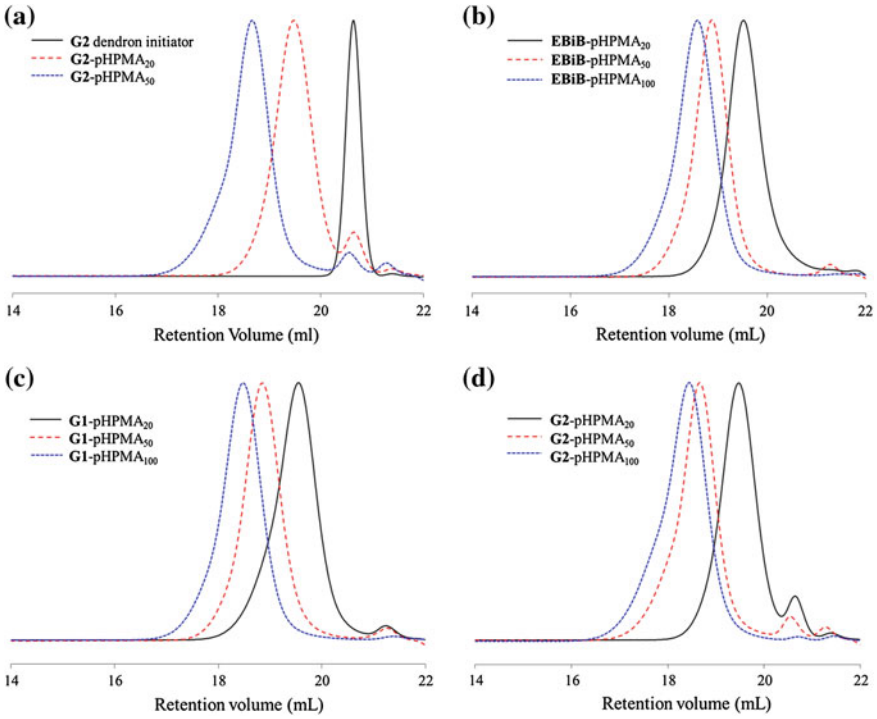

Fig. 2.8 GPC RI chromatogram overlays of **a G2** dendron initiator with **G2**-pHPMA$_{20}$ and **G2**-pHPMA$_{50}$, **b EBiB**-pHPMA$_{20}$, **EBiB**-pHPMA$_{50}$ and **EBiB**-pHPMA$_{100}$, **c G1**-pHPMA$_{20}$, **G1**-pHPMA$_{50}$ and **G1**-pHPMA$_{100}$ and **d G2**-pHPMA$_{20}$, **G2**-pHPMA$_{50}$ and **G2**-pHPMA$_{100}$

The GPC RI overlays for each linear polymer (DP$_{20}$, DP$_{50}$ and DP$_{100}$) synthesised with each initiator are shown in Fig. 2.8b for the **EBiB** initiated, Fig. 2.8c for **G1** dendron initiated and Fig. 2.8d for **G2** dendron initiated. The GPC chromatograms show in each case that the linear and linear-dendritic polymers have a monomodal distribution, and the higher the targeted DP$_n$ the lower the retention volume, indicating that the higher the targeted DP$_n$ the higher the molecular weights obtained. In some of the linear samples a slight shoulder is visible on the high molecular weight side of the peak. This could either be due to coupling of chain ends at high conversions [19] or the fact that the HPMA monomer contains a small amount of a dimethacrylate impurity as a result of the synthetic route utilised in the production of the monomer [20], which can also result in the coupling of chains.

2.3.2 Hyp-*polymer and* Hyp-*polydendron Synthesis*

Incorporation of a difunctional monomer into the polymerisation allows for large branched polymer structures to be obtained [10]. The ratio of initiator to brancher

was crucial to the polymerisation success as, in theory, a molar ratio of 1:1 or more will cause cross-linking of polymer chains and ultimately macroscopic gelation [21, 22]. Although theoretically a ratio of 1:0.95, initiator:brancher, would give the large branched structures desired, it was found that due to the initiator efficiencies being lower than 100 %, at this level of brancher the polymers formed a cross-linked insoluble network, therefore the ratio of initiator to brancher was kept lower at 1:0.8. This was also affected by the concentration of the polymerisation, as the more dilute the polymerisation the more likely intramolecular looping will occur rather than the desired intermolecular branching. Therefore concentrations were maintained constant across all polymerisations at 50 v/v% with respect to the monomer.

The GPC overlays of **EBiB** initiated polymers (Fig. 2.9a, b) highlight the difference between the linear and *hyp*-polymer samples via the RI (Fig. 2.9a) and right angle light scattering (RALS) (Fig. 2.9b) detector chromatograms. The GPC chromatograms indicate that introduction of the difunctional monomer, EGDMA, affords high molecular weight branched polymers, eluting at lower retention volumes. Due to the statistical nature of branching in ATRP there is a broad distribution of materials present, ranging from linear chains to highly branched macromolecules [10]. The RI detector response is dependent upon the concentration of the polymer species present, whereas the RALS detector response is dependent upon the size of the polymeric species present. Therefore, although a small RI response is detected for the *hyp*-polymers around an elution volume of 12 mL (for **EBiB**-pHPMA$_{100}$-EGDMA$_{0.8}$), there is a huge RALS detector response due to the

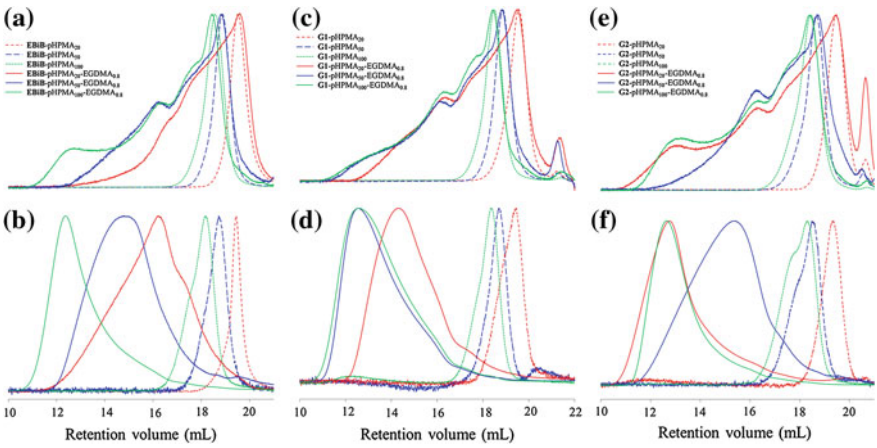

Fig. 2.9 GPC chromatograms overlays of **a** RI chromatograms and **b** RALS chromatograms for **EBiB**-pHPMA$_{20}$-EGDMA$_{0.8}$, **EBiB**-pHPMA$_{50}$-EGDMA$_{0.8}$, **EBiB**-pHPMA$_{100}$-EGDMA$_{0.8}$ and the linear equivalents with dotted lines. **c** RI chromatograms and **d** RALS chromatograms for **G1**-pHPMA$_{20}$-EGDMA$_{0.8}$, **G1**-pHPMA$_{50}$-EGDMA$_{0.8}$, **G1**-pHPMA$_{100}$-EGDMA$_{0.8}$ and the linear equivalents with *dotted lines*. **e** RI chromatograms and **f** RALS chromatograms for **G2**-pHPMA$_{20}$-EGDMA$_{0.8}$, **G2**-pHPMA$_{50}$-EGDMA$_{0.8}$, **G2**-pHPMA$_{100}$-EGDMA$_{0.8}$ and the linear equivalents with *dotted lines*

presence of highly branched polymeric species which scatter considerably more light than the small polymeric species. It is worth noting, however, that in Figs. 2.8 and 2.9 the height of each peak has been normalised so this does not reflect the true differences in detector response, however, if the differences in detector responses needed to be compared it would be the area under the curve which would allow a true comparison.

Figure 2.9 shows the GPC overlays for the **G1** dendron initiated (Fig. 2.9c, d) and **G2** dendron initiated (Fig. 2.9e, f) linear-dendritic and *hyp*-polydendrons, with RI (Fig. 2.9c, e) and RALS (Fig. 2.9d, f) detector chromatograms.

These linear dendritic and *hyp*-polydendron samples follow the same trend as the **EBiB** initiated polymers; those with the inclusion of EGDMA all elute at a much lower retention volume than their linear equivalents. For example, the **G1**-pHPMA$_{50}$-EGDMA$_{0.8}$ sample begins to elute at an approximate retention volume of 11 mL, whilst the **G1**-pHPMA$_{50}$ only begins to elute at approximately 17.5 mL. Each of the **G2** initiated *hyp*-polydendrons elute between 10 and 12 mL, whilst their linear-dendritic equivalents elute between 16 and 18 mL.

The linear polymers and branched polymers were analysed by ^{1}H NMR spectroscopy, as discussed previously, Fig. 2.10 shows each linear DP$_{50}$ polymer ^{1}H NMR spectrum overlaid, with the major peaks present in each polymer assigned. The aromatic protons attributed to the two dendron initiators are also highlighted. The DP$_{20}$ and DP$_{100}$ linear polymer ^{1}H NMR spectra are shown in the Appendix; Figs. A.10 and A.12 respectively.

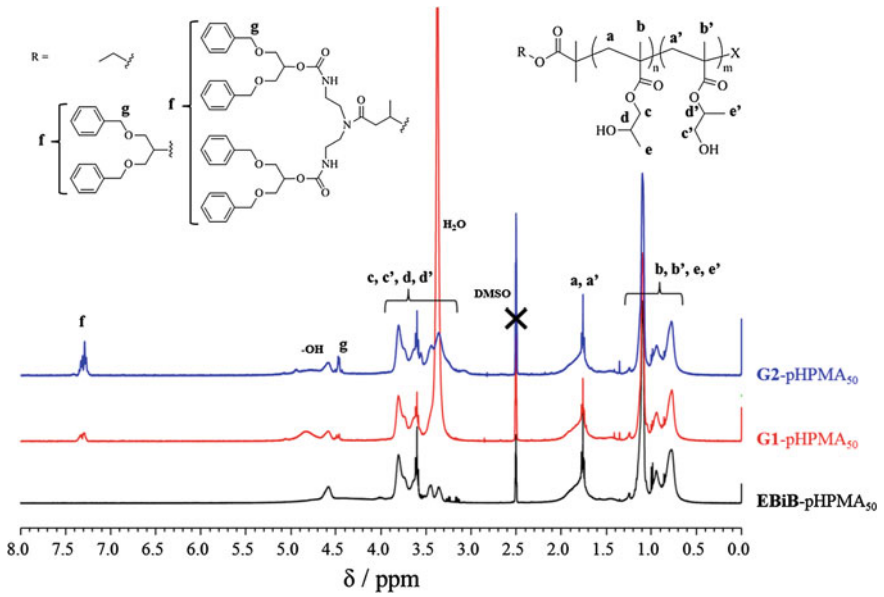

Fig. 2.10 ^{1}H NMR (d_6-DMSO, 400 MHz) spectra overlay for **EBiB**-pHPMA$_{50}$, **G1**-pHPMA$_{50}$ and **G2**-pHPMA$_{50}$ with major peaks assigned

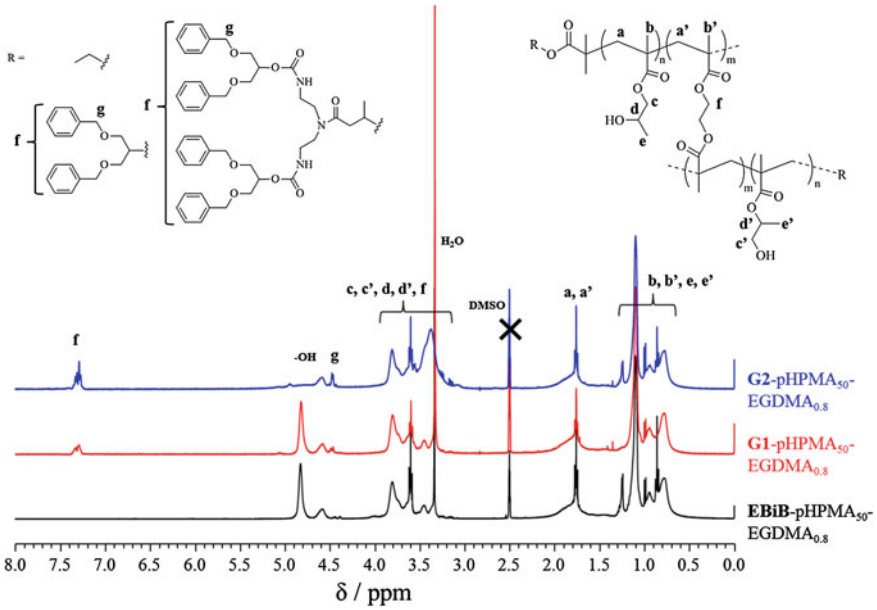

Fig. 2.11 ^{1}H NMR (d_6-DMSO, 400 MHz) spectra overlay for **EBiB**-pHPMA$_{50}$-EGDMA$_{0.8}$, **G1**-pHPMA$_{50}$-EGDMA$_{0.8}$ and **G2**-pHPMA$_{50}$-EGDMA$_{0.8}$with major peaks assigned

The DP$_{50}$ *hyp*-polymer and *hyp*-polydendrons' ^{1}H NMR spectra are overlaid in Fig. 2.11 with major peaks assigned. It is worth noting that the only difference between the linear and branched equivalent polymers is the presence of EGDMA in the branched polymers, which contains protons with similar environments to the HPMA monomer and therefore cannot be distinguished in the ^{1}H NMR spectra. The DP$_{20}$ and DP$_{100}$ *hyp*-polymer and *hyp*-polydendron ^{1}H NMR spectra are shown in the Appendix in Figs. A.11 and A.13.

2.4 Kinetic Experiments

Kinetic experiments were undertaken for each of the linear and branched polymerisations that targeted a DP$_n$ of 50 monomer units to confirm that each polymerisation followed first order kinetics with respect to the monomer concentration, and to follow the evolution of molecular weight with respect to monomer conversion.

2.4.1 Linear Polymerisation Kinetics

The kinetic plots for each linear polymerisation, Fig. 2.12, show that each polymerisation reached high conversion within 6–7 h (Fig. 2.12a, c, e) and followed first order kinetics as expected [17]. The evolution of M_n with conversion was linear and was close to that expected from the targeted M_n (Fig. 2.12b, d, f).

Figure 2.13 shows the ^{1}H NMR spectra of the **G1**-pHPMA$_{50}$ polymerisation at various time points throughout the polymerisation. As the reaction proceeds, the vinyl peaks at 5.65 and 6.05 ppm decrease as the monomer is consumed. The aromatic peaks attributed to the initiator are observed at 7.26–7.38 ppm which remain constant throughout the polymerisation and were therefore used as a reference to calculate conversion. The conversion for the **EBiB** initiated polymerisations used the pendant CH_3 of the monomer as a reference at 1.2 ppm as this

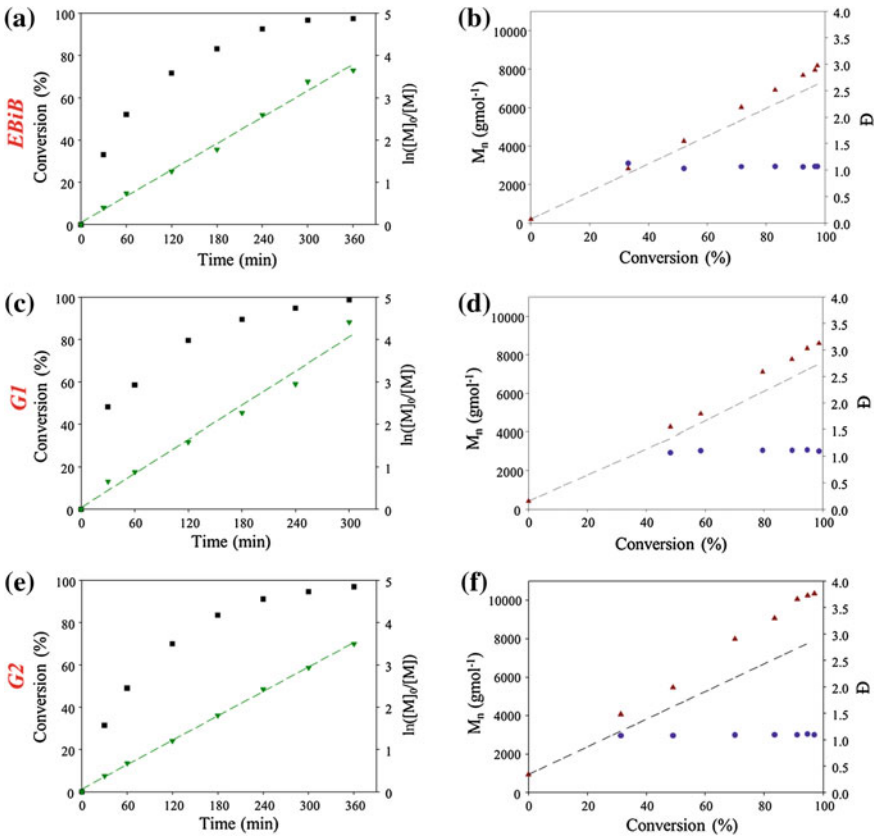

Fig. 2.12 Kinetic plots for linear DP_{50} polymers. **a** and **b** **EBiB**-pHPMA$_{50}$, **c** and **d** **G1**-pHPMA$_{50}$, **e** and **f** **G2**-pHPMA$_{50}$. Conversion (*black squares*), ln([M]$_0$/[M]) (*green down triangles*), M_n (*red up triangles*), Đ (*blue circles*) and theoretical M_n (*black dotted lines*)

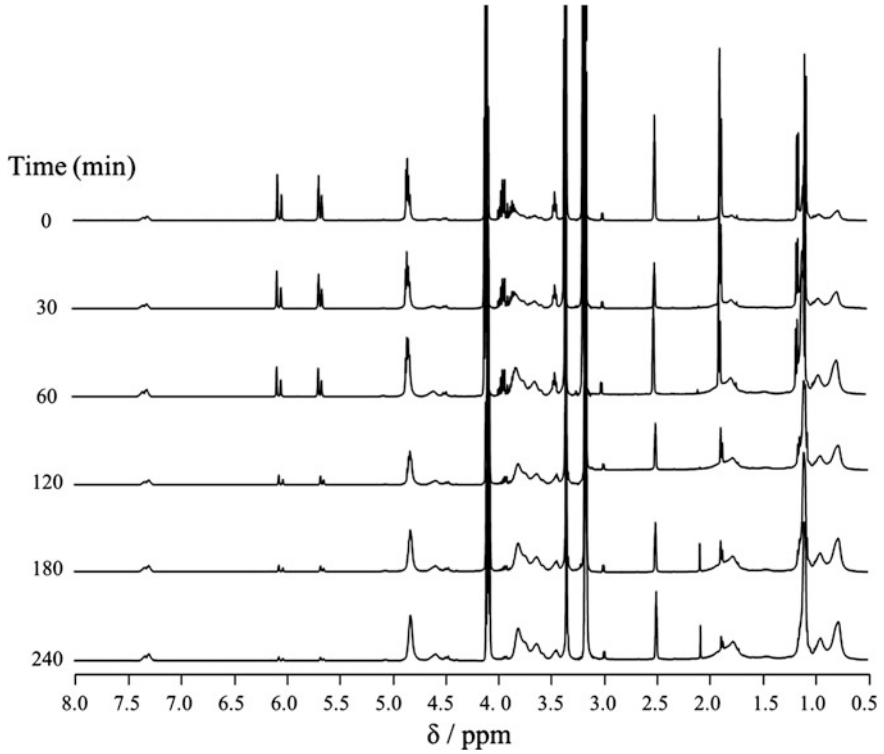

Fig. 2.13 ^{1}H NMR (d_6-DMSO, 400 MHz) overlay of kinetic samples for **G1**-pHPMA$_{50}$ polymerisation

signal remains constant in the monomeric and polymeric form of HPMA, when compared to the vinyl peaks (5.65 and 6.05 ppm).

2.4.2 Branched Polymerisation Kinetics

The kinetic plots for each branched polymerisation with targeted DP_{50}, shown in Fig. 2.14, also show that these polymerisations followed first order kinetics, and reached high conversion within 8–9 h (Fig. 2.14a, c, e). The M_n and M_w increased linearly at the beginning of the polymerisations, until the conversion reached 80–90 %, where the M_w increases steeply indicating large branched polymers are being formed at high conversion (Fig. 2.14b, d, f). This steep increase in M_w is indicative of the linear chains joining to form a high M_w branched structure via intermolecular reaction.

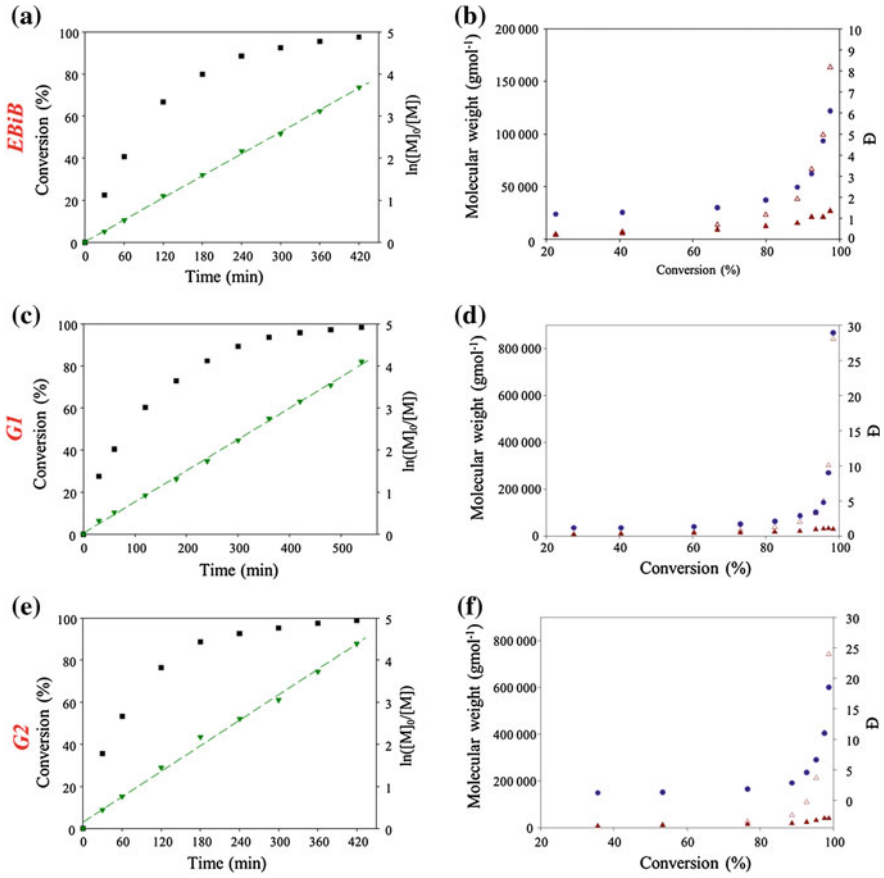

Fig. 2.14 Kinetic plots for linear DP_{50} polymers. **a** and **b EBiB**-pHPMA$_{50}$-EGDMA$_{0.8}$, **c** and **d G1**-pHPMA$_{50}$-EGDMA$_{0.8}$, **e** and **f G2**-pHPMA$_{50}$-EGDMA$_{0.8}$. Conversion (*black squares*), ln ($[M]_0/[M]$) (*green down triangles*), M_n (*red filled up triangles*) M_w (*red open up triangles*), Đ (*blue circles*)

2.5 Solvent Driven Self-assembly of Hydrophobic Polymers

In order to assess whether these *hyp*-polydendrons could be used to produce nanoparticles, a nanoprecipitation approach was utilised [23]. While conventional nanoprecipitation typically uses water as the anti-solvent [24, 25], here the hydrophobic nature of both the initiator and polymer warranted use of two organic solvents. This approach is highlighted in Fig. 2.15. It is worth noting that the vials used were kept sealed at all times except when anti-solvent addition was occurring. Anti-solvent was added using a syringe pump set at 0.5 mL/min through the inlet needle, an outlet needle was used to prevent a build-up of pressure.

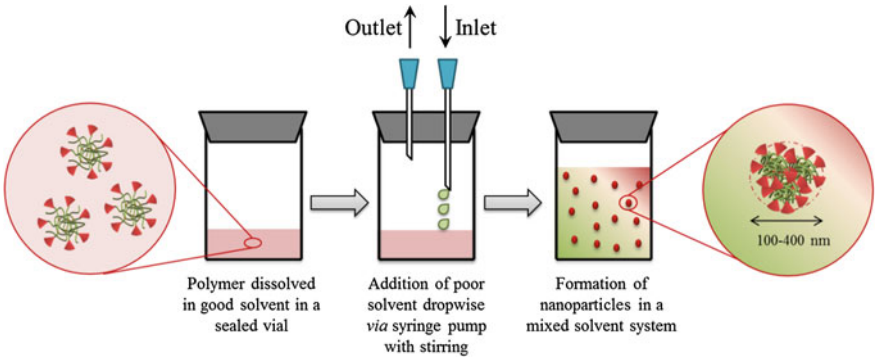

Fig. 2.15 Graphical representation of how organic nanoparticles are formed via the use of addition of an anti-solvent to polymer dissolved in a good solvent

Acetone was used as the good solvent for both the pHPMA core and the initiator groups at the end of each polymer chain. Nanoprecipitation was induced by dropwise addition of hexane (an anti-solvent for the pHPMA core but a good solvent for the initiator groups, henceforth described as an anti-solvent). Therefore theoretically, the initiator groups around the surface of each branched macromolecule should stabilise the particle with increased amounts of anti-solvent introduced into the system. A further reason for using acetone/hexane was that their refractive indices and viscosities are both very similar. An initial concentration of 5 mg/mL polymer in acetone was used, unless stated otherwise, therefore depending upon how much hexane has been added (hexane fraction, Φ_{hex}) the final polymer concentration would vary.

2.5.1 *Nanoparticle Formation Utilising* Hyp-*polymers and* Hyp-*polydendrons*

The formation of nanoparticles was followed primarily by dynamic light scattering (DLS). A clear trend was observed for the branched polymers (Figs. 2.16a, 2.18a and 2.20b): with the addition of a low fraction of hexane, the solvated branched polymers appear to decrease in z-average diameter (D_z) slightly, until enough hexane was added to force the branched dendritic polymers to aggregate into larger spherical particles. These particles have low polydispersities (PdI), below 0.2, and appear to shrink slightly with the addition of more anti-solvent until they increase in size due to precipitation. Figures 2.16b, 2.18b and 2.20b each highlights various stages of nanoparticle formation in the acetone/hexane solvent mixtures of **EBiB**-pHPMA$_{50}$-EGDMA$_{0.8}$, **G1**-pHPMA$_{50}$-EGDMA$_{0.8}$ and **G2**-pHPMA$_{50}$-EGDMA$_{0.8}$ respectively via scanning electron microscopy (SEM).

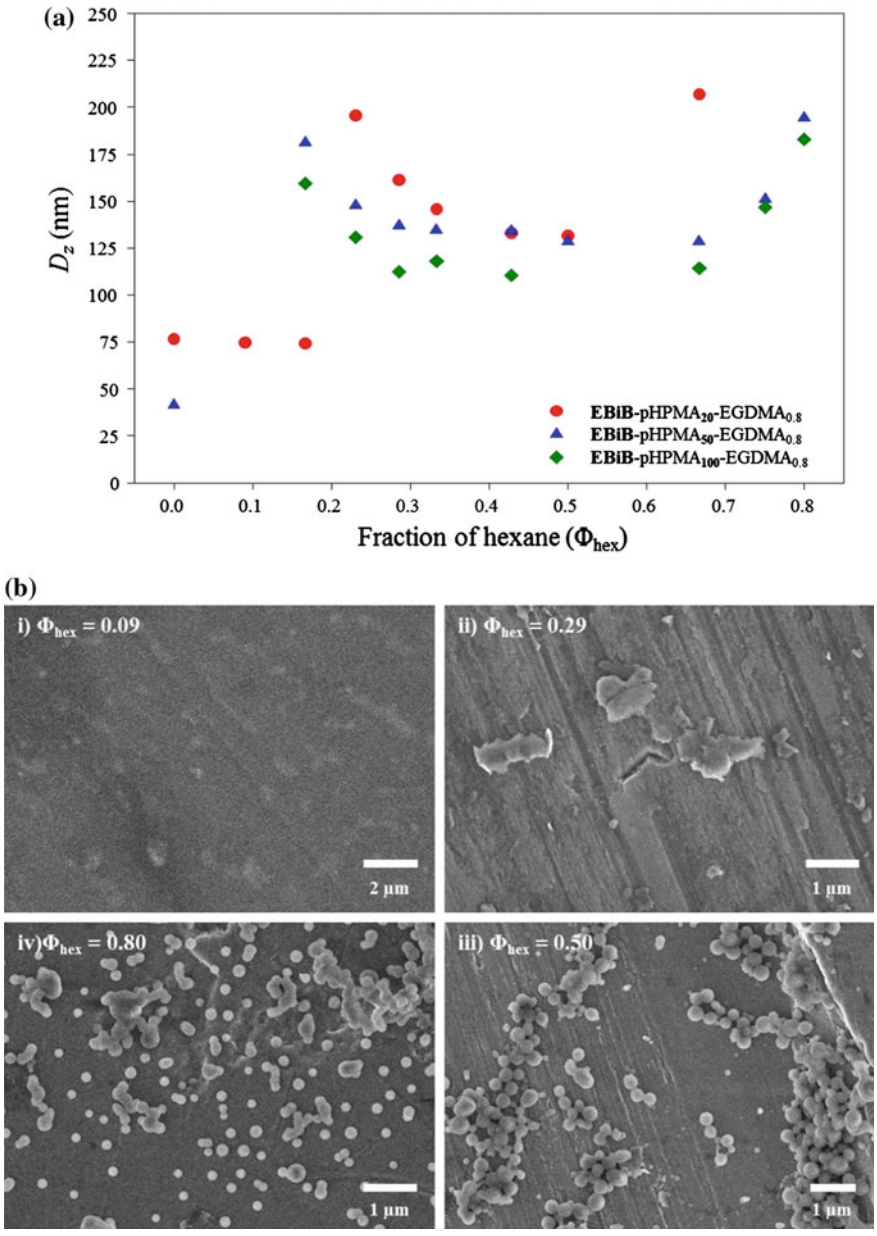

Fig. 2.16 The formation of nanoparticles followed via **a** DLS of each **EBiB** initiated branched polymer DP_{20} (*red circles*) DP_{50} (*blue triangles*) DP_{100} (*green diamonds*) and **b** SEM images of the formation of nanoparticles with **EBiB**-pHPMA$_{50}$-EGDMA$_{0.8}$ at various hexane solvent fractions; (*i*) 0.09, (*ii*) 0.29, (*iii*) 0.50 and (*iv*) 0.80

Figure 2.16a shows the trend of formation for each of the **EBiB** initiated *hyp*-polymers (see Table 2.2 for the D_z and PdI values). At low hexane fractions the polymers were fully solvated by the good solvent, acetone, and may be described as individual objects. This is why in some cases (**EBiB**-pHPMA$_{50}$-EGMDA$_{0.8}$ at Φ_{hex} = 0.09 and **EBiB**-pHPMA$_{100}$-EGDMA$_{0.8}$ at Φ_{hex} = 0 and 0.09) the samples were not suitable for measurement by DLS as the sample was too polydisperse (therefore there are no values in Table 2.2 for these measurements), and in other case the PdI is quite high (**EBiB**-pHPMA$_{20}$-EGDMA$_{0.8}$ at Φ_{hex} = 0, 0.09 and 0.17 have PdI values of 0.493, 0.496 and 0.408). This is due to the fact that when fully solvated the DLS is measuring the distribution of polymeric species present in the sample—ranging from linear chains to highly branched materials. The polymers self-assembled into nanoparticles at Φ_{hex} = 0.17 (for DP$_{50}$ and DP$_{100}$) or 0.23 (DP$_{20}$ sample) which were of a uniform size and had low polydispersities (<0.1). Upon further addition of hexane the D_z of these nanoparticles decreased until a hexane fraction around 0.5, most probably due to the nanoparticles being highly swollen with good solvent at low hexane fractions. The addition of hexane lowers the good solvent fraction causing the nanoparticles to de-swell or compress. The **EBiB**-pHPMA$_{20}$-EGDMA$_{0.8}$ sample showed a decrease in D_z from 196 to 132 nm between Φ_{hex} 0.23–0.50, the **EBiB**-pHPMA$_{50}$-EGDMA$_{0.8}$ nanoparticles showed a decrease in D_z from 181 to 128 nm between Φ_{hex} 0.17–0.67 and the **EBiB**-pHPMA$_{100}$-EGDMA$_{0.8}$ sample showed a decrease in D_z from 160 to 111 nm between Φ_{hex} 0.17–0.43. When the hexane fraction was increased above those hexane fractions, up to 0.80, the nanoparticles increased in size, then ultimately precipitated after an excess of hexane was added. After self-assembly, the corresponding nanoparticle D_z followed a general trend of DP$_{20}$ > DP$_{50}$ > DP$_{100}$.

The formation of nanoparticles using **EBiB**-pHPMA$_{50}$-EGDMA$_{0.8}$ was followed by SEM (Fig. 2.16b) by taking a sample at various hexane fractions (0.09, 0.29, 0.50 and 0.80) and dropping the samples onto an SEM stub, whereby rapid solvent evaporation occurred leaving a dry nanoparticulate polymer sample. At the lowest hexane fraction of 0.09 (Fig. 2.16b-i) the polymer was still fully solvated by the good solvent and no self-assembly has occurred, therefore it was expected that upon drying a polymer film would form, the SEM shows no hierarchical structure and small deposits of polymer are barely distinguishable. Once self-assembly had occurred (Φ_{hex} = 0.29) it was expected that some structure would be seen by SEM, however, possibly due to the effect of drying none could be seen (Fig. 2.16b-ii). It was proposed that upon drying, due to the larger fraction of good solvent that the nanoparticles became aggregated upon drying to form uneven polymer deposits on the surface of the stub. When hexane fractions of 0.50 and 0.80 were imaged via SEM (Fig. 2.16b-iii and iv) it was clear that a level of anti-solvent had been reached that allowed the nanoparticle to retain their structure upon solvent evaporation. Both SEM images show spherical nanoparticles which have diameters that are in accordance with the D_z by DLS. The SEM images for the **EBiB**-pHPMA$_{50}$-EGDMA$_{0.8}$ sample with Φ_{hex} = 0.80 (Fig. 2.16b-iv) were studied in more detail by measuring the particle size from the SEM images and calculating a number average from the SEM analysis which could be compared to the number average as

Table 2.2 D_z and PdI measurements by DLS corresponding to Figs. 2.16, 2.18 and 2.20 of each *hyp*-polymer or *hyp*-polydendron at various hexane fractions

Fraction of hexane present (Φ_{hex})	**EBiB** (Fig. 2.16)						**G1** (Fig. 2.18)						**G2** (Fig. 2.20)					
	$pHPMA_{20}$-$EGDMA_{0.80}$		$pHPMA_{50}$-$EGDMA_{0.80}$		$pHPMA_{100}$-$EGDMA_{0.80}$		$pHPMA_{20}$-$EGDMA_{0.80}$		$pHPMA_{50}$-$EGDMA_{0.80}$		$pHPMA_{100}$-$EGDMA_{0.80}$		$pHPMA_{20}$-$EGDMA_{0.80}$		$pHPMA_{50}$-$EGDMA_{0.80}$		$pHPMA_{100}$-$EGDMA_{0.80}$	
	D_z (nm)	PdI	D_z (nm)	PdI	D_z (nm)	PdI	D_z (nm)	PdI	D_z (nm)	PdI	D_z (nm)	PdI	D_z (nm)	PdI	D_z (nm)	PdI	D_z (nm)	PdI
0	76	0.493	42	0.396	–	–	35	0.271	46	0.369	–	–	59	0.404	37	0.382	64	0.400
0.09	75	0.469	–	–	–	–	32	0.309	42	0.361	–	–	54	0.384	35	0.371	58	0.426
0.17	74	0.408	181	0.055	160	0.02	30	0.294	40	0.325	180	0.227	53	0.367	33	0.349	146	0.217
0.23	196	0.003	148	0.005	131	0.036	204	0.094	163	0.021	146	0.031	209	0.043	178	0.018	140	0.020
0.29	161	0.008	137	0.014	112	0.066	169	0.012	141	0.027	140	0.049	166	0.014	155	0.017	129	0.031
0.33	146	0.018	135	0.038	118	0.083	173	0.032	149	0.075	135	0.084	156	0.019	155	0.036	135	0.031
0.43	133	0.038	134	0.058	111	0.091	168	0.067	140	0.056	129	0.054	157	0.027	152	0.050	127	0.068
0.50	132	0.037	129	0.043	–	–	167	0.016	136	0.072	135	0.093	150	0.057	142	0.056	123	0.058
0.67	207	0.016	128	0.037	114	0.043	172	0.073	133	0.060	129	0.055	385	0.014	145	0.054	116	0.061
0.75	*	*	151	0.020	147	0.011	176	0.010	161	0.033	171	0.052	211	0.033	170	0.007	153	0.026
0.80	*	*	195	0.019	183	0.019	210	0.025	201	0.013	190	0.014	317	0.077	233	0.097	201	0.039

Sample not suitable for measurement by DLS due to '–' Lack of scattering or '*' Sample precipitated
D_z z-average diameter

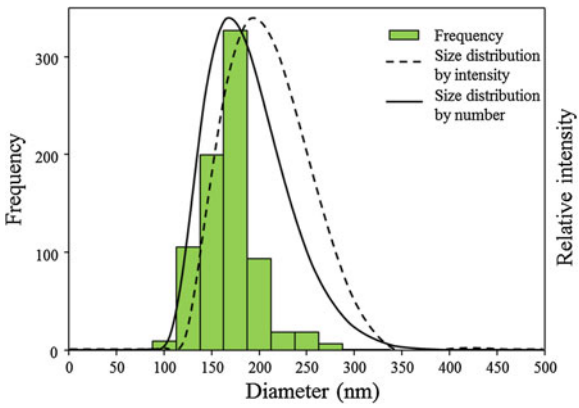

Fig. 2.17 Histogram analysis of nanoparticles via SEM imaging (784 particles from 2 images) overlaid with the DLS size distribution by intensity and number traces for **EBiB-**pHPMA$_{50}$-EGDMA$_{0.8}$, Φ_{hex} = 0.80

measured by DLS. Figure 2.17 shows the histogram analysis of two SEM images, totalling 784 particles. The number average diameter (D_n) measured by DLS for this sample was 179 nm, whilst the D_z was 195 nm. The estimated mean calculated from the histogram was 156 nm. This was slightly lower than observed via DLS measurements, however, DLS was measuring the diameter of the particles dispersed in the organic solvent mixture, whilst SEM imaging was conducted on a dry sample. Therefore some shrinkage upon solvent evaporation was to be expected.

The same experiment was conducted with the **G1** dendron initiated *hyp*-polydendron materials (see Fig. 2.18a and Table 2.2). When there was only good solvent present DLS analysis was of solvated polymer samples which contained a distribution of linear to highly branched materials and therefore had high PdI values. For example, the PdI values for the **G1**-pHPMA$_{50}$-EGDMA$_{0.8}$ sample at hexane fractions of 0, 0.09 and 0.17 were 0.369, 0.361 and 0.325 respectively. This was indicative of multiple populations of sizes being present in the sample measured via DLS. There are no values present in the table for **G1**-pHPMA$_{100}$-EGDMA$_{0.8}$ with Φ = 0 and 0.09 due to the samples being too polydisperse for measurement, which predominantly occurred with low hexane fractions, as with the **EBiB** series. Once a hexane fraction of 0.23 had been reached the solvated polymers underwent self-assembly to produce nanoparticles of uniform size and low polydispersities (<0.1). After self-assembly had occurred, further addition of hexane caused the nanoparticles to decrease in size until a hexane fraction around 0.50–0.67 was reached. **G1**-pHPMA$_{20}$-EGDMA$_{0.8}$ decreased in D_z from 204 to 167 nm (from Φ_{hex} = 0.23 to 0.50), **G1**-pHPMA$_{50}$-EGDMA$_{0.8}$ decreased in D_z from 162 to 133 nm (from Φ_{hex} = 0.23 to 0.67) and **G1**-pHPMA$_{100}$-EGDMA$_{0.8}$ decreased in D_z from 180 to 130 nm (from Φ_{hex} = 0.17 to 0.67). This series of materials also followed the trend observed with the **EBiB** series of branched polymers whereby the nanoparticles formed with the DP$_{20}$ sample were larger than those with the DP$_{50}$, and the nanoparticle formed with the DP$_{50}$ sample were larger than those with the DP$_{100}$ sample (DP$_{20}$ > DP$_{50}$ > DP$_{100}$).

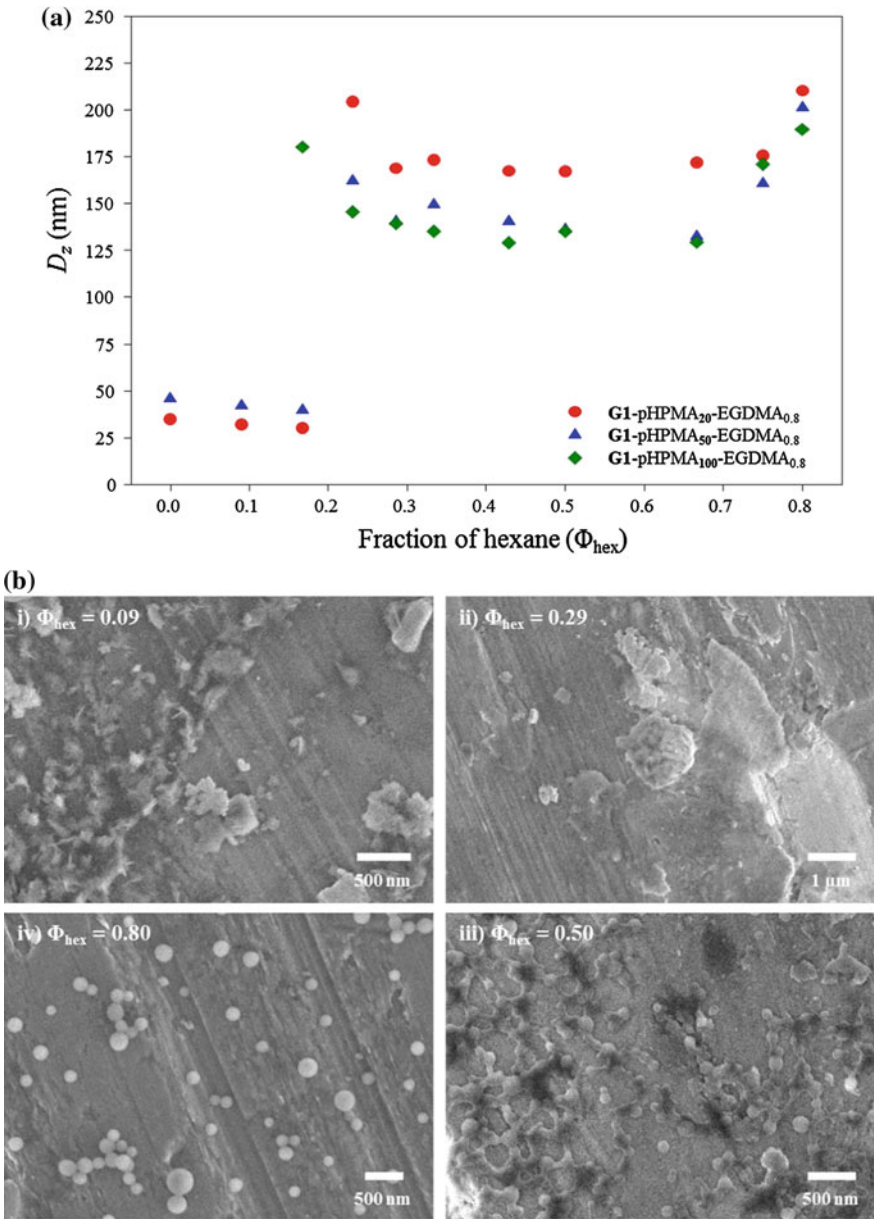

Fig. 2.18 The formation of nanoparticles followed via **a** DLS of each **G1** dendron initiated *hyp*-polydendron DP_{20} (*red circles*) DP_{50} (*blue triangles*) DP_{100} (*green diamonds*) and **b** SEM images of the formation of nanoparticles with **G1**-pHPMA$_{50}$-EGDMA$_{0.8}$ at various hexane solvent fractions; (*i*) 0.09, (*ii*) 0.29, (*iii*) 0.50 and (*iv*) 0.80

SEM investigations of the formation of nanoparticles using the **G1**-pHPMA$_{50}$-EGDMA$_{0.8}$ *hyp*-polydendron were also studied at hexane fractions 0.09, 0.29, 0.5 and 0.8 (Fig. 2.18b). It was immediately obvious that at the two lowest hexane fractions (0.09 and 0.29, Fig. 2.18b-i, ii) no hierarchical structure was observed, even though self-assembly was measured by DLS at a hexane fraction of 0.23. The cause for this at Φ_{hex} = 0.09 (Fig. 2.18b-i) was again most probably due to the fact that the polymer was well solvated by the good solvent, acetone, and therefore upon drying an uneven polymer film was formed. At Φ_{hex} = 0.29 there was still a large good solvent fraction present, therefore, possibly the nanoparticle structure was lost upon solvent evaporation. Figure 2.18b-iii shows the sample at a hexane fraction of 0.5, where spherical particles were observed, however, they appear to have dried in a manner to suggest that they adhere to one another and appear slightly different from those observed at the same solvent fraction for the equivalent **EBiB** initiated branched polymer (Fig. 2.16b-iii). This may be due to the fact that the dendron moiety at the chain end is in fact soluble in the anti-solvent, hexane, for the polymer core, therefore this may affect the properties of the nanoparticles upon drying.

This was not the case for the corresponding **G2** sample (Fig. 2.20b-iii) which could suggest that it is dependent upon which area of the stub is being imaged. This phenomena was not observed for the sample taken at Φ_{hex} = 0.80 where discreet spherical nanoparticles are observed (Fig. 2.18b-iv). SEM analysis of three images of the **G1**-pHPMA$_{50}$-EGDMA$_{0.8}$ samples at Φ_{hex} = 0.80 (Fig. 2.18b-iv) was conducted totalling 462 particles. Figure 2.19 shows the histogram analysis of measuring the diameters of these nanoparticles via SEM and DLS. The D_n and D_z of this sample as measured by DLS were 186 and 201 nm respectively. The mean diameter calculated from the SEM images was 182 nm, which is incredibly close to the number mean diameter calculated via DLS.

The formation of nanoparticles using the **G2** dendron initiated *hyp*-polydendrons, followed by DLS, (see Fig. 2.20a and Table 2.2) also followed the same trends as the **EBiB** *hyp*-polymers and the **G1** *hyp*-polydendron materials. As mentioned previously, at low hexane fractions the DLS measurements gave smaller D_z and higher PdI values. For example, at Φ_{hex} = 0 and 0.09 all of the samples, and at Φ_{hex} = 0.17 the

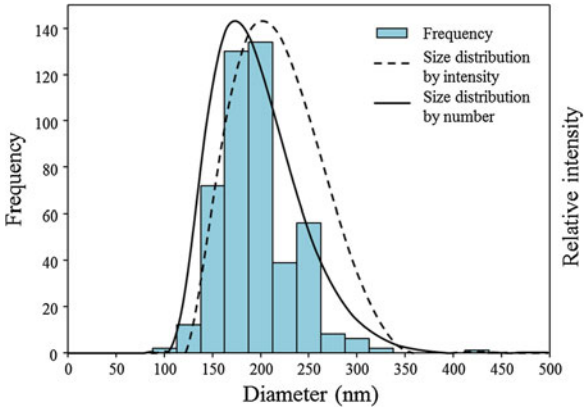

Fig. 2.19 Histogram analysis of nanoparticles via SEM imaging (462 particles from 3 images) overlaid with the DLS size distribution by intensity and number traces for **G1**-pHPMA$_{50}$-EGDMA$_{0.8}$, Φ_{hex} = 0.80

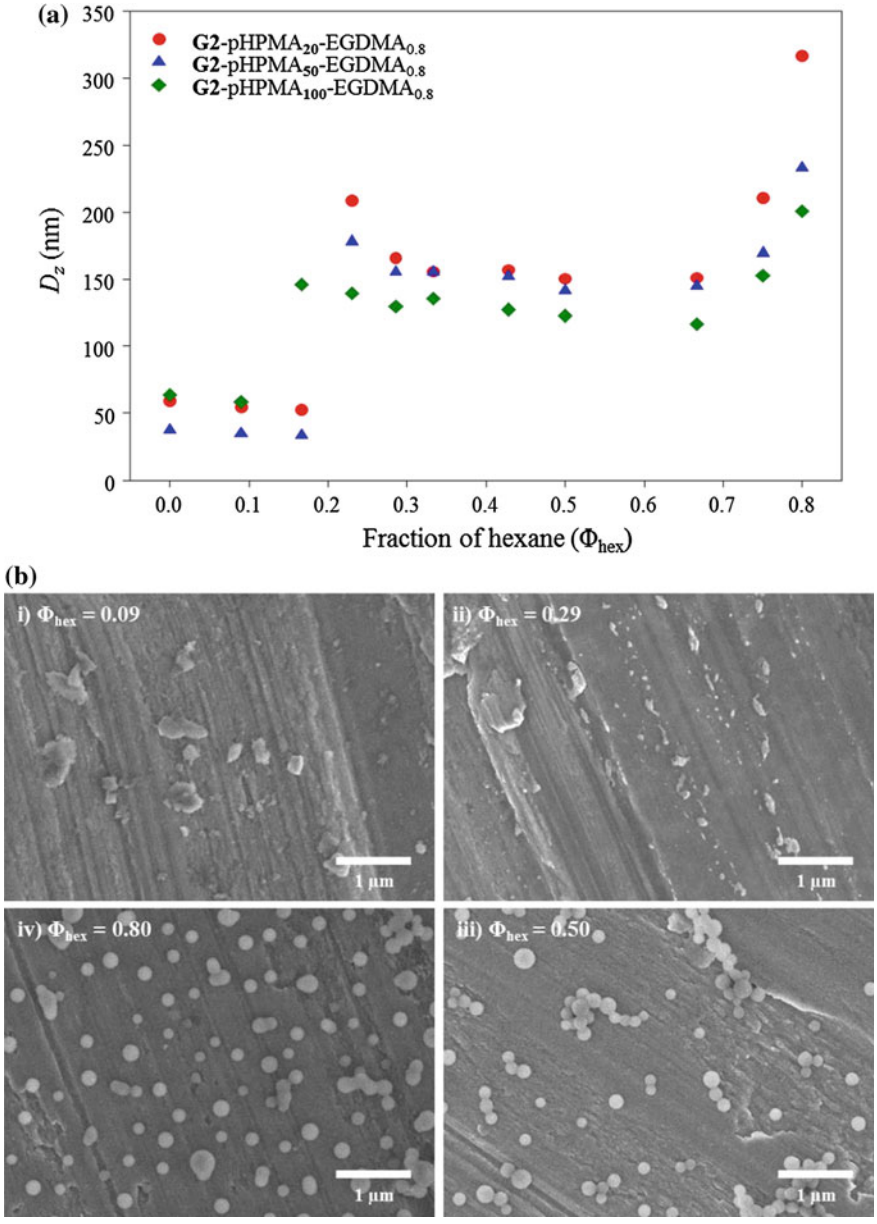

Fig. 2.20 The formation of nanoparticles followed via **a** DLS of each **G2** dendron initiated *hyp*-polydendron DP_{20} (*red circles*) DP_{50} (*blue triangles*) DP_{100} (*green diamonds*) and **b** SEM images of the formation of nanoparticles with **G2**-$pHPMA_{50}$-$EGDMA_{0.8}$ at various hexane solvent fractions; (*i*) 0.09, (*ii*) 0.29, (*iii*) 0.50 and (*iv*) 0.80

DP_{20} and DP_{50} samples had D_z less than 65 nm and high PdI values (>0.34). Interestingly, in the case of both the DP_{20} and DP_{50} *hyp*-polydendron samples when the hexane fraction was increased from 0 to 0.17 the corresponding PdI values decreased, as did the D_z. This suggests that as more anti-solvent is added the fully solvated polymer chains are minimising their interactions with the hexane by collapsing slightly and subsequently reducing in size and polydispersity. Once a hexane fraction of 0.17 (DP_{100}) or 0.23 (DP_{20} and DP_{50}) was reached the *hyp*-polydendrons self-assembled into nanoparticles with low PdI values (<0.1). As the hexane fraction increased to around 0.50 the resulting nanoparticle decreased in D_z (from 209 to 150 nm, from $\Phi_{hex} = 0.23$ to 0.5 for **G2**-pHPMA$_{20}$-EGDMA$_{0.8}$, from 178 to 142 nm, from $\Phi_{hex} = 0.23$ to 0.5 for **G2**-pHPMA$_{50}$-EGDMA$_{0.8}$ and from 146 to 116 nm, from $\Phi_{hex} = 0.17$ to 0.67 for **G2**-pHPMA$_{100}$-EGDMA$_{0.8}$).

With increasing hexane fraction after this point the D_z increased in size further to 317, 233 and 201 nm for the DP_{20}, DP_{50} and DP_{100} *hyp*-polydendrons, respectively. This was thought to be due to the nanoparticles aggregating, and with an excess of hexane, the samples would ultimately precipitate. It is worth noting that once again the order of size of the nanoparticles formed followed the same trend as the **EBiB** *hyp*-polymers and **G1** *hyp*-polydendrons, where $DP_{20} > DP_{50} > DP_{100}$.

SEM images for various hexane fractions corresponding to the **G2**-pHPMA$_{50}$-EGDMA$_{0.8}$ sample are shown in Fig. 2.20b. Here the lowest hexane fraction studied ($\Phi_{hex} = 0.09$, Fig. 2.20b-i) showed only polymer deposits on the SEM stub due to the polymer being solvated by the good solvent, therefore upon drying an uneven polymer film was formed. Although self-assembly was observed at $\Phi_{hex} = 0.23$, there was minimal structure present in the corresponding SEM image (Fig. 2.20b-ii), again most probably due to the large good solvent fraction present affecting the drying of the sample on the SEM stub. At hexane fractions of 0.50 and 0.80 (Fig. 2.20iii, iv) discreet spherical polymeric nanoparticles were observed with diameters that closely correlated with the D_z measured by DLS. Analysis of the SEM images for the **G2**-pHPMA$_{50}$-EGDMA$_{0.8}$ nanoparticle sample with $\Phi_{hex} = 0.80$ was conducted by measuring the diameter of nanoparticles from two images, totalling 314 particles, see Fig. 2.21.

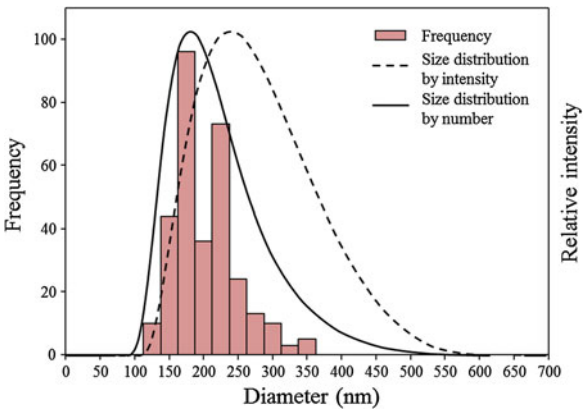

Fig. 2.21 Histogram analysis of nanoparticles via SEM imaging (314 particles from 2 images) overlaid with the DLS size distribution by intensity and number traces for **G2**-pHPMA$_{50}$-EGDMA$_{0.8}$, $\Phi_{hex} = 0.80$

The D_z measured by DLS was 234 nm, whilst the D_n was 203 nm. The mean diameter calculated from the histogram analysis was 190 nm, which was smaller than that measured via DLS most likely due to the SEM analysis performed on dry particles whilst DLS measurements occur when the particles are in the organic solvent mixture.

This mechanism of *hyp*-polymer or *hyp*-polydendron self-assembly is outlined graphically in Fig. 2.22, and has only been observed when using the branched polymers. When the linear polymers and linear-dendritic polymers are subjected to the same treatment the results were quite different.

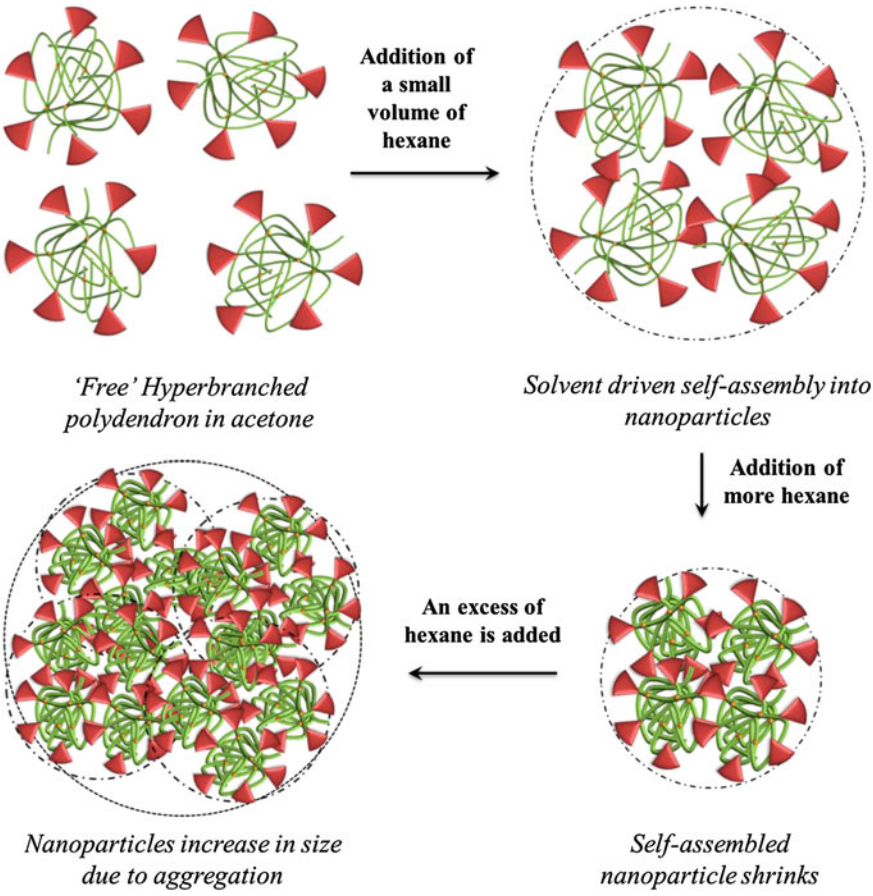

Fig. 2.22 Proposed mechanism of nanoparticle formation in organic solvent mixtures

2.5.2 Nanoparticle Formation Utilising Linear Polymers and Linear-Dendritic Polymers

DLS investigations of the self-assembly of the linear and linear-dendritic polymer analogues of those discussed in Sect. 2.5.1 showed that they did not follow the same trend. In fact it was difficult to find a trend which was applicable to all the linear polymers when they are subjected to the same treatment (dissolving the polymers in acetone (5 mg/mL) and adding various volumes of hexane in an attempt to induce self-assembly). They required a larger fraction of anti-solvent to be added before any form of nanoprecipitation was observed and thus be measured by DLS. Once formed these particles were larger in size (between 500 and 900 nm in diameter, D_z) and had broader polydispersities (approx. 0.5).

The DLS measurements of nanoparticles formed by addition of hexane to polymers dissolved in acetone for each of the **EBiB** initiated linear polymers is shown in Fig. 2.23a and Table 2.3. The DLS measurements at hexane fractions lower than $\Phi_{hex} = 0.29$ all failed on the DLS quality control criteria due to very high polydispersity, or the linear chains which are solvated were too small to be detected

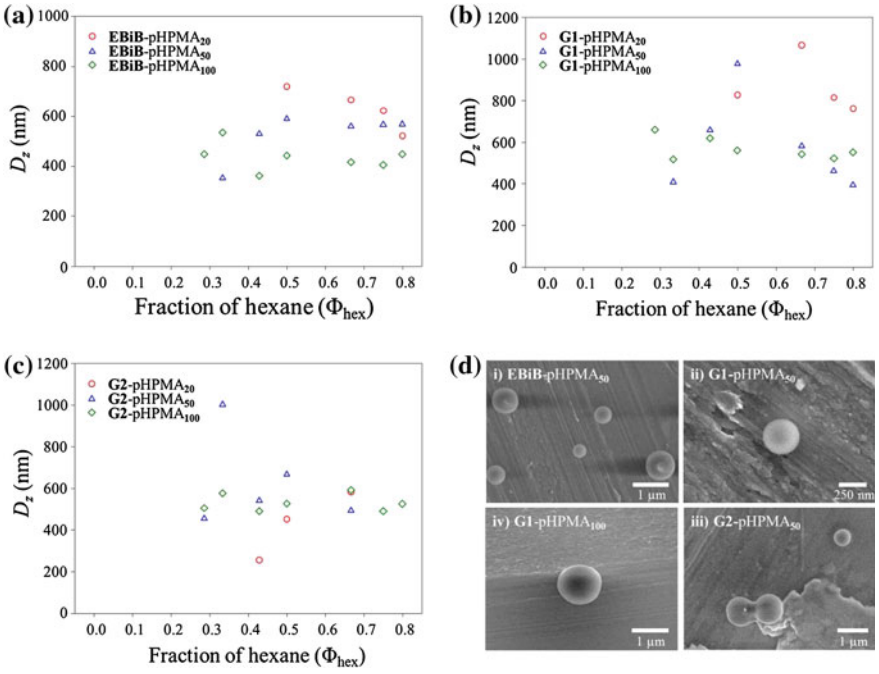

Fig. 2.23 Solvent manipulation as followed by DLS of **a EBiB** linear polymers **b G1** linear-dendritic polymers, **c G2** linear-dendritic polymers. DP_{20} (*red open circles*), DP_{50} (*blue open triangles*) DP_{100} (*green open diamonds*). **d** SEM images of nanoparticle samples with a hexane fraction $\Phi_{hex} = 0.80$ for (i) **EBiB**-pHPMA$_{50}$, (ii) **G1**-pHPMA$_{50}$, (iii) **G2**-pHPMA$_{50}$ and (iv) **G1**-pHPMA$_{100}$

Table 2.3 D_z and PdI measurements by DLS corresponding to Fig. 2.23a for **EBiB** linear polymers

Fraction of hexane added (Φ_{hex})	**EBiB**-pHPMA$_{20}$		**EBiB**-pHPMA$_{50}$		**EBiB**-pHPMA$_{100}$	
	D_z (nm)	PdI	D_z (nm)	PdI	D_z (nm)	PdI
0.29	–	–	–	–	447	0.224
0.33	–	–	352	0.210	534	0.331
0.43	–	–	529	0.173	361	0.117
0.50	719	0.519	590	0.075	443	0.051
0.67	665	0.095	559	0.046	416	0.053
0.75	622	0.139	566	0.091	405	0.067
0.80	522	0.076	568	0.076	448	0.103

D_z z-average diameter

accurately. Once enough hexane had been added, nanoprecipitates were formed. This was Φ_{hex} = 0.5 for **EBiB-**pHPMA$_{20}$ (719 nm), Φ_{hex} = 0.33 for **EBiB-**pHPMA$_{50}$ (352 nm) and Φ_{hex} = 0.29 for **EBiB-**pHPMA$_{100}$ (447 nm), which were larger in size than the branched equivalents (see Sect. 2.5.1). The nanoparticles formed were between 350–720 nm in D_z and their formation did not appear to follow a trend. The DP$_{20}$ polymer sample decreased in size with increasing hexane fraction (to 522 nm at Φ_{hex} = 0.80), whilst the DP$_{50}$ increased in size up to Φ_{hex} = 0.50 where it reached a plateau to Φ_{hex} = 0.80 (568 nm). The DP$_{100}$ appeared to vary with increasing hexane fraction but is the same size at Φ_{hex} = 0.80 (448 nm) as at Φ_{hex} = 0.29 (447 nm).

The **G1** dendron initiated linear-dendritic polymers (Fig. 2.23b and Table 2.4) also formed nanoparticles at hexane fractions above Φ_{hex} = 0.29. The **G1-**pHPMA$_{20}$ sample did not give a reliable DLS measurement until Φ_{hex} = 0.50 (827 nm), **G1-**pHPMA$_{50}$ formed nanoparticles at Φ_{hex} = 0.33 (408 nm) and the **G1-**pHPMA$_{100}$ at Φ_{hex} = 0.29 (660 nm). The increasing hexane fractions appears to have similar effects upon **G1-**pHPMA$_{20}$ and **G1-**pHPMA$_{50}$ whereby with

Table 2.4 D_z and PdI measurements by DLS corresponding to Fig. 2.23b for **G1** linear-dendritic polymers

Fraction of hexane added (Φ_{hex})	**G1**-pHPMA$_{20}$		**G1**-pHPMA$_{50}$		**G1**-pHPMA$_{100}$	
	D_z (nm)	PdI	D_z (nm)	PdI	D_z (nm)	PdI
0.29	–	–	–	–	660	0.511
0.33	–	–	408	0.212	517	0.258
0.43	–	–	658	0.25	618	0.116
0.50	827	0.226	977	0.228	560	0.073
0.67	1066	0.203	581	0.148	543	0.11
0.75	814	0.186	460	0.136	522	0.09
0.80	761	0.167	394	0.048	552	0.207

D_z z-average diameter

increasing hexane fraction, the nanoprecipitates increased in size then subsequently decreased in size. **G1-**pHPMA$_{20}$ reached a maximum D_z at Φ_{hex} = 0.67 of 1066 nm, then decreased to 761 nm at Φ_{hex} = 0.80. **G1**-pHPMA$_{50}$ reached a maximum D_z at Φ_{hex} = 0.50 of 977 nm, then decreased to 394 nm at Φ_{hex} = 0.80. This trend was not observed with the **G1**-pHPMA$_{100}$ sample which instead varied slightly with increasing hexane fraction and at Φ_{hex} = 0.80 was 552 nm.

Figure 2.23c and Table 2.5 show the resulting DLS measurements for the same experiment using the **G2** dendron initiated linear dendritic polymers. In this case again the DLS readings were not reliable until solvent fractions of Φ_{hex} = 0.43 was reached for **G2-**pHPMA$_{20}$ (255 nm) and Φ_{hex} = 0.29 for **G2-**pHPMA$_{50}$ (454 nm) and **G2-**pHPMA$_{100}$ (504 nm). The DP$_{20}$ linear-dendritic polymer samples increased in D_z between solvent fractions 0.43–0.67 (from 255 to 581 nm) then, at higher hexane fractions, precipitate was observed in the sample, which therefore could not be measured by DLS as the result would be inaccurate due to the sedimentation of material. The **G2-**pHPMA$_{50}$ polymer sample followed a similar trend as that observed for **G1-**pHPMA$_{20}$ and **G1-**pHPMA$_{50}$, where the nanoparticles formed initially increased in size up to 1001 nm (Φ_{hex} = 0.33) then decreased to 493 nm (Φ_{hex} = 0.67). For this polymer at a hexane fraction of 0.75 the DLS measurement appeared reliable, however, the size obtained (1754 nm) is usually not reliably measured using this technique and with increasing the hexane fraction again to 0.80 the sample precipitated, therefore the size measured at Φ_{hex} = 0.75 must have been at the onset of aggregation. The **G2-**pHPMA$_{100}$ linear-dendritic polymer remained around the same D_z throughout the experiment and the final size at Φ_{hex} = 0.80 was 525 nm.

In each case the DP$_{20}$ polymers required a much higher hexane fraction (Φ_{hex} = 0.5 for the **EBiB**-pHPMA$_{20}$ and **G1**-pHPMA$_{20}$ polymers and Φ_{hex} = 0.43 for the **G2**-pHPMA$_{20}$ sample). The DP$_{50}$ polymers required a lower hexane fraction to induce self-assembly; Φ_{hex} = 0.33 for the **EBiB**-pHPMA$_{50}$ and **G1**-pHPMA$_{50}$ polymers and Φ_{hex} = 0.29 for the **G2**-pHPMA$_{50}$ sample, and then all the DP$_{100}$ required a hexane fraction of 0.29 to self-assemble.

Table 2.5 D_z and PdI measurements by DLS corresponding to Fig. 2.23c for **G2** linear-dendritic polymers

Fraction of hexane added (Φ_{hex})	**G2**-pHPMA$_{20}$		**G2**-pHPMA$_{50}$		**G2**-pHPMA$_{100}$	
	D_z (nm)	PdI	D_z (nm)	PdI	D_z (nm)	PdI
0.29	–	–	454	0.203	504	0.315
0.33	–	–	1001	0.438	575	0.148
0.43	255	0.233	540	0.119	490	0.052
0.50	451	0.401	666	0.165	525	0.083
0.67	581	0.138	493	0.104	592	0.208
0.75	–	–	1754[a]	0.294	489	0.077
0.80	–	–	–	–	525	0.179

[a]Too high for accurate measurement by DLS
D_z z-average diameter

SEM images of some linear samples are shown in Fig. 2.23d; (i) **EBiB**-pHPMA$_{50}$, (ii) **G1**-pHPMA$_{50}$, (iii) **G1**-pHPMA$_{100}$ and (iv) **G2**-pHPMA$_{50}$. They show that spherical discreet particles are formed, although the sizes observed by SEM would vary somewhat with those observed by DLS. This could be due to the linear nanoprecipitates aggregating as the solvent evaporated when being prepared on the SEM stub.

2.5.3 *Comparison of Nanoparticle Formation of Linear Versus Branched*

A comparison of the linear and branched nanoparticles formed via this organic solvent nanoprecipitation approach showed a huge difference in the mechanism of formation and the characteristics of the nanoparticles. Whilst all the branched samples follow the same trend with addition of an anti-solvent to the polymer dissolved in a good solvent, the behaviour of the linear equivalents was quite erratic. These trends have been discussed in detail previously (see Sects. 2.5.1 and 2.5.2), however, it is the differences between the linear and branched samples which were most interesting. Figure 2.24 exemplifies the huge difference in nanoparticles size and shows the DP$_{100}$ branched and linear polymers plotted on the same graph. The linear equivalents were approximately 3–4 times larger than the branched polymers and generally had higher polydispersities.

Variables which may affect the sizes of the resulting nanoparticles such as the rate of anti-solvent addition, the temperature and the age of the sample were

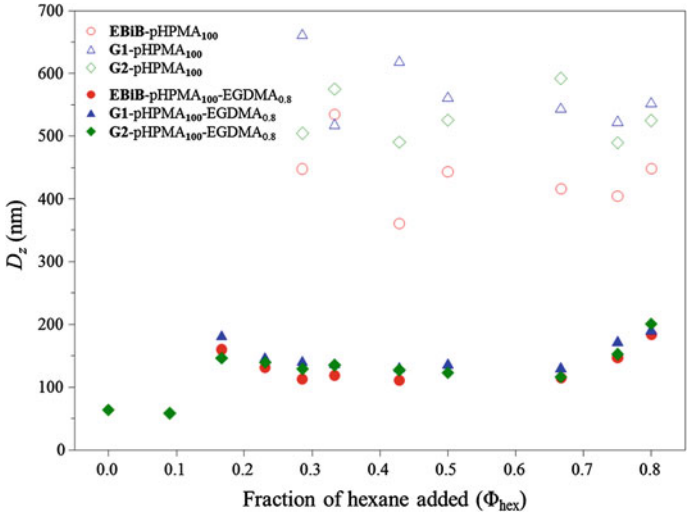

Fig. 2.24 DLS measurements of nanoparticles formed using DP$_{100}$ polymers, highlighting the difference between linear polymers (*open symbols*) and branched polymers (*closed symbols*)

investigated. The rate of hexane addition of 0.5 mL/min was chosen, a temperature difference between 16 and 20 °C had no significant effects on nanoparticle sizes or PdIs. The only factor affecting the samples was the age of the sample; the nanoparticles appeared to precipitate over time. This was probably due to solvent evaporation even though the samples were sealed, as the acetone evaporates the polymers aggregate more, this is observed by the increase of nanoparticle size and eventually the precipitation of the polymers.

2.5.4 Controlling Nanoparticle Size

To determine whether particle size could be tailored to a certain degree, nanoparticles of **G1**-pHPMA$_{50}$-EGDMA$_{0.8}$ were studied by DLS at various initial concentrations; 0.5, 5.0 and 20 mg/mL. Figure 2.25 shows that at each concentration studied the same trend was observed, as previously discussed, suggesting that the mechanism of nanoparticle formation remains the same.

Increasing the initial concentration of polymer dissolved in acetone increased the subsequent size of the nanoparticles formed. This suggests the self-assembly of numerous branched molecules into a nanoparticle, as at higher concentrations, more molecules are available in a confined area to form the nanoparticle. In the more dilute system there were fewer molecules available in the same area to form the nanoparticle, resulting in smaller sizes. The D_z and PdI values for these samples are shown in the Appendix, Table A.1.

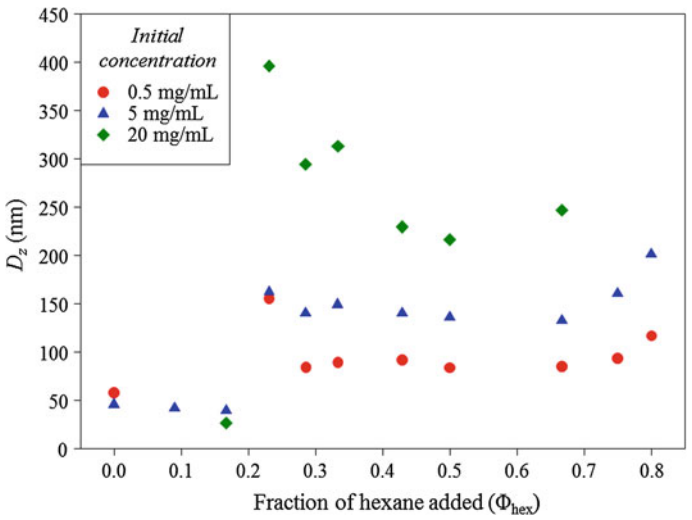

Fig. 2.25 Formation of nanoparticles with varying the initial concentration of **G1**-pHPMA$_{50}$-EGDMA$_{0.8}$ in acetone at 20 mg/mL (*red circles*), 5.0 mg/mL (*blue triangles*) and 0.5 mg/mL (*green diamonds*)

2.5.5 Dilution Experiments

To understand the formation of the nanoparticles dilution experiments were performed. The first, where a nanoparticle formulation was diluted with acetone (a good solvent for both the initiator surface groups and the polymer core) and the second was the dilution of a nanoparticle formulation without altering the solvent system.

2.5.5.1 Dilution with Good Solvent, Acetone

The nanoparticle formulation used for this dilution experiment was **G1**-pHPMA$_{50}$-EGDMA$_{0.8}$ nanoparticles at Φ_{hex} = 0.67 with an initial concentration of 5 mg/mL. Figure 2.26 shows the DLS measurements of the formation of the corresponding nanoparticles (red dotted line) and with increasing the solvent fraction of acetone present (blue dotted line). With addition of acetone the nanoparticles become slightly more solvated by a slight increase in size at the anti-solvent fraction of Φ_{hex} = 0.5, then decreased in size due to complete solvation, returning to their original state of freely dissolved molecules. The D_z and PdI values corresponding to Fig. 2.26 are shown in the Appendix in Table A.2.

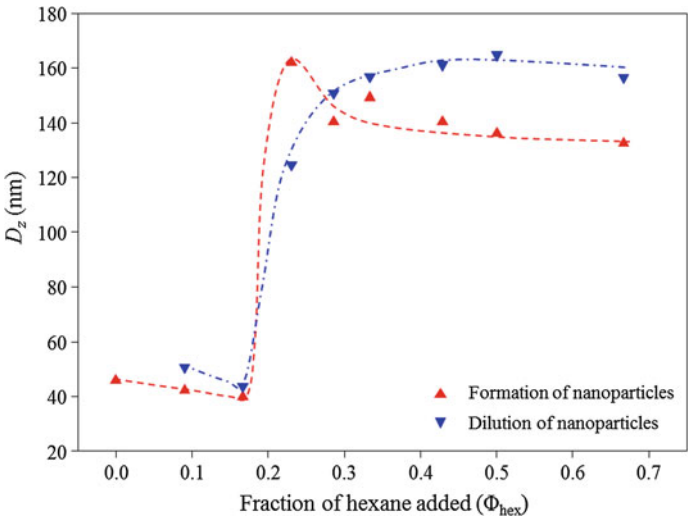

Fig. 2.26 Formation of **G1**-pHPMA$_{50}$-EGDMA$_{0.8}$ nanoparticles (*red up triangles*) and dilution with good solvent, acetone (*blue down triangles*). Trend lines added for ease of viewing only

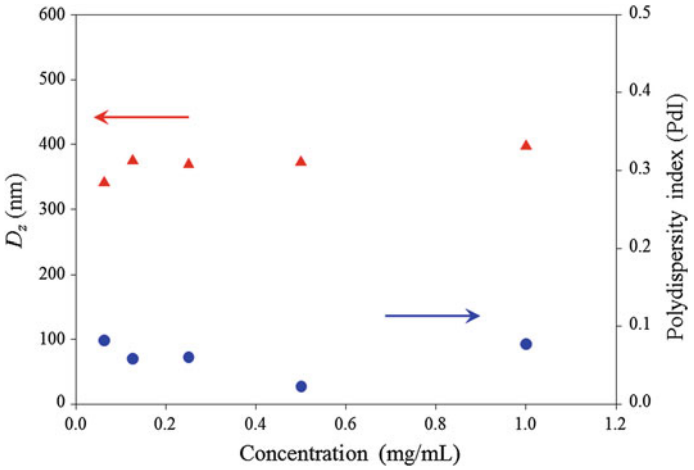

Fig. 2.27 Dilution experiment of **G1**-pHPMA$_{50}$-EGDMA$_{0.8}$ nanoparticles at a hexane fraction of 0.80 and initial concentration of 5 mg/mL, diluting with the same solvent system. D_z (*red triangles*) and PdI (*blue circles*)

2.5.5.2 Dilution with the Same Solvent System

To investigate the nanoparticles' stability, a nanoparticle sample of **G1-**pHPMA$_{50}$-EGDMA$_{0.80}$ at an initial concentration 5.0 mg/mL and solvent fraction of hexane Φ_{hex} = 0.80 was diluted with the same solvent system (Φ_{hex} = 0.8, Φ_{ace} = 0.20). Figure 2.27 shows with increasing dilution the size of the nanoparticles is stable until the sample is too dilute for accurate DLS measurement. Therefore once formed the nanoparticles are stable to dilution. The D_z and PdI values corresponding to Fig. 2.27 are shown in Table A.3, in the Appendix.

2.6 Aqueous Nanoprecipitation of Hydrophobic Polymers

The overall aim of the project was to produce aqueous nanoparticles for drug delivery, therefore, even though at this stage of the project each polymer synthesised was hydrophobic, they were nanoprecipitated into water, firstly to see if they would produce stable nanoparticles, and secondly, if so, to study their properties. Nanoprecipitation of hydrophobic polymers into water has been reported and is a facile method of producing polymeric nanoparticles [26–28]. The polymers were dissolved in a good solvent, tetrahydrofuran (THF), at two different initial concentrations (5 and 10 mg/mL) and underwent rapid addition to water [11]. The THF was allowed to evaporate overnight to give a final concentration of polymer in water. The final concentration could be altered by either changing the initial

polymer concentration within the good solvent, changing the volume of polymer/THF added or by changing the volume of water used. The relationship between initial concentration, final concentration and dilution factor can be described by Eq. (2.1). Throughout this thesis the initial and final concentration of samples prepared by aqueous nanoprecipitation will be described as $\boldsymbol{i_x}$-$\boldsymbol{f_y}$, where $\boldsymbol{x}$ represents the initial concentration and $\boldsymbol{y}$ the final concentration in mg/mL, whilst the dilution factor will be referred to as *df*.

$$initial\ concentration\ (\boldsymbol{i_x})\ x\ dilution\ factor\ (df)\ =\ final\ concentration\ (\boldsymbol{f_y}) \quad (2.1)$$

2.6.1 *Aqueous Nanoprecipitations with* Hyp-*polymers and* Hyp-*polydendrons*

The aqueous nanoprecipitation process is represented graphically in Fig. 2.28 below with a *hyp*-polydendron depicted. Table 2.6 highlights the different concentrations and dilution factors used and the resulting nanoparticle D_z, PdI and zeta potential values after evaporation of the volatile good solvent (THF). The zeta potential is a measure of the surface charge of the particles and is quoted in mV.

The data in Table 2.6 shows that when the initial concentration was increased in conjunction with a constant dilution factor (*df*), hence an increase in the final concentration, the resultant nanoparticle size increased. This effect is evident when analysing the size distribution by intensity traces for each sample. Figure 2.29a–c show these traces for the nanoparticle dispersions formulated using polymers **EBiB**-pHPMA$_{20}$-EGDMA$_{0.8}$, **EBiB**-pHPMA$_{50}$-EGDMA$_{0.8}$ and **EBiB**-pHPMA$_{100}$-EGDMA$_{0.8}$ respectively. When the initial concentration was increased but the *df*

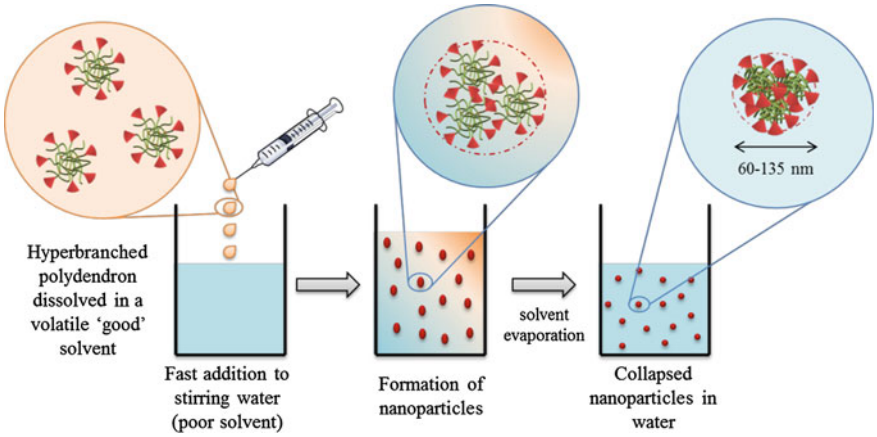

Fig. 2.28 Graphical representation of aqueous nanoparticle formation via a nanoprecipitation approach

Table 2.6 D_z, PdI and zeta potential measurements for all *hyp*-polymer and *hyp*-polydendron aqueous nanoprecipitations at various initial and final concentrations

Nanoprecipitation conditions				**DP$_{20}$**			**DP$_{50}$**			**DP$_{100}$**		
	i_x (mg/mL)	f_y (mg/mL)	*df*	D_z (nm)	PdI	Zeta potential (mV)	D_z (nm)	PdI	Zeta potential (mV)	D_z (nm)	PdI	Zeta potential (mV)
EBiB	10	2	0.2	91	0.127	−51.7	83	0.111	−60.6	101	0.121	−43.2
	10	0.1	0.01	81	0.135	−38.5	76	0.114	−34.8	103	0.112	−28.1
	5	1	0.2	71	0.278	−71.6	66	0.190	−57.0	78	0.125	−44.5
	5	0.05	0.01	65	0.182	−31.3	62	0.216	−30.2	79	0.140	−23.7
G1	10	2	0.2	87	0.108	−61.3	86	0.110	−42.1	96	0.079	−47.3
	10	0.1	0.01	112	0.112	−47.4	91	0.101	−37.8	110	0.106	−41.0
	5	1	0.2	62	0.117	−59.6	64	0.130	−64.5	70	0.070	−54.3
	5	0.05	0.01	69	0.108	−37.1	67	0.160	−24.6	73	0.114	−26.1
G2	10	2	0.2	124	0.080	−46.4	106	0.083	−38.0	109	0.113	−50.2
	10	0.1	0.01	128	0.086	−46.1	134	0.064	−34.3	111	0.127	−41.3
	5	1	0.2	81	0.076	−42.6	81	0.083	−52.5	81	0.119	−62.1
	5	0.05	0.01	82	0.084	−30.0	93	0.071	−37.6	83	0.172	−31.0

D_z z-Average diameter, i_x Initial concentration, f_y Final concentration, *df* Dilution factor

remains constant (e.g. i_{10}-f_2 and i_5-f_1), the size of the nanoparticle formed was increased. In Fig. 2.29a–c those sample pairs which show this are i_{10}-f_2 versus i_5-f_1 (black solid line vs. blue dotted line) and i_{10}-$f_{0.1}$ versus i_5-$f_{0.05}$ (red dashed line vs. green long-dashed line). Compared to when the same initial concentration but different dilution factors were used (e.g. i_{10}-f_2 and i_{10}-$f_{0.1}$), the sizes observed were very similar in this case, even though the final concentration produced varied by 20-fold. The samples which matched this trend in Fig. 2.29a–c were i_{10}-f_2 and i_{10}-$f_{0.1}$ (black solid line vs. red dashed line) and i_5-f_1 and i_5-$f_{0.05}$ (blue dotted line vs. green long-dashed line).

These described trends were also observed with the **G1** dendron (Fig. 2.30) and **G2** dendron (Fig. 2.31) initiated *hyp*-polydendrons to varying degrees. For example, nanoparticle dispersions formed using **G1**-pHPMA$_{50}$-EGDMA$_{0.8}$ (Fig. 2.30b, Table 2.6) have very similar sizes for the same initial concentrations; i_{10}-f_2 and i_{10}-$f_{0.1}$ (86 and 91 nm) and i_5-f_1 and i_5-$f_{0.05}$ samples (64 and 67 nm). Whilst the

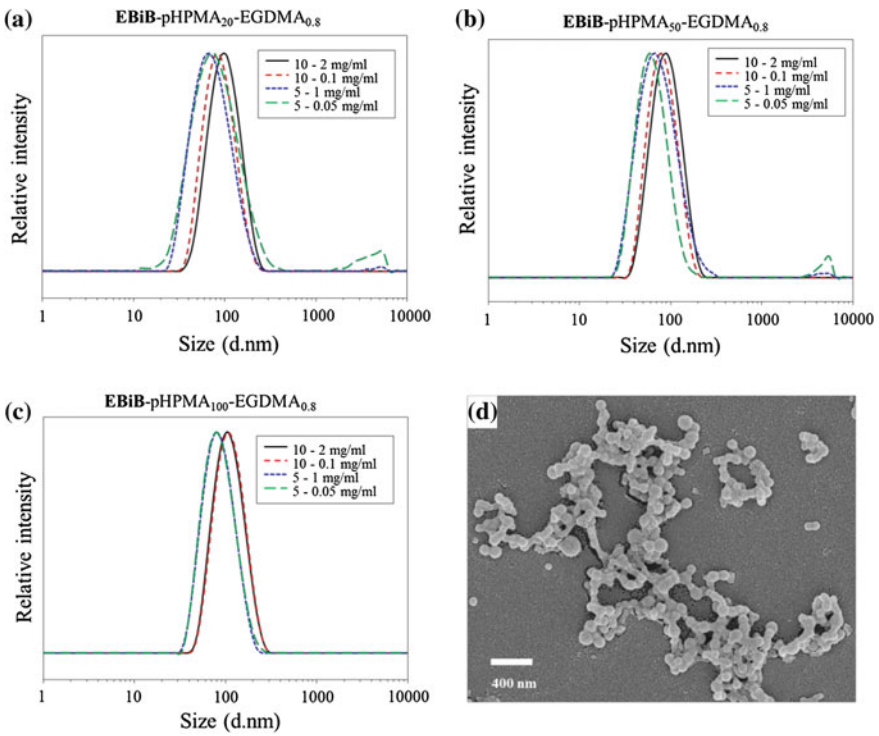

Fig. 2.29 DLS size distribution by intensity traces of aqueous nanoparticle dispersions of; **a** **EBiB**-pHPMA$_{20}$-EGDMA$_{0.8}$, **b** **EBiB**-pHPMA$_{50}$-EGDMA$_{0.8}$ and **c** **EBiB**-pHPMA$_{100}$-EGDMA$_{0.8}$ with various initial and final concentrations, indicated in the legends, and **d** SEM image of the **EBiB**-pHPMA$_{50}$-EGDMA$_{0.8}$ (i_5-f_1) diluted to 0.1 mg/mL for imaging

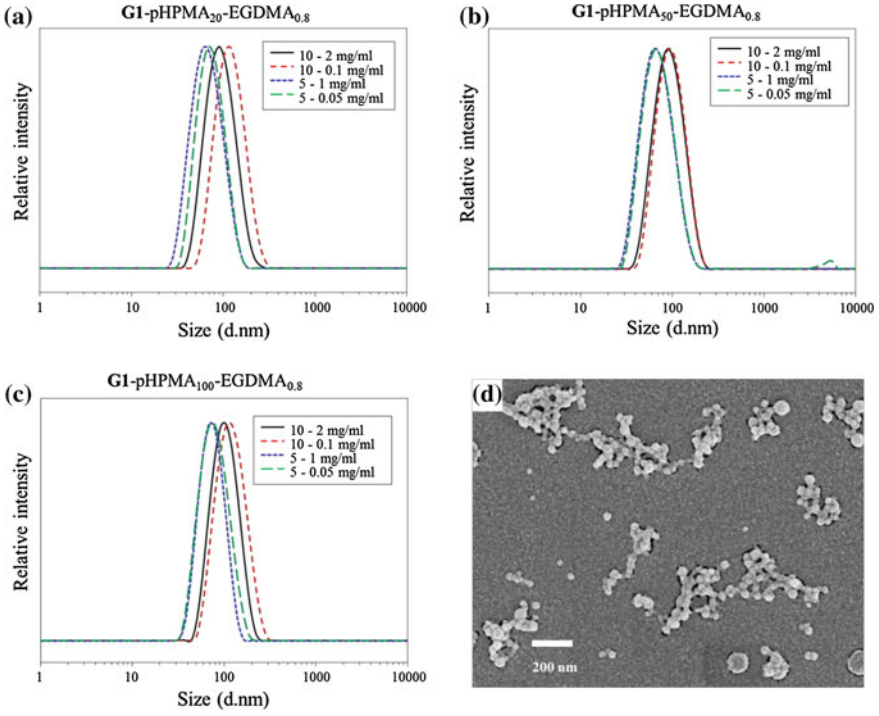

Fig. 2.30 DLS size distribution by intensity traces of aqueous nanoparticle dispersions of; **a** **G1**-pHPMA$_{20}$-EGDMA$_{0.8}$, **b** **G1**-pHPMA$_{50}$-EGDMA$_{0.8}$ and **c** **G1**-pHPMA$_{100}$-EGDMA$_{0.8}$ with various initial and final concentrations, indicated in the legends, and **d** SEM image of the **G1**-pHPMA$_{50}$-EGDMA$_{0.8}$ (***i*$_5$-*f*$_1$**) diluted to 0.1 mg/mL for imaging

samples which have the same dilution factor but different initial and final concentrations (***i*$_{10}$-*f*$_2$** and ***i*$_5$-*f*$_1$**; 86 and 64 nm, and ***i*$_{10}$-*f*$_{0.1}$** and ***i*$_5$-*f*$_{0.05}$**; 91 and 67 nm) show that with a higher initial concentration the resulting nanoparticle D_z was larger.

Again these trends are well exemplified by both **G2**-pHPMA$_{20}$-EGDMA$_{0.8}$ (Fig. 2.31a, Table 2.6) and **G2**-pHPMA$_{100}$-EGDMA$_{0.8}$ (Fig. 2.31c, Table 2.6). The **G2**-pHPMA$_{50}$-EGDMA$_{0.8}$ nanoparticles (Fig. 2.31b, Table 2.6) produced show an increase in size with increasing the initial concentration and maintaining *df*, however, when using the same initial concentration and different *df* the resulting particle also vary in size.

The presence of spherical nanoparticles was confirmed by the SEM images of nanoparticles formed using an initial concentration of 5 mg/mL in THF and a final concentration of 1 mg/mL in water with; **EBiB**-pHPMA$_{50}$-EGDMA$_{0.8}$ (Fig. 2.29d), **G1**-pHPMA$_{50}$-EGDMA$_{0.8}$ (Fig. 2.30d) and **G2**-pHPMA$_{50}$-EGDMA$_{0.8}$ (Fig. 2.31d).

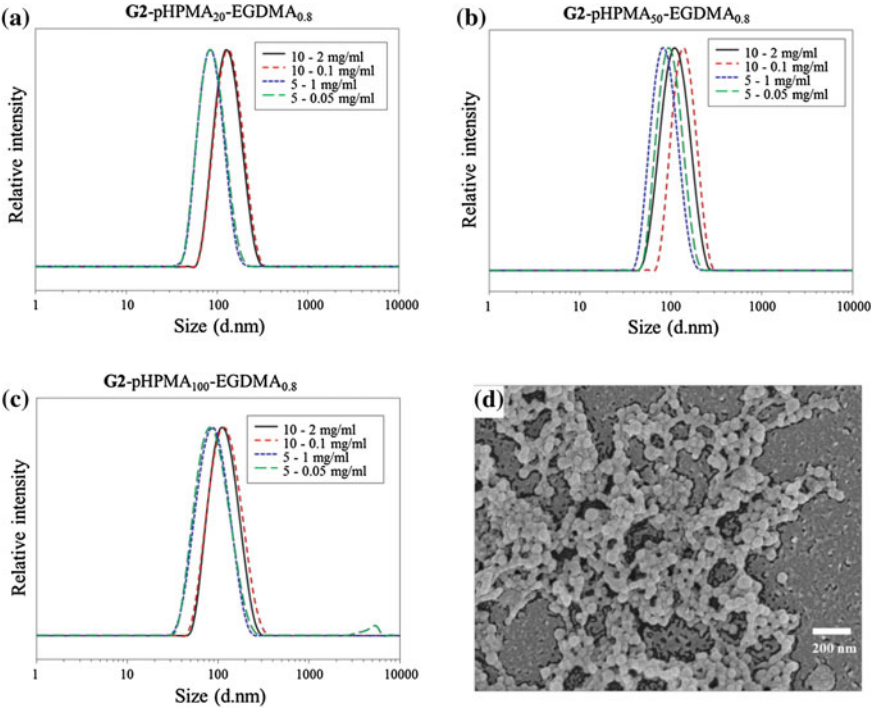

Fig. 2.31 DLS size distribution by intensity traces of aqueous nanoparticle dispersions of; **a G2**-pHPMA$_{20}$-EGDMA$_{0.8}$, **b G2**-pHPMA$_{50}$-EGDMA$_{0.8}$ and **c G2**-pHPMA$_{100}$-EGDMA$_{0.8}$ with various initial and final concentrations, indicated in the legends, and **d** SEM image of the **G2**-pHPMA$_{50}$-EGDMA$_{0.8}$ ($\boldsymbol{i_5}$-$\boldsymbol{f_1}$) diluted to 0.1 mg/mL for imaging

Table 2.7 DLS measurements for linear DP$_{50}$ polymers

Sample name	Nanoprecipitation conditions			D_z (nm)	PdI	Zeta potential (mV)
	i_x (mg/mL)	f_y (mg/mL)	*df*			
EBiB-pHPMA$_{50}$	5	1	0.2	331	0.166	−56.7
	5	0.05	0.01	186	0.077	−50.2
G1-pHPMA$_{50}$	5	1	0.2	228	0.147	−62.6
	5	0.05	0.01	193	0.156	−57
G2-pHPMA$_{50}$	5	1	0.2	142	0.107	−62
	5	0.05	0.01	138	0.123	−54.6

D_z z-average diameter, i_x Initial concentration, f_y Final concentration, *df* Dilution factor

2.6.2 Aqueous Nanoprecipitations with Linear and Linear-Dendritic Polymers

The linear and linear-dendritic polymers were subjected to a similar aqueous nanoprecipitation approach using the **EBiB-**pHPMA$_{50}$, **G1-**pHPMA$_{50}$ and **G2-**pHPMA$_{50}$. DLS measurements of the linear nanoprecipitates are shown in Table 2.7, whilst the DLS size by intensity plots are shown in Fig. 2.32a–c.

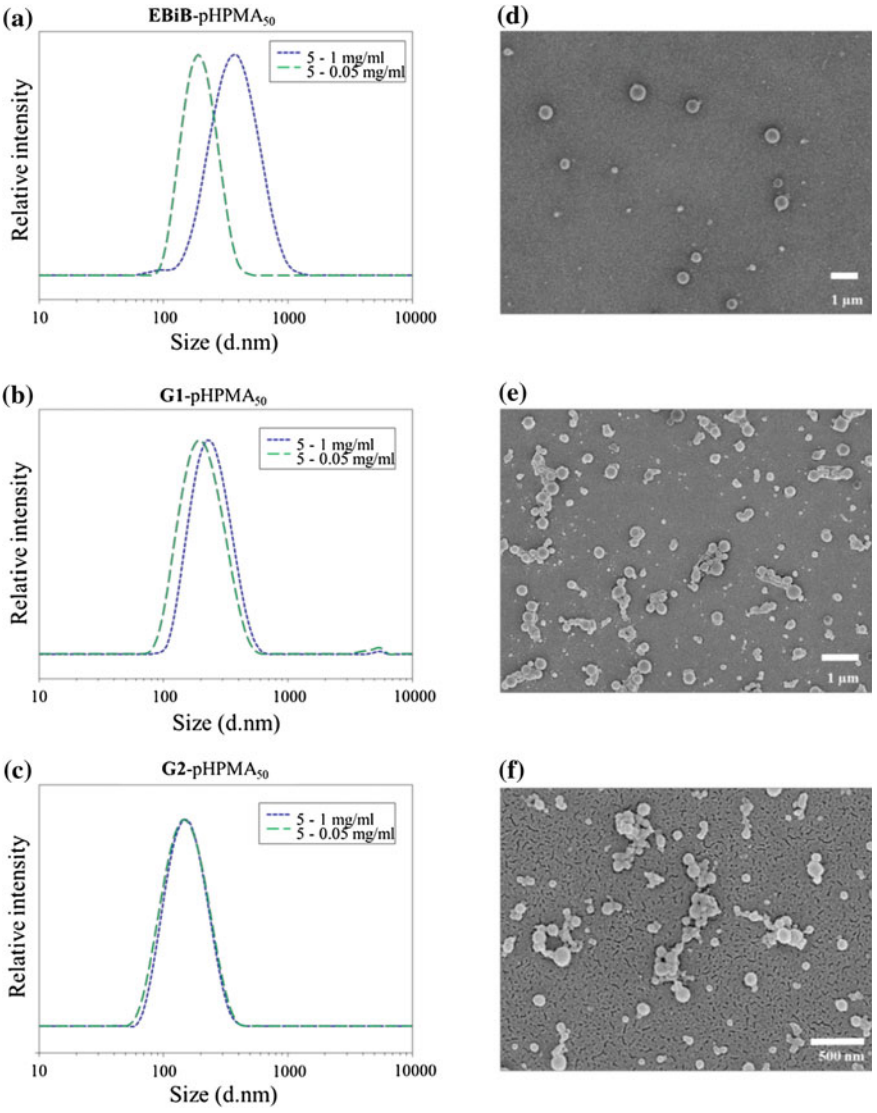

Fig. 2.32 DLS size distribution by intensity traces of aqueous nanoparticle dispersions (i_5-f_1) and SEM images of; **EBiB**-pHPMA$_{50}$ (**a** and **d**), **G1**-pHPMA$_{50}$ (**b** and **e**) and **G2**-pHPMA$_{50}$ (**c** and **f**)

Table 2.8 Nanoprecipitation samples prepared (***i*$_5$-*f*$_1$**) for stability over time study with **EBiB**, **G1** and **G2** initiated linear and branched DP_{50} polymers

Sample name	Original		+23 months	
	D_z (nm)	PdI	D_z (nm)	PdI
EBiB-pHPMA$_{50}$	844	0.238	–	–
G1-pHPMA$_{50}$	562	0.278	612	0.517
G2-pHPMA$_{50}$	315	0.322	–	–
EBiB-pHPMA$_{50}$-EGDMA$_{0.8}$	68	0.125	88	0.438
G1-pHPMA$_{50}$-EGDMA$_{0.8}$	84	0.063	83	0.105
G2-pHPMA$_{50}$-EGDMA$_{0.8}$	63	0.076	72	0.251

'–' Not suitable for measurement by DLS due to precipitation
D_z z-average diameter

The nanoprecipitates formed from the equivalent linear polymers to the previously discussed branched polymers are generally larger in size. For example, the ***i*$_5$-*f*$_1$** sample for **EBiB**-pHPMA$_{50}$ was 331 nm in diameter, whilst the **EBiB**-pHPMA$_{50}$-EGDMA$_{0.8}$ had a diameter of 66 nm. The **G1**-pHPMA$_{50}$ and **G1**-pHPMA$_{50}$-EGDMA$_{0.8}$ nanoprecipitates formed were 228 and 64 nm in diameter, respectively, with the ***i*$_5$-*f*$_1$** samples. This is also true for the **G2** dendron initiated polymers; **G2**-pHPMA$_{50}$ had a diameter of 142 nm and the **G1**-pHPMA$_{50}$-EGDMA$_{0.8}$ equivalent had a diameter of 81 nm.

Figure 2.32d–f show SEM images of the **EBiB**-pHPMA$_{50}$, **G1**-pHPMA$_{50}$ and **G2**-pHPMA$_{50}$, for each ***i*$_5$-*f*$_1$** sample which show spherical particles that correlate with the D_z measured by DLS.

2.6.3 Colloidal Stability of Aqueous Nanoparticles

The nanoprecipitates produced in this chapter were originally not expected to be stable when dispersed in water due to the fact that every component of the polymeric materials were hydrophobic in nature. The stability of the particles was studied over time by storing the samples at ambient temperature out of the light. Samples prepared at ***i*$_5$-*f*$_1$** were used for the study and a separate batch was prepared using the linear and branched DP_{50} polymers (**EBiB**-pHPMA$_{50}$, **EBiB**-pHPMA$_{50}$-EGDMA$_{0.8}$, **G1**-pHPMA$_{50}$, **G1**-pHPMA$_{50}$-EGDMA$_{0.8}$, **G2**-pHPMA$_{50}$ and **G2**-pHPMA$_{50}$-EGDMA$_{0.8}$). Table 2.8 shows the D_z and PdIs for the original sample and repeat measurement after 23 months. Figure 2.33 shows the DLS size distribution by intensity traces for the original measurement and repeat measurement after 23 months.

It is evident from these measurements that the *hyp*-polymer and *hyp*-polydendrons were much more stable over time than their linear polymer equivalents. Two of the linear nanoparticle samples had fully precipitated; **EBiB**-pHPMA$_{50}$ and **G2**-pHPMA$_{50}$. The only linear sample which could be measured by DLS after

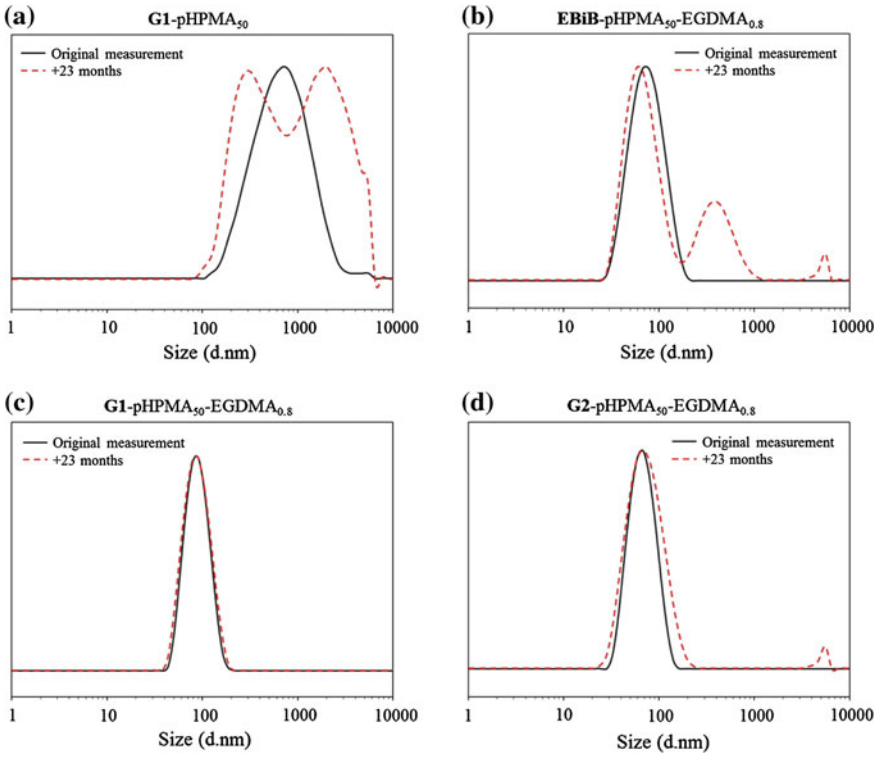

Fig. 2.33 DLS size by intensity traces for **a G1**-pHPMA$_{50}$, **b EBiB**-pHPMA$_{50}$-EGDMA$_{0.8}$, **c G1**-pHPMA$_{50}$-EGDMA$_{0.8}$ and **d G2**-pHPMA$_{50}$-EGDMA$_{0.8}$ original measurements and measurements after 23 months

23 months was the **G1**-pHPMA$_{50}$ sample (see Fig. 2.33a), which had increased in size from 562 to 612 nm and the PdI had almost doubled, from 0.278 to 0.517. All of the branched polymer samples were suitable for DLS measurement and had not increased in size significantly over 23 months. The **EBiB**-pHPMA$_{50}$-EGDMA$_{0.8}$ had increased the most from 68 to 88 nm, with an increase in PdI from 0.125 to 0.438. This was attributed to aggregation of the nanoparticles, which is evident from the two new populations present in the size distribution by intensity traces (see Fig. 2.33b). The **G1**-pHPMA$_{50}$-EGDMA$_{0.8}$ sample remained the same size over 23 months of storage and the PdI only increased slightly from 0.063 to 0.105, see Fig. 2.33c for the DLS size distribution by intensity traces. The **G2**-pHPMA$_{50}$-EGDMA$_{0.8}$ nanoparticle dispersion had only increased from 63 to 72 nm, however an increase in PdI from 0.076 to 0.251 was observed and an extra population was observed in the size distribution by intensity trace after 23 months indicating some aggregation had occurred.

Although the nanoparticles formed using the *hyp*-polymer and *hyp*-polydendron remained stable over time, the zeta potentials measured for each sample were very

negative (<−20 mV) which indicates that the nanoparticles were charge stabilised. The negative charges at the surface of each particle repel one another therefore preventing flocculation or aggregation which can lead to sedimentation and precipitation. Charge stabilised colloids can easily be de-stabilised by addition of electrolytes, such as NaCl, due to the screening of colloidal charges by the ions present [29]. This screening of charges stops the negatively charged particles from repelling one another and they can aggregate and ultimately precipitate. Therefore it is desirable to produce sterically stabilised nanoparticles when designing them for use in biological systems due to the presence of various salts present in the human body [30].

2.7 Conclusion

The synthesis of dendron initiators for ATRP was achieved, with successful synthesis of linear and branched vinyl polymers using the monomer HPMA and divinyl monomer EGDMA. These polymerisations proceeded via 1st order kinetics, as expected, and produced monomodal distributions of polymer chains when a linear polymer was targeted and a much more broad disperse polymer species when the divinyl monomer was incorporated and a branched polymer was targeted. The resulting branched polymers and *hyp*-polydendrons were exposed to two different nanoprecipitation approaches to produce nanoparticles. Solvent manipulation to form nanoparticles in mixtures of good and anti-solvents (acetone and hexane) showed a huge difference in the formation of particles when comparing the *hyp*-polymers and *hyp*-polydendrons to their linear polymer equivalents. When aqueous nanoprecipitation was conducted, surprisingly these hydrophobic polymers produced nanoparticles which were stable over time due to charge stabilisation. The *hyp*-polymers and *hyp*-polydendrons were much more stable over time than their linear polymer equivalents.

References

1. V. Gajbhiye, V.K. Palanirajan, R.K. Tekade, N.K. Jain, J. Pharm. Pharmacol. **61**, 989–1003 (2009)
2. S. Svenson, D.A. Tomalia, Adv. Drug Deliver. Rev. **57**, 2106–2129 (2005)
3. F. Lecolley, C. Waterson, A.J. Carmichael, G. Mantovani, S. Harrisson, H. Chappell, A. Limer, P. Williams, K. Ohno, D.M. Haddleton, J. Mater. Chem. **13**, 2689–2695 (2003)
4. J. Madsen, S.P. Armes, K. Bertal, S. MacNeil, A.L. Lewis, Biomacromolecules **10**, 1875–1887 (2009)
5. J. Rosselgong, S.P. Armes, W.R.S. Barton, D. Price, Macromolecules **43**, 2145–2156 (2010)
6. S.P. Rannard, N.J. Davis, Org. Lett. **2**, 2117–2120 (2000)
7. S.P. Rannard, N.J. Davis, I. Herbert, Macromolecules **37**, 9418–9430 (2004)
8. H. Willcock, A.I. Cooper, D.J. Adams, S.P. Rannard, Chem. Commun. **2009**, 3095–3097 (2009)

9. K. Hemminki, Chem-Biol. Interact. **34**, 323–331 (1981)
10. I. Bannister, N.C. Billingham, S.P. Armes, S.P. Rannard, P. Findlay, Macromolecules **39**, 7483–7492 (2006)
11. R.A. Slater, T.O. McDonald, D.J. Adams, E.R. Draper, J.V.M. Weaver, S.P. Rannard, Soft Matter **8**, 9816–9827 (2012)
12. F. Isaure, P.A.G. Cormack, S. Graham, D.C. Sherrington, S.P. Armes, V. Butun, Chem. Commun. **2004**, 1138–1139 (2004)
13. F. Isaure, P.A.G. Cormack, D.C. Sherrington, Macromolecules **37**, 2096–2105 (2004)
14. Y.T. Li, S.P. Armes, Macromolecules **38**, 5002–5009 (2005)
15. J.S. Wang, K. Matyjaszewski, Macromolecules **28**, 7901–7910 (1995)
16. K. Matyjaszewski, J.H. Xia, Chem. Rev. **101**, 2921–2990 (2001)
17. J.H. Xia, S.G. Gaynor, K. Matyjaszewski, Macromolecules **31**, 5958–5959 (1998)
18. P.A. Gurr, M.F. Mills, G.G. Qiao, D.H. Solomon, Polymer **46**, 2097–2104 (2005)
19. K. Matyjaszewski, Prog. Polym. Sci. **30**, 858–875 (2005)
20. M. Save, J.V.M. Weaver, S.P. Armes, P. McKenna, Macromolecules **35**, 1152–1159 (2002)
21. P.J. Flory, J. Am. Chem. Soc. **63**, 3083–3090 (1941)
22. W.H. Stockmayer, J. Chem. Phys. **12**, 125–131 (1944)
23. H. Fessi, F. Puisieux, J.P. Devissaguet, N. Ammoury, S. Benita, Int. J. Pharm. **55**, R1–R4 (1989)
24. C. Vauthier, K. Bouchemal, Pharm. Res. **26**, 1025–1058 (2009)
25. J.P. Rao, K.E. Geckeler, Prog. Polym. Sci. **36**, 887–913 (2011)
26. O. Thioune, H. Fessi, J.P. Devissaguet, F. Puisieux, Int. J. Pharm. **146**, 233–238 (1997)
27. S. Schubert, J.T. Delaney, U.S. Schubert, Soft Matter **7**, 1581–1588 (2011)
28. C. Zhang, V.J. Pansare, R.K. Prud'homme, R.D. Priestley, Soft Matter **8**, 86–93 (2012)
29. J.W. Goodwin, *Colloids and Interfaces with Surfactants and Polymers*, 2nd edn. (Wiley, UK, 2009)
30. T. Riley, T. Govender, S. Stolnik, C.D. Xiong, M.C. Garnett, L. Illum, S.S. Davis, Colloid Surface B **16**, 147–159 (1999)

Chapter 3
Mixing Dendron and PEG Initiators for the Polymerisation of Branched pHPMA and Aqueous Nanoparticle Formation

3.1 Introduction

To further investigate the scope of the novel *hyp*-polydendron material class, a mixed initiator approach was utilised. This would allow for a new functionality to be incorporated with the dendron functionality. Varying the ratio of two different initiators (A and B) for a branched polymerisation via ATRP should generate macromolecules which contain chain ends containing either functionality A or functionality B, tethered by the branching unit between linear chains, to produce a high molecular weight branched polymer with multi-functional chain ends.

In this case it was thought that facile incorporation of a poly(ethylene glycol) (PEG) chain could be exploited by using a PEG macroinitiator for the polymerisation of branched pHPMA. To maintain the dendron functionality of the branched materials (termed *hyp*-polydendrons, discussed in Chap. 2) the **G2** dendron initiator and the PEG macroinitiator were mixed in a statistical manner in the polymerisation mixture. A range of *hyp*-polydendrons were synthesised with varying ratios of **G2** dendron initiator:PEG macroinitiator (100:0, 90:10, 75:25, 50:50, 25:75, 10:90 and 0:100). A graphical representation of this type of mixed initiator *hyp*-polydendron materials is shown in Fig. 3.1. When a PEG macroinitiator is present the branched polymers have been described as *hyp*-block copolymers.

Publication arising from this chapter: "Hyperbranched Polydendrons: a new nanomaterials platform with tuneable permeation through model gut epithelium", Fiona L. Hatton, Lee M. Tatham, Louise R. Tidbury, Pierre Chambon, Tao He, Andrew Owen and Steven P. Rannard, *Chem. Sci.*, **2015**, 6, 326–334.

F.L. Hatton, *Hyperbranched Polydendrons*,
Springer Theses, DOI 10.1007/978-3-319-18753-2_3

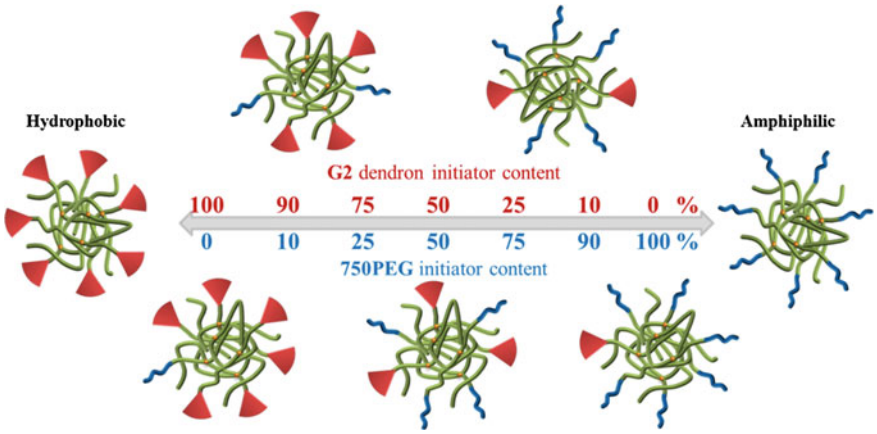

Fig. 3.1 Graphical representation of the type of *hyp*-polydendron materials targeted in this chapter

3.2 Initiator Synthesis

3.2.1 G2 Dendron Initiator

The synthesis of the **G2** dendron initiator, **6**, is highlighted below in Scheme 3.1. It is discussed in more detail in Chap. 2, Sect. 2.2.2.

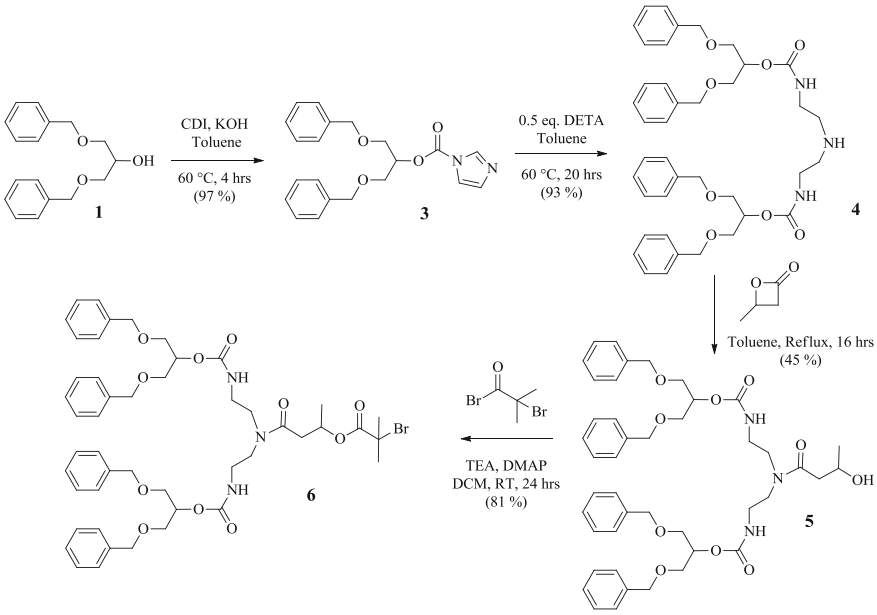

Scheme 3.1 Synthesis of the **G2** DBOP dendron initiator

3.2.2 750PEG Macroinitiator

The **750PEG** macroinitiator, **8**, was synthesised as previously reported [1] from monomethoxy PEG with an average molecular weight of 750 $gmol^{-1}$ via an esterification reaction with α-bromoisobutyryl bromide, shown below in Scheme 3.2.

The formation of **8** could be observed by ^{1}H NMR spectroscopy, shown in Fig. 3.2. The ratio of the integration of peaks corresponding to protons **a** and **h** (Fig. 3.2) fit the proposed structure of **8** being 3:6. The ^{13}C NMR spectrum for the

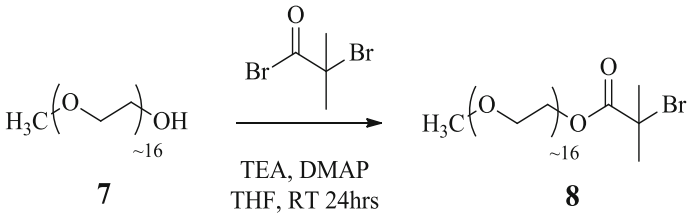

Scheme 3.2 Synthesis of **750PEG** initiator

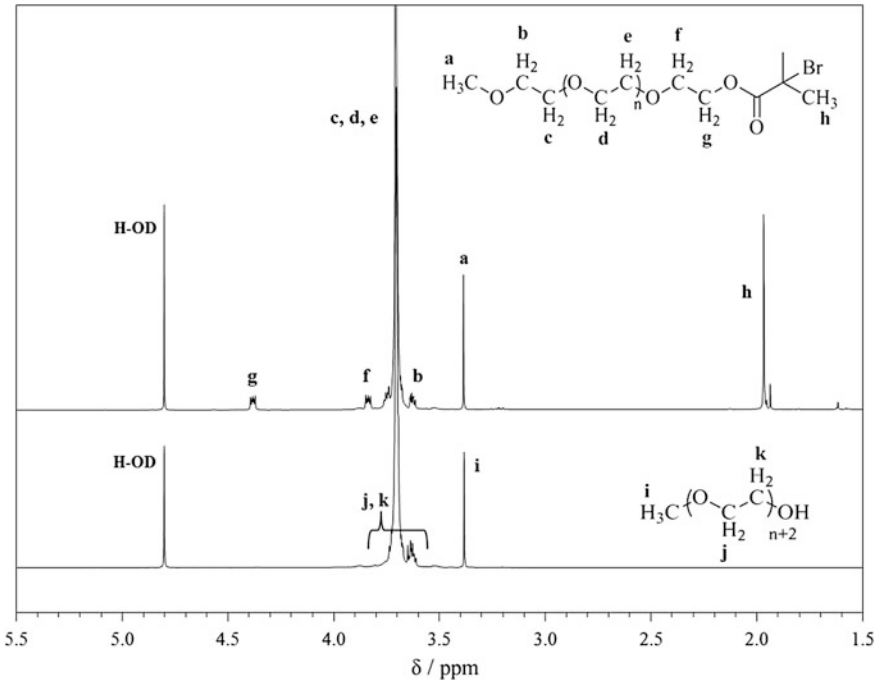

Fig. 3.2 ^{1}H NMR (D_2O, 400 MHz) of 750PEG OH and **750PEG** initiator, theoretical n = 14

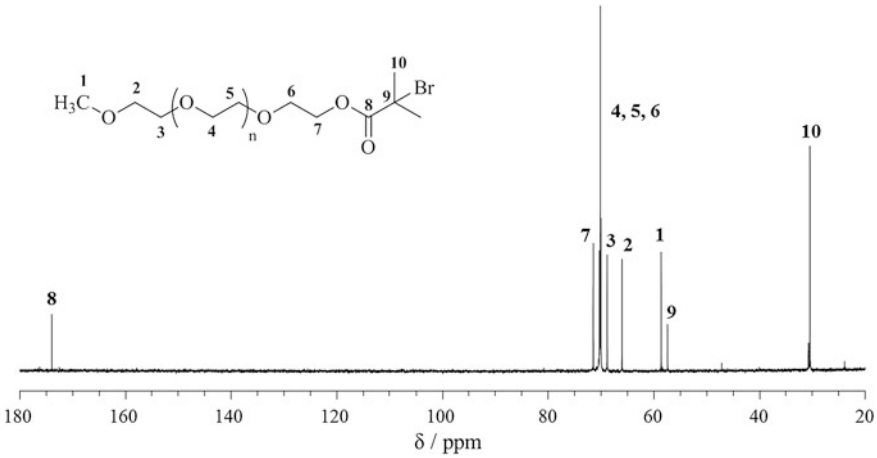

Fig. 3.3 ^{13}C NMR (D_2O, 100 MHz) of **750PEG** initiator, theoretical n = 14

750PEG initiator shown in Fig. 3.3, also indicates the correct structure due to the appearance of new peaks at 174, 57 and 30 ppm which correspond to carbons C8, C9 and C10 respectively, which represent the new functional group added to the PEG chain. The matrix-assisted laser desorption/ionisation time of flight (MALDI-TOF) mass spectrometry analysis of the **750PEG** initiator can be seen in the appendices (Appendix, Fig. A.14).

3.3 Polymer Synthesis

The **G2** dendron initiator and **750PEG** initiator were used to polymerise linear and branched (through the introduction of EGDMA) pHPMA via ATRP, targeting a DP_n of 50 monomer units. The use of the **G2** dendron initiator had already been extensively studied via kinetic experiments for linear and branched polymerisation, see Chap. 2 (Sects. 2.3 and 2.4), and the use of PEG macroinitiators is well documented [2–5]. Therefore, combining the two initiators within the same polymerisation was studied to see the various effects that the different chain end functionality may have. Ratios of the **G2**:**750PEG** initiators were as follows; 100:0, 90:10, 75:25, 50:50, 25:75, 10:90 and 0:100 %. Obviously when mixing the initiators for a linear polymerisation some chains will bear the **G2** dendron and some the **750PEG** functionality, this study was aimed at the branched polymerisation, where due to the mechanism of branching in ATRP, the two different chain end functionalities are likely to be statistically incorporated into the same branched macromolecule.

3.3.1 Linear Polymers

Linear polymers were synthesised using either 100 % **G2** dendron initiator or 100 % **750PEG** initiator and the kinetics of these two polymerisations were also studied. To confirm a lack of complications when conducting ATRP in the presence of both initiators, a linear polymerisation was conducted using the 50:50 **G2**:**750PEG** initiator mixture. If dramatically different initiation or polymerisation rates were evident there would be two distinct populations present when the samples were analysed by GPC. The molecular weights determined for the samples derived from 100:0, 50:50 and 0:100 **G2**:**750PEG** initiators are shown in Table 3.1 and the RI GPC chromatograms are shown in Fig. 3.4.

Interestingly, the molecular weights (see Table 3.1) of these linear polymers appeared to be increasing when more **G2** dendron initiator is present. This would lead to the conclusion that the **750PEG** initiator has higher initiator efficiency than the **G2** dendron initiator, therefore allowing more polymer chains to grow and decreasing the overall average molecular weight of the sample. The **G2** dendron initiator, with a lower initiator efficiency, appears to initiate fewer polymer chains during the polymerisation and therefore, at any given conversion, the molecular weights will be higher than an initiator with a higher initiating efficiency. The mixed initiator polymer sample has a molecular weight between the two single

Table 3.1 Linear polymers; molecular weights and dispersity data

Sample name	Initiator (%)		GPC data (THF)		
	G2 dendron	**750PEG**	M_n ($gmol^{-1}$)	M_w ($gmol^{-1}$)	Đ
G2-pHPMA$_{50}$	100	0	15,300	20,700	1.35
G2:**750PEG** 50:50-pHPMA$_{50}$	50	50	13,000	16,900	1.30
750PEG-pHPMA$_{50}$	0	100	11,700	15,900	1.37

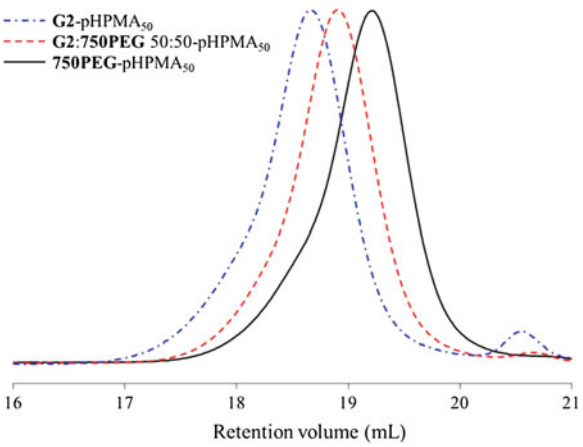

Fig. 3.4 Refractive index GPC chromatogram overlay of **750PEG**-pHPMA$_{50}$, **G2:750PEG** 50:50-pHPMA$_{50}$ and **G2**-pHPMA$_{50}$

initiator polymerisations, and this can be easily seen in the GPC chromatogram overlay in Fig. 3.4.

The ^{1}H NMR spectrum for the **G2**-pHPMA$_{50}$ linear-dendritic polymer is shown in Chap. 2, Fig. 2.10, with major peaks assigned. The **750PEG**-pHPMA$_{50}$ ^{1}H NMR spectrum is shown in the Appendix, Fig. A.15.

3.3.2 750PEG Initiator Kinetic Experiments

The polymerisation kinetics studies of linear and branched DP$_{50}$ polymerisations initiated with **750PEG** were conducted at 30 °C in methanol with a catalytic system of CuCl:bpy (1:2) [6, 7], and a monomer concentration of 50 wt% with respect to the solvent. First order kinetics were observed for both the **750PEG**-pHPMA$_{50}$ and **750PEG**-pHPMA$_{50}$-EGDMA$_{0.8}$ polymerisations due to the linear semi-logarithmic plot (green triangles) in Fig. 3.5a, c, respectively. High conversions (>95 %) were achieved within 6 h for the linear, and 8 h for the branched, polymerisation. The molecular weight (M$_n$) evolution with conversion occurs linearly for the linear polymerisation (Fig. 3.5b), which was expected, and the dispersities (Đ) remain below 1.4 throughout the polymerisation, decreasing slightly with increasing conversion (from 1.42 at 29.9 % conversion to 1.29 at 98.1 % conversion).

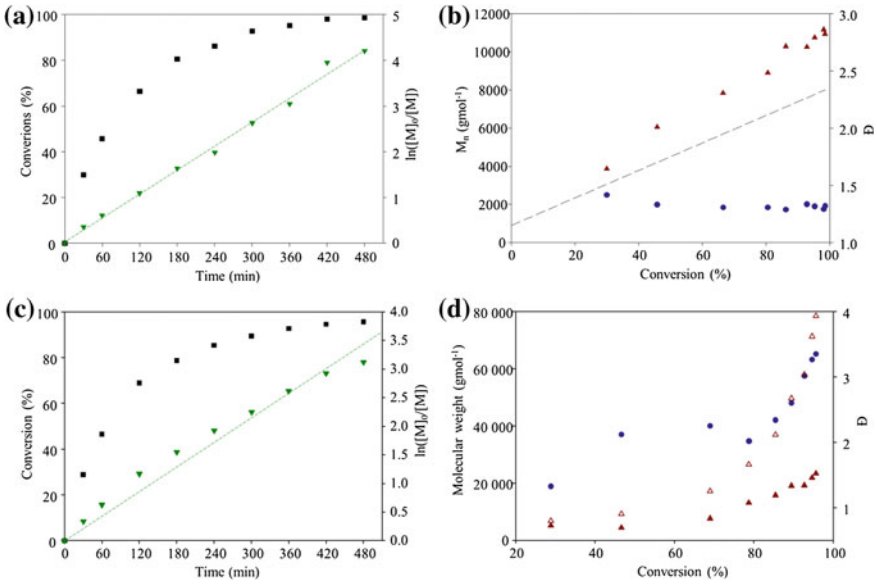

Fig. 3.5 Kinetic experiment data for the **750PEG** initiated polymerisations. **750PEG**-pHPMA$_{50}$: (**a**, **b**), **750PEG**-pHPMA$_{50}$-EGDMA$_{0.8}$: (**c**, **d**). Conversion (*black squares*) and ln([M]$_0$/[M]) (*green down triangles*), M$_n$ (*red up triangles*), M$_w$ (*red empty up triangles*) theoretical Mn (*black dotted line*) and Đ (*blue circles*)

The evolution of molecular weight is considerably different when compared to a branched polymerisation (Fig. 3.5d), which includes a divinyl monomer in the polymerisation (EGDMA), whereby the M_n and M_w increase almost linearly up to about 60–70 % conversion then, due to the intermolecular coupling of polymer chains, the M_w increases steeply and the M_n also increases. This occurs at high conversions as the majority of the monomer has been consumed, and the relative concentration of pendant vinyl groups (with respect to the monomer) has increased, therefore the reaction of a reactive chain ends with a pendant vinyl group is much more likely at high conversions [2, 8, 9].

3.3.3 *Mixed Initiator* Hyp-*block Copolymers and* Hyp-*polydendrons*

A series of branched pHPMA polymers were synthesised, varying only the ratios of **G2** dendron initiator and **750PEG** macroinitiator; 100:0, 90:10, 75:25, 50:50, 25:75, 10:90 and 0:100 %. The targeted DP_n of HPMA was kept constant ($DP_n = 50$ monomer units), as was the ratio of total initiator:EGDMA used (1:0.8). Table 3.2 highlights the molecular weights and Đ for each polymer in the series. Entries 1–3 correspond to the linear polymers discussed previously and are repeated here for comparison.

Table 3.2 Molecular weights and dispersity data for linear, linear-dendritic, *hyp*-block copolymers and *hyp*-polydendrons

Entry no.	Initiator (%)		Target polymer composition	GPC (THF)		
	G2 dendron	**750PEG**		M_n ($gmol^{-1}$)	M_w ($gmol^{-1}$)	Đ
1	100	0	$pHPMA_{50}$	15,300	20,700	1.35
2	50	50	$pHPMA_{50}$	13,000	16,900	1.30
3	0	100	$pHPMA_{50}$	11,700	15,900	1.37
4	100	0	$pHPMA_{50}$-$EGDMA_{0.8}$	90,500	1,304,000	14.4
5	90	10	$pHPMA_{50}$-$EGDMA_{0.8}$	68,500	1,495,000	21.8
6	75	25	$pHPMA_{50}$-$EGDMA_{0.8}$	52,400	987,800	18.9
7	50	50	$pHPMA_{50}$-$EGDMA_{0.8}$	39,400	480,700	12.2
8	25	75	$pHPMA_{50}$-$EGDMA_{0.8}$	36,200	315,300	8.73
9	10	90	$pHPMA_{50}$-$EGDMA_{0.8}$	37,700	286,000	7.61
10	0	100	$pHPMA_{50}$-$EGDMA_{0.8}$	68,100	296,200	4.35
11	25	75	$pHPMA_{50}$-$EGDMA_{0.9}$	60,700	675,100	11.1
12	100	0	$pHPMA_{50}$-$EGDMA_{0.95}$	*-Gelled-*		
13	50	50	$pHPMA_{50}$-$EGDMA_{0.95}$	121,900	1,779,000	14.6
14	0	100	$pHPMA_{50}$-$EGDMA_{0.95}$	74,700	642,700	8.60

A general trend can be observed from the GPC data; when increasing the amount of **750PEG** initiator the molecular weights of the resulting polymers decreased (Table 3.2, entries 4–10) consistently. This can be attributed to the individual initiator efficiency of the two initiators. It is important to take the initiator efficiency into consideration when introducing a divinyl monomer, or brancher, into the polymerisation. As previously discussed, a ratio of initiator to brancher greater than or equal to 1, by theory, will yield an insoluble cross-linked network or gel. An initiator:brancher ratio of 1:0.95 should give the branched, high molecular weight, soluble polymer without forming a gel. However, if the initiator has an initiator efficiency which is lower than 100 % the effective initiator to brancher ratio will decrease and gelation is possible. The **G2** dendron initiator has a lower initiator efficiency than the **750PEG** initiator and therefore when introducing EGDMA into the polymerisation the more **G2** dendron initiator present the higher the resulting molecular weights of the polymers produced. This trend can also be observed when looking at the GPC chromatograms obtained, shown here in Fig. 3.6. Figure 3.6a shows the RI trace overlays for each **G2**:**750PEG**-pHPMA$_{50}$-EGDMA$_{0.8}$ polymer with each polymer indicated, whilst Fig. 3.6b shows the RALS detector overlays. The RI overlay shows that for the polymers with a higher amount of **G2** dendron initiator present, polymer species are eluting at a much lower retention volume than the branched polymers containing less **G2** dendron initiator and therefore more **750PEG** initiator. This is also true for the RALS overlay, where there is light scattering occurring at much lower retention volumes for the high **G2** dendron materials when compared to the low **G2** dendron materials, indicating larger molecular species at high **G2** initiator concentrations.

To further highlight the difference of initiator efficiency between the **G2** dendron and **750PEG** initiators three of the series were chosen (100:0, 50:50, and 0:100) and the same polymerisations were conducted but with a higher ratio of EGDMA, (initiator:EGDMA 1:0.95), see Table 3.2, entries 12–14. The 100 % **G2** dendron initiated polymerisation at 1:0.95 initiator:EGDMA formed an insoluble cross-linked network or gel, however the 50:50 and 100 % **750PEG** initiated polymerisations gave rise to polymers with higher molecular weights than the corresponding polymers with a ratio of 1:0.8 initiator:EGDMA present which was as predicted (see Appendix, Fig. A.16, for GPC chromatograms, RI and RALS, of 50:50 and 0:100–pHPMA$_{50}$-EGDMA$_{0.95}$). The 25:75 *hyp*-polydendron was also polymerised with an increased initiator:EGDMA ratio of 1:0.9, see entry 11, Table 3.2. This polymerisation gave rise to a *hyp*-polydendron with higher molecular weights and a broader dispersity than when the ratio used was 1:0.8. The GPC chromatogram RI and RALS overlay can be seen in the Appendix Fig. A.17.

The set of *hyp*-polydendrons and *hyp*-block copolymer were analysed by ^{1}H NMR spectroscopy to ascertain whether the **G2** dendron initiator and **750PEG** initiators had been included in the ratios which were targeted. The aromatic protons attributed to the four benzyl groups in the **G2** dendron initiator were used (7.3 ppm) and integrated with respect to the $-CH_3$ group at the end of the **750PEG** initiator. These signals could be compared to the two $-CH_3$ groups present in the repeat monomer unit along polymer chain ($-CH_3$ along the backbone and the

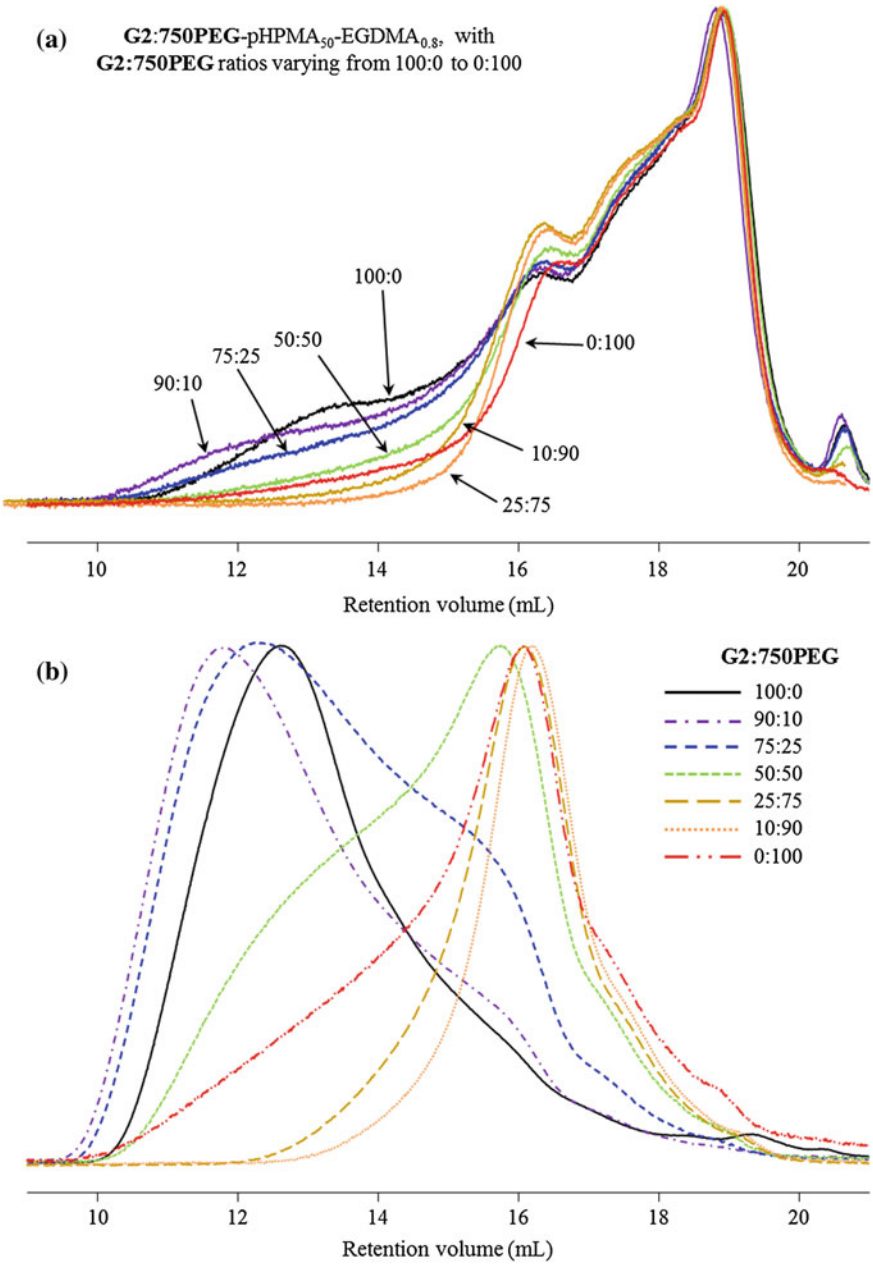

Fig. 3.6 GPC chromatogram overlays of **a** refractive index detector, and **b** *right angle* light scattering detector for the **G2**:**750PEG**-pHPMA$_{50}$-EGDMA$_{0.8}$ series ranging from 100 % **G2** dendron (100:0) to 100 % **750PEG** (0:100) initiators

pendant $-CH_3$ of the monomer). The ^{1}H NMR spectrum for the 25:75-pHPMA$_{50}$-EGDMA$_{0.8}$ *hyp*-polydendron is shown in Fig. 3.7 with major peaks assigned. Figure 3.8 shows an overlay of several ^{1}H NMR spectra for the *hyp*-polydendrons and the *hyp*-block copolymer, with varying **G2**:**750PEG** content. The other *hyp*-polydendrons ^{1}H NMR spectra not shown (90:10, 50:50 and 10:90-pHPMA$_{50}$-EGDMA$_{0.8}$) here are shown in the Appendix, Fig. A.18.

As can be seen from Fig. 3.7, the aromatic protons (**k**) on the **G2** dendron initiator can be clearly distinguished from the other proton environments present in the *hyp*-polydendron, however the $-CH_3$ group at the end of the **750PEG** initiator (**j**) is less easily distinguished. This peak does not quite reach the baseline on either side, therefore there will be errors when integrating this peak. Hence the ratio of initiators calculated by ^{1}H NMR spectroscopy is an estimate.

The ratio of each initiator was calculated with respect to the monomer present by analysis of the ^{1}H NMR spectra. Figure 3.9 shows the mol% of each initiator with respect to the HPMA. The **G2** dendron content was observed to lower than targeted, probably due to a lower initiation efficiency then the **750PEG** initiator.

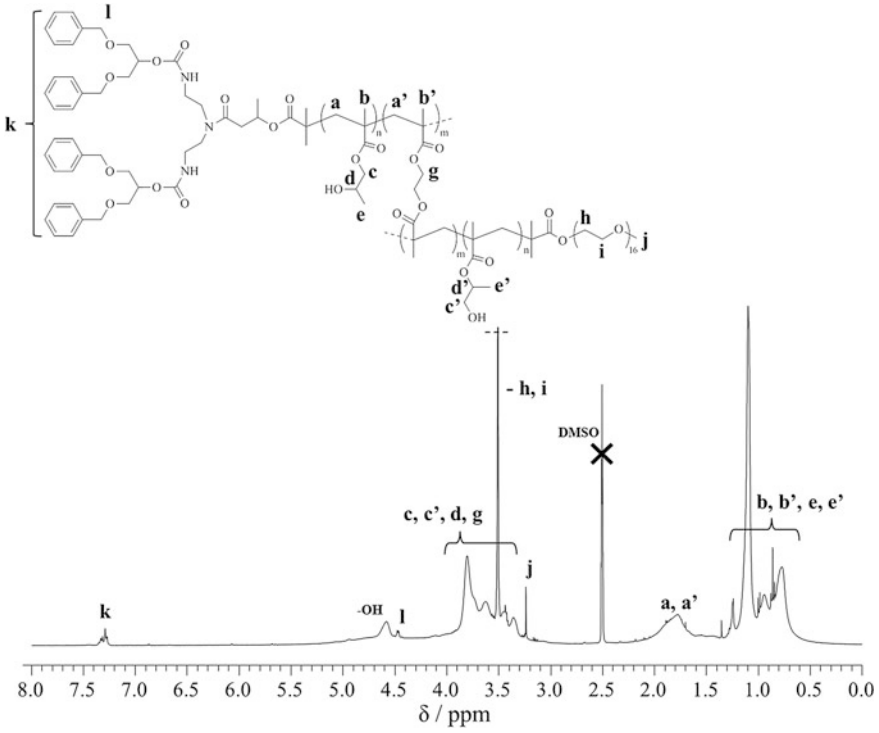

Fig. 3.7 ^{1}H NMR spectrum (400 MHz, d_6-DMSO) of **G2**:**750PEG**-25:75-pHPMA$_{50}$-EGDMA$_{0.8}$ with major peaks assigned

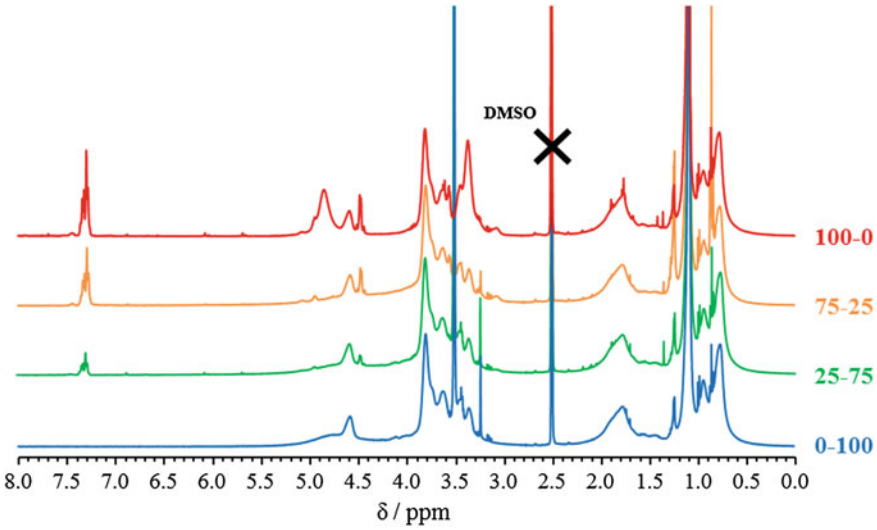

Fig. 3.8 ^{1}H NMR (d_6-DMSO, 400 MHz) spectra overlay for 100:0, 75:25, 25:75 and 0:100-pHPMA$_{50}$-EGDMA$_{0.8}$ polymers

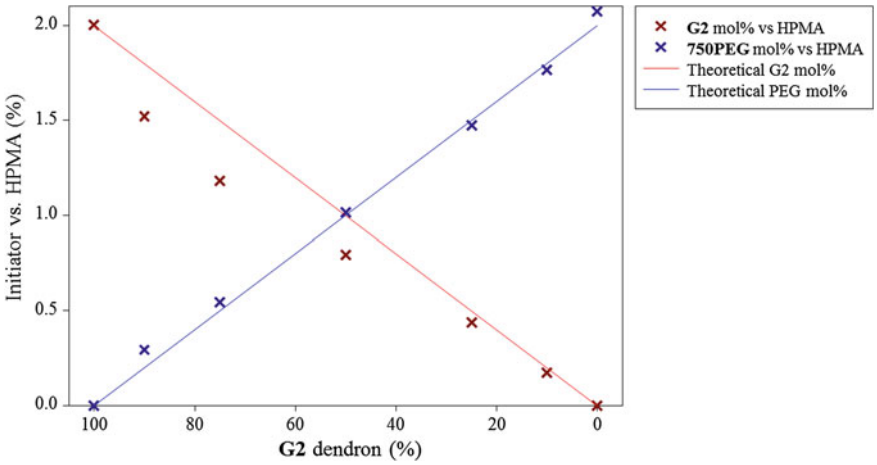

Fig. 3.9 Initiator mol% versus HPMA mol% for each *hyp*-polydendron observed by ^{1}H NMR spectroscopy (*blue* and *red crosses*) and the theoretical values (*blue* and *red lines*)

3.4 Nanoprecipitation of *Hyp*-polydendrons

As previously reported, the formation of polymeric nanoparticles via nanoprecipitation is a facile and reproducible technique [10–13]. Nanoprecipitation of *hyp*-polydendrons and linear polymers was achieved by dissolving the polymers in a

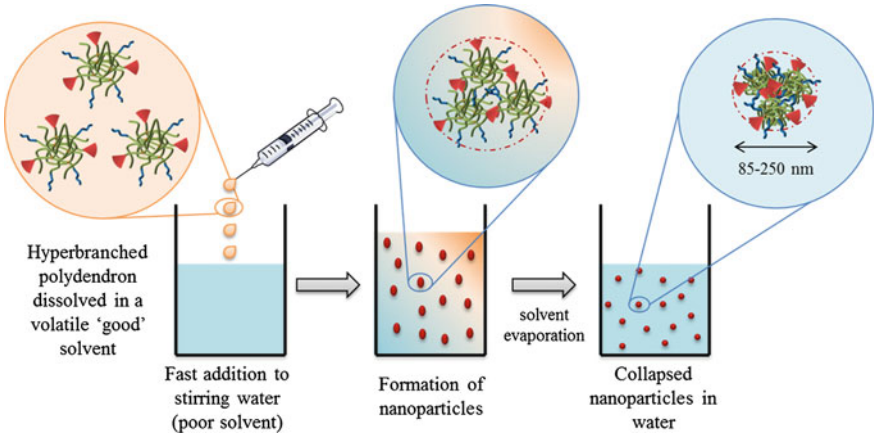

Fig. 3.10 Schematic representation of aqueous nanoparticle formation via nanoprecipitation

good solvent, tetrahydrofuran (THF), then adding the polymer in good solvent to an excess of anti-solvent, water. The volatile good solvent was allowed to evaporate, leaving the nanoparticles in water. This process is highlighted in Fig. 3.10, and has been discussed in Chap. 2, Sect. 2.6.

The resulting size of nanoparticles formed could be tuned by altering the concentration of polymer in good solvent, or initial concentration, and also the final concentration, how much anti-solvent (water) it was added to. The relationship between the initial and final concentrations and the dilution factor (*df*) can be described as is shown in Eq. (3.1) below.

$$initial\ concentration\ (i_x)\ x\ dilution\ factor\ (df)\ =\ final\ concentration\ (f_y) \quad (3.1)$$

These nanoprecipitations have been labelled throughout this thesis as described in the format $\boldsymbol{i_x}$-$\boldsymbol{f_y}$ mg/mL where $\boldsymbol{i_x}$ is the initial concentration and $\boldsymbol{f_y}$ is the final concentration. Nanoparticle dispersions were analysed via DLS to measure the D_z of the particles and polydispersity index (PdI). Increasing the initial concentration, whilst maintaining the same *df*, gave rise to a series of nanoparticles which increased in size (D_z). This is highlighted in Fig. 3.11 with samples varying from a starting concentration of 5, 10 and 25 mg/mL with *df* = 0.2, therefore giving resultant nanoparticles with final concentrations of 1, 2 and 5 mg/mL respectively ($\boldsymbol{i_5}$-$\boldsymbol{f_1}$, $\boldsymbol{i_{10}}$-$\boldsymbol{f_2}$ and $\boldsymbol{i_{25}}$-$\boldsymbol{f_5}$). Those nanoprecipitates with a final concentration of 5 mg/mL are larger than those at 2 mg/mL which are larger than those with a final concentration of 1 mg/mL. This trend is also observed in Fig. 3.12 which shows nanoprecipitations with starting concentrations of 5, 10 and 25 mg/mL also, however, with *df* = 0.01, resulting in final concentrations of 0.05, 0.1 and 0.25 mg/mL ($\boldsymbol{i_5}$-$\boldsymbol{f_{0.05}}$, $\boldsymbol{i_{10}}$-$\boldsymbol{f_{0.1}}$ and $\boldsymbol{i_{25}}$-$\boldsymbol{f_{0.25}}$). Again those samples with a final concentration of 0.25 mg/mL are generally larger in size than those with a final concentration of 0.1 mg/mL which in turn are larger than those at 0.05 mg/mL. These two figures also highlight that the trend of sizes across

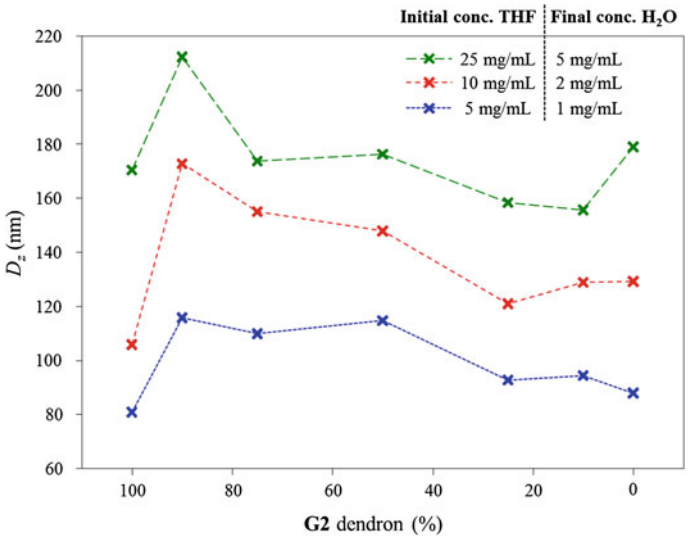

Fig. 3.11 Resulting D_z of nanoparticles formed via nanoprecipitation of the **G2**:**750PEG** *hyp*-polydendrons. Samples $\boldsymbol{i_{25}\text{-}f_5}$ (*green crosses*), $\boldsymbol{i_{10}\text{-}f_2}$ (*red crosses*) and $\boldsymbol{i_5\text{-}f_1}$ (*blue crosses*)

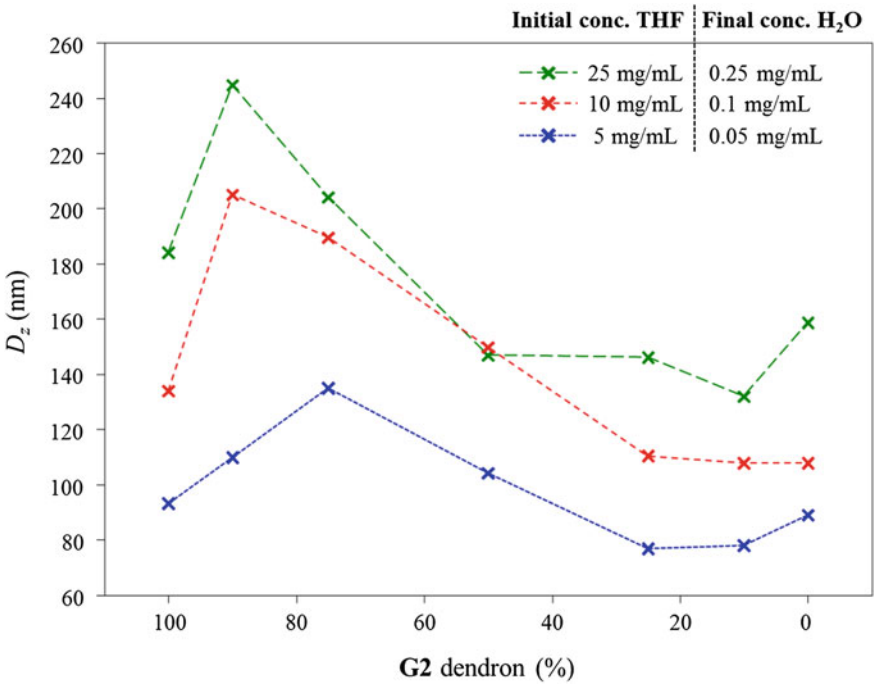

Fig. 3.12 Resulting D_z of nanoparticles formed via nanoprecipitation of the **G2**:**750 PEG** *hyp*-polydendrons. Samples $\boldsymbol{i_{25}\text{-}f_{0.25}}$ (*green crosses*), $\boldsymbol{i_{10}\text{-}f_{0.1}}$ (*red crosses*) and $\boldsymbol{i_5\text{-}f_{0.05}}$ (*blue crosses*)

the range of polymeric materials (from 100:0 to 0:100-pHPMA$_{50}$-EGDMA$_{0.8}$). Although no specific trend is followed across the materials, the same trend is observed at different concentrations.

Interestingly when the same initial concentration was used, but the *df* was changed, for example ***i*$_{10}$-*f*$_{2}$** and ***i*$_{10}$-*f*$_{0.1}$**, the resultant nanoparticles were very similar in size. This is more clearly seen when examining the D_z in Table 3.3 which also includes the PdI values for each measurement and the zeta potential, which gives an indication of surface charge. Generally the nanoparticles formed have low polydispersity indexes (<0.1) and have a negative zeta potential (>−20 mV) suggesting that these nanoparticles are charge stabilised. It is worth noting for samples ***i*$_{25}$-*f*$_{5}$** the final concentration of 5 mg/mL was too high to measure an accurate zeta potential.

The DLS size distribution by intensity traces obtained for each sample described in Figs. 3.11, 3.12 and Table 3.3 are shown in the Appendix, Fig. A.19.

SEM images of nanoparticles prepared at ***i*$_{5}$-*f*$_{1}$** (Fig. 3.13) shows that spherical particles are formed; however as the content of PEG increases the resulting particles appear to become more aggregated. This could be because PEG is hydrophilic and,

Table 3.3 D_z, PdI and zeta potential measurements for **G2**:**750PEG**-pHPMA$_{50}$-EGDMA$_{0.8}$ nanoparticles prepared with various nanoprecipitation conditions

G2:**750PEG**-pHPMA$_{50}$-EGDMA$_{0.8}$	***i*$_{25}$-*f*$_{5}$**			***i*$_{10}$-*f*$_{2}$**			***i*$_{5}$-*f*$_{1}$**		
	D_z (nm)	PdI	Zeta potential (mV)	D_z (nm)	PdI	Zeta potential (mV)	D_z (nm)	PdI	Zeta potential (mV)
100:0	171	0.194	*	106	0.083	−38.0	81	0.083	−38.2
90:10	212	0.197	*	173	0.076	−30.4	116	0.069	−25.9
75:25	174	0.136	*	155	0.086	−25.6	110	0.074	−26.5
50:50	176	0.076	*	148	0.061	−29.3	115	0.067	−28.2
25:75	158	0.101	*	121	0.072	−28.7	93	0.078	−30.4
10:90	156	0.107	*	129	0.058	−31.3	94	0.091	−29.9
0:100	179	0.038	*	129	0.083	−39.8	88	0.083	−39.7
G2:**750PEG**-pHPMA$_{50}$-EGDMA$_{0.8}$	***i*$_{25}$-*f*$_{0.25}$**			***i*$_{10}$-*f*$_{0.1}$**			***i*$_{5}$-*f*$_{0.05}$**		
	D_z (nm)	PdI	Zeta potential (mV)	D_z (nm)	PdI	Zeta potential (mV)	D_z (nm)	PdI	Zeta potential (mV)
100:0	184	0.279	−56.9	134	0.064	−34.3	93	0.071	−20.4
90:10	245	0.370	−61.4	205	0.087	−33.1	110	0.087	−17.6
75:25	204	0.258	−58.0	190	0.097	−39.0	135	0.092	−30.2
50:50	147	0.185	−60.6	150	0.073	−29.6	104	0.072	−20.7
25:75	146	0.112	−56.9	110	0.104	−24.0	77	0.140	−16.5
10:90	132	0.068	−49.7	108	0.073	−23.2	78	0.090	−28.9
0:100	159	0.078	−46.5	108	0.083	−30.0	89	0.160	−27.8

*Not suitable for measurement—too concentrated

D_z z-average diameter

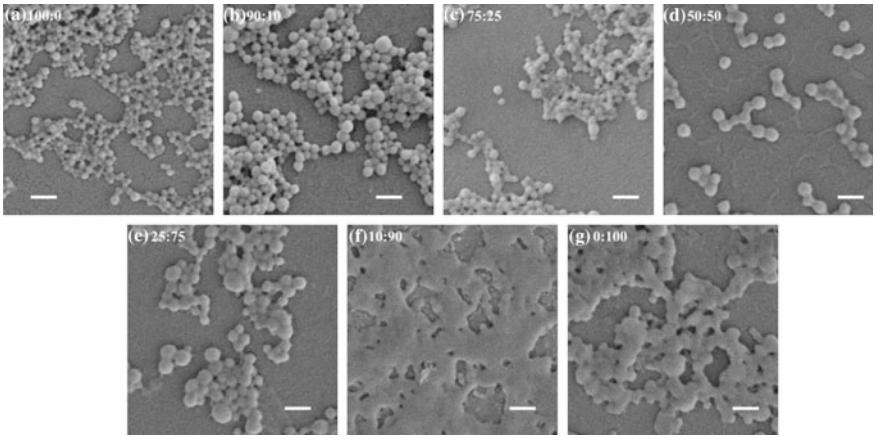

Fig. 3.13 SEM images for each **G2**:**750PEG**-pHPMA$_{50}$-EGDMA$_{0.8}$ polymer prepared from $\boldsymbol{i_5}$-$\boldsymbol{f_1}$ nanoprecipitation. Scale bars are 200 nm

as the aqueous samples dry on the SEM stub (silicon wafer), the presence of more PEG may lead to film formation when drying. This could also be caused by the glass transition temperature (*T*g) of the polymers. The increasing mol% of PEG could be reducing the *T*g of the resulting polymers which would cause them to 'flow' more at room temperature than a higher *T*g polymer. Therefore this 'flow' could result in the nanoparticles losing their spherical structures. However, the *T*g of these polymers was not measured during this work; it would be interesting to see if there is a trend in *T*g with varying PEG:pHPMA content.

3.4.1 Factors Affecting Nanoprecipitation

Factors that might affect the formation of nanoparticles and their resultant sizes were considered such as the molecular weights of the *hyp*-polydendrons and *hyp*-block copolymer. The D_z of the polymers dissolved in a good solvent, THF, were measured via DLS. The correlation between the D_z in THF and molecular weights are shown in Fig. 3.14, with the R^2 values included to highlight the positive correlation observed. The best correlation between D_z in THF and molecular weight was with the M_w. This is probably because M_w takes into account the higher molecular weight species present than the M_n and the D_z being measured will be mainly representative of the higher molecular weights species in the sample, as lower molecular weight polymer species scatter less light.

To ascertain whether the molecular weight had an influence on the D_z of nanoparticles formed via nanoprecipitation dispersed in water, the D_z of particles formed from each polymer with $\boldsymbol{i_5}$-$\boldsymbol{f_1}$ were plotted with the M_n and M_w of the corresponding polymers, see Fig. 3.15. It was immediately obvious that unlike the

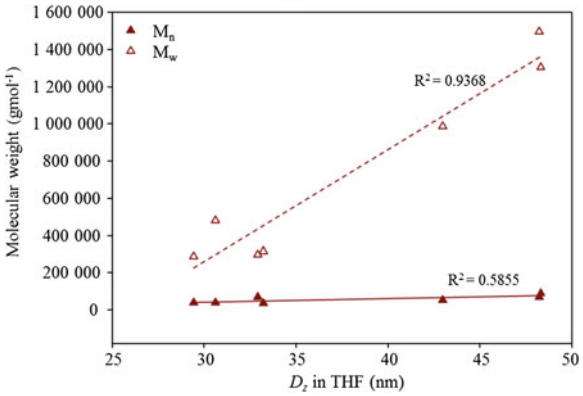

Fig. 3.14 Correlation between molecular weights of polymers and their D_z in THF, M_n (*red closed triangles*) and M_w (*red open triangles*)

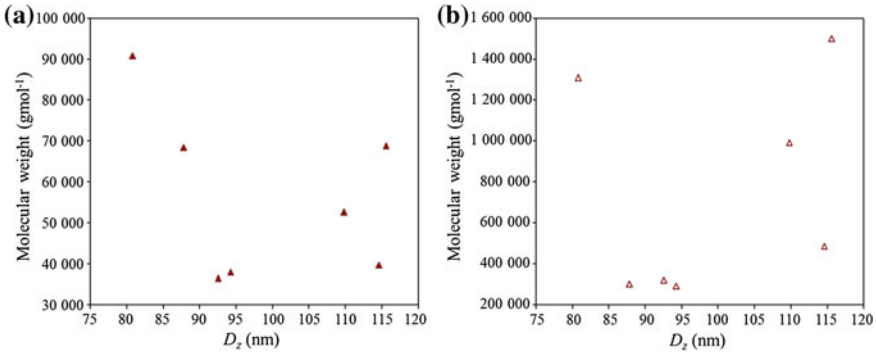

Fig. 3.15 Molecular weights of polymers versus the corresponding nanoparticle D_z, formed via nanoprecipitation using $\boldsymbol{i_5\text{-}f_1}$; **a** M_n (*closed triangles*) and **b** M_w (*open triangles*)

D_z of the polymers in THF, the D_z of the aqueous nanoparticles had no correlation with the corresponding polymer molecular weights. This is true for both the Mn (Fig. 3.15a) and Mw (Fig. 3.15b) where the R^2 values are 0.1416 and 0.0624 respectively, indicating no correlation.

As discussed previously, for various ratios of **G2**:**750PEG** initiated *hyp*-polydendrons higher ratios of initiator:EGDMA were used, which resulted in polymers with higher molecular weights and broader dispersities. Two examples of these were the 25:75 *hyp*-polydendron and 0:100 *hyp*-block copolymer. The 25:75-$pHPMA_{50}$-$EGDMA_{0.8}$ (entry 8, Table 3.2) had a M_n and M_w of 36,200 and 315,300 $gmol^{-1}$ respectively with Đ = 8.73, whilst 25:75-$pHPMA_{50}$-$EGDMA_{0.9}$ (entry 11, Table 3.2) had a M_n and M_w of 60,700 and 675,100 $gmol^{-1}$ respectively with Đ = 11.12. These two polymers underwent the same nanoprecipitations conditions ($\boldsymbol{i_{10}\text{-}f_2}$, $\boldsymbol{i_{10}\text{-}f_{0.2}}$, $\boldsymbol{i_5\text{-}f_1}$

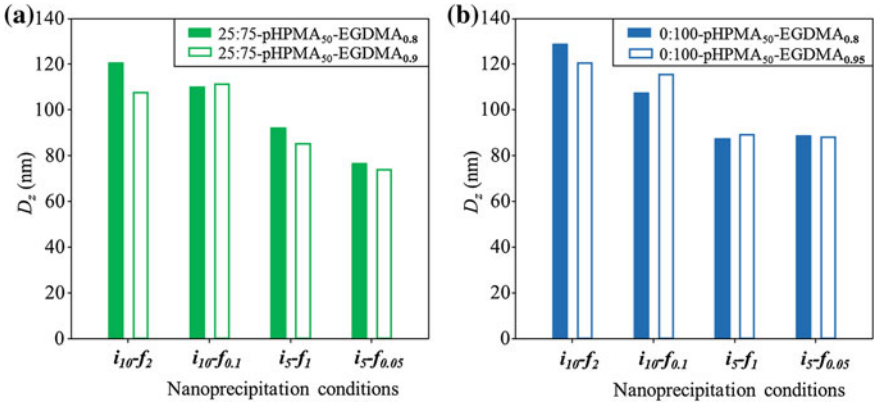

Fig. 3.16 Nanoparticle sizes, measured by DLS, of **a** 25:75-pHPMA$_{50}$-EGDMA$_{0.8}$ and 25:75-pHPMA$_{50}$-EGDMA$_{0.9}$ and **b** 0:100-pHPMA$_{50}$-EGDMA$_{0.8}$ and 0:100-pHPMA$_{50}$-EGDMA$_{0.95}$

and ***i*$_5$-*f*$_{0.05}$**) and despite having very different molecular weights, both samples gave nanoparticles with very similar D_z, see Fig. 3.16a. The filled bars show the D_z for the 25:75-pHPMA$_{50}$-EGDMA$_{0.8}$ *hyp*-polydendron, whilst the unfilled bars show the D_z for the 25:75-pHPMA$_{50}$-EGDMA$_{0.9}$.

The same experiment was conducted with 0:100-pHPMA$_{50}$-EGDMA$_{0.8}$ (entry 10, Table 3.2, M_n = 68,100 gmol^{-1}, M_w = 296,200 gmol^{-1} and Đ = 4.35) and 0:100-pHPMA$_{50}$-EGDMA$_{0.95}$ (entry 14, Table 3.2, M_n = 74,700 gmol^{-1}, M_w = 642,700 gmol^{-1} and Đ = 8.60). Figure 3.16b shows the D_z of the nanoparticles formed using four different nanoprecipitation conditions. Again the D_z are very similar for the nanoparticles formed from two *hyp*-block copolymers with very different molecular weights, filled bars and open bars show the 0:100-pHPMA$_{50}$-EGDMA$_{0.8}$ and 0:100-pHPMA$_{50}$-EGDMA$_{0.95}$ nanoparticle dispersions.

3.4.2 Mechanism of Nanoparticle Formation

Each polymer showed an increase in size with an increase in the initial and final concentrations, however, when increasing the *df* the resulting effect on nanoparticle size is relatively small, giving similar sizes for the samples made from the same initial concentration but with different *df*. This suggests that the nanoparticle formation occurs instantaneously upon addition to the water (anti-solvent) to give colloidally stable nanoparticles. This is in agreement with one suggested mechanism of nanoparticle formation via nucleation and aggregation [14, 15], discussed in more depth in Chap. 1 (Sect. 1.4.3).

3.4.3 Stability of Nanoparticles

The colloidal stability of the nanoparticles was studied over time and to dilution with good solvent and anti-solvent.

The stability of the nanoparticles was studied by measuring the D_z and PdI over time, as in Chap. 2 (Sect. 2.6.3) aqueous nanoparticles showed stability over extended periods of time (>20 months). New samples were prepared for the study with the **G2**:**750PEG**-pHPMA$_{50}$-EGDMA$_{0.8}$ series of *hyp*-polydendrons and *hyp*-block copolymer using a formulation of ***i*$_5$-*f*$_1$**. After 11 months of storage at ambient temperature, out of direct light, the D_z and PdI values remain similar to those originally measured, see Table 3.4. The largest difference in size measure was with the 25:75-pHPMA$_{50}$-EGDMA$_{0.8}$ samples which was originally 82 nm (PdI = 0.060) and after 11 months of storage the D_z measured was 91 nm (PdI = 0.190), which was an increase of <10 nm in diameter. Therefore it can be inferred that these particles are stable over time as the variation in size and polydispersity was not significant.

The *hyp*-polydendrons nanoparticles were also studied for their stability to dilution with the anti-solvent and the addition of a good solvent for the polymer core. The **G2**:**750PEG**-50:50-pHPMA$_{50}$-EGDMA$_{0.8}$ *hyp*-polydendron was used for these studies formulated using a sample prepared with ***i*$_5$-*f*$_1$**. Figure 3.17 shows the D_z and PdI for the dilution of this sample with distilled water (anti-solvent). As the sample was diluted the D_z varied slight from 75 nm at 1 mg/mL to 72 nm at 0.0156 mg/mL and the corresponding PdI values were 0.064 and 0.074. These D_z and PdI values are shown in the Appendix, Table A.4.

The addition of a good solvent for the hydrophobic polymer core of the nanoparticles was also studied by adding THF to a sample of **G2**:**750PEG**-50:50-pHPMA$_{50}$-EGDMA$_{0.8}$ *hyp*-polydendron formulated using ***i*$_5$-*f*$_1$**. This was performed by using 1 mL of the nanoparticle dispersion and adding increasing volumes of THF. The D_z and PdI was measured via DLS between each addition, see Fig. 3.18. The D_z increased with increasing volumes of THF added, suggesting that with addition of

Table 3.4 D_z and PdI measured by DLS for various ratios of **G2**:**750PEG**-pHPMA$_{50}$-EGDMA$_{0.8}$ ***i*$_5$-*f*$_1$** samples stored over 11 months

G2:**750PEG-**(pHPMA$_{50}$-EGDMA$_{0.8}$)	***i*$_5$-*f*$_1$**		***i*$_5$-*f*$_1$** + 11 months	
	D_z (nm)	PdI	D_z (nm)	PdI
100:0	58	0.096	60	0.108
90:10	90	0.030	89	0.030
75:25	71	0.082	69	0.037
50:50	68	0.056	68	0.050
25:75	82	0.060	91	0.190
10:90	63	0.103	68	0.118
0:100	140	0.058	145	0.051

D_z z-average diameter

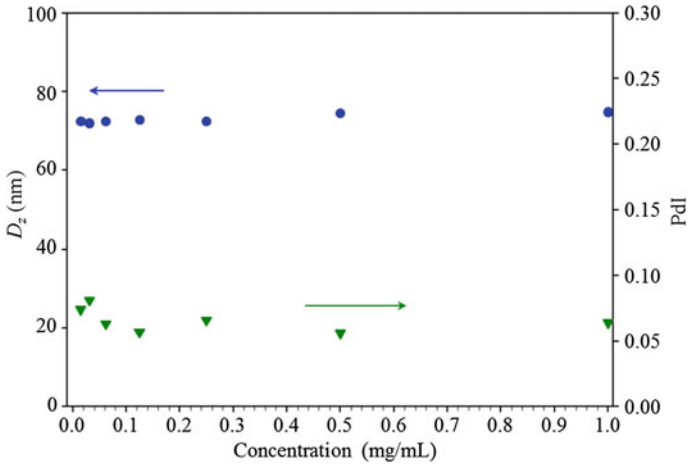

Fig. 3.17 Dilution experiment using **G2**:**750PEG**-50:50-pHPMA$_{50}$-EGDMA$_{0.8}$ *hyp*-polydendron formulated at i_5-f_1 and diluted to 0.0156 mg/mL with distilled water

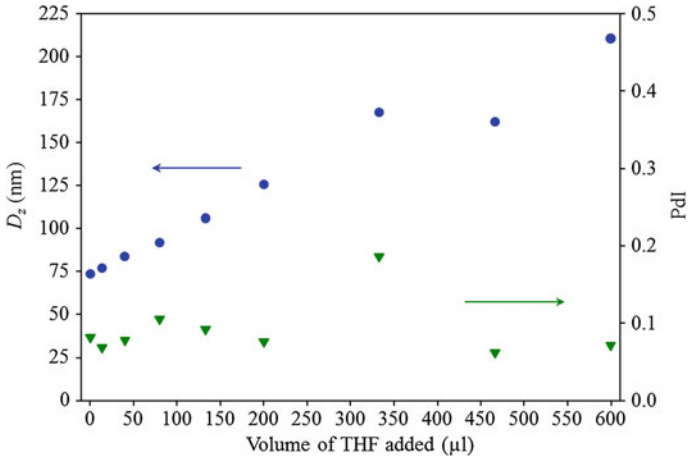

Fig. 3.18 Swelling experiment using **G2**:**750PEG**-50:50-pHPMA$_{50}$-EGDMA$_{0.8}$ *hyp*-polydendron formulated at i_5-f_1 with addition of THF

good solvent the nanoparticles swell and therefore increase in diameter. When varying the composition of the dispersant media the refractive index and viscosity of the solution may vary. This should be accounted for when measuring the size and PdI of nanoparticles dispersed in mixed media. Therefore the refractive index of each different water:THF mixture was measured and entered into the DLS software to account for the change in refractive index. The refractive index of water was measured using a refractometer and was found to be 1.3334 which is in accordance with

literature values. When at the highest volume of THF added the refractive index had increased to 1.3722. The D_z, PdI values and refractive indices of the solvent mixtures are shown in Table A.5 in the Appendix. The viscosity of the dispersant media was not accounted for as an accurate measurement of the viscosity of the varying water: THF ratios was unsuccessful.

3.4.4 Linear Polymers for Nanoprecipitation

The linear polymers synthesised using the **G2** dendron initiator and the **750PEG** macroinitiator were also subjected to the nanoprecipitation conditions described for the *hyp*-polydendrons, using an initial concentration of 5 mg/mL and final concentration of 1 mg/mL (***i*$_5$-*f*$_1$**). The **G2**-pHPMA$_{50}$ discussed here is also discussed in Chap. 2, where the ***i*$_5$-*f*$_1$** nanoprecipitation gave D_z of 142 nm (PdI = 0.107) which is very close to that of the repeat discussed in this chapter (Fig. 3.19a and Table 3.5); D_z = 157 nm and PdI = 0.111. This linear nanoprecipitate is also much larger than the branched polymer equivalent (nanoprecipitates of **G2**-pHPMA$_{50}$-EGDMA$_{0.8}$ had a D_z of 81 nm and PdI = 0.083 at ***i*$_5$-*f*$_1$**) which was also observed for the linear and branched equivalent nanoprecipitates discussed in Chap. 2.

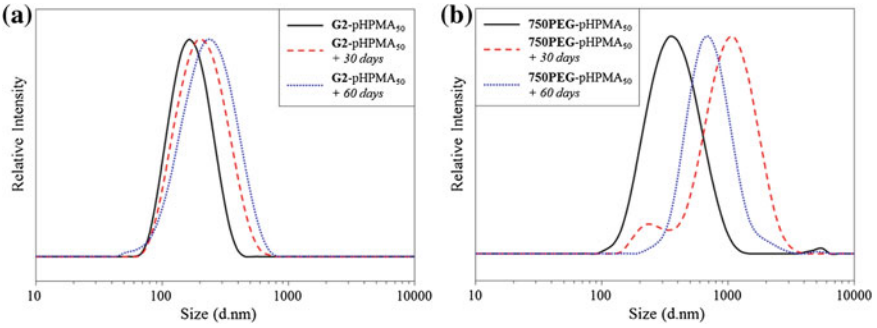

Fig. 3.19 DLS traces overlays for **a G2**-pHPMA$_{50}$ and **b 750PEG**-pHPMA$_{50}$ nanoprecipitates at t = 0, t = 30 and t = 60 days

Table 3.5 Table of DLS measurements of nanoprecipitates of linear polymers at t = 0 and under ambient storage for t = 30 and t = 60 days (corresponding to Fig. 3.19)

Linear polymer	Time (days)	D_z (nm)	PdI
G2-pHPMA$_{50}$	1	157	0.111
	30	190	0.156
	60	208	0.178
750PEG-pHPMA$_{50}$	1	342	0.197
	30	827	0.251
	60	657	0.144

D_z z-average diameter

The **G2**-pHPMA$_{50}$ linear nanoprecipitates had quite a narrow polydispersity, however, over time the PdI increased (from 0.111 to 0.156 after 30 days and to 0.178 after 60 days) as did the D_z from 157 to 190 nm after 30 days and to 208 nm after 60 days. This is apparent also from the DLS traces in Fig. 3.19a. This would appear to be due to aggregation over time which ultimately leads to precipitation. This aggregation of polymeric nanoparticles does not occur with the branched polymer equivalents over time, as discussed in Chap. 2, therefore the nanoparticles formed from the *hyp*-block copolymer or *hyp*-polydendrons are colloidally more stable than those made using linear polymers. What is unclear is whether or not this is due to the topology of the polymer or the molecular weight of the polymer.

The **750PEG**-pHPMA$_{50}$ linear polymer nanoprecipitates (see Fig. 3.19b and Table 3.5) at $\boldsymbol{i_5}$-$\boldsymbol{f_1}$ (342 nm with a PdI value of 0.197) were much larger in diameter and had a broader polydispersity than the equivalent branched polymer nanoprecipitate (**750PEG**-pHPMA$_{50}$-EGDMA$_{0.8}$; 88 nm, PdI = 0.083). Nanoprecipitates from this linear sample increased in size and polydispersity after 30 days (827 nm and PdI = 0.251); however, after 60 days it then decreased in size and polydispersity (657 nm, PdI = 0.144) probably due to precipitation of the larger species present.

3.4.5 Encapsulation of Fluorescent Molecules

The encapsulation of guest molecules inside the nanoparticles can be achieved by incorporating the guest molecule with the polymer when dissolving into the good solvent (THF). Depending upon the nature of the desired guest molecule the good solvent may be varied, however, the two fluorescent guest molecules chosen for this study, Nile red and pyrene, were both soluble in THF. Their chemical structures are shown in Fig. 3.20.

3.4.5.1 Nile Red Encapsulation

Nile red is a lipophilic dye which can be used to stain intracellular lipid droplets [16]. It fluoresces strongly in lipophilic environments, and does not fluoresce at all

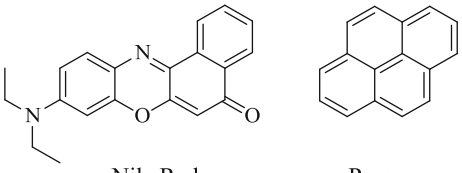

Fig. 3.20 Chemical structures of the two fluorescent dyes used; Nile red and Pyrene

in hydrophilic, polar solvents [17]. It was chosen due to this fluorescence dependence upon the solvent environment as it allowed investigation into the interior hydrophobicity/lipophilicity of the nanoparticles cores. When excited at 552 nm an emission maxima is observed at 630 nm; the intensity of this peak gives information about the internal environment of nanoparticles.

The nanoparticle formulation chosen for this study was ***i*$_5$-*f*$_1$**. Two different weight percentages of Nile red incorporation were attempted; 1 and 0.1 w/w% with respect to the final mass of polymer. The 0.1 w/w% formulation was chosen as the 1 w/w% formulation showed some Nile red that had crystallised from solution (see Appendix Fig. A.20). It was imperative that the presence of encapsulated Nile red did not change the size of the resulting nanoparticles, and as Fig. 3.21 shows, this was not the case. The PdI values also remained very similar to the nanoparticles formed in the absence of Nile red, all being below 0.11, see Table A.6 in the Appendix for D_z and PdI values.

The fluorescence emission spectra showed that over the series of *hyp*-polydendrons, ranging from 100 % hydrophobic **G2** dendron initiator to 100 % hydrophilic **750PEG** macroinitiator, each with the same hydrophobic pHPMA core, there was a trend, from the 100 % **G2** dendron initiated having a higher fluorescence intensity at 630 nm, which generally decreased across the series as more **750PEG** initiator was introduced. This can be seen in Fig. 3.22, where Fig. 3.22a shows the fluorescence spectra with the emission at 630 nm, and Fig. 3.22b shows the intensity maxima plotted against **G2** dendron initiator %.

There was a clear trend across the nanoparticle series; this can also be observed visually as seen in Fig. 3.23. The 100 % **G2** dendron initiated nanoparticles had a

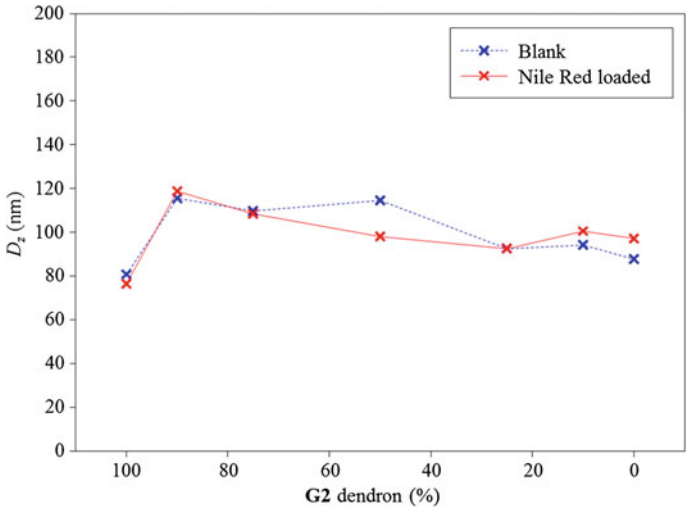

Fig. 3.21 Nanoparticle sizes for **G2**:**750PEG**-pHPMA$_{50}$-EGDMA$_{0.8}$ blank nanoparticles (*blue crosses*) and with 0.1 w/w% Nile red encapsulated (*red crosses*) prepared at ***i*$_5$-*f*$_1$**

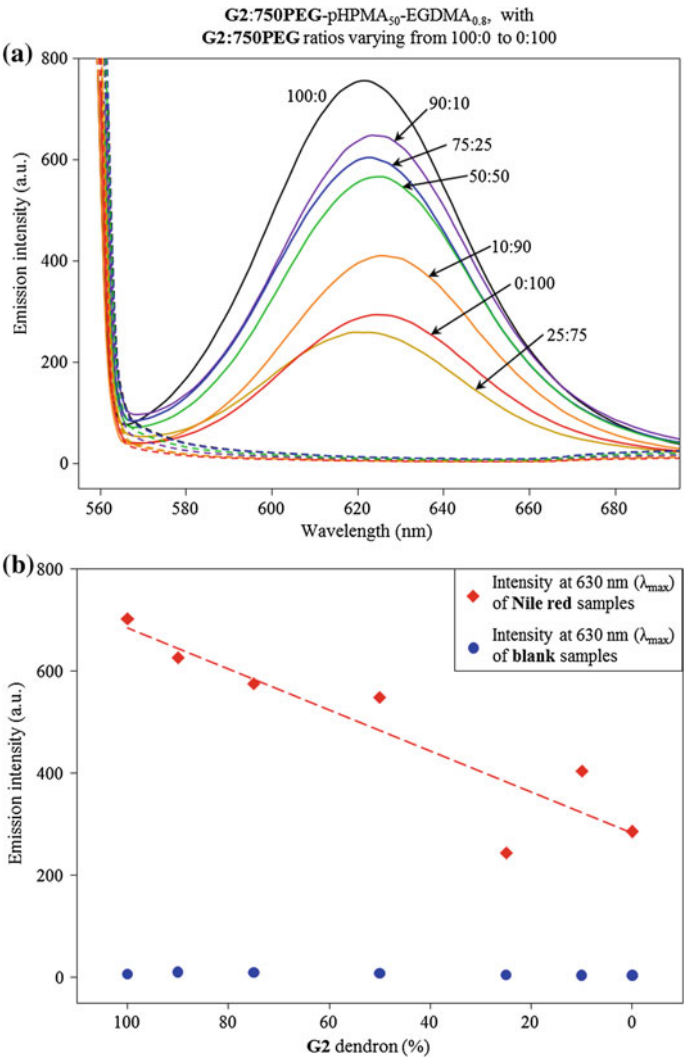

Fig. 3.22 **a** Fluorescence emission spectra for **G2**:**750PEG**-pHPMA$_{50}$-EGDMA$_{0.8}$ nanoparticles with encapsulated Nile red and blank nanoparticles (i_5-f_1). **b** The relationship between maximum intensity at 630 nm and **G2** dendron initiator (%)

more hydrophobic interior as the fluorescence intensity was higher than the 100 % **750PEG** initiated nanoparticles, which had a lower fluorescence intensity for Nile red. This was due to the manner in which the nanoparticles form, as it has been described previously (see Fig. 3.10 and Chap. 2, Sect. 2.6.1) it was hypothesised that the particles form from an aggregation of polymer species present in the good solvent, as the sizes of the nanoparticles are much larger than an individual

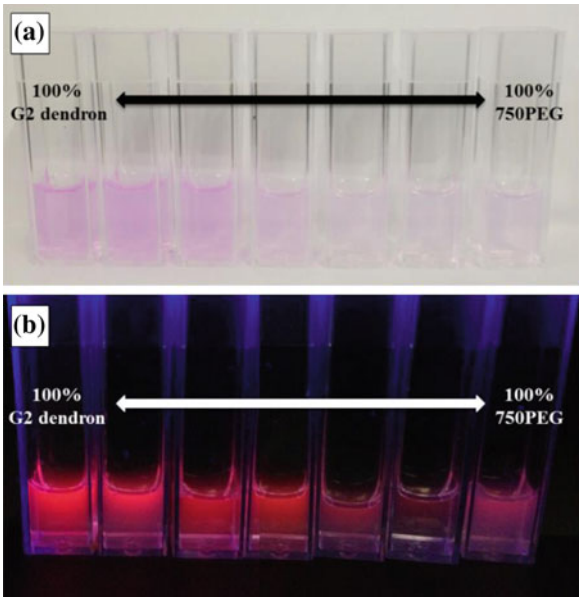

Fig. 3.23 Photographs of the nanoparticulate **G2**:**750PEG**-pHPMA$_{50}$-EGDMA$_{0.8}$ series prepared at i_5-f_1 with 0.1 w/w% Nile red encapsulated; **a** under normal light and **b** short wavelength UV lamp

hyp-polydendron macromolecule. Therefore there was a possibility for the **G2** dendron and **750PEG** functionality to be present in the core of the nanoparticles as well as at the surface. Hence, if the internal environment of the particles was altered by varying the ratios of **G2** dendron initiator and **750PEG** initiator, the environment in which the Nile red was located would also be varied, therefore, a variation in Nile red fluorescence would be expected. This also shows that the Nile red is being held within the core of the nanoparticles as otherwise the Nile red would not fluoresce.

The main disadvantage of evaluating the interior environment of the nanoparticles using Nile red as a fluorescent probe is that the fluorescence intensity at 630 nm is also dependent upon the concentration of Nile red present. This brings in errors with weighing out the Nile red, creating a stock solution in THF which may evaporate over time and also when pipetting out the desired amount. Therefore a different fluorescent probe (pyrene) which gave information independent of concentration was used.

3.4.5.2 Pyrene Encapsulation

Pyrene was also used as a probe for the internal environment as its fluorescence emission spectrum is highly sensitive to solvent polarity. Pyrene has various vibronic bands, five predominate bands, whereby the intensity of band 0–0 is strongly enhanced in polar solvents at the expense of other vibronic bands [18]. The ratio of this 0–0 band or peak 1 in the fluorescence emission spectra to the third predominant

peak, peak 3, gives rise to the reported use of the I_1/I_3 ratio. In non-polar solvents such as hexane this value is around 0.61, whereas in polar solvents this value can be dramatically higher; for example the I1/I3 ratio in water is 1.58 [19].

To probe the internal environment of each polymeric nanoparticle species, samples were prepared via nanoprecipitations using $\boldsymbol{i_5}$-$\boldsymbol{f_1}$, with 0.1 w/w% pyrene added to the good solvent with respect to the final polymer concentration. Pyrene was dissolved in THF to make a stock solution of a known concentration and the mass of pyrene needed was taken using a pipette. The nanoprecipitates showed only slight deviations from the sizes of blank nanoparticles; this can be seen in Fig. 3.24. The D_z and PdI values are shown in Table A.6 in the Appendix.

The five predominant vibronic bands can be seen in Fig. 3.25, with the I_1 and I_3 bands highlighted. It is the ratio between these two peaks which indicates the polarity of the solvent environment. Plotting this ratio against **G2** dendron initiator % shows a clear trend across the *hyp*-polydendron series, as shown in Fig. 3.26.

The fluorescence results for the Nile red and pyrene loaded nanoparticles across the series suggests that the internal environment of the nanoparticles varies from being more hydrophobic and less polar using the 100:0 *hyp*-polydendron, to being less hydrophobic and more polar to the 0:100 *hyp*-block copolymer. This trend is highlighted graphically in Fig. 3.27. To ascertain whether the varying environments present in the series of nanoparticles affected the pharmacological studies, nanoparticles across the range of **G2**:**750PEG** 100:0 to 0:100 were investigated further.

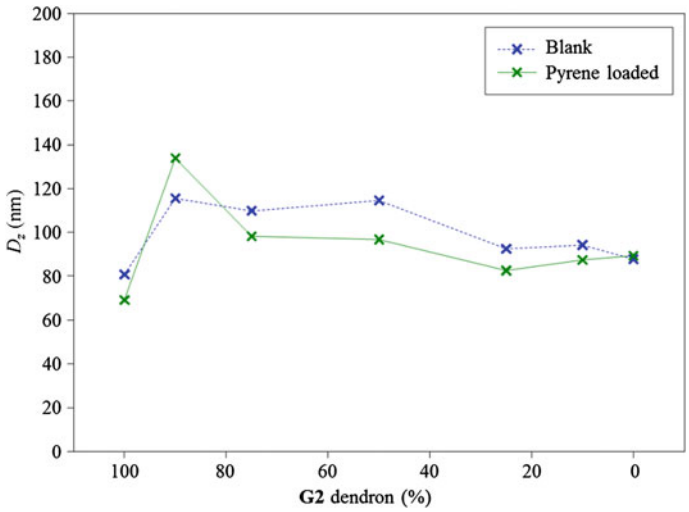

Fig. 3.24 Nanoparticle sizes for **G2**:**750PEG**-pHPMA$_{50}$-EGDMA$_{0.8}$ blank nanoparticles (*blue crosses*) and with 0.1 w/w% Nile red encapsulated (*green crosses*) prepared at $\boldsymbol{i_5}$-$\boldsymbol{f_1}$

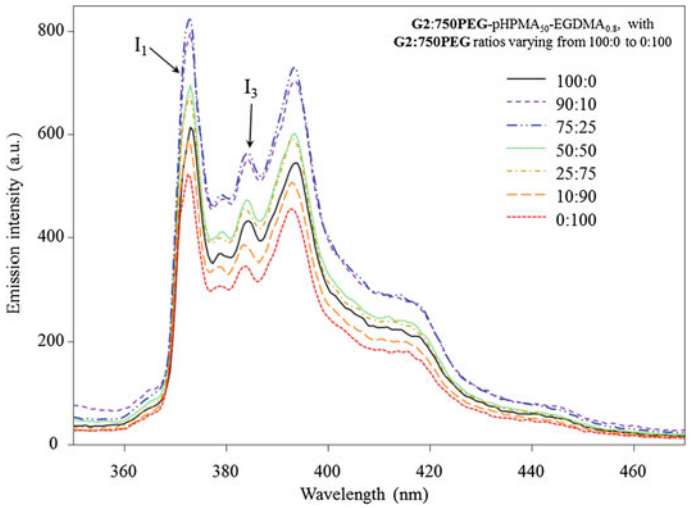

Fig. 3.25 Fluorescence emission spectra for **G2:750PEG** polymeric nanoparticles with encapsulation of 0.1 w/w% Pyrene

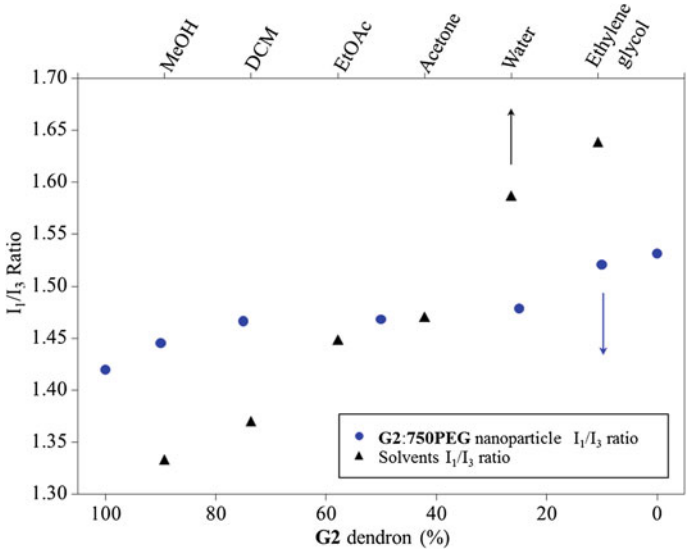

Fig. 3.26 I1/I3 ratio for **G2:750PEG-**pHPMA$_{50}$-EGDMA$_{0.8}$ series of nanoparticles with pyrene encapsulated (*blue circles*) and common solvents as a reference (*black triangles*)

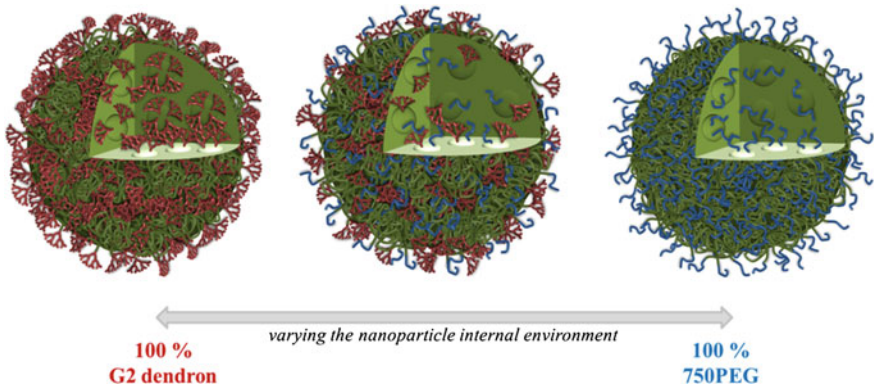

Fig. 3.27 Graphical representation of the varying environments present in the nanoparticles when using *hyp*-polydendrons and *hyp*-block copolymers with varying ratios of initiators

3.5 Pharmacological Evaluation of Materials

When designing polymeric drug carriers two main routes of administration are usually targeted; intravenous and oral. Treatment of infectious diseases such as the human immunodeficiency virus (HIV), which is a life-long condition where any break in therapy results in viral re-bound with potential damage to the immune system, is typically administered intravenously. Frequent dosing via intravenous administration is not viable, although recently, long-acting antiretroviral formulations have been developed which require infrequent dosing (every 1–3 months) intravenously [20]. However until these therapies are widely available it remains desirable to dose drug delivery vehicles orally, to achieve permeation through the intestinal epithelial cells into the systemic circulation to allow for drug accumulation in macrophage cells, for example, as macrophages are a sanctuary sites for HIV in the human body.

To assess whether *hyp*-polydendron nanoparticles would be able to act as drug carriers, targeting oral dosing, several initial pharmacological experiments were performed. These pharmacological experiments were conducted by researchers in the Molecular and Clinical Pharmacology department at the University of Liverpool, through collaboration between the Owen and Rannard research groups. Initially toxicology assays were performed [21] to ascertain whether the *hyp*-polydendron nanoparticles were toxic to the intestinal epithelial cells. An in vitro transwell plate experiment [22] was also conducted to investigate the ability of the *hyp*-polydendron nanoparticles to permeate the intestinal epithelial cells. These types of pharmacological assays are discussed in more detail below.

3.5.1 Cytotoxicity Assays

Typical toxicity assays include the 3-[4,5-dimethylthiazol-2-yl]-2,5 diphenyl tetrazolium bromide (MTT) assay and adenosine triphosphate (ATP) assay. The MTT assay is based on the conversion of MTT to formazan crystals by living cells to determine mitochondrial activity. The mitochondrial activity is related to the number of viable living cells, therefore this assay can be used to assess a drug or material's cytotoxic effects [21].

The ATP assay method starts with either the extraction of cells in suspension from continuous cell culture when using the THP-1 cell line, or for Caco-2 and ATHP-1 cell lines they firstly need to be 'trypsinised' to remove the cells from a substrate to suspend them. The assay uses a serum free medium and polypropylene plates to prevent the growth of non-neoplastic cells over a 6-day incubation period followed by detergent based extraction of cellular ATP. The cell production of ATP is a measure of the cell viability as viable cells produce ATP whereas dead cells do not. ATP is measured by luciferin-luciferase assay in a luminometer which measure the presence of a single cell up to 10^8 cells [23].

3.5.2 Caco-2 Cell Transwell Plate Assay

The Caco-2 transwell plate assay is a model of the intestinal epithelium and is widely used to predict the adsorption of materials across the 'gut wall'. The Caco-2 cell line is a continuous line of heterogeneous human epithelial colorectal adenocarcinoma cells, which can be cultured to differentiate and become polarised to resemble the enterocytes lining the small intestine [22]. The cells express the same enzymes and transporters which are characteristic of enterocytes, such as; peptidases, esterases and P-glycoprotein. The cells are grown as a confluent monolayer with tight junctions between cells, so that movement of drug across this monolayer is predominantly restricted to permeation or active transport through the cell. Figure 3.28 shows a graphical representation of the transwell plate experiment. In Fig. 3.28a the apical (A) and basolateral (B) chambers are represented with the monolayer and membrane in the transwell plate experiment.

The apical chamber (A) represents the gut side of the epithelium whilst the basolateral chamber (B) represents the blood side of the epithelium. The experiment is conducted incubating the monolayer with sample deposited in the apical compartment measuring the amount of movement across the monolayer over a 4 h period from the apical to basolateral compartment (A > B), Fig. 3.28b, and deposited in the basolateral compartment measuring the movement from the basolateral to apical compartment (B > A), Fig. 3.28c.

The movement of sample across the membrane is typically reported as apparent permeability (P_{app}) which describes the flux at which the material traverses per unit area of the cell barrier [24]. P_{app} is estimated using Eq. (4): where P_{app} is apparent permeability ($\times 10^{-6}$ cm^{-1}); dQ/dt is the rate of transport (nMmin^{-1}); v is the

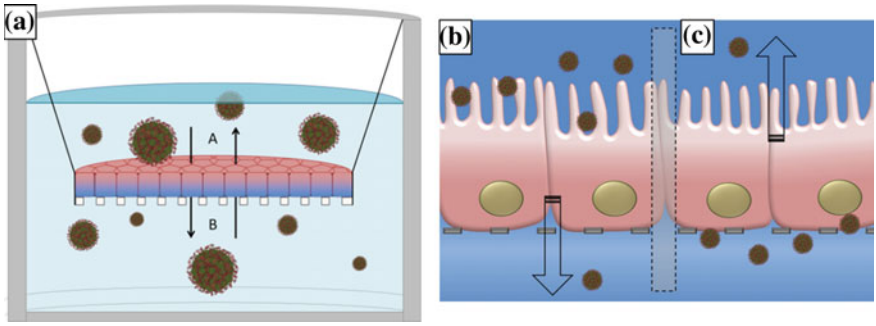

Fig. 3.28 Graphical representation of the Caco-2 monolayer in the epithelial model

volume of the receiver compartment; A is the surface area of the membrane (cm^2); and C_0 is the initial donor concentration (nM).

$$P_{app} = \frac{(dQ/dt) \times v}{A \times C_0} \tag{4}$$

Several assumptions are made for an accurate measure of permeability. These are that the drug accumulated in the receiver compartment is proportional to time, the system complies with 'sink conditions' and that cellular accumulation, metabolism and non-specific binding to plasticware are absent [22]. 'Sink conditions' implies that once the material has traversed the monolayer it does not pass back across, however this is not always the case with permeable materials. Once permeability is achieved further studies may be conducted to assess the mechanism of transport across the Caco-2 cell monolayer. Transcellular movement describes the movement of the material through the cells, whereas paracellular movement the movement of material between the cells. Paracellular permeation is possible and has been shown for several nanoparticle systems [25].

To conduct this experiment the cells are grown to a confluent monolayer over 21 days, where the integrity of the monolayer is checked by measuring the trans-epithelial electrical resistance (TEER) before experiments commence. The apical (A) and basolateral (B) compartments were treated with the materials to assess movement from A > B and B > A, which can also be described as the apparent permeability (P_{app}) of the material, over an incubation period of 4 h. Therefore if this assay is being used to assess the permeation of materials across the monolayer, it is important to ensure those materials are not toxic to the cells, which would compromise the monolayer and lead to inaccurate results. Cytotoxicity assays conducted using Caco-2 cells include the ATP and MTT assays (see Sect. 3.5.1). When conducting the pharmacological experiments an aqueous preparation of the dye (Nile red) is also assessed in the same manner as the loaded nanoparticles to ascertain the toxicity and/or permeability of the free dye. The free dye treatment was prepared by solubilising it in DMSO prior to being spiked into transport buffer, the final volume of DMSO was <0.1 % of the final volume.

3.5.3 Hyp-*polydendron Nanoparticles for Pharmacological Assays*

The *hyp*-polydendron nanoparticle samples loaded with Nile red were readily detectable by fluorescence spectroscopy for quantification methods. The formulations used were $\boldsymbol{i_5\text{-}f_1}$ with 0.1 w/w% Nile red (therefore 1 mg/mL polymer, 1 μg/mL Nile red). To ensure the variation between different batches of Nile red loaded nanoparticles prepared was not significant, six batches were prepared and analysed by DLS, see Table 3.6. The Nile red loaded nanoparticles from batch 2 were studied over time to assess the colloidal stability over 7 weeks, see Fig. 3.29 for the D_z measurements over time.

3.5.4 *Cytotoxicity Assay Results*

Toxicity experiments were conducted to assess whether the materials were toxic to the Caco-2 cells used for the model intestinal epithelial transwell plate experiment. ATP and MTT assays were conducted with incubation periods of 1 and 5 days across a range of concentrations (1–1000 nM Nile red).

3.5.4.1 MTT Assays

Following 24 h incubation of Caco-2 cells with each *hyp*-polydendron, analysis of cytotoxicity by MTT assay (Appendix, Fig. A.21) showed that aqueous Nile red and each *hyp*-polydendron did not affect metabolic turnover of Caco-2 cells compared to untreated cells at the range of concentrations investigated. It can be inferred that metabolic turnover correlates to cell viability in which case each material was not cytotoxic.

Following 120 h incubation of Caco-2 cells with each *hyp*-polydendron, analysis of cytotoxicity by an MTT assay (see Fig. 3.30) also showed that aqueous Nile red and each *hyp*-polydendron at the range of concentrations investigated did not affect the viability of Caco-2 cells.

3.5.4.2 ATP Assays

Following 24 h incubation of Caco-2 cells with each *hyp*-polydendron, analysis of cytotoxicity by an ATP assay using a CellTiter-Glo® kit, (Promega, UK) (see Appendix, Fig. A.22) indicated that ATP presence was not affected in cells treated with aqueous Nile red solution and *hyp*-polydendron formulated Nile red at the range of concentrations investigated compared to untreated cells. It can be inferred

Table 3.6 D_z and PdI measurements by DLS for various batches of Nile red loaded **G2**:**750PEG**-pHPMA$_{50}$-EGDMA$_{0.8}$ nanoparticle samples

G2:**750PEG**-(pHPMA$_{50}$-EGDMA$_{0.8}$)	Batch 1		Batch 2		Batch 3		Batch 4		Batch 5		Batch 6	
	D_z (nm)	PdI	D_z (nm)	PdI	D_z (nm)	PdI	D_z (nm)	PdI	D_z (nm)	PdI	D_z (nm)	PdI
100:0	76	0.109	70	0.064	69	0.081	75	0.087	70	0.108	67	0.233
90:10	119	0.061	128	0.052	118	0.071	106	0.057	118	0.060	93	0.116
75:25	108	0.067	102	0.062	98	0.056	89	0.086	86	0.080	77	0.216
50:50	98	0.069	100	0.053	104	0.049	87	0.083	85	0.120	69	0.166
25:75	92	0.081	93	0.058	91	0.071	85	0.093	88	0.113	82	0.250
10:90	101	0.075	84	0.089	81	0.117	82	0.130	94	0.235	87	0.259
0:100	97	0.095	89	0.106	91	0.094	84	0.155	102	0.225	101	0.252

D_z z-average diameter

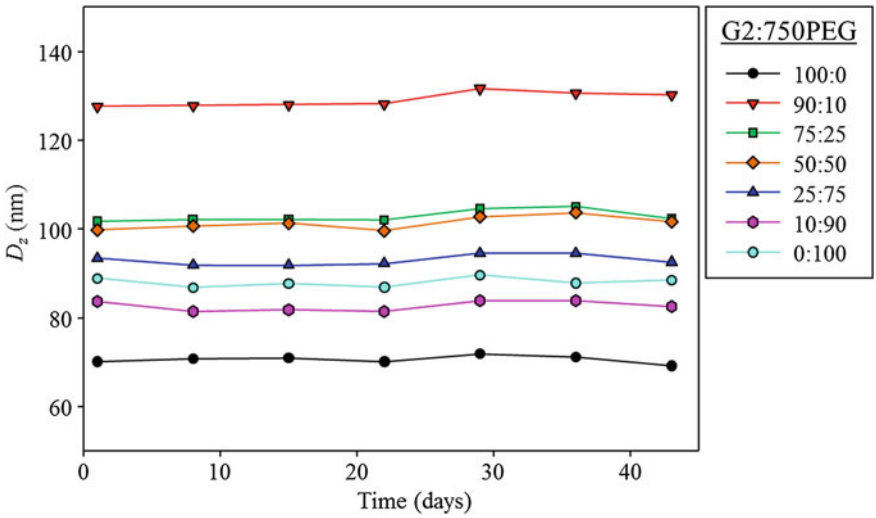

Fig. 3.29 D_z by DLS over time for Nile red loaded **G2:750PEG**-pHPMA$_{50}$-EGDMA$_{0.8}$ nanoparticles from batch 2 in Table 3.6

that the presence of ATP correlates to cell viability in which case each material was not cytotoxic.

Following 120 h incubation of Caco-2 cells with each *hyp*-polydendron, analysis of cytotoxicity by ATP assay using a CellTiter-Glo® kit, (Promega, UK) (see Fig. 3.31) also indicated viability was not affected in cells treated with aqueous Nile red solution and each *hyp*-polydendron material at the range of concentrations investigated compared to untreated cells.

3.5.5 Caco-2 Cell Transwell Plate Assay Results

The use of the Caco-2 monolayer in the prediction of the absorption of drugs is well documented [22] and was discussed in Chap. 1 (Sect. 1.5.3.2).

Transcellular permeability of Nile red through Caco-2 cell monolayers (to model the intestinal epithelium) was assessed over a 4 h period, see Fig. 3.32. The transcellular permeation of the **G2:750PEG**-10:90 Nile red *hyp*-polydendron preparation was significantly higher in the apical to basolateral (A > B, gut to blood) direction compared to an aqueous solution of Nile red. Some of the formulations (75:25, 50:50, 25:75) showed a slightly higher permeability of Nile red from the apical to basolateral (A > B) whereas as the 100:0 and 0:100 were comparable to the aqueous Nile red sample. For one of the formulations (90:10) there was no A > B or B > A movement as there was no Nile red detectable in the acceptor compartment. The reason for this was not clear—possibly due to the poor colloidal stability of the particles under physiological conditions.

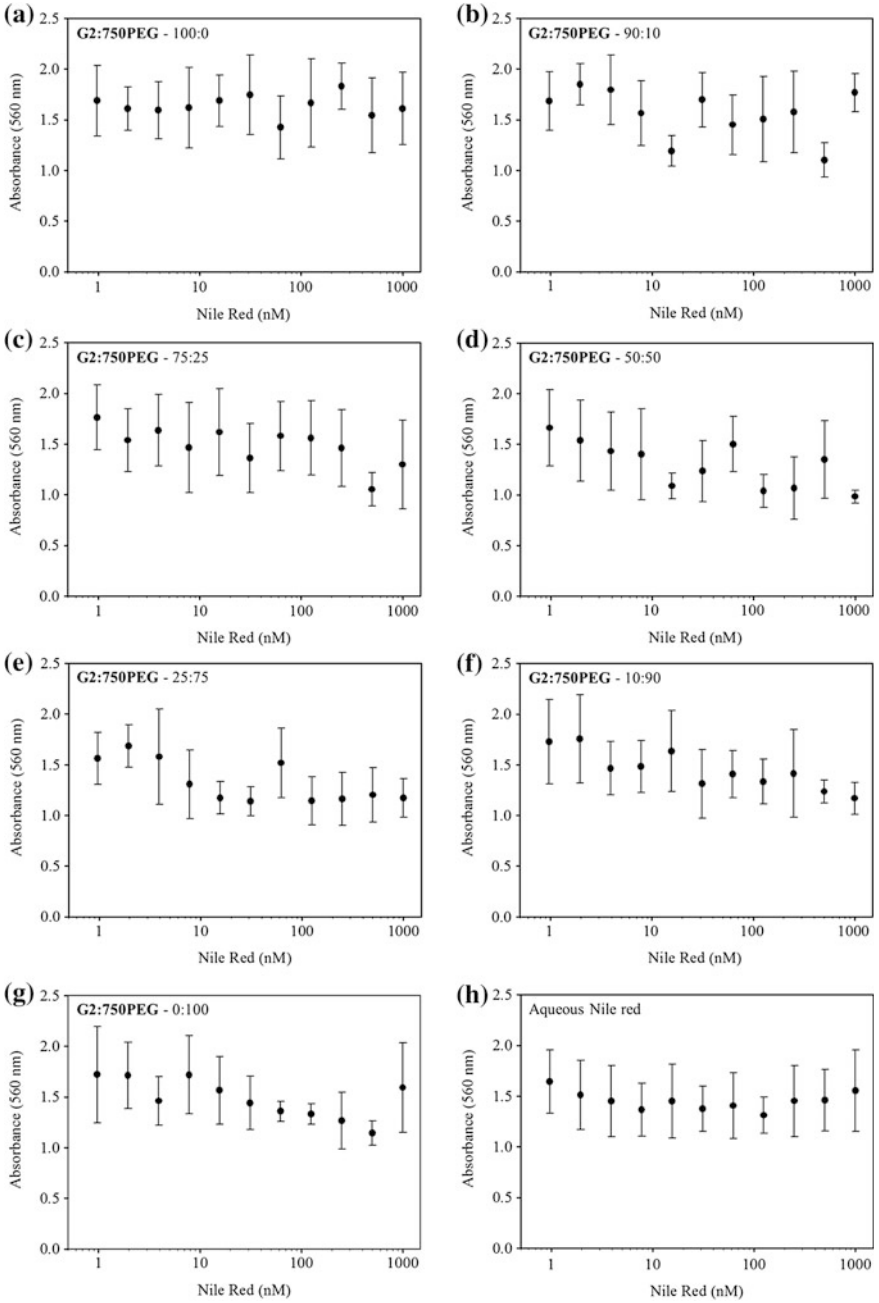

Fig. 3.30 MTT assay of Caco-2 cells following 5 day incubation with aqueous Nile red and each **G2**:**750PEG**-pHPMA$_{50}$-EGDMA$_{0.8}$ *hyp*-polydendron. **a** 100:0, **b** 90:10, **c** 75:25, **d** 50:50, **e** 25:75, **f** 10:90, **g** 0:100 and **h** Aqueous. Error = standard deviation

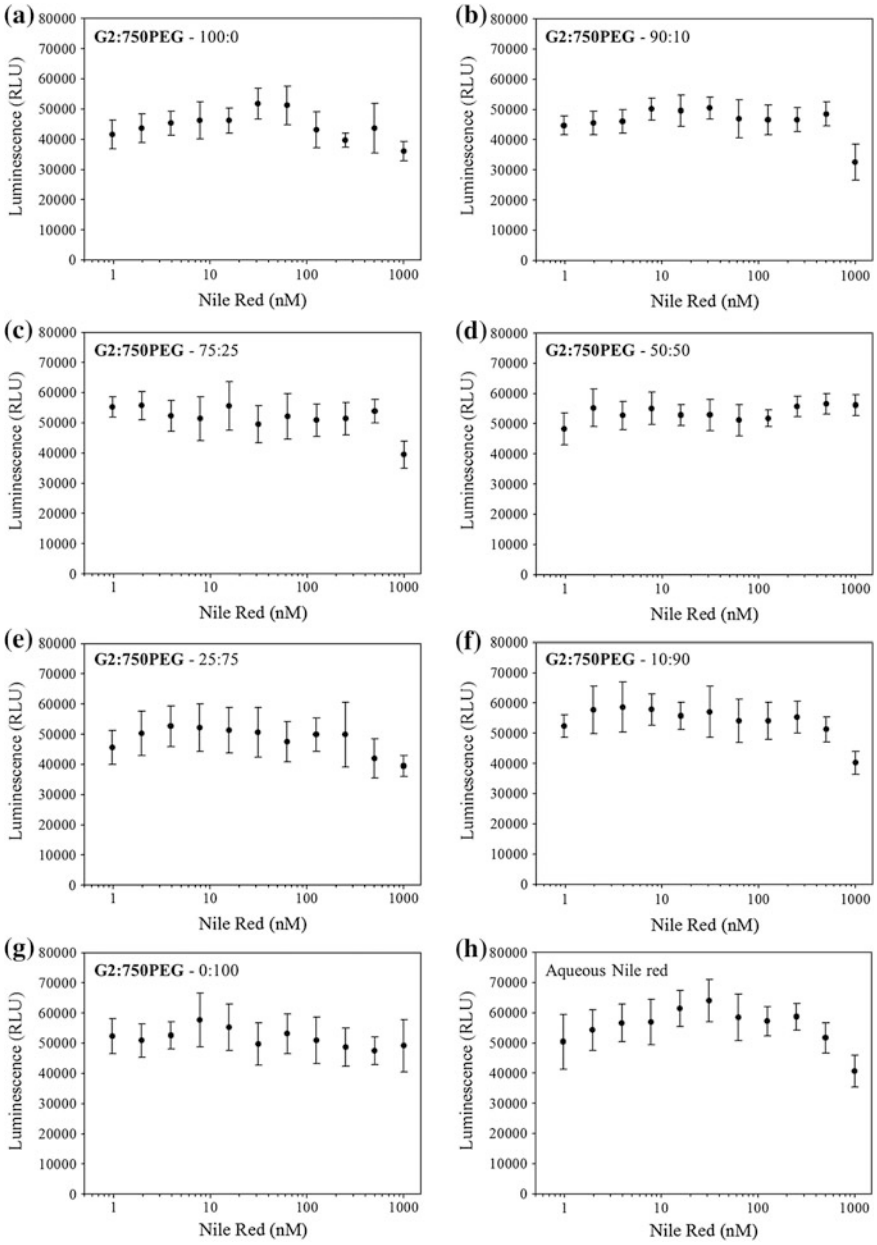

Fig. 3.31 ATP assay of Caco-2 cells following 5 day incubation with aqueous Nile red and each **G2**:**750PEG**-pHPMA$_{50}$-EGDMA$_{0.8}$ *hyp*-polydendron. **a** 100:0, **b** 90:10, **c** 75:25, **d** 50:50, **e** 25:75, **f** 10:90, **g** 0:100 and **h** Aqueous. Error = standard deviation

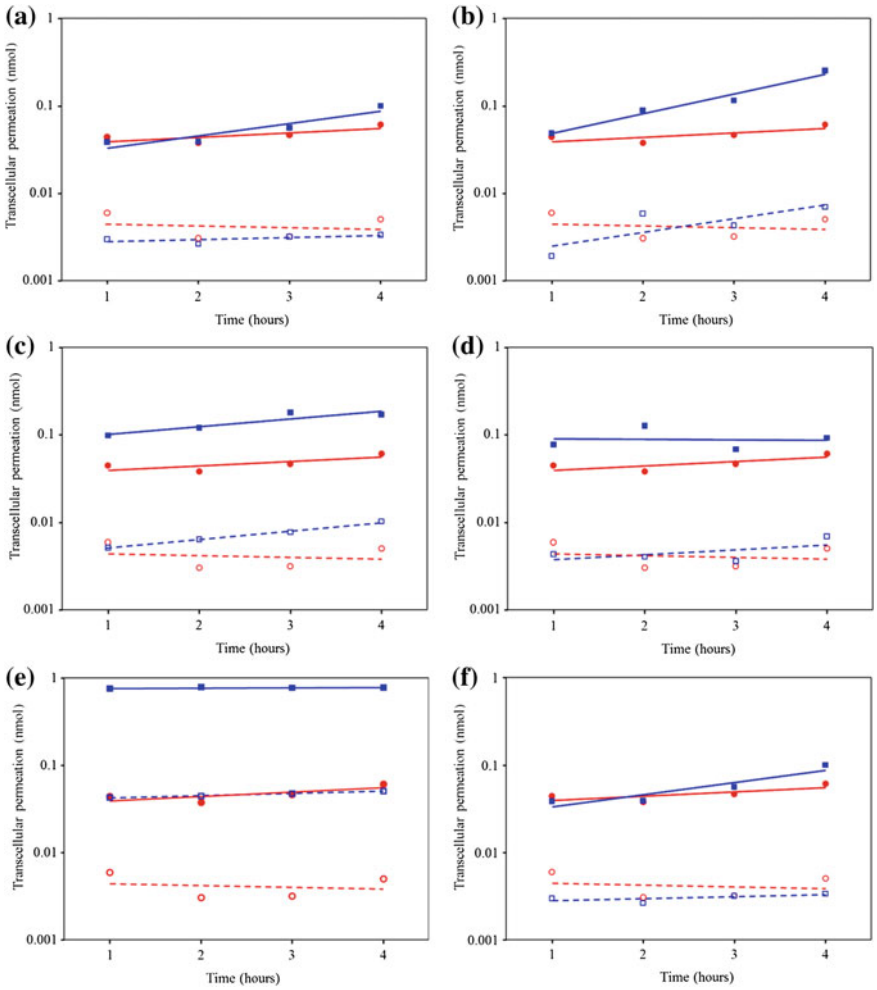

Fig. 3.32 The transcellular permeation across Caco-2 cell monolayers of *hyp*-polydendron formulated Nile red relative to an aqueous solution of Nile red. Data are given as the mean of experiments conducted in biological triplicate. **G2**:**750PEG**; **a** 100:0, **b** 75:25, **c** 50:50, **d** 25:75, **e** 10:90 and **f** 0:100, A > B (*closed blue squares*) and B > A (*open blue squares*). Aqueous Nile red alone; A > B (*closed red circles*) and B > A (*open red circles*)

All the *hyp*-polydendron materials produced a greater P_{app} ratio than an aqueous preparation of Nile red following 1 h incubation (Fig. 3.33). A statistically significant correlation ($P \leq 0.05$) between the ratio of **G2** dendron initiator and **750PEG** macroinitiator used in the *hyp*-polydendron formulation and the ratio of apical to basolateral (A > B, gut to blood), basolateral to apical (B > A, blood to gut) movement of Nile red across the Caco-2 monolayer was observed.

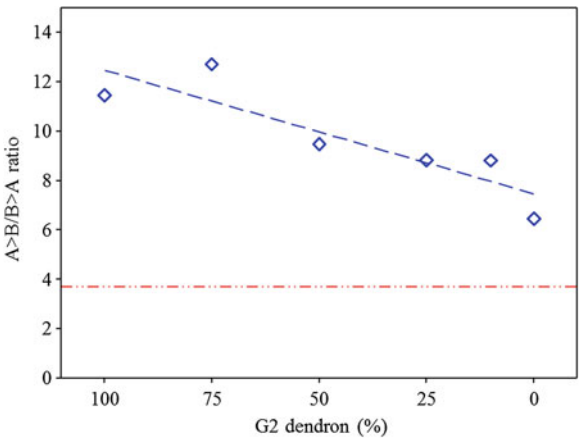

Fig. 3.33 Correlation between **G2**:**750PEG**-pHPMA$_{50}$-EGDMA$_{0.8}$ *hyp*-polydendron formulation and the ratio of Nile red transported (A > B/B > A) across Caco-2 cell monolayers (R^2 0.784)

Therefore the pharmacological experiments showed that the *hyp*-polydendron and *hyp*-block copolymer nanoparticles were not toxic to Caco-2 cells, they showed an increase in Nile red apparent permeability across the Caco-2 cell monolayer compared to the aqueous Nile red and also had a trend in the P_{app} ratio across the **G2**:**750PEG** series.

3.5.6 Nanoparticle Stability in Salt and Transport Buffer

The *hyp*-polydendron and *hyp*-block copolymer nanoparticles had negative zeta-potentials which indicated charge stabilisation of the particles. As discussed briefly in Chap. 2, Sect. 2.6.3, it is desirable for nanoparticle to have steric stabilisation when biological applications are targeted. This is due to the presence of various salts in physiological conditions, which causes screening of charges in charge stabilised nanoparticles. As the charge on the particles repel one another, when the charges are screened in a salt solution the nanoparticles aggregate and ultimately precipitate.

Investigations into the stability of particles under physiological conditions are commonly conducted using buffered solutions which contain a concentration of salts to mimic the physiological ionic strength ($\sim$0.15 M). Therefore to assess how stable these **G2**:**750PEG** nanoparticles would be in physiologically relevant conditions, firstly, a solution of 0.14 M NaCl was used, to assess the stability of particles to dilution with a salt solution, and secondly, transport buffer (TB). TB consists of Hank's balanced salt solution, 25 mM of 4-(2-hydroxyethyl)-1-piperazineethane sulfonic acid and 0.1 % bovine serum albumin, which is commonly used for in vitro assays such as the Caco-2 transwell plate experiment (see Chap. 1, Sect. 1.5.3.2).

Therefore each sample prepared with Nile red was diluted with 0.14 M NaCl and TB to assess how stable they were in physiologically relevant conditions. Unfortunately, aggregation was observed after dilution with either salt solution or TB, indicating that the nanoparticles were indeed charge stabilised and did not shows stability in physiologically relevant conditions. This was interesting as although the nanoparticles were aggregated, they still showed movement across the Caco-2 cell monolayer experiment, suggesting that the polymer enhanced the permeation of Nile red across the Caco-2 cell.

3.6 Conclusion

To conclude, a series of hyperbranched polymers were produced via a mixed initiator approach to ATRP. The initiators employed included a **G2** dendron initiator and a **750PEG** macroinitiator. This series of materials included six *hyp*-polydendron materials and one *hyp*-block copolymer (0:100-pHPMA$_{50}$-EGDMA$_{0.8}$, not containing any dendrons). These materials were subjected to a nanoprecipitation approach to produce nanoparticles with varying internal and external environments. The corresponding sizes of these nanoparticles were controllable via tuning either the initial concentration of polymer in the good solvent or the final concentration in water. They were also utilised in the encapsulation of hydrophobic fluorescent dye molecules to probe the interior environment, and also to act as a model drug molecule demonstrating the possibility of drug loading in these materials. Even though the loading described in this chapter was low (0.1 w/w%) encapsulation is possible and could be improved. The applicability of these materials to nanomedicine was investigated, utilising an intestinal epithelium model to predict transcellular permeability of the nanoparticles. These results are promising, showing that these materials show an enhanced apparent permeability of encapsulated Nile red across the Caco-2 cell monolayer when compared to free Nile red. Due to the instability in physiologically relevant conditions, further work was needed to improve the stability of the nanoparticles to achieve steric stabilisation.

References

1. K. Jankova, X.Y. Chen, J. Kops, W. Batsberg, Macromolecules **31**, 538–541 (1998)
2. R.A. Slater, T.O. McDonald, D.J. Adams, E.R. Draper, J.V.M. Weaver, S.P. Rannard, Soft Matter **8**, 9816–9827 (2012)
3. K.H. Kim, J. Kim, W.H. Jo, Polymer **46**, 2836–2840 (2005)
4. K.L. Robinson, M.A. Khan, M.V.D. Banez, X.S. Wang, S.P. Armes, Macromolecules **34**, 3155–3158 (2001)
5. Y.T. Li, S.P. Armes, X.P. Jin, S.P. Zhu, Macromolecules **36**, 8268–8275 (2003)
6. J.S. Wang, K. Matyjaszewski, Macromolecules **28**, 7901–7910 (1995)
7. J.H. Xia, S.G. Gaynor, K. Matyjaszewski, Macromolecules **31**, 5958–5959 (1998)

8. I. Bannister, N.C. Billingham, S.P. Armes, S.P. Rannard, P. Findlay, Macromolecules **39**, 7483–7492 (2006)
9. F. Isaure, P.A.G. Cormack, S. Graham, D.C. Sherrington, S.P. Armes, V. Butun, Chem. Commun. **2004**, 1138–1139 (2004)
10. P.V. Kumar, A. Asthana, T. Dutta, N.K. Jain, J. Drug Target. **14**, 546–556 (2006)
11. S. Schubert, J.T. Delaney, U.S. Schubert, Soft Matter **7**, 1581–1588 (2011)
12. C. Zhang, V.J. Pansare, R.K. Prud'homme, R.D. Priestley, Soft Matter **8**, 86–93 (2012)
13. H. Fessi, F. Puisieux, J.P. Devissaguet, N. Ammoury, S. Benita, Int. J. Pharm. **55**, R1–R4 (1989)
14. V.K. Lamer, R.H. Dinegar, J. Am. Chem. Soc. **72**, 4847–4854 (1950)
15. D. Horn, J. Rieger, Angew. Chem. Int. Edit. **40**, 4331–4361 (2001)
16. P. Greenspan, E.P. Mayer, S.D. Fowler, J. Cell Biol. **100**, 965–973 (1985)
17. T. He, D.J. Adams, M.F. Butler, C.T. Yeoh, A.I. Cooper, S.P. Rannard, Angew. Chem. Int. Edit. **46**, 9243–9247 (2007)
18. D.S. Karpovich, G.J. Blanchard, J. Phys. Chem. **99**, 3951–3958 (1995)
19. T. He, D.J. Adams, M.F. Butler, A.I. Cooper, S.P. Rannard, J. Am. Chem. Soc. **131**, 1495–1501 (2009)
20. C.D. Andrews, W.R. Spreen, H. Mohri, L. Moss, S. Ford, A. Gettie, K. Russell-Lodrigue, R.P. Bohm, C. Cheng-Mayer, Z. Hong, M. Markowitz, D.D. Ho, Science **343**, 1151–1154 (2014)
21. J. Meerloo, G. L. Kaspers and J. Cloos, in *Cancer Cell Culture*, 1st edn, ed. by A. Cree (Humana Press, 2011), pp. 237–245
22. H. Sun, E.C.Y. Chow, S. Liu, Y. Du, K.S. Pang, Expert Opin Drug Met **4**, 395–411 (2008)
23. S. Glaysher, I. Cree, in *Cancer Cell Culture*, 1st edn, ed. by A. Cree (Humana Press, 2011), pp. 247–257
24. R. Elsby, D.D. Surry, V.N. Smith, A.J. Gray, Xenobiotica **38**, 1140–1164 (2008)
25. Y.H. Lin, C.K. Chung, C.T. Chen, H.F. Liang, S.C. Chen, H.W. Sung, Biomacromolecules **6**, 1104–1112 (2005)

Chapter 4
Mixing Dendron and PEG Initiators for the Polymerisation of Branched pHPMA and Formation of Sterically Stabilised Nanoparticles

4.1 Introduction

Due to the observed precipitation of the *hyp*-polydendron nanoparticles formed via nanoprecipitation, discussed in Chap. 3, in physiologically relevant conditions, it was desirable to produce nanoparticles which were sterically stabilised rather than charge stabilised. Steric stabilisation can be achieved through the incorporation of a hydrophilic moiety to the nanoparticle—usually a hydrophilic polymer [1]. Hydrophilic polymers which have been used as such to stabilise hydrophobic nanoparticles in aqueous environments include; PEG, pluronics, polycyclodextrin, polyglutamate, PLA/PGA/PLGA [2].

To improve the stability of nanoparticles formed via nanoprecipitation a longer PEG chain was used in order to generate additional steric stability as the short PEG_{16} chain was not able to provide enough hindrance to prevent aggregation as discussed in Chap. 3.

4.2 Initiator Synthesis

The initiators chosen for this study were the generation 2 (**G2**) hydrophobic benzyl dendron and a PEG ($\sim$2,000 $gmol^{-1}$) macroinitiator. A more facile synthesis was achieved for the **G2** benzyl dendron which is discussed below. This new **G2** dendron initiator was very similar in structure to the **G2** dendron initiator described in Chaps. 2 and 3, therefore throughout this chapter the new **G2** dendron will be termed as the **G2′** dendron initiator.

F.L. Hatton, *Hyperbranched Polydendrons*,
Springer Theses, DOI 10.1007/978-3-319-18753-2_4

4.2.1 G2′ DBOP Dendron Initiator—Alternative Synthesis

The method for the **G2′** dendron synthesis is shown below in Scheme 4.1. Rather than coupling two molecules of 1,3-dibenzyloxy-2-propanol, then subsequent ring opening of β-butyrolactone to give a reactive focal point for esterification to give the final ATRP initiator, instead molecule **9** (AB_2 brancher) was used. This removes the need for purification by column chromatography before the final step.

As discussed in Chap. 2 (Sect. 2.2.2) the reaction of 1,3-dibenzyloxy-2-propanol and 1,1′-carbonyldiimidazole gave **3**, (see Appendix Figs. A.1, A.2 and A.3 for ^{1}H and ^{13}C NMR spectra analysis and ES mass spectrometry analysis respectively). The reaction of two equivalents of **3** with one equivalent of **9** (AB_2 brancher) gave a generation 2 dendron, **10**, with a free hydroxyl group at the focal point for further reaction. The AB_2 brancher, **9**, was developed within the research group [3–5] and the synthesis is discussed in the Appendix (Sect. 3.1, p. 303, see Scheme A.1 and Figs. A.23–A.25). The two primary amines on the AB_2 brancher selectively react with the imidazole carboxylic ester, **3**, to give **10** in good yields (94 %). The ^{1}H NMR spectrum and ^{13}C NMR spectrum of **10** can be seen in the Appendix, Figs. A. 26 and A.27, respectively. The ES mass spectrometry analysis, Fig. A.28 in the Appendix shows the correct $[M + H]^+$ molecular ion peak at 756.4 m/z.

The hydroxyl group at the focal point of **10** was subsequently reacted with α-bromo isobutyryl bromide to give the new **G2′** dendron initiator, **11**, which was purified by column chromatography and analysed by ^{1}H NMR and ^{13}C NMR spectroscopy which confirmed the correct structure; the ^{1}H NMR spectrum (Fig. 4.1) and ^{13}C NMR spectrum (Fig. 4.2) show all assigned peaks. Analysis by

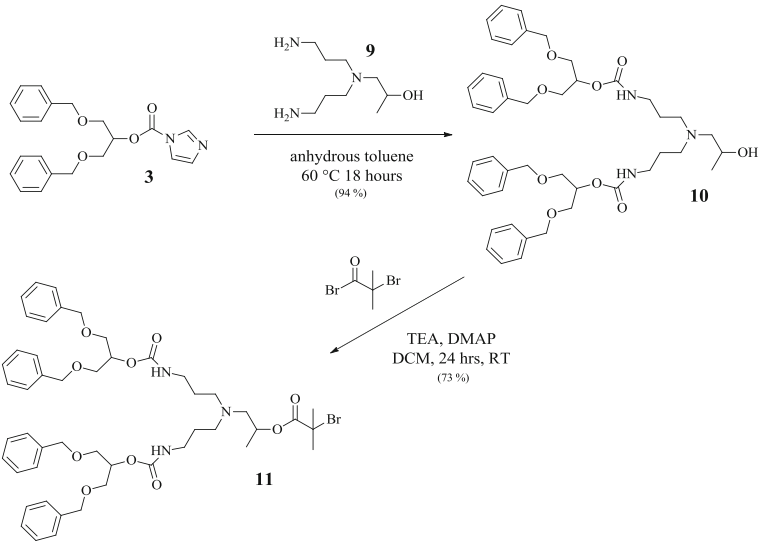

Scheme 4.1 Synthesis of new **G2′** dendron initiator via AB_2 brancher

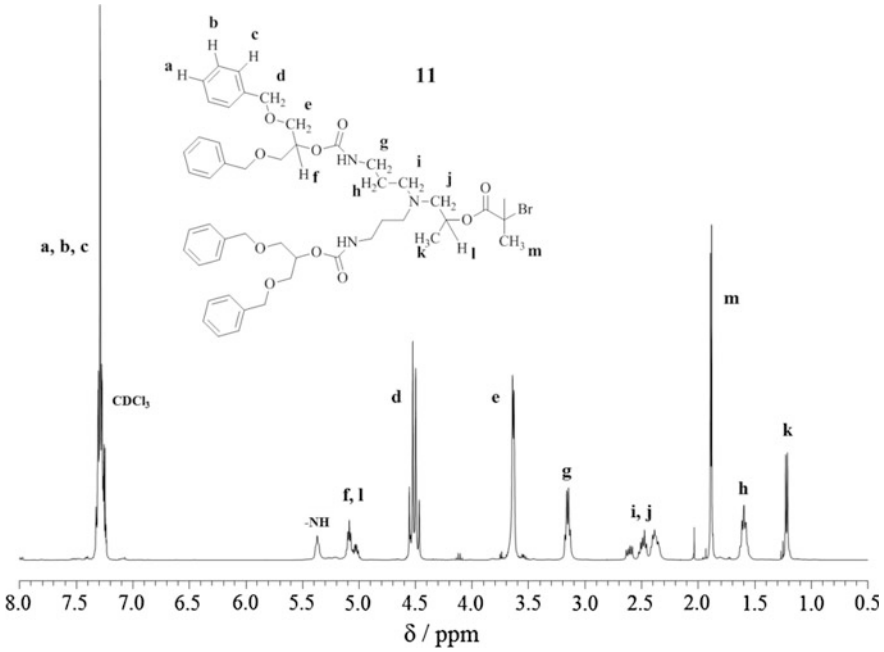

Fig. 4.1 ^{1}H NMR ($CDCl_3$, 400 MHz) of **G2′** dendron initiator, **11**

ES mass spectrometry, Fig. 4.3, shows the correct molecular ion peak, $[M + H]^+$ at 936 m/z, and also $[M + Na]^+$ and $[M + K]^+$ at 958 and 974 m/z; the bromine isotope pattern is also visible.

4.2.2 2000PEG Macroinitiator Synthesis

The PEG macroinitiator used in this chapter was synthesised via the esterification of monomethoxy PEG (average molecular weight 2,000 $gmol^{-1}$) with α-bromo isobutyryl bromide [6]. The same method was used as discussed in Chap. 3 for the synthesis of the **750PEG** macroinitiator. Scheme 4.2 shows the synthesis of this **2000PEG** macroinitiator.

The monomethoxy PEG ($\sim$2,000 $gmol^{-1}$) was dissolved in THF which required warming ($\sim$40 °C) for full dissolution. This was then degassed with dry N_2 for approximately 20 min, placed in an ice bath and DMAP and TEA were added. The α-bromoisobutyryl bromide was added dropwise over 20 min. A precipitate was observed immediately which indicated reaction as the salt formed is $NEt_3H^+Br^-$. The reaction was allowed to warm to room temperature and left stirring and sealed under dry N_2 for 24 h. The precipitate was filtered, solvent removed in vacuo to give the crude product which was dissolved in acetone and precipitated into cold

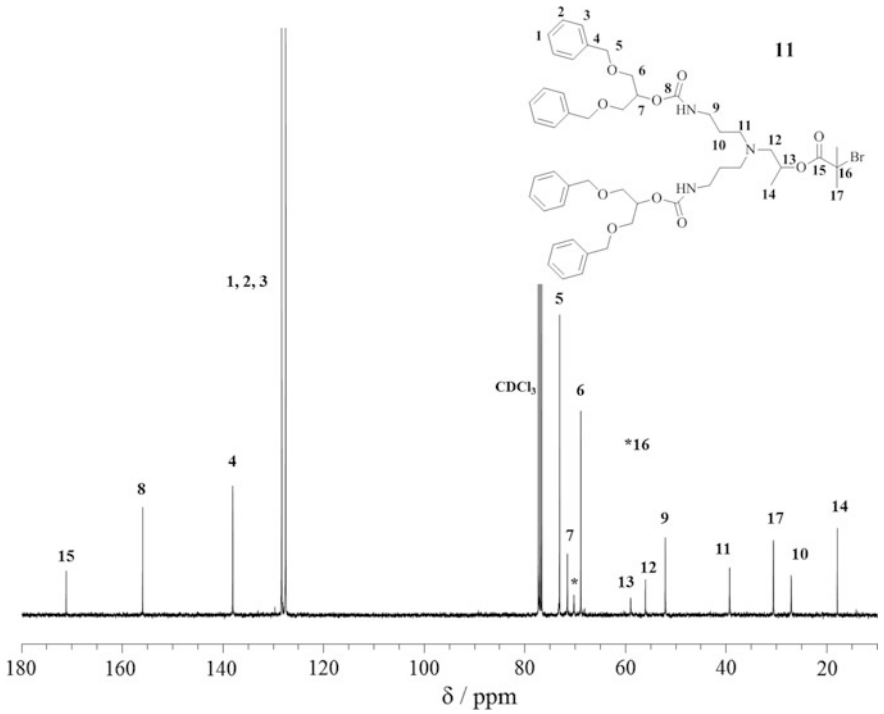

Fig. 4.2 ^{13}C NMR ($CDCl_3$, 100 MHz) of **G2′** dendron, **11**

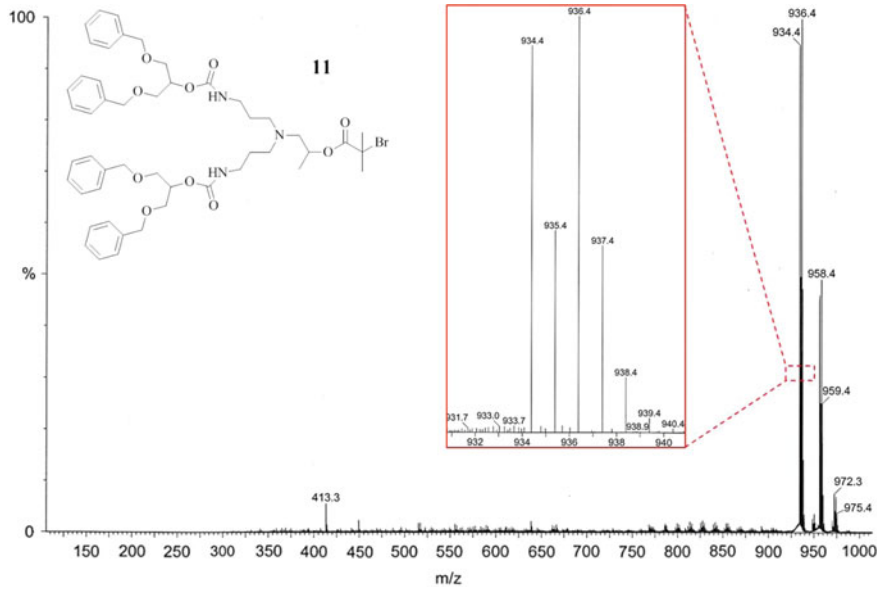

Fig. 4.3 Mass spectrum (ES-MS) of **G2′** dendron initiator, **11**, including the $[M + H]^+$ peak enlarged to see the bromine isotope pattern

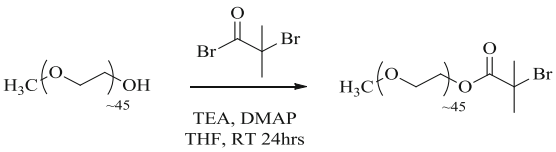

Scheme 4.2 **2000PEG** macroinitiator synthesis

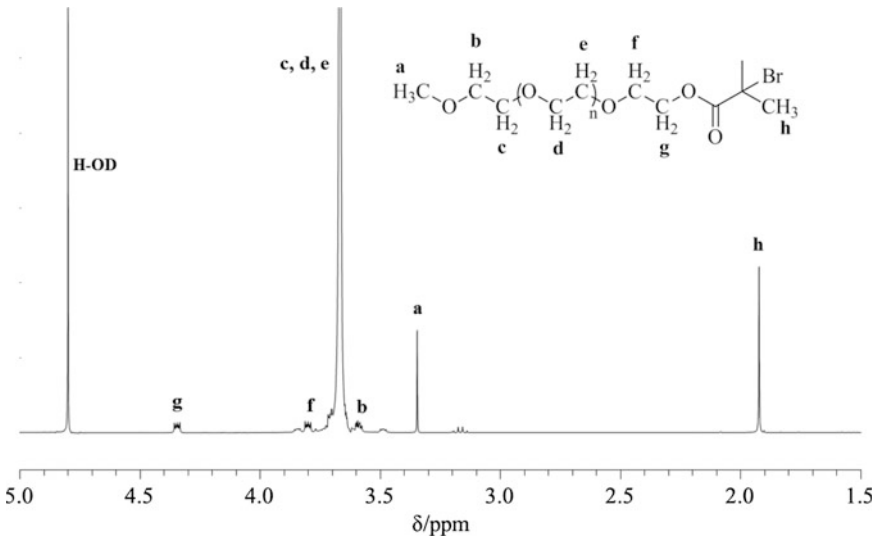

Fig. 4.4 ^{1}H NMR (D_2O, 400 MHz) of **2000PEG** macroinitiator with major peaks assigned (n = 43)

petroleum ether (30–40 °C). The ^{1}H NMR spectrum can be seen in Fig. 4.4 below and mass spectrometric analysis by MALDI-TOF is shown in the Appendix, Fig. A.29.

4.3 Polymer Synthesis

The new **G2′** dendron initiator and **2000PEG** macroinitiator were used to initiate the polymerisation of pHPMA via ATRP with a targeted number average degree of polymerisation (DP_n) of 20, 50 and 100 monomer units. The reactions were carried out in methanol at 30 ºC at 50 wt%, with respect to monomer, employing the CuCl: bpy catalytic system (1:2). Kinetic experiments were conducted to ensure that the behaviour of this new **G2′** dendron initiator was consistent with that of the previous **G2** dendron initiator (used in Chaps. 2 and 3), and that the **2000PEG** macroinitiator was also suitable as an initiator for the polymerisation. The inclusion of a divinyl

monomer, EGDMA, afforded branched polymers with high molecular weights and broad polydispersities as previously reported in the literature [7, 8] and previous chapters (see Chaps. 2 and 3). It is worth noting that due to the increased PEG length present in the polymers synthesised in this chapter, analysis by GPC was conducted using a GPC with a different eluent from Chaps. 2 and 3 (used THF GPC). Here the GPC eluent used was dimethylformamide (DMF) at 60 °C with 0. 01 M LiBr, utilising triple detection.

4.3.1 Linear Polymer Synthesis

Linear polymers were produced using both the initiators described with targeted DP_n of 20, 50 and 100 monomer units. The molecular weights and dispersities of these polymers are shown in Table 4.1, with the reaction times and monomer conversions reached.

The RI GPC chromatogram overlays for each **G2′** dendron initiated linear-dendritic polymer synthesised are shown in Fig. 4.5a. The GPC analysis shows that each linear-dendritic polymer was monomodal as expected, however, a slight shoulder at higher molecular weight was observed. This shoulder could be due to either termination by combination or disproportionation which can occur in radical polymerisations [9], or due to a dimethacrylate impurity which is present in low amounts in the HPMA monomer as supplied [10]. Figure 4.5b shows the linear polymers produced by the linear polymerisations of HPMA utilising the **2000PEG** macroinitiator. These polymers can be described as amphiphilic block copolymers [11] due to the **2000PEG** macroinitiator being a hydrophilic polymer and the pHPMA block being hydrophobic. For each amphiphilic block copolymer produced a monomodal peak is observed, however, a slight shoulder at high molecular weight is also observed, and most pronounced in the **2000PEG**-$pHPMA_{50}$ sample.

Table 4.1 Molecular weights and dispersities of **G2′** dendron initiated linear-dendritic polymers and 2000PEG initiated diblock copolymers

Target polymer composition	Reaction time (h)	Conv (%)[a]	GPC[b]		
			M_n ($gmol^{-1}$)	M_w ($gmol^{-1}$)	Đ
G2′-$pHPMA_{20}$	6	99.5	7,000	8,900	1.26
G2′-$pHPMA_{50}$	7	93.6	12,300	15,500	1.26
G2′-$pHPMA_{100}$	24	96.5	28,500	40,400	1.42
2000PEG-$pHPMA_{20}$	6	99.4	5,900	7,900	1.34
2000PEG-$pHPMA_{50}$	21	99.6	13,000	17,800	1.37
2000PEG-$pHPMA^{c}_{100}$	22	99.2	22,400	27,800	1.24

[a]Determined by ^{1}H NMR analysis in d_6-DMSO
[b]Analysed using triple detection with the DMF GPC
[c]Synthesised using purified HPMA

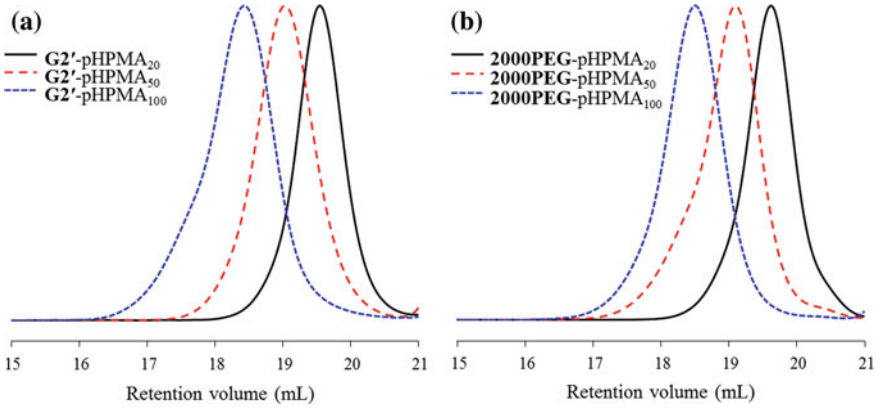

Fig. 4.5 GPC chromatogram overlays of the refractive index (RI) traces of **a G2′**-pHPMA$_{20}$, **G2′**-pHPMA$_{50}$, **G2′**-pHPMA$_{100}$ and **b 2000PEG**-pHPMA$_{20}$, **2000PEG**-pHPMA$_{50}$, **2000PEG**-pHPMA$_{100}$

4.3.2 Branched Polymer Synthesis

The two initiators chosen for study in this chapter were used to synthesise branched pHPMA to produce three *hyp*-polydendrons when the **G2′** dendron was used and three amphiphilic branched block copolymers (*hyp*-block copolymers) when the **2000PEG** initiator was used. The molecular weights and dispersities of these polymers are shown in Table 4.2, with the linear equivalent polymers included for easy comparison.

Analysis of each of the *hyp*-polydendrons and *hyp*-block copolymers by GPC shows that with the inclusion of EGDMA, high molecular weight polymeric species were formed with broader dispersities than the linear polymer equivalents. Figure 4.6 highlights each targeted DP_n linear and branched polymer chromatograms shown in Table 4.2. Figure 4.6a shows the RI chromatogram overlays for the **G2′** initiated linear-dendritic polymers and *hyp*-polydendrons, with the RALS chromatograms shown in Fig. 4.6b. The *hyp*-polydendrons elute at much lower retention volumes (between 12 and 13 mL) than the linear equivalents, which do not elute until around 16–18 mL. The *hyp*-polydendron peaks in both the RI and RALS chromatograms are much broader than the linear-dendritic polymers.

The RI and RALS chromatogram overlays of the **2000PEG** initiated linear and branched block copolymers are shown in Fig. 4.6c, d respectively. The *hyp*-block copolymers eluted at a much lower retention volumes (13–15 mL) than the linear block copolymers (17–19 mL), indicating high molecular weight polymer species are present. The branched polymers also have much broader dispersities than the linear equivalents.

Table 4.2 Molecular weights and dispersities of **G2′** dendron initiated and **2000PEG** initiated linear and branched polymers

Target polymer composition	Reaction time (h)	Conv (%)[a]	GPC[b]		
			M_n ($gmol^{-1}$)	M_w ($gmol^{-1}$)	Đ
G2′-pHPMA$_{20}$	6	99.5	7,000	8,900	1.26
G2′-pHPMA$_{50}$	7	93.6	12,300	15,500	1.26
G2′-pHPMA$_{100}$	24	96.5	28,500	40,400	1.42
G2′-pHPMA$_{20}$-EGDMA$_{0.8}$	18	>99	66,544	1,296,000	19.5
G2′-pHPMA$_{50}$-EGDMA$_{0.8}$	20	99.4	193,600	2,225,000	11.5
G2′-pHPMA$_{100}$-EGDMA$_{0.8}$	30	96.1	124,650	1,936,000	15.5
2000PEG-pHPMA$_{20}$	6	99.4	5,873	7,842	1.34
2000PEG-pHPMA$_{50}$	21	99.6	13,000	17,800	1.37
2000PEG-pHPMA$_{100}$[c]	22	99.2	22,400	27,800	1.24
2000PEG-pHPMA$_{20}$-EGDMA$_{0.8}$	6	>99	14,483	138,437	9.56
2000PEG-pHPMA$_{50}$-EGDMA$_{0.95}$	20	99.5	32,200	477,000	14.8
2000PEG-pHPMA$_{100}$-EGDMA$_{0.8}$	24	98.2	53,850	335,300	6.23

[a]Determined by ^{1}H NMR analysis in d_6-DMSO
[b]Analysed using triple detection with the DMF GPC
[c]Synthesised using purified HPMA

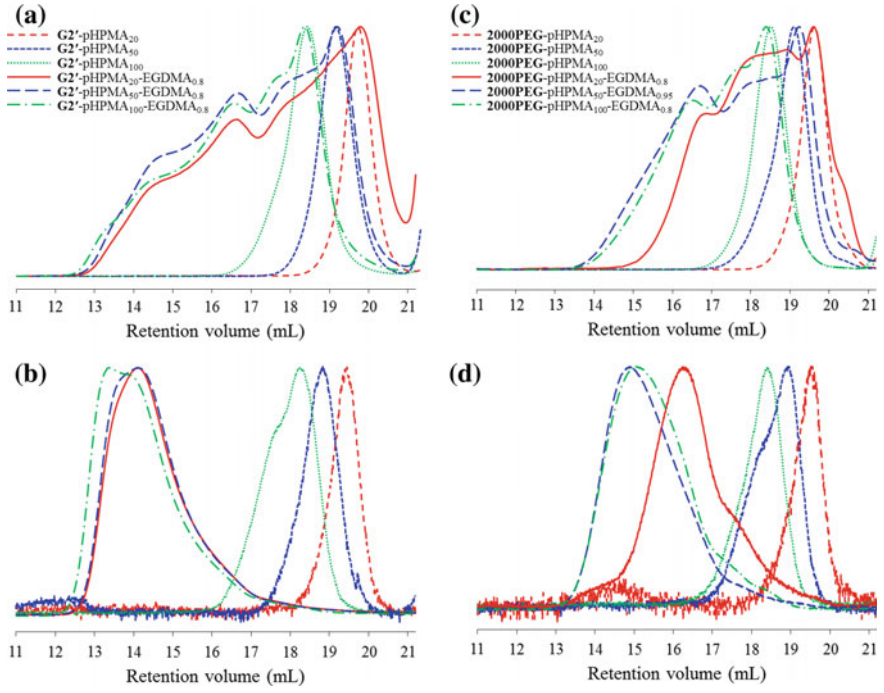

Fig. 4.6 GPC chromatogram overlays of **G2′** initiated polymers: **a** RI traces and **b** RALS traces. **2000PEG** initiated polymers: **c** RI traces and **d** RALS traces

4.3.3 Kinetic Experiments

Initially kinetic studies were conducted utilising the **2000PEG** initiator for both linear and branched polymerisations with targeted DP_n of 20, 50 and 100 monomer units. As expected, and previously reported [12], when targeting lower DP_n the time required to reach 100 % conversion is reduced. The DP_{20} polymerisations (Fig. 4.7) reached 99 % conversion within 4 h reaction time, whereas the DP_{50} polymerisations (Fig. 4.8) had reached 87–88 % (the linear was 87 % and branched was 88 %) and the DP_{100} polymerisations (Fig. 4.9) had only reached 73 % for the linear and 62 % conversion for the branched polymerisation after 4 h reaction time.

The linear and branched DP_{20} kinetic studies (Fig. 4.7) both show that the polymerisations proceed with first order kinetics, with respect to the monomer, as the $\ln([M]_0/[M])$ versus time plots for both the linear (Fig. 4.7a) and the branched (Fig. 4.7c) follow a linear relationship. Comparing the evolution of molecular weight, the M_n increased linearly with conversion for the linear polymerisation (Fig. 4.7b), whereas with the incorporation of divinyl monomer in the branched polymerisation (Fig. 4.7d) the M_n and M_w increased rapidly over ~80 % conversion. The dispersity observed for the linear experiment showed initially a value of 1.26 at 67 % conversion which reduced to 1.14 at high conversion (>99 %).

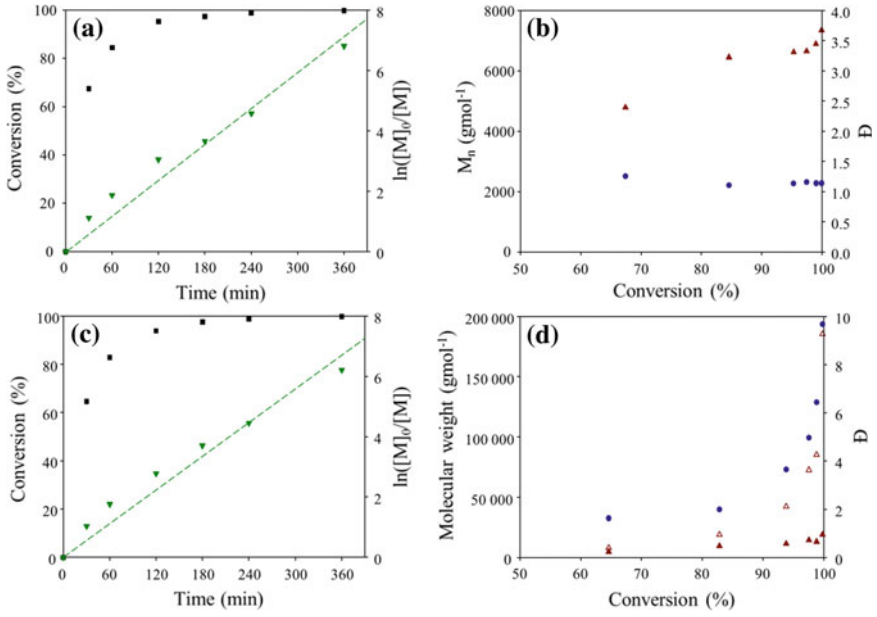

Fig. 4.7 Kinetic plots for the **2000PEG** initiated linear and branched DP_{20} polymerisations. **a** and **b** **2000PEG**-pHPMA$_{20}$, **c** and **d** **2000PEG**-pHPMA$_{20}$-EGDMA$_{0.95}$. Conversion (*black squares*) and $\ln([M]_0/[M])$ (*green down triangles*), M_n (*red up triangles*), M_w (*red empty up triangles*) and Đ (*blue circles*)

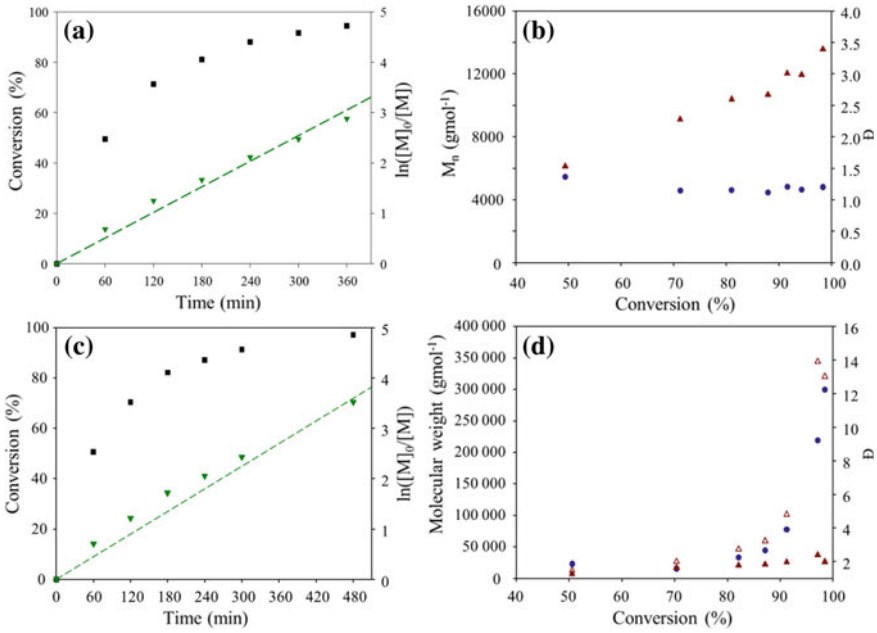

Fig. 4.8 Kinetic plots for the **2000PEG** initiated linear and branched DP_{50} polymerisations. **a** and **b** **2000PEG**-pHPMA$_{50}$, **c** and **d** **2000PEG**-pHPMA$_{50}$-EGDMA$_{0.95}$. Conversion (*black squares*) and ln($[M]_0$/[M]) (*green down triangles*), M_n (*red up triangles*), M_w (*red empty up triangles*) and Đ (*blue circles*)

Đ was measured as 1.6 at 65 % conversion for the branched polymerisation and increased up to 9.7 at high conversion (>99 %).

Similar results were also observed when the DP_{50} linear and branched polymerisation kinetics were studied. The conversion versus time and ln($[M]_0$/[M]) versus time plots (Fig. 4.8a for linear and Fig. 4.8c for the branched) are both very similar, showing that first order kinetics were observed. The M_n of the linear polymer increased in a linear fashion with increasing conversion (see Fig. 4.8b) and the dispersities remained below 1.5 throughout. The branched polymerisation showed a steep increase in M_n, M_w and Đ when conversion reached >80 % conversion (see Fig. 4.8d).

The linear DP_{100} polymerisation showed a possible decrease in propagating radical concentration over the course of the reaction. This is indicated by the ln ($[M]_0$/[M]) versus time plots deviating from linearity as time progressed, see Fig. 4.9a. This loss of propagating radicals did not appear to affect the control of the polymerisation as the dispersities remained low, between 1.12 and 1.22 throughout the experiment, and the increase in M_n was relatively linear with increasing conversion (Fig. 4.9b). The branched DP_{100} also showed a possible decrease in propagating radicals due to the non-linear semi-logarithmic plot, Fig. 4.10c. The M_n

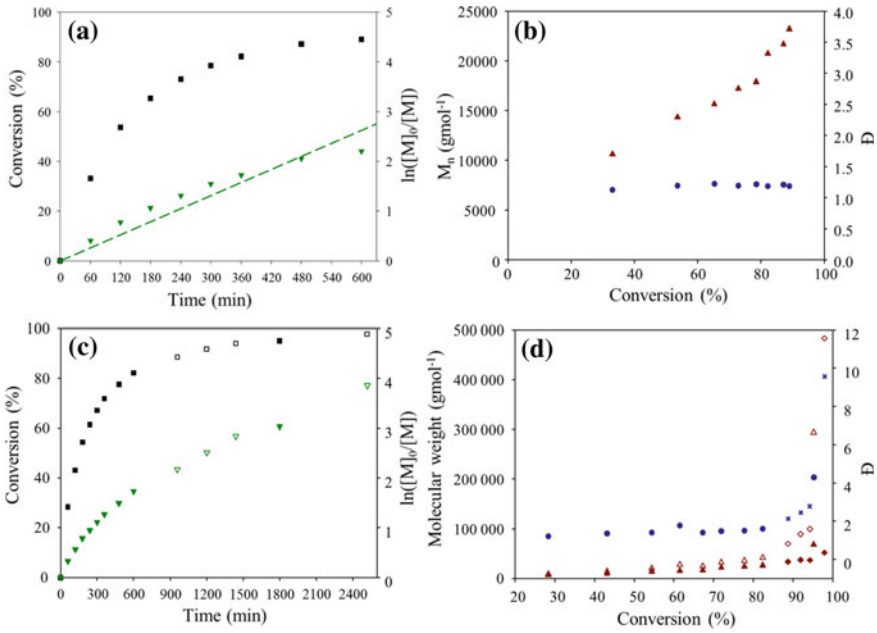

Fig. 4.9 Kinetic plots for the **2000PEG** initiated linear and branched DP_{100} polymerisations. **a** and **b** **2000PEG**-pHPMA$_{100}$, **c** and **d** **2000PEG**-pHPMA$_{100}$-EGDMA$_{0.8}$. Conversion (*black squares*) and $\ln([M]_0/[M])$ (*green down triangles*), M_n (*red up triangles*), M_w (*red empty up triangles*) and **d** (*blue circles*). The **2000PEG**-pHPMA$_{100}$-EGDMA$_{0.8}$ repeat experiment (**c**); conversion (*black empty squares*), $\ln([M]_0/[M])$ (*green empty triangles*), and **d**; M_n (*red diamonds*), M_w (*red empty diamonds*) and Đ (*blue crosses*)

and M_w increased relatively linearly up to ~80 % conversion, where they increased steeply, which was also observed for the dispersity. Two different reactions which were set up for the polymerisation of the **2000PEG**-pHPMA$_{100}$-EGDMA$_{0.8}$ branched polymer (see Fig. 4.9c, d) so as to collect complete data between 90 and 98 % conversion. The two experiments were prepared under the same conditions and as the data points fit well between the two experiments it was deemed appropriate to plots the data sets on the same graphs. The apparent loss in propagating radicals in both DP_{100} polymerisations was probably due to the rate of propagation being lower than for the DP_{50} and DP_{20} polymerisations and, therefore, the rate of termination was not negligible as is required for first order kinetics in ATRP. The termination may be caused by unwanted side reactions of propagating radicals with other radical species (radical-radical coupling), impurities in the reaction such as oxygen or the solvent.

To ensure that the new **G2′** dendron initiator would yield similar kinetic profiles as the previously discussed **G2** dendron (see Chap. 2, Sect. 2.4), firstly kinetic studies were conducted on the DP_{20} linear and branched polymerisations, Fig. 4.10.

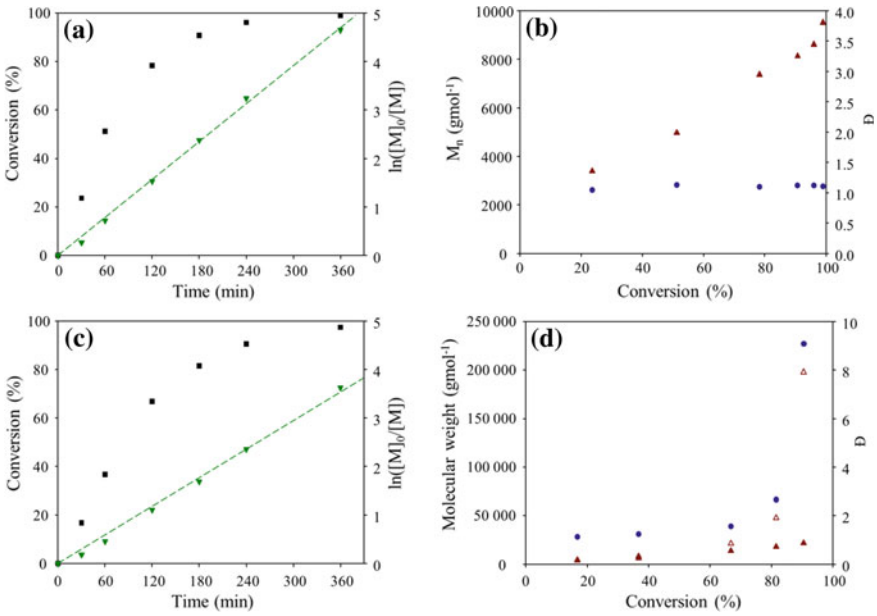

Fig. 4.10 Kinetic plots for the **G2′** initiated linear and branched DP_{20} polymerisations. **a** and **b** **G2′**-pHPMA$_{20}$, **c** and **d** **G2′**-pHPMA$_{20}$-EGDMA$_{0.8}$. Conversion (*black squares*) and ln ($[M]_0/[M]$) (*green down triangles*), M_n (*red up triangles*), M_w (*red empty up triangles*) and Đ (*blue circles*)

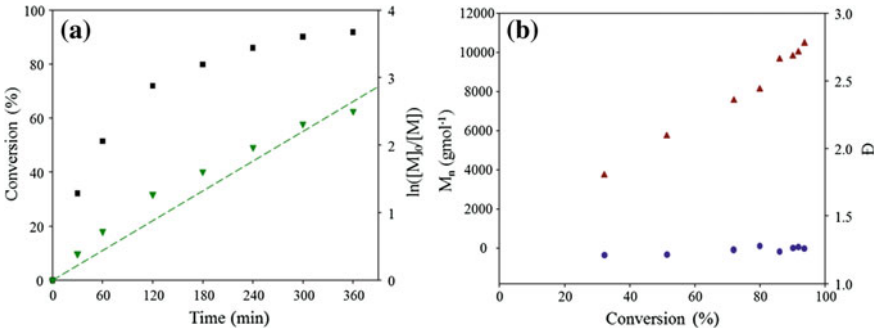

Fig. 4.11 Kinetic plots for **G2′**-pHPMA$_{50}$ polymerisation. Conversion (*black squares*) and ln ($[M]_0/[M]$) (*green down triangles*), M_n (*red up triangles*), and Đ (*blue circles*)

The conversion versus time and semi-logarithmic plots for the linear (Fig. 4.10a) and branched (Fig. 4.10c) polymerisation show that high conversion (>97 %) was reached within 6 h of reaction and that the polymerisations both followed first order

kinetics. The linear polymerisation showed a linear increase in M_n with increasing conversion, as expected, and dispersities below 1.13. The M_n and M_w for the branched polymerisation increased linearly up to approximately 70 % conversion where a moderate increase in M_n was observed and a steep increase in M_w and Đ was observed (Fig. 4.10b, d).

These kinetic experiments indicated that the new **G2′** dendron initiator was indeed suitable for use in polymerisations, however, in Chap. 2 the kinetic experiments conducted were with DP_{50} polymerisations and, therefore, to draw a direct comparison of the kinetics a DP_{50} polymerisation was conducted with the **G2′** dendron initiator for the linear polymerisation, see Fig. 4.11.

The $\ln([M]_0/[M])$ versus time plots shows that the polymerisation followed first order kinetics, as previously observed. The evolution of M_n with conversion was linear and the dispersity remained low throughout the reaction, between 1.21 and 1.27. Therefore the **G2′** dendron initiator was used in further polymerisations.

The kinetic evaluation of the **G2′** dendron initiator was sufficient to warrant the use of it in place of the previously described **G2** dendron initiator. Further kinetic studies were not required, and were not conducted to preserve the **G2′** dendron initiator for subsequent mixed initiator polymerisations.

4.3.4 Mixed Initiator Polymerisations

Similar to the series of *hyp*-polydendrons described in Chap. 3 (**G2** dendron and **750PEG** mixed initiator system), this chapter describes the mixed initiator system utilising the new **G2′** dendron initiator and **2000PEG** macroinitiator in various ratios. This approach was utilised to produce a series of DP_{20}, DP_{50} and DP_{100} polymers, ranging from 100:0, 90:10, 75:25, 50:50, 25:75, 10:90 and 0:100 % **G2′**:**2000PEG** initiators. The molecular weights and dispersities of all these *hyp*-polydendrons, and in the case of 100 % **2000PEG** initiated; *hyp*-block copolymers, are shown in Table 4.3 with the reaction times and monomer conversion reached. The final polymer GPC chromatogram overlays are shown in Fig. 4.12 for selected entries in Table 4.3.

Various ratios of EGDMA were used with each initiator ratio in the DP_{50} series (Table 4.3, entries 10–20) initially to determine the highest amount of EGDMA that could be used to produce high molecular weight soluble branched polymers. Therefore the DP_{50} series of mixed initiator *hyp*-polydendrons contained varying amounts of EGDMA. The 100 % **G2′** initiated *hyp*-polydendron contained an initiator:brancher ratio of 1:0.8, whereas the 100 % **2000PEG** initiated branched polymer contained 1:0.95 initiator:brancher. Therefore, with increasing **2000PEG** content, more EGDMA could be incorporated into the polymerisation before gelation would occur. This trend agrees with the observation in Chap. 3 that with increasing the percentage of the **750PEG** macroinitiator to **G2** dendron initiator,

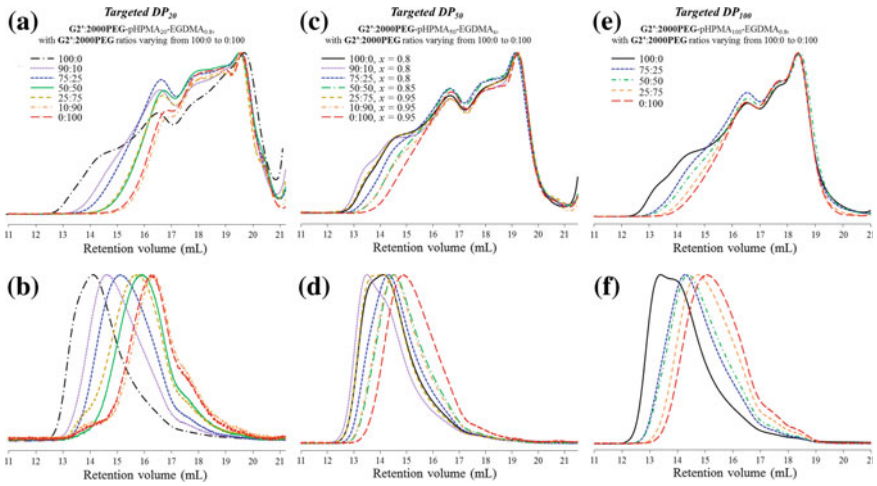

Fig. 4.12 GPC chromatogram overlays of mixed initiator branched polymers. **G2′:2000PEG**-pHPMA$_{20}$-EGDMA$_{0.8}$: **a** RI traces and **b** RALS traces. **G2′:2000PEG**-pHPMA$_{50}$-EGDMA$_x$: **c** RI traces and **d** RALS traces. **G2′:2000PEG**-pHPMA$_{100}$-EGDMA$_{0.8}$: **e** RI traces and **f** RALS traces

and maintaining the same level of EGDMA, the molecular weights obtained decreased. This was thought to be due to the initiator efficiency of the **750PEG** initiator being higher than the **G2** dendron initiator. As various ratios of EGDMA were used in the polymerisation, samples were selected for further study based on the molecular weights and a preliminary study of their nanoprecipitation (see below, Sect. 4.4). Therefore entry numbers 10–16 in Table 4.3 were used for further studies in this chapter, and the GPC chromatograms for these polymers are shown in Fig. 4.12; Fig. 4.12c shows the RI chromatogram overlays and Fig. 4.12d shows the RALS chromatogram overlays. The *hyp*-polydendrons from the DP_{50} series which were not used for further study include entries 17–20. The RI and RALS GPC chromatograms for each of these samples are shown in the Appendix (Fig. A.30c–f).

When the DP_{20} and DP_{100} series were synthesised, the ratio of initiator:brancher was maintained at 1:0.8 to ascertain whether or not the previous trend, described above, was still applicable in the **G2′:2000PEG** series of *hyp*-polydendrons. In the case of the DP_{20} series with an initiator:brancher ratio 1:0.8 (Table 4.3, entries 1–7), the same general trend is observed, with increasing the percentage of **2000PEG** initiator the molecular weights and dispersities decrease, from: M_n = 66,500 gmol^{-1}, M_w = 1,296,000 gmol^{-1} and Đ = 19.48 with the **G2′**-pHPMA$_{20}$-EGDMA$_{0.8}$, to: M_n = 14,500 gmol^{-1}, M_w = 138,400 gmol^{-1} and Đ = 9.56 for the **2000PEG**-pHPMA$_{20}$-EGDMA$_{0.8}$. The GPC chromatograms for these samples are shown in Fig. 4.12a, b. The RI chromatogram overlays are shown in Fig. 4.12a and the RALS chromatogram overlays in Fig. 4.12b. Two further polymerisations were conducted with higher levels of EGDMA to show that this

Table 4.3 Molecular weights and dispersities of **G2′**:**2000PEG** *hyp*-polydendron and *hyp*-block copolymers produced

Entry no.	Initiator (%)		Target polymer composition	Reaction time (h)	Conv (%)[a]	GPC[b]		
	G2′ dendron	**2000PEG**				M_n	M_w	Đ
1	100	0	$pHPMA_{20}$-$EGDMA_{0.8}$	18	>99	66,500	1,296,000	19.5
2	90	10	$pHPMA_{20}$-$EGDMA_{0.8}$	5	98.2	25,800	557,600	21.6
3	75	25	$pHPMA_{20}$-$EGDMA_{0.8}$	5	98.6	22,200	364,600	16.4
4	50	50	$pHPMA_{20}$-$EGDMA_{0.8}$	6	99.7	13,700	190,700	14.0
5	25	75	$pHPMA_{20}$-$EGDMA_{0.8}$	24	>99	24,800	263,000	10.6
6	10	90	$pHPMA_{20}$-$EGDMA_{0.8}$	24	>99	15,300	115,600	7.54
7	0	100	$pHPMA_{20}$-$EGDMA_{0.8}$	6	>99	14,500	138,400	9.56
8	50	50	$pHPMA_{20}$-$EGDMA_{0.85}$	6	>99	141,700	3,236,000	22.8
9	0	100	$pHPMA_{20}$-$EGDMA_{0.95}$	18	>99	81,700	1,607,000	19.7
10	100	0	$pHPMA_{50}$-$EGDMA_{0.80}$	20	99.4	193,600	2,225,000	11.5
11	90	10	$pHPMA_{50}$-$EGDMA_{0.80}$	17	98.8	348,000	2,464,000	7.08
12	75	25	$pHPMA_{50}$-$EGDMA_{0.80}$	17	99.4	55,000	1,067,000	19.4
13	50	50	$pHPMA_{50}$-$EGDMA_{0.85}$	19	99.7	29,400	709,200	24.2
14	25	75	$pHPMA_{50}$-$EGDMA_{0.95}$	20	99.7	141,300	1,862,000	13.2
15	10	90	$pHPMA_{50}$-$EGDMA_{0.95}$	20	99.7	40,200	795,300	19.8
16	0	100	$pHPMA_{50}$-$EGDMA_{0.95}$	20	99.5	32,200	477,000	14.8
17	75	25	$pHPMA_{50}$-$EGDMA_{0.85}$	19	99.2	129,500	1,809,000	14.0
18	50	50	$pHPMA_{50}$-$EGDMA_{0.90}$	19	99.5	70,800	1,135,000	16.0
19	25	75	$pHPMA_{50}$-$EGDMA_{0.90}$	20	99.9	78,800	1,211,000	15.4
20	10	90	$pHPMA_{50}$-$EGDMA_{0.90}$	20	99.8	26,100	428,800	16.4
21	100	0	$pHPMA_{100}$-$EGDMA_{0.8}$	30	96.1	124,650	1,936,000	15.5

(continued)

Table 4.3 (continued)

Entry no.	Initiator (%)		Target polymer composition	Reaction time (h)	Conv (%)[a]	GPC[b]		
	G2′ dendron	**2000PEG**				M_n	M_w	Đ
22	75	25	$pHPMA_{100}$-$EGDMA_{0.8}$	29	95.9	71,800	838,700	11.7
23	50	50	$pHPMA_{100}$-$EGDMA_{0.8}$	28	98.0	58,300	511,050	8.77
24	25	75	$pHPMA_{100}$-$EGDMA_{0.8}$	24	97.5	54,800	443,150	8.09
25	0	100	$pHPMA_{100}$-$EGDMA_{0.8}$	24	98.2	53,850	335,300	6.23

[a]Determined by ^{1}H NMR analysis in d_6-DMSO

[b]Analysed using triple detection with the DMF GPC

would increase the resultant molecular weights of the polymers. **G2′**:**2000PEG**-50:50-pHPMA$_{20}$-EGDMA$_{0.85}$ (Table 4.3, entry 8) and **G2′**:**2000PEG**-0:100-pHPMA$_{20}$-EGDMA$_{0.95}$ (Table 4.3, entry 9) were also synthesised and both showed much higher molecular weights and dispersities than the equivalent polymer with an initiator:brancher ratio of 1:0.8. The RI and RALS GPC chromatogram overlays for these two polymers are shown in the Appendix Fig. A.30a, b.

The DP$_{100}$ series (Table 4.3, entries 21–25) was synthesised with only the 100:0, 75:25, 50:50, 25:75 and 0:100 ratios of initiators, the 90:10 and 10:90 were not synthesised to conserve **G2′** dendron material. Again the molecular weights and dispersities decrease with increasing levels of **2000PEG** initiator. As the reaction times required for high conversion (>98 %) were much longer for the targeted DP$_{100}$ polymers, they were polymerised ensuring that a conversion >95 % was achieved in each case. The GPC chromatograms for these polymers are shown in Fig. 4.12e, f, with the RI chromatogram overlays (Fig. 4.12e) and RALS chromatogram overlays (Fig. 4.12f).

It was clear from the GPC chromatograms that high molecular weight polymer species had been synthesised due to the elution of polymeric species at low retention volumes (between 12 and 15 mL) whereas, even in the case of the DP$_{100}$ linear polymers, elution was not observed until after a retention volume of 16 mL. Entries 1–7, 10–16 and 22–26 of Table 4.3 were investigated further for their behaviour under nanoprecipitation conditions.

Analysis of the **G2′**:**2000PEG** series of *hyp*-polydendrons by ^{1}H NMR spectroscopy is discussed in Chap. 5 (see Sect. 5.2.2).

4.4 Nanoprecipitation of G2′ and 2000PEG Initiated Polymers

As previously described, nanoprecipitation is a facile method of preparing polymeric nanoparticles [13, 14] and has been employed here to produce nanoparticles with various dendron content. The nanoprecipitation of linear polymers and *hyp*-polydendrons synthesised in this chapter were studied and discussed below. The primary technique used for nanoparticle characterisation was DLS, as in Chaps. 2 and 3, to measure the D_z and PdI values of nanoparticle samples. SEM characterisation of selected nanoparticle samples was also conducted.

4.4.1 Linear Polymers for Nanoprecipitation

The linear polymers synthesised; **G2′**-pHPMA$_{20}$, **G2′**-pHPMA$_{50}$, **G2′**-pHPMA$_{100}$, **2000PEG**-pHPMA$_{20}$, **2000PEG**-pHPMA$_{50}$ and **2000PEG**-pHPMA$_{100}$ were subjected to nanoprecipitation from a good solvent (THF) into an anti-solvent for the

Table 4.4 DLS measurements for the linear polymer nanoprecipitations; **G2′**-pHPMA$_{20}$, **G2′**-pHPMA$_{50}$, **G2′**-pHPMA$_{100}$, **2000PEG**-pHPMA$_{20}$, **2000PEG**-pHPMA$_{50}$ and **2000PEG**-pHPMA$_{100}$

Initiator	Nanoprecipitation conditions			**DP$_{20}$**		**DP$_{50}$**		**DP$_{100}$**	
	i_x (mg/mL)	f_y (mg/mL)	*df*	D_z (nm)	PdI	D_z (nm)	PdI	D_z (nm)	PdI
G2′ dendron	25	5	0.2	354	0.192	280	0.222	151	0.153
	10	2	0.2	540	0.392	–	–	–	–
	5	1	0.2	204	0.164	882	0.241	250	0.035
	1	0.2	0.2	151	0.116	170	0.187	870	0.625
	25	0.25	0.01	191	0.097	496	0.224	310	0.154
	10	0.1	0.01	406	0.185	238	0.036	257	0.128
	5	0.05	0.01	161	0.090	228	0.036	208	0.038
	1	0.01	0.01	179	0.035	179	0.061	282	0.156
2K PEG	25	5	0.2	*	*	32	0.123	712	0.221
	10	2	0.2	47	0.396	48	0.286	336	0.130
	5	1	0.2	*	*	56	0.423	267	0.112
	1	0.2	0.2	*	*	96	0.491	179	0.190
	25	0.25	0.01	*	*	42	0.389	139	0.183
	10	0.1	0.01	*	*	*	*	101	0.127
	5	0.05	0.01	*	*	*	*	79	0.135
	1	0.01	0.01	*	*	*	*	130	0.276

Not suitable for measurement by DLS due to '–' precipitation or '*' lack of scattering/high polydispersity, i_x Initial concentration, f_y Final concentration, *df* Dilution factor

G2′ dendron and pHPMA chain (water). Starting concentrations of 25, 10, 5 and 1 mg/mL were chosen for the study using two different *df* (0.2 and 0.01), see Table 4.4.

When using the linear-dendritic polymers (**G2′** initiated) for nanoprecipitations, nanoparticles were generally formed, except for the $\boldsymbol{i_{10}\text{-}f_2}$ for both the DP$_{50}$ and DP$_{100}$ polymers, as they precipitated out of the solution and no DLS measurement could be taken. With each of the linear-dendritic polymers, generally, narrower dispersities were observed at lower concentration and under more dilute nanoprecipitation conditions. DLS size distribution by intensity traces for selected nanoprecipitations are shown in Fig. 4.13. Figure 4.13a, c, e show the DLS traces for the linear-dendritic nanoprecipitations with $\boldsymbol{i_5\text{-}f_1}$, $\boldsymbol{i_{25}\text{-}f_5}$ and $\boldsymbol{i_5\text{-}f_{0.05}}$ respectively. Most of the samples contained a monomodal distribution of particles, however, most of the PdI values were higher than 0.1 (see Table 4.4) except for the $\boldsymbol{i_5\text{-}f_{0.05}}$ nanoprecipitations which produced nanoparticles with a narrow polydispersities: 0.090, 0.036 and 0.038 for **G2′**-pHPMA$_{20}$ (160 nm), **G2′**-pHPMA$_{50}$ (228 nm) and **G2′**-pHPMA$_{100}$ (208 nm) respectively.

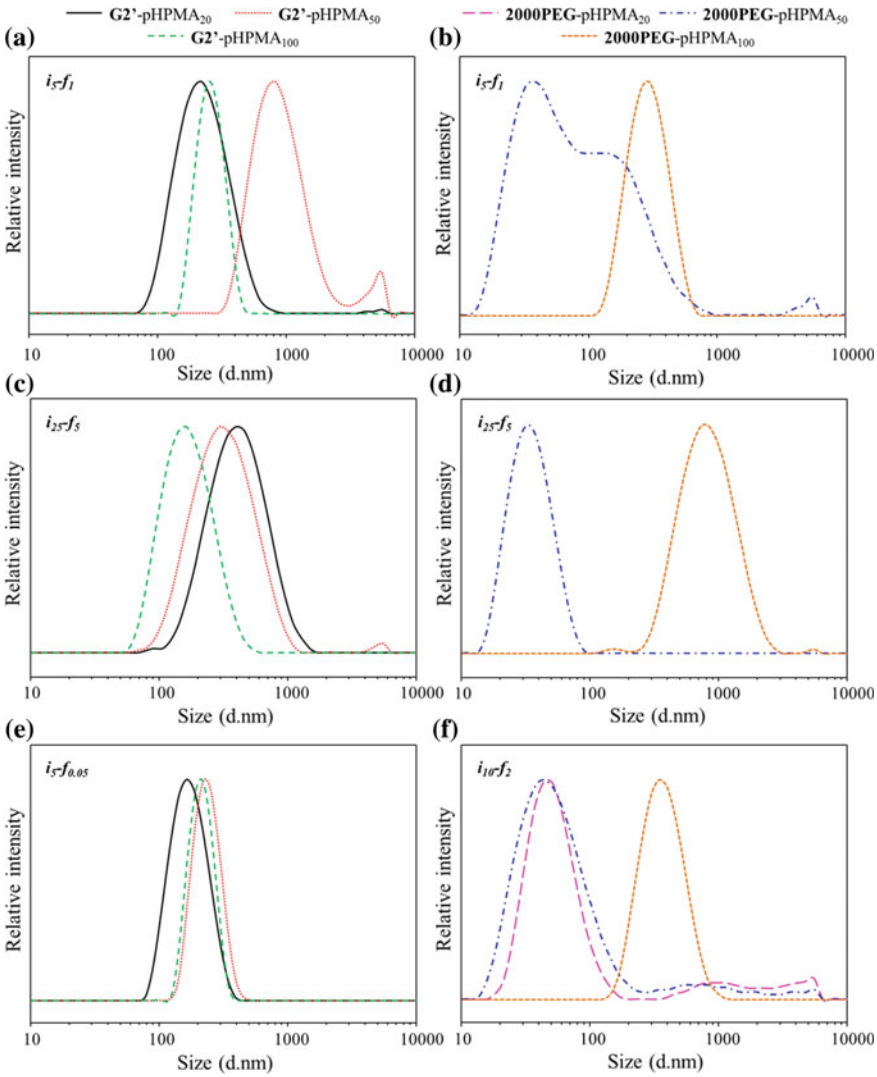

Fig. 4.13 DLS size distribution by intensity traces for nanoprecipitations; i_5-f_1: **a G2′** linear-dendritic polymers, **b 2000PEG** block copolymers, i_{25}-f_5: **c G2′** linear-dendritic polymers, **d 2000PEG** block copolymers and **e** i_5-$f_{0.05}$ **G2′** linear-dendritic polymers and **f** i_{10}-f_2 **2000PEG** block copolymers

The nanoprecipitations of the **2000PEG**-pHPMA$_n$ polymers were expected to differ from the linear-dendritic polymers as they were amphiphilic diblock copolymers and the opportunity for micelle formation is present [15]. When the hydrophobic polymer chain was pHPMA$_{20}$ only one of the samples prepared could be analysed via DLS. This was probably because the polymer was too water-soluble

and, therefore, produced very little light scattering for detection by DLS. Only with the sample prepared at $\boldsymbol{i_{10}\text{-}f_2}$ was analysis by DLS possible which gave a D_z of 47 nm and a PdI of 0.396, which suggests micelles were present. The more dilute samples which failed measurement showed a high attenuator value and a lower count rate, implying that they were below the CMC of the polymer and present only as unimers. However, it was unclear why the more concentrated sample ($\boldsymbol{i_{25}\text{-}f_5}$) could not be accurately analysed as it did have an acceptable count rate; the sample may have had micelles present but was too polydisperse for adequate data collection and correlation to the DLS scattering model.

The **2000PEG**-pHPMA$_{50}$ polymers did form structures upon nanoprecipitation, possibly micelles, at final concentrations higher than 0.2 mg/mL, with D_z ranging from 32 to 96 nm and PdI values between 0.123 and 0.491. Interestingly, with increasing concentration and maintaining the *df* at 0.2, the D_z of the particles decreased, as did the dispersity. The **2000PEG**-pHPMA$_{100}$ polymer produced nanoparticles ranging from 79 to 712 nm with PdI values between 0.130 and 0.276. This huge range in particle diameters could possibly be due to different morphologies formed, for example, micelles and vesicles; however, possible vesicle formation was not investigated further.

Figure 4.13 highlights the DLS traces for some of the nanoprecipitations performed with the **2000PEG** block copolymers. Figure 4.13b, d, f show DLS traces for the block copolymer samples prepared using $\boldsymbol{i_5\text{-}f_1}$, $\boldsymbol{i_{25}\text{-}f_5}$ and $\boldsymbol{i_{10}\text{-}f_2}$ respectively.

4.4.2 Study of G2′:2000PEG-pHPMA$_{50}$-EGDMA$_x$ Materials

Following the nanoprecipitation studies performed in Chap. 3, the **G2′**:**2000PEG** DP$_{50}$ series was investigated utilising nanoprecipitation to assess whether the introduction of a longer stabilising hydrophilic PEG chain would achieve stability under physiologically relevant conditions, and if so, which combination of initiators within the mixed polymerisations would achieve such stability.

Firstly, two different good solvents for the nanoprecipitations were assessed maintaining one initial and final concentration, $\boldsymbol{i_5\text{-}f_1}$. THF and acetone were both chosen for the nanoprecipitations as THF had previously been used in Chaps. 2 and 3, whilst acetone was also a good solvent for the *hyp*-polydendrons and volatile, which is desirable for use in the nanoprecipitation technique. Figure 4.14 shows the D_z and PdI values observed for the $\boldsymbol{i_5\text{-}f_1}$ nanoprecipitations using THF and acetone as the good solvent (see Appendix, Table A.8). The diameters of the resulting nanoparticles formulated using acetone were generally larger than the corresponding from THF and had higher PdI values. The nanoprecipitation using the **G2′**-pHPMA$_{50}$-EGDMA$_{0.8}$ *hyp*-polydendron from acetone was not stable and precipitate was present in the sample. Therefore, THF was used as the solvent of choice for the nanoprecipitations. The *hyp*-polydendrons with high **2000PEG** content (>75 %) showed the least variation between the two solvents.

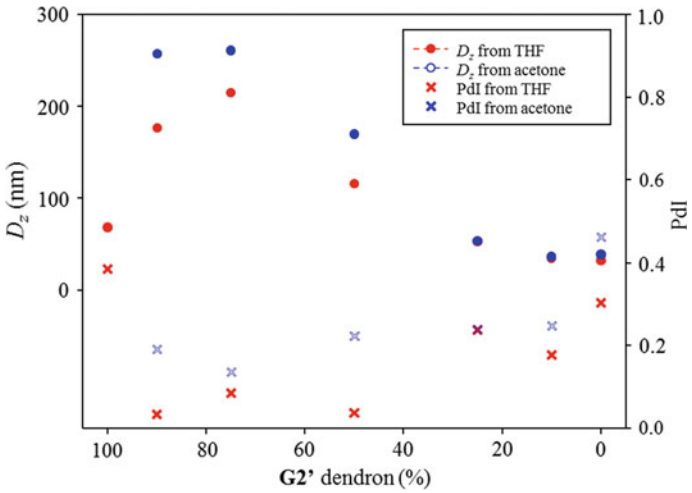

Fig. 4.14 D_z and PdI values for **G2′**:**2000PEG**-pHPMA$_{50}$-EGDMA$_x$ samples prepared with $\boldsymbol{i_5}$-$\boldsymbol{f_1}$ from THF and acetone as a function of **G2′** dendron content (%)

Further nanoprecipitations were performed using THF to study the scope of the nanoprecipitation methodology with these materials. Initial concentrations in THF studied were 50, 25, 10, 5 and 1 mg/mL with two different *df* (0.2 and 0.01) giving a series of nanoparticles with varying concentration and varying **G2′**:**2000PEG** functionality, see Table 4.5 for DLS measurements.

The data shows that perhaps the best nanoprecipitation conditions were those utilising $\boldsymbol{i_5}$-$\boldsymbol{f_1}$, $\boldsymbol{i_1}$-$\boldsymbol{f_{0.2}}$ and $\boldsymbol{i_{50}}$-$\boldsymbol{f_{0.5}}$ as the PdI values for these samples were generally lower than for other initial and final concentrations studied. The DLS size distribution by intensity traces for each polymer prepared under these nanoprecipitation conditions are shown in Fig. 4.15.

Each of the $\boldsymbol{i_5}$-$\boldsymbol{f_1}$ samples was prepared for imaging by SEM by dropping the sample on a silicon wafer mounted on an aluminium SEM stub with a carbon tab, and allowed to dry overnight at ambient temperature. Sputter coating was needed for imaging with Au at 20 mA for 2 min. SEM images are shown in Fig. 4.16.

It became apparent that for the 10:90 and 0:100 sample the resulting D_z and PdI of the particles were independent of the initial or final concentration. Across all the various nanoprecipitations the 10:90 particles were between 34 and 39 nm (D_z) with PdIs ranging from 0.175 to 0.301. The 0:100 particles had D_z of 29–34 nm and PdI values between 0.210 and 0.304. These observations did not agree with the nanoprecipitations previously studied (Chaps. 2 and 3) whereby the z-average diameter of nanoparticles usually increased with increasing the concentration of the initial polymer dissolved in good solvent. It was also observed that at low final concentrations (0.01–0.25 mg/mL, see Table 4.5) the resulting nanoparticle samples were not suitable for measurement by DLS. This was because of insufficient scattering for an accurate measurement, which is usually due to the sample being

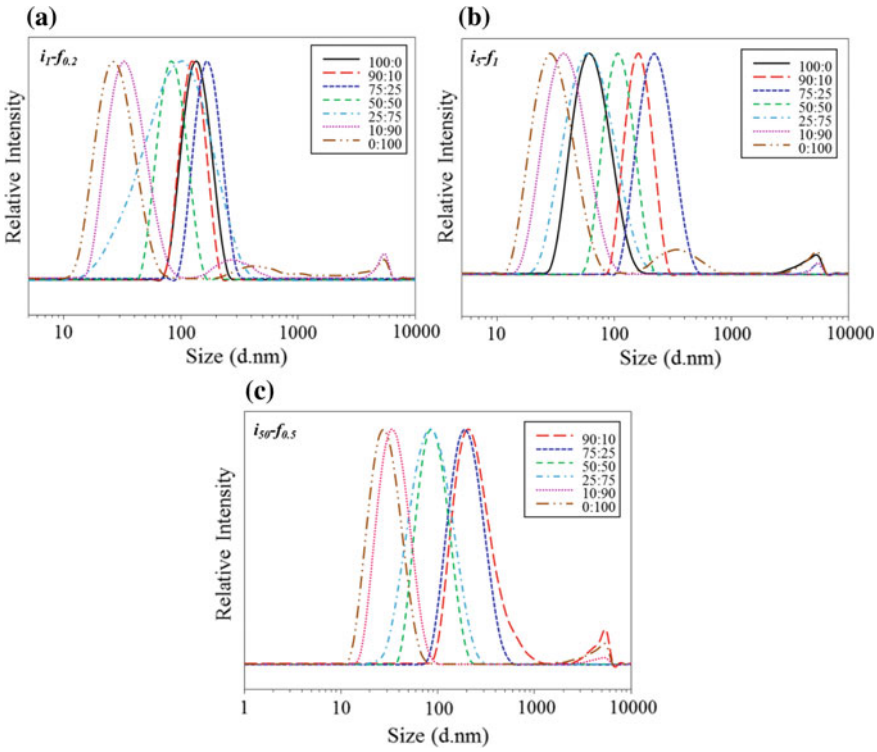

Fig. 4.15 DLS size distribution by intensity trace overlays for the **G2′**:**2000PEG**-pHPMA$_{50}$-EGDMA$_x$ series with initial and final concentrations: **a** i_1-$f_{0.2}$, **b** i_5-f_1 and **c** i_{50}-$f_{0.05}$

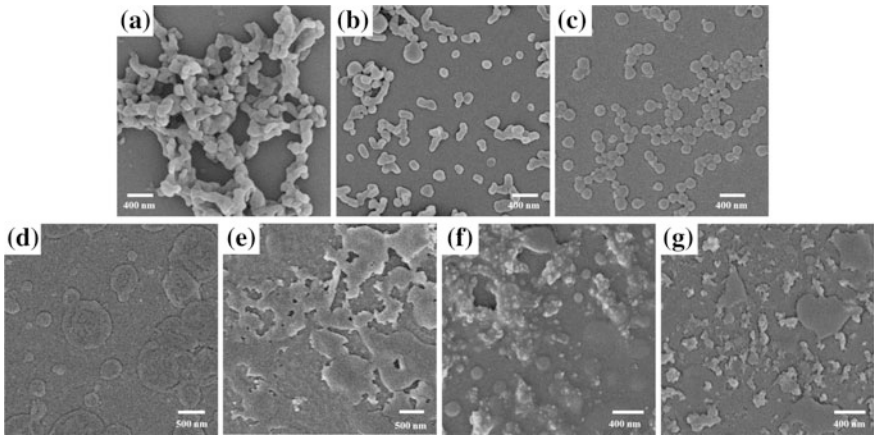

Fig. 4.16 SEM images of nanoprecipitations with i_5-f_1 for the **G2′**:**2000PEG**-pHPMA$_{50}$-EGDMA$_x$ *hyp*-polydendron series: **a** 100:0, **b** 90:10, **c** 75:25, **d** 50:50, **e** 25:75, **f** 10:90 and **g** 0:100

Table 4.5 DLS measurements for various nanoprecipitations utilising the **G2′:2000PEG**-pHPMA$_{50}$-EGDMA$_x$ series of *hyp*-polydendrons

G2′:2000PEG-pHPMA$_{50}$-EGDMA$_x$	***i*$_{50}$-*f*$_{10}$**		***i*$_{25}$-*f*$_5$**		***i*$_{10}$-*f*$_2$**		***i*$_5$-*f*$_1$**		***i*$_1$-*f*$_{0.2}$**	
	D_z (nm)	PdI	D_z (nm)	PdI	D_z (nm)	PdI	D_z (nm)	PdI	D_z (nm)	PdI
100:0$_{x\ =\ 0.8}$	111	0.335	77	0.383	96	0.481	64	0.211	132	0.042
90:10$_{x\ =\ 0.8}$	165	0.207	693	0.191	459	0.217	158	0.020	125	0.014
75:25$_{x\ =\ 0.8}$	65	0.342	73	0.389	93	0.085	215	0.085	165	0.030
50:50$_{x\ =\ 0.85}$	27	0.318	42	0.163	105	0.138	106	0.058	82	0.032
25:75$_{x\ =\ 0.95}$	35	0.370	60	0.198	63	0.200	60	0.223	75	0.262
10:90$_{x\ =\ 0.95}$	35	0.196	37	0.175	38	0.194	38	0.207	39	0.301
0:100$_{x\ =\ 0.95}$	34	0.210	33	0.248	32	0.269	33	0.304	30	0.294
G2′:2000PEG-pHPMA$_{50}$-EGDMA$_x$	***i*$_{50}$-*f*$_{0.5}$**		***i*$_{25}$-*f*$_{0.25}$**		***i*$_{10}$-*f*$_{0.1}$**		***i*$_5$-*f*$_{0.05}$**		***i*$_1$-*f*$_{0.01}$**	
	D_z (nm)	PdI	D_z (nm)	PdI	D_z (nm)	PdI	D_z (nm)	PdI	D_z (nm)	PdI
100:0$_{x\ =\ 0.8}$	–	–	–	–	–	–	136	0.044	289	0.152
90:10$_{x\ =\ 0.8}$	246	0.290	390	0.395	197	0.128	156	0.086	300	0.196
75:25$_{x\ =\ 0.8}$	184	0.121	217	0.161	104	0.099	84	0.043	103	0.079
50:50$_{x\ =\ 0.85}$	84	0.106	63	0.059	81	0.344	91	0.391	64	0.236
25:75$_{x\ =\ 0.95}$	76	0.169	74	0.175	61	0.339	62	0.217	*	*
10:90$_{x\ =\ 0.95}$	35	0.190	35	0.237	*	*	*	*	*	*
0:100$_{x\ =\ 0.95}$	29	0.232	*	*	*	*	*	*	*	*

'*' DLS measurements failed due to insufficient scattering. '–' Precipitation had occurred so the sample could not be measured by DLS. x Amount of EGDMA present in the *hyp*-polydendron

too dilute, or not being dense enough or large enough to scatter enough light. The SEM images for these samples (Fig. 4.16f, g) prepared at ***i*$_5$-*f*$_1$** show no hierarchical structure and appear to resemble dried polymer deposits.

It was proposed that due to the high hydrophilic PEG content of these polymers that they were actually water-soluble in spite of the hydrophobic pHPMA branched core within each of these polymers. Therefore the water-solubility of each DP$_{50}$ *hyp*-polydendron was studied by weighing out 20 mg of polymer and adding 1 mL of distilled water and leaving the samples rolling overnight. Figure 4.17 shows the results of this simple experiment, showing that 100:0, 90:10 and 75:25 were not water-soluble, whilst the other *hyp*-polydendrons (50:50, 25:75, 10:90 and 0:100) were all fully water-soluble under these conditions.

Therefore the non-nanoprecipitation behaviour of the 10:90 and 0:100 polymers discussed above was explained; the polymer was dissolved in a good solvent (THF) and added to a good solvent (water), therefore nanoprecipitation would not be expected. However, due to the fact that light scattering was sufficient to achieve accurate DLS measurement in many cases, it was proposed that the hydrophobic pHPMA core of the macromolecules was still collapsing into a dense particle. Although with a high content of PEG to stabilise the particles these collapsed

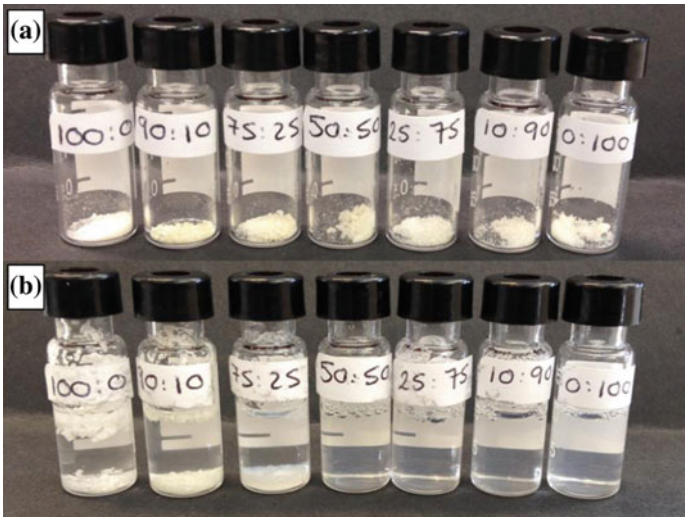

Fig. 4.17 Photograph highlighting the variation in aqueous solubility of each **G2′:2000PEG**-pHPMA$_{50}$-EGDMA$_x$ sample, 20 mg in 1 mL water: **a** before and **b** after addition of water

macromolecules did not aggregate (or self-assemble) as previously observed for nanoprecipitation of more hydrophobic polymers.

The water-insoluble polymers (100:0, 90:10 and 75:25) generally followed the previously observed nanoprecipitation mechanism, where the D_z of the particles increased with increasing initial concentration in good solvent. The SEM images of these samples, prepared at $\boldsymbol{i_5}$-$\boldsymbol{f_1}$, (Fig. 4.16a–c) show individual particles that appear slightly aggregated, probably due to drying of the samples. When the initial concentrations of the nanoparticle formulations exceeded 5 mg/mL, the PdI values observed were higher than those usually observed via nanoprecipitation. The DLS size distribution by intensity traces for these samples were usually multi-modal and therefore contained more than one population of nanoprecipitate species. Therefore, one limitation of the nanoprecipitation of these hydrophobic *hyp*-polydendrons appears to be the concentrations that may be achievable: further work is required to confirm this.

Perhaps most unexpected was the behaviour of the 25:75 and 50:50 samples. They usually gave larger nanoparticles than the other two water-soluble polymers (10:90 and 0:100), and with a broader range of sizes, which was expected for water-insoluble polymers. The 25:75 *hyp*-polydendron gave particles in the range 34–76 nm with PdI values 0.169–0.370. It appeared that although water-soluble, larger particles could be obtained. However, the polydispersity of those samples was larger (>0.100) than those expected for normal nanoprecipitation (generally <0.100). Interestingly, when comparing each sample with the *df* of 0.2, increasing the initial and final concentrations resulted on a decrease in D_z, which is opposite to the general trend observed with previously nanoprecipitated hydrophobic polymers.

The SEM image of the 25:75 sample (Fig. 4.16e) prepared at $\boldsymbol{i_5\text{-}f_1}$ shows similarly to the 10:90 and 0:100 no hierarchical structure, and appears to resemble dried polymer deposits. The 50:50 sample gave particles between 26 and 106 nm and PdI values from 0.032 to 0.391. This particular polymer appeared to exhibit PdI values consistent with nanoprecipitation under certain conditions ($\boldsymbol{i_{25}\text{-}f_{0.25}}$; D_z = 63.15 nm, PdI = 0.059, $\boldsymbol{i_5\text{-}f_1}$; D_z = 105.5 nm, PdI = 0.058 and $\boldsymbol{i_1\text{-}f_{0.2}}$; D_z = 81.88, PdI = 0.032). However, it also exhibits the same behaviour as the other water-soluble polymers (25:75, 10:90 and 0:100) under other conditions ($\boldsymbol{i_{50}\text{-}f_{10}}$; D_z = 26.52 nm, PdI = 0.318 and $\boldsymbol{i_{25}\text{-}f_5}$; D_z = 42.47, PdI = 0.163). The SEM images of this particular sample (prepared at $\boldsymbol{i_5\text{-}f_1}$) appeared to show spherical particles and much larger species that seem to look like vesicle type structures dried on the SEM stub. This was unexpected as the DLS measurement indicates that only one size distribution of nanoparticles was present in this sample before preparation for SEM imaging. To determine whether or not vesicles were formed upon the drying of the sample, TEM imaging would be necessary; however this was not investigated further.

The variation of nanoparticle sizes across the DP_{50} *hyp*-polydendron series with different nanoprecipitation conditions can be seen in Fig. 4.18, where the D_z of samples have been plotted against the **G2′** dendron content for different initial and final concentrations. Figure 4.18a shows those nanoprecipitations with a *df* of 0.2, and Fig. 4.18b shows those with a *df* of 0.01.

Due to the differences observed when nanoprecipitating the DP_{50} series of *hyp*-polydendrons with varying **G2′**:**2000PEG** content, the water insoluble polymers which exhibited classical nanoprecipitation behaviour (i.e. narrow polydispersities with $D_z > 50$ nm) have been described as 'nanoprecipitates' throughout this chapter, whilst the water soluble *hyp*-polydendrons which do not conform to the typical nanoprecipitation behaviour have been described as 'individual objects' throughout this chapter. Therefore DP_{50} samples with **G2′**:**2000PEG** 100:0, 90:10 and 75:25 were described as nanoprecipitates and the 50:50, 25:75, 10:90 and 0:100 samples were described as individual objects. This variation across the range of DP_{50} *hyp*-polydendrons is shown graphically in Fig. 4.19. Further investigations of these

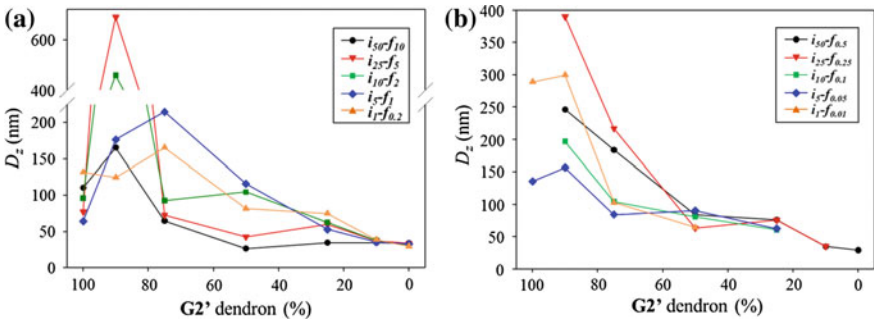

Fig. 4.18 Nanoparticle sizes versus **G2′** dendron content for nanoprecipitations with **a** *df* = 0.2 and **b** *df* = 0.01

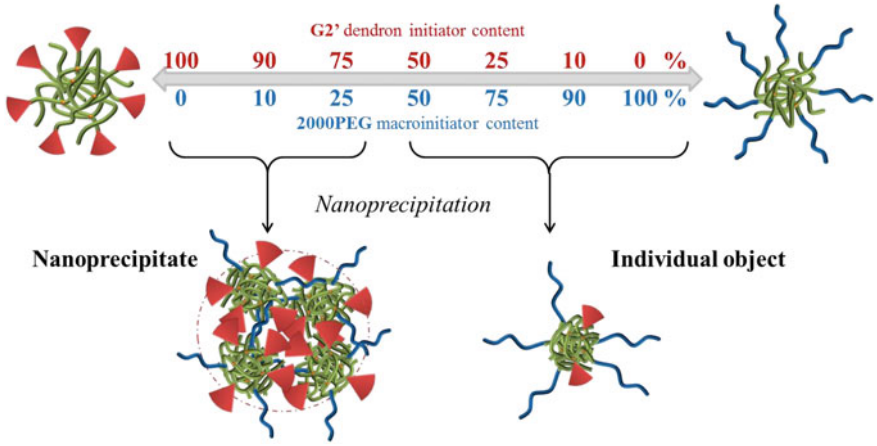

Fig. 4.19 Graphical representation of the difference in nanoprecipitation behaviour across the DP-$_{50}$ *hyp*-polydendron series

materials included the stability under physiologically relevant conditions to ascertain whether the longer PEG chain used afforded increased stability compared to the materials studied in Chap. 3 (**G2:750PEG** materials).

4.4.2.1 Stability of G2′:2000PEG DP_{50} Series Under Physiologically Relevant Conditions

Drug delivery vehicles need to be stable under physiologically relevant conditions to be considered for drug encapsulation. The ionic strength of buffer solutions used in pharmacological experiments is approximately 0.15 M; therefore the samples were diluted with 0.14 M NaCl and transport buffer (TB). TB consists of Hank's balanced salt solution, 25 mM of 4-(2-hydroxyethyl)-1-piperazine ethane sulfonic acid and 0.1 % bovine serum albumin, which is commonly used for in vitro assays such as the Caco-2 transwell plate experiment (see Chap. 1, Sect. 1.5.3.2) [16]. The stability of these materials under physiologically relevant conditions was assessed by diluting 1 mL of each sample with 1 mL of either 0.14 M NaCl or TB. Table 4.6 shows the DLS data of the samples prepared at $\boldsymbol{i_5}$-$\boldsymbol{f_1}$ before and immediately after dilution to 0.25 mg/mL with either 0.14 M NaCl or TB. Whilst the 90:10 and 75:25 nanoparticles showed salt stability when immediately measured, the samples showed some aggregation after 3 days. The most stable samples were the 50:50, 25:75, 10:90 and 0:100, which remained stable with no aggregation for over a week. The 100:0 sample was not stable under physiologically relevant conditions and precipitated out of solution almost instantaneously after addition of either 0.14 M NaCl or TB.

Table 4.6 DLS data for the **G2′**:**2000PEG**-pHPMA$_{50}$-EGDMA$_x$ ***i*$_5$-*f*$_1$** samples with NaCl and TB stability

G2′:**2000PEG**-pHPMA$_{50}$-EGDMA$_x$	***i*$_5$-*f*$_1$**		+0.14 M NaCl		**+TB**	
	D_z (nm)	PdI	D_z (nm)	PdI	D_z (nm)	PdI
100:0$_{x\ =\ 0.8}$	64	0.211	–	–	–	–
90:10$_{x\ =\ 0.8}$[a]	176	0.034	179	0.032	176	0.029
75:25$_{x\ =\ 0.8}$[a]	174	0.026	177	0.021	177	0.049
50:50$_{x\ =\ 0.85}$[a]	116	0.038	114	0.032	112	0.060
25:75$_{x\ =\ 0.95}$[a]	53	0.238	53	0.255	55	0.271
10:90$_{x\ =\ 0.95}$[a]	35	0.178	38	0.229	36	0.244
0:100$_{x\ =\ 0.95}$	33	0.304	34	0.287	30	0.279

[a]New samples were prepared for the stability testing

4.4.3 *Pharmacological Studies of G2':2000PEG-pHPMA$_{50}$-EGDMA$_x$ Materials*

In order to assess the suitability of *hyp*-polydendron materials in drug delivery, toxicity assays and studies of transport across the Caco-2 gut wall model were conducted, as discussed previously (Chap. 1, Sect. 1.5.3 and Chap. 3, Sect. 3.5). In order to perform these assays the most stable samples (50:50, 25:75, 10:90 and 0:100) were used to encapsulate Nile red, by dissolution of the Nile red in the good solvent (THF) with the polymer, to give each formulation with a final concentration of 10 mg/mL polymer and 0.02 mg/mL Nile red. The Nile red loaded samples could not be measured by the same DLS instrument as the blank samples—the samples failed on the measurement criteria possibly because wavelength of the laser was 633 nm and the Nile red excitation and emission wavelengths are 552 and 630 nm respectively; it was proposed that this was affecting the measurement. Therefore a different DLS machine was used which had a laser wavelength of 830 nm. The DLS results for the Nile red loaded particles are shown in Table 4.7 and Fig. 4.20.

Table 4.7 DLS data for the blank and Nile red loaded particles used for pharmacological assessment

G2′:**2000PEG**-pHPMA$_{50}$-EGDMA$_x$	Blank samples		Nile red loaded		
	D_z (nm)	PdI	D_z (nm)	PdI	Standard deviation
50:50$_{x\ =\ 0.85}$[a]	106	0.058	187	0.356	3.47
25:75$_{x\ =\ 0.95}$[b]	60	0.223	49	–[c]	5.13
10:90$_{x\ =\ 0.95}$[b]	38	0.207	34	–[c]	6.71
0:100$_{x\ =\ 0.95}$[b]	33	0.304	28	–[c]	10.2

[a]Ran on the DLS with laser at 633 nm
[b]Ran on DLS with laser at 830 nm
[c]The software for the DLS machine (830 nm) for these measurements only reported the standard deviation for the measurements and not PdI values

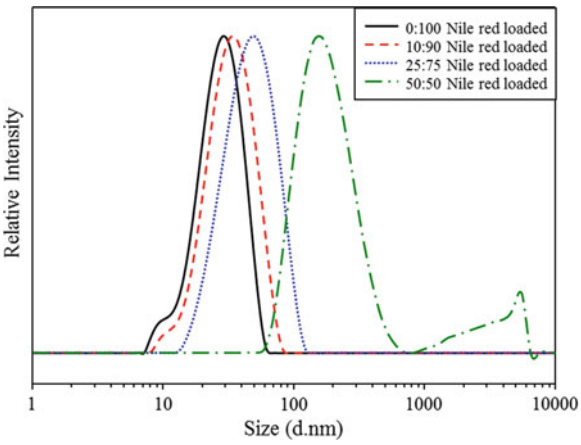

Fig. 4.20 DLS size distribution by intensity trace overlays for the Nile red loaded samples: **G2′**:**2000PEG** 50:50, 25:75, 10:90 and 0:100-pHPMA$_{50}$-EGDMA$_x$

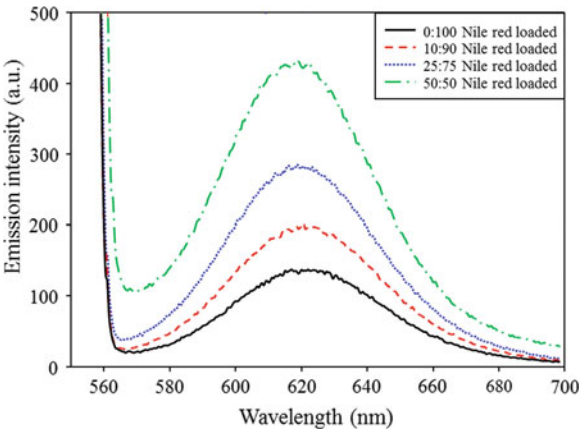

Fig. 4.21 Fluorescence spectroscopy overlays for the Nile red loaded samples: **G2′**:**2000PEG** 50:50, 25:75, 10:90 and 0:100-pHPMA$_{50}$-EGDMA$_x$

Nile red can give an indication of the environment it is in, as discussed in Chap. 3, due to the nature of fluorescence from the molecule. Nile red fluorescences with increased intensity in a hydrophobic environment when compared to a more hydrophilic environment. Fluorescence spectra of the Nile red loaded samples are shown in Fig. 4.21, which shows that at the same concentration of Nile red with increasing the **2000PEG** content of the formulations the intensity observed at 630 nm (when excited at 552 nm) decreased systematically.

4.4.3.1 Cytotoxicity Assays

The four Nile red containing *hyp*-polydendron samples were assessed by ATP and MTT toxicology assays using the Caco-2 cell line. Cells were incubated for 1 and

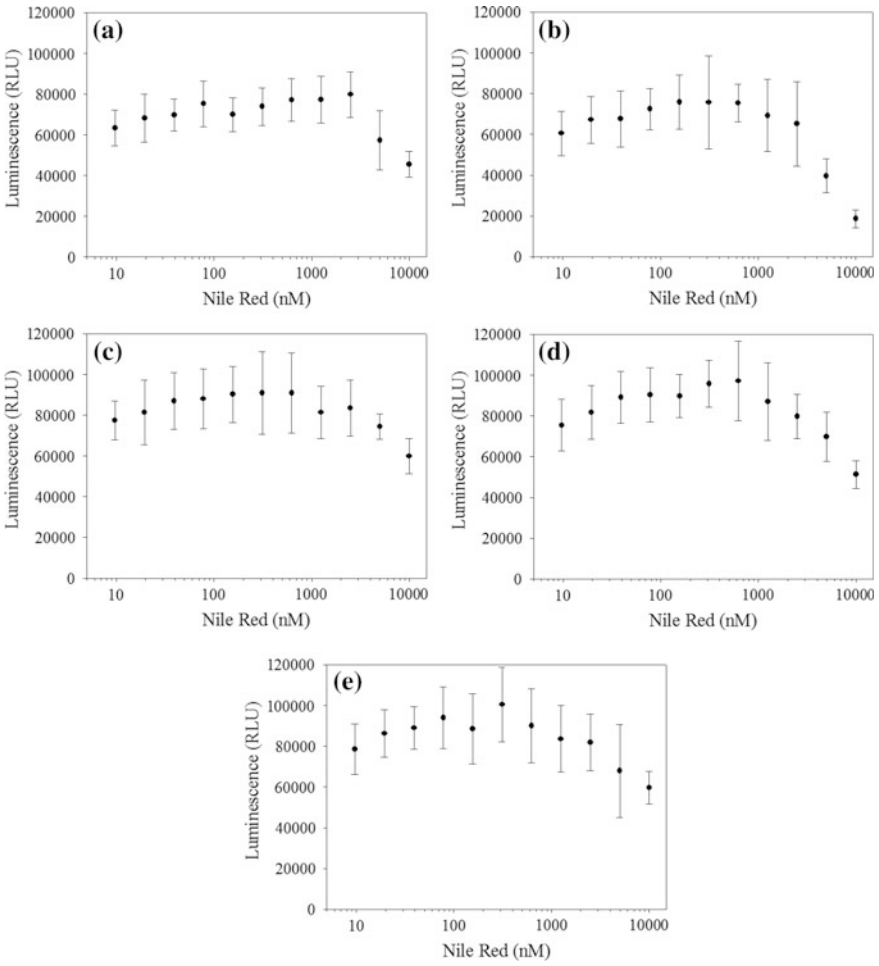

Fig. 4.22 ATP assay of Caco-2 cells following 5 day incubation with aqueous Nile Red and each *hyp*-polydendron. **a** Aqueous Nile red. **b** 50:50. **c** 25:75. **d** 10:90. **e** 0:100. Error calculated using the standard deviation

5 days to ascertain whether the Nile red loaded samples were toxic. Figure 4.22 shows the ATP assay results after a 5 day incubation period.

None of the samples showed an increase in toxicity compared to the aqueous formulation. Each sample shows a slight decrease in luminescence at higher concentrations of Nile red (above 2500 nm), however, the aqueous preparation of Nile red also shows this decrease of luminescence, therefore it can be concluded that the toxicity at higher Nile red concentrations is due to the Nile red concentration and not a necessary effect arising from the polymer. The 1 day incubation for the ATP

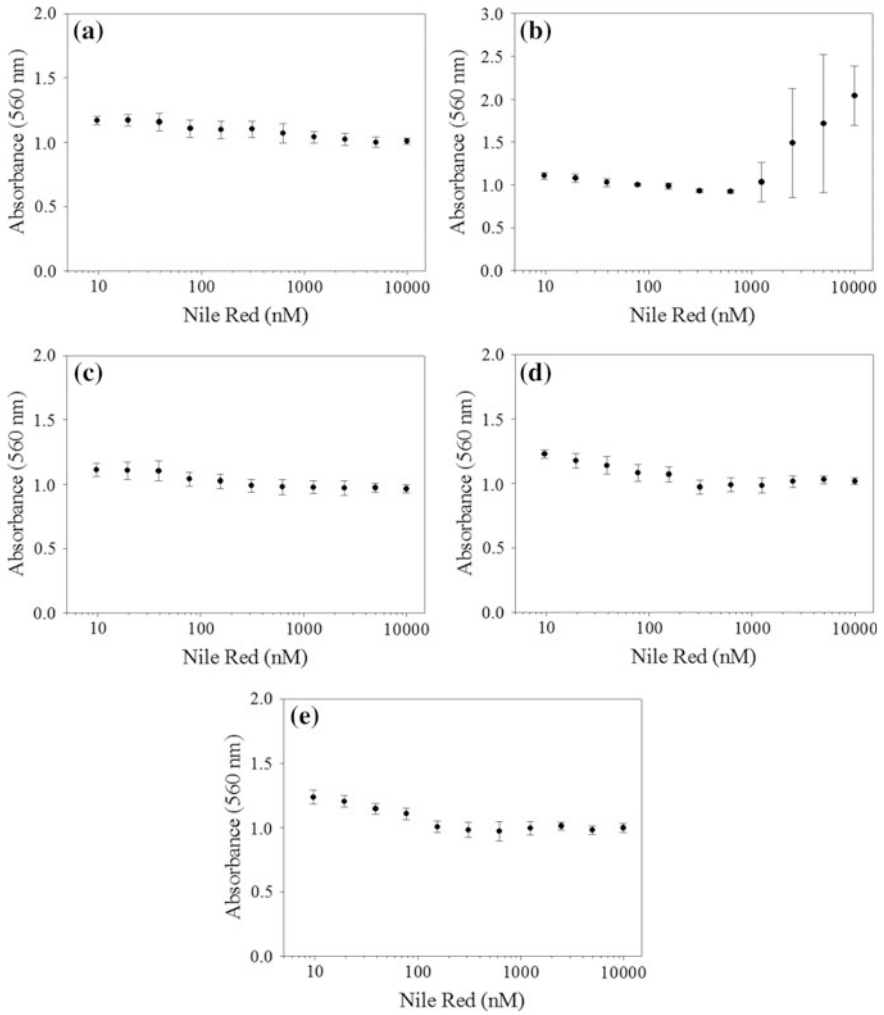

Fig. 4.23 MTT assay of Caco-2 cells following 5 day incubation with aqueous Nile Red and each *hyp*-polydendron. **a** Aqueous Nile Red. **b** 50:50. **c** 25:75. **d** 10:90. **e** 0:100. Error calculated using the standard deviation

assay is shown in the Appendix (Fig. A.31) and shows that there is no observable toxicity to the Caco-2 cells over a 24 h period as the measured luminescence remains the same (within experimental error) across each concentration of Nile red.

The MTT toxicity assay over an incubation period of 5 days is shown in Fig. 4.23. Again, none of the samples showed an increase in toxicity compared to the aqueous Nile red formulation. The 50:50-pHPMA$_{50}$-EGDMA$_{0.85}$ shows an

increase in absorbance above a Nile red concentration of 1000 nm with significant error arising. The reasons for this behaviour are not fully understood and may be due to possible interference from the assay. The MTT toxicity assays over a 24 h incubation period are shown in the Appendix, Fig. A.32, also showing that the materials caused no toxicity to the cells at the concentration studied.

4.4.3.2 Transcellular Permeability Assay

The transcellular permeability of the Nile red loaded *hyp*-polydendrons was also studied, utilising the Caco-2 polarised monolayer previously discussed (see Chap. 1, Sect. 1.5.3.2). The P_{app} for each Nile red loaded *hyp*-polydendron was compared to the P_{app} measured for the aqueous preparation of Nile red, shown here in Fig. 4.24.

Movement of the aqueous preparation of Nile red from the apical to basolateral (A > B) compartments was ~75 % of the total Nile red whilst the basolateral to apical movement (B > A) was 12 % after 4 h. However, the Nile red loaded *hyp*-polydendron materials studied showed poor transcellular permeability as very little Nile red movement was observed across the Caco-2 cell monolayer when compared to the aqueous preparation, see Fig. 4.25.

Therefore whilst these samples (0:100, 10:90, 25:75 and 50:50-pHPMA$_{50}$-EGDMA$_x$) were stable under physiologically relevant conditions they appeared to offer few pharmacological benefits. These results suggested that the *hyp*-polydendrons containing high levels of PEG which did not nanoprecipitate showed no promise as drug delivery vehicles, therefore it was proposed that by increasing the ratio of hydrophobic: hydrophilic content of the *hyp*-polydendrons, the resulting polymers would form hydrophobic nanoparticles rather than individual objects.

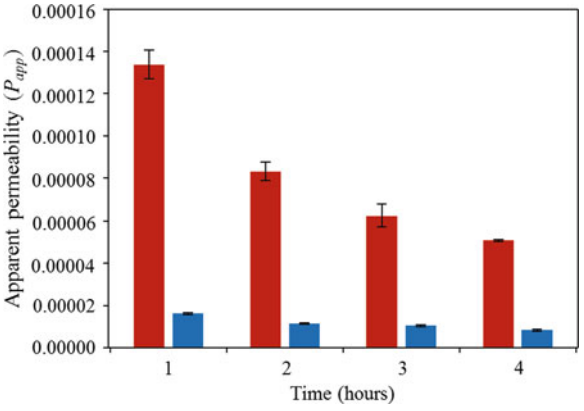

Fig. 4.24 Apparent permeability (P_{app}) of aqueous preparation of Nile red across Caco-2cell monolayers over a 4 h incubation period. A > B *red bars*, B > A *blue bars*. Error is from the standard deviation

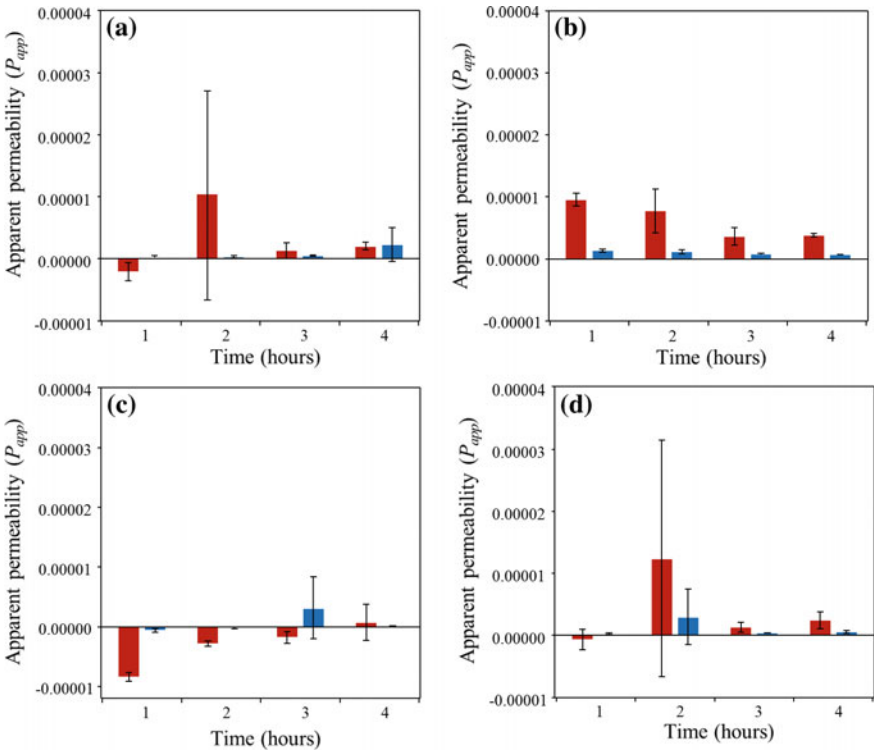

Fig. 4.25 Apparent permeability (P_{app}) of **G2′**:**2000PEG**-pHPMA$_{50}$-EGDMA$_x$ *hyp*-polydendron formulated Nile Red across caco-2 cell monolayers over a 4 h incubation period. **a** 50:50; **b** 25:75; **c** 10:90; **d** 0:100. A > B *red bars*, B > A *blue bars*. Error bars are using the standard deviation

4.4.4 Study of G2':2000PEG-pHPMA$_{100}$-EGDMA$_{0.8}$ Materials

The **G2′**:**2000PEG**-pHPMA$_{100}$-EGDMA$_{0.8}$ series was subjected to the same nanoprecipitation conditions as the **G2′**:**2000PEG**-pHPMA$_{50}$-EGDMA$_x$ series discussed previously. Firstly, the aqueous solubility of these DP$_{100}$ polymers was investigated as previously discussed, the DP$_{50}$ polymers which were water soluble did not produce nanoprecipitates and were less uniform than those which were not water soluble. Figure 4.26 shows that although the higher PEG content polymers appear to swell and indicate a level of solvation, none of the **G2′**:**2000PEG**-pHPMA$_{100}$-EGDMA$_{0.8}$ polymers were soluble in water. This was due to the increased hydrophobicity of the polymers, achieved by doubling the primary pHPMA chain length, and therefore decreasing the overall hydrophilic PEG content.

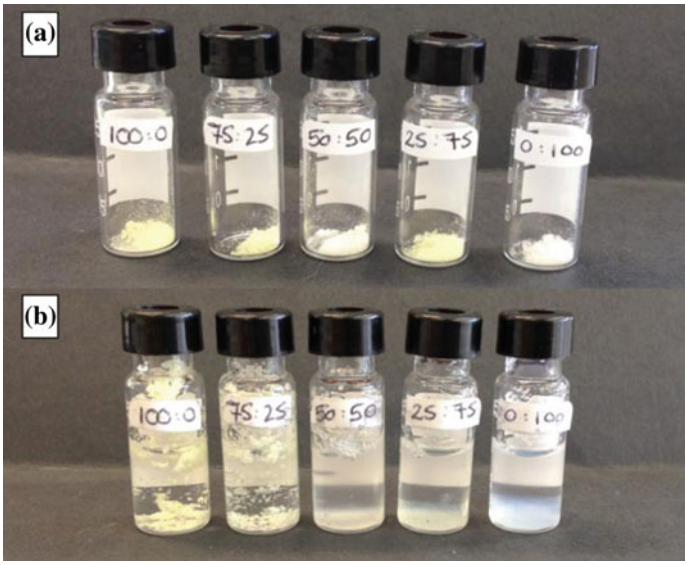

Fig. 4.26 Photograph highlighting the variation in aqueous solubility of each **G2′**:**2000PEG**-pHPMA$_{100}$-EGDMA$_{0.8}$ sample, 20 mg in 1 mL water: **a** before and **b** after addition of water

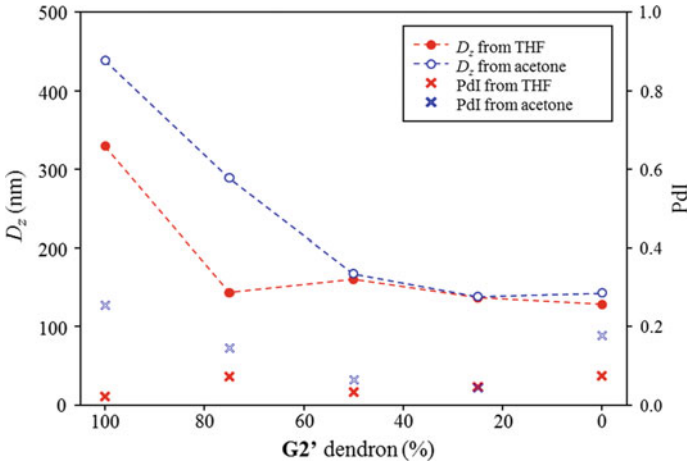

Fig. 4.27 D_z and PdI values for **G2′**:**2000PEG**-pHPMA$_{100}$-EGDMA$_{0.8}$ samples prepared with $\boldsymbol{i_5}$-$\boldsymbol{f_1}$ from THF and acetone

The nanoprecipitations were conducted from THF and acetone to ascertain which solvent would provide the most uniform particle sizes. Figure 4.27 shows the D_z and PdI values from the nanoprecipitations of the DP$_{100}$ *hyp*-polydendrons using initial and final concentrations $\boldsymbol{i_5}$-$\boldsymbol{f_1}$, (also see Appendix, Table A.9). The

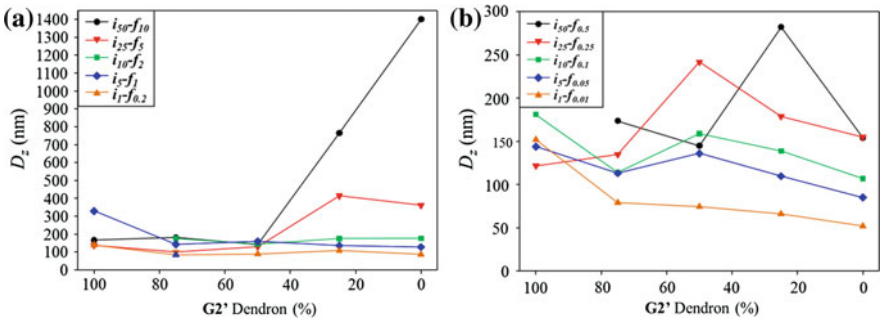

Fig. 4.28 Nanoparticle diameters versus **G2′** dendron content for nanoprecipitations with **a** *df* = 0.2 and **b** *df* = 0.01

Table 4.8 DLS data for various nanoprecipitations utilising the **G2′**:**2000PEG**-pHPMA$_{100}$-EGDMA$_{0.8}$ series of *hyp*-polydendrons

G2′:**2000PEG**-pHPMA$_{100}$-EGDMA$_{0.8}$	i_{50}-f_{10}		i_{25}-f_5		i_{10}-f_2		i_5-f_1		i_1-$f_{0.2}$	
	D_z (nm)	PdI	D_z (nm)	PdI	D_z (nm)	PdI	D_z (nm)	PdI	D_z (nm)	PdI
100:0	166.8	0.241	136.8	0.276	–	–	329.4	0.022	139.2	0.009
75:25	181.3	0.246	100.0	0.155	175.0	0.051	143.2	0.073	83.60	0.032
50:50	141.1	0.240	129.3	0.434	144.8	0.168	160.1	0.034	88.09	0.030
25:75	766.1	0.406	415.2	0.183	174.8	0.126	136.8	0.047	108.7	0.020
0:100	1401	0.277	362.5	0.267	176.1	0.173	128.2	0.074	87.09	0.052
G2′:**2000PEG**-pHPMA$_{100}$-EGDMA$_{0.8}$	i_{50}-$f_{0.5}$		i_{25}-$f_{0.25}$		i_{10}-$f_{0.1}$		i_5-$f_{0.05}$		i_1-$f_{0.01}$	
	D_z (nm)	PdI	D_z (nm)	PdI	D_z (nm)	PdI	D_z (nm)	PdI	D_z (nm)	PdI
100:0	–	–	121.7	0.135	181.0	0.090	143.9	0.076	152.0	0.063
75:25	173.6	0.420	134.9	0.192	114.0	0.080	113.2	0.089	78.98	0.147
50:50	145.0	0.275	241.6	0.193	159.0	0.117	136.1	0.114	74.31	0.155
25:75	282.0	0.612	178.7	0.150	138.9	0.092	109.8	0.092	65.93	0.185
0:100	154.1	0.402	154.8	0.228	106.8	0.136	84.98	0.133	51.88	0.250

'–' Not suitable for DLS measurement due to precipitation of the sample

D_z z-average diameter

nanoparticles prepared using acetone as the good solvent generally possessed larger D_z and broader dispersities, however, the 25:75-pHPMA$_{100}$-EGDMA$_{0.8}$ sample exhibited different behaviour. Therefore THF was the solvent of choice when nanoprecipitating this series of polymers, as with the DP$_{50}$ series (see Fig. 4.14).

The **G2′**:**2000PEG**-pHPMA$_{100}$-EGDMA$_{0.8}$ *hyp*-polydendrons were also subjected to nanoprecipitations with initial concentrations; 50, 25, 10, 5 and 1 mg/mL with *df* 0.2 and 0.01, see Fig. 4.28 and Table 4.8. The nanoprecipitation conditions which gave the narrowest polydispersity indices for this series of nanoprecipitations were i_5-f_1 and i_1-$f_{0.2}$. DLS size distribution by intensity traces for selected samples with various nanoprecipitation conditions are shown in Fig. 4.29.

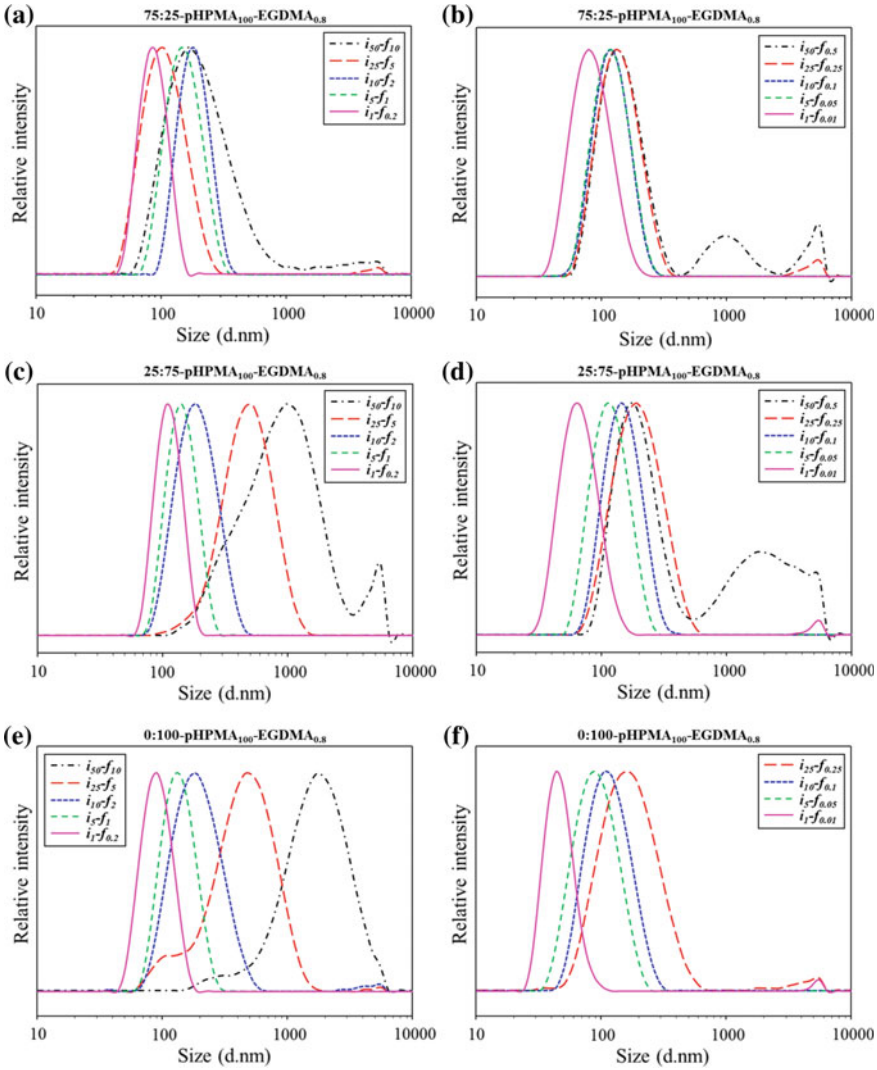

Fig. 4.29 DLS trace overlays for nanoprecipitations of **G2′**:**2000PEG**-pHPMA$_{100}$-EGDMA$_{0.8}$ with various different initial and final concentrations for two dilution factors: **a** 75:25 *df* = 0.2, **b** 75:25 *df* = 0.01, **c** 25:75 *df* = 0.2, **d** 75:25 *df* = 0.01, **e** 0:100 *df* = 0.2, **f** 0:100 *df* = 0.01

As observed for the DP_{50} series the nanoparticles prepared from a minimum initial concentration of 10 mg/mL had higher PdI values than those from an initial concentration of 1 or 5 mg/mL. However, each of these DP_{100} *hyp*-polydendrons exhibited the classical nanoprecipitation behaviour expected from hydrophobic polymers. Generally when increasing the initial and final concentrations of the nanoprecipitations whilst maintaining the *df*, the resulting nanoparticles increased in

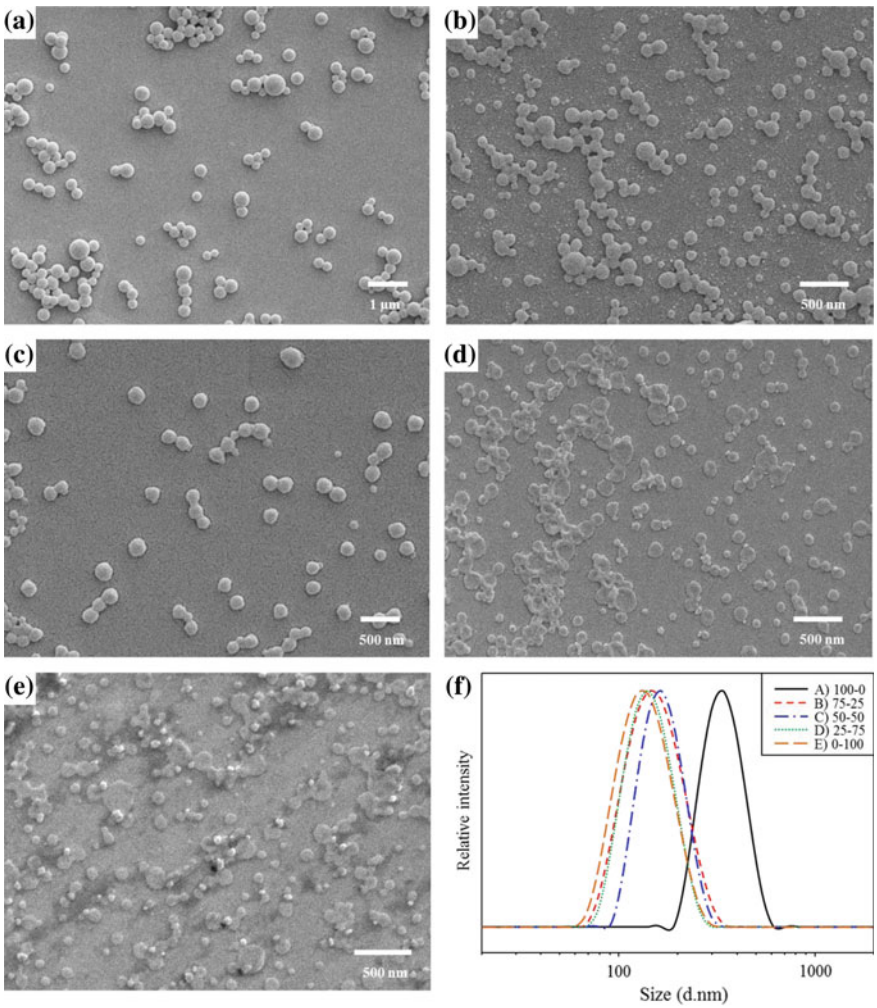

Fig. 4.30 SEM images of **a** 100:0, **b** 75:25, **c** 50:50, **d** 25:75, **e** 0:100—**G2′**:**2000PEG**-pHPMA$_{100}$-EGDMA$_{0.8}$ series of *hyp*-polydendrons at $\boldsymbol{i_5}$-$\boldsymbol{f_1}$ and **f** corresponding DLS traces

size. This trend is observed across all the nanoprecipitations which were conducted for the 75:25, 25:75 and 0:100-pHPMA$_{100}$-EGDMA$_{0.8}$; the DLS traces overlays for these samples are shown in Fig. 4.30. The other two *hyp*-polydendrons in this series (100:0 and 50:50) generally fit this trend, however, there are notable exceptions. It is also exemplified by plotting the D_z versus the **G2′** dendron initiator content as a function of the nanoprecipitation conditions ($\boldsymbol{i_x}$-$\boldsymbol{f_y}$), which highlights this trend, see Fig. 4.28.

The samples were also studied by SEM, Fig. 4.30, each sample prepared at $\boldsymbol{i_5}$-$\boldsymbol{f_1}$ were prepared in the same manner as the DP$_{50}$ samples. The samples were initially

imaged at 1 mg/mL, however, the 25:75 and 0:100-pHPMA$_{100}$-EGDMA$_{0.8}$ samples required diluting to 0.1 mg/mL to achieve the images in Fig. 4.30, as at 1 mg/mL the particles appeared aggregated. The 100:0, 75:25 and 50:50 samples (Fig. 4.30a–c) show spherical discreet particles which agree with the D_z measured by DLS. However, the 25:75 and 0:100 samples (Fig. 4.30d, e) appear to have dried on the SEM stub surfaces as flat, compressed particles, and look vesicle-like, as observed in the 50:50 DP$_{50}$ SEM image (see Fig. 4.16d). This may be due to the drying of the nanoparticles on the SEM surface. To assess whether vesicles are present in the samples TEM investigations would be needed. This may also be due to drying effects or to the *T*g of the polymers (also refer to Chap. 3, Sect. 3.4 and Fig. 3.13). The corresponding DLS size distribution by intensity traces for the SEM images are shown in Fig. 4.30f.

4.4.4.1 Stability of G2′:2000PEG DP$_{100}$ Series Under Physiologically Relevant Conditions

The stability of the nanoparticles formulated from ***i*$_5$-*f*$_1$** were studied under physiologically relevant conditions: diluted from 1 to 0.25 mg/mL with 0.14 M NaCl solution. All of the samples were stable under these conditions except for the 100:0-pHPMA$_{100}$-EGDMA$_{0.8}$, which is to be expected due to the lack of the sterically stabilising hydrophilic PEG chains. Table 4.9 shows the measurements via DLS for the samples before and after the salt addition over time.

Whilst the 75:25, 50:50, 25:75 and 0:100 samples remained stable and no aggregation was observed, the D_z of the nanoparticles did increase in size. This was observed when the DLS measurement was performed 18 h and 5 days after salt addition. The D_z increase is approximately double after 5 days and in most cases, with a subsequent increase in PdI.

To study this in more detail one of the samples (75:25-pHPMA$_{100}$-EGDMA$_{0.8}$ prepared with ***i*$_5$-*f*$_1$**) was measured at 20 min intervals over 65 h. Figure 4.31 shows the evolution of D_z, PdI and the mean count rate over time.

The D_z appeared to plateau after about 40 h, with the PdI increasing very slightly over time. This increase in size could be attributed to either aggregation of

Table 4.9 DLS data for the ***i*$_5$-*f*$_1$** samples with 0.14 M NaCl stability over time

G2′:2000PEG-pHPMA$_{100}$-EGDMA$_{0.8}$	***i*$_5$-*f*$_1$**		+0.14 M NaCl, 18 h		+0.14 M NaCl, 5 days	
	D_z (nm)	PdI	D_z (nm)	PdI	D_z (nm)	PdI
100:0	329	0.022	–	–	–	–
75:25	143	0.073	199	0.058	284	0.190
50:50	160	0.034	168	0.039	218	0.087
25:75	137	0.047	153	0.074	247	0.100
0:100	128	0.074	131	0.094	232	0.149

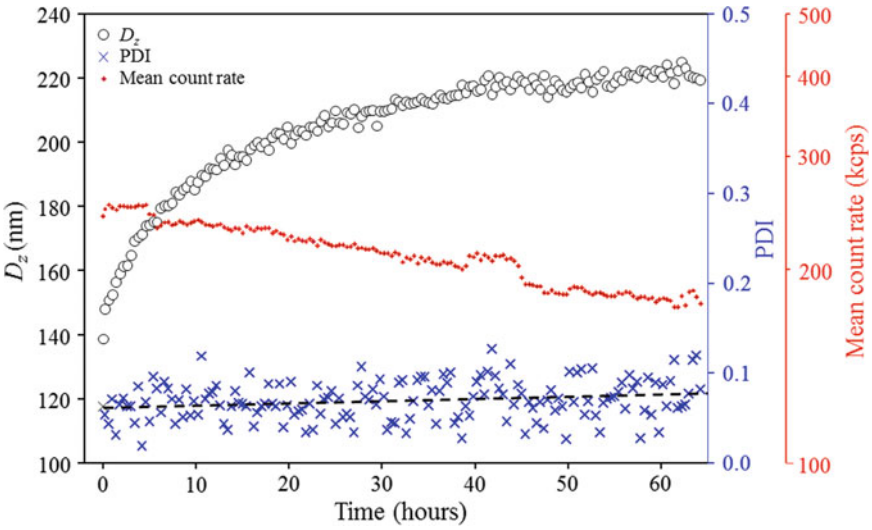

Fig. 4.31 DLS measurements over time after 0.14 M NaCl addition to a sample of **G2′:2000PEG** 75:25-pHPMA$_{100}$-EGDMA$_{0.8}$ (***i*$_5$-*f*$_1$**)

nanoparticles or swelling of the existing particles; due to the decreasing mean count rate, it was assumed that a small degree of aggregation was most likely.

The aim of this work was to study the pharmacological behaviour of the particles; the nanoparticles would be encapsulating a hydrophobic drug or dye molecule. As this increase in size with salt addition was observed for the unloaded or blank nanoparticles it was not investigated further. The stability of dye loaded nanoparticles is discussed in detail below.

4.4.5 Pharmacological Studies of G2':2000PEG-pHPMA$_{100}$-EGDMA$_{0.8}$ Materials

Due to developments within the research group a new model drug molecule was chosen for further pharmacological assays. Fluoresceinamine (FA) is a hydrophobic dye with limited water solubility; the chemical structure is shown in Fig. 4.32. FA was encapsulated in the nanoprecipitates at various weight percents (w/w%) to assess the loading capacity of the *hyp*-polydendron nanoprecipitates (Table 4.10).

The optimum loading achieved across all the DP$_{100}$ materials was using 1 w/w% dye with respect to the mass of polymer used, and nanoprecipitating from THF. Therefore as the samples had a final concentration of 1 mg/mL of polymer, the amount of FA present within each aqueous dispersion was 0.01 mg/mL. This is not a particularly high loading of a material for drug delivery applications, however the

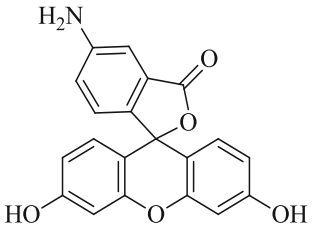

Fig. 4.32 Chemical structure of fluoresceinamine (isomer I)

Table 4.10 Fluoresceinamine formulated nanoparticles using the **G2′:2000PEG** DP_{100} samples stable under physiologically relevant conditions, utilising either THF or acetone as the good solvent

G2′:2000PEG-pHPMA$_{100}$-EGDMA$_{0.8}$	Blank		1 w/w% FA		2.5 w/w% FA		5 w/w% FA		10 w/w% FA	
	D_z (nm)	PdI	D_z (nm)	PdI	D_z (nm)	PdI	D_z (nm)	PdI	D_z (nm)	PdI
THF										
75:25	143	0.073	167	0.024	–	–	–	–	–	–
50:50	160	0.034	216	0.006	614	0.548	*	*	475	0.235
25:75	137	0.047	181	0.162	471	0.509	945	0.492	*	*
0:100	128	0.074	146	0.097	438	0.216	702	0.248	*	*
Acetone										
75:25	289	0.146	*	*	–	–	*	*	490	0.208
50:50	168	0.065	1087	0.542	–	–	1559	0.568	585	0.314
25:75	139	0.044	*	*	–	–	*	*	328	0.227
0:100	143	0.179	*	*	–	–	798	0.160	168	0.035

Not suitable for measurement by DLS due to '*'high polydispersity or '–' precipitation of the sample

pharmacological benefits, if any, of these materials were to be assessed before further loading studies were conducted.

Sample preparations were repeated for pharmacology testing and their stability over time was conducted on the samples as formulated in distilled water and with the addition of 0.14M NaCl and TB to determine the material's stability in physiologically relevant conditions and, therefore, suitability for further pharmacological assessment.

Repeats of these preparations are shown in Table 4.11, showing slight but not significant variation of D_z and PdI when the samples were repeated. Batch 4 was used to study the stability over time (80 days), see Fig. 4.33, where the 75:25, 50:50 and 25:75 FA loaded formulations remain stable with no significant alteration in size or dispersity, whereas the 0:100 decreases in size from 117 nm (PdI = 0.141) to 65 nm (PdI = 0.093). The D_z and PdI values for these samples can be found in the Appendix, Table A.10.

Table 4.11 DLS data for various batches of **G2′**:**2000PEG**-pHPMA$_{100}$-EGDMA$_{0.8}$ FA loaded nanoparticles

G2′:**2000PEG**-pHPMA$_{100}$-EGDMA$_{0.8}$	Batch 1		Batch 2		Batch 3		Batch 4			Batch 5		
	D_z (nm)	PdI	D_z (nm)	PdI	D_z (nm)	PdI	D_z (nm)	PdI	Zeta potential (mV)	D_z (nm)	PdI	Zeta potential (mV)
75:25	160	0.033	175	0.045	169	0.024	173	0.041	−23.9	160	0.032	−32.5
50:50	203	0.062	255	0.149	260	0.081	250	0.073	−15.8	212	0.034	−18.9
25:75	153	0.124	153	0.080	157	0.098	153	0.090	−13.4	192	0.135	−17.1
0:100	118	0.073	118	0.064	120	0.075	117	0.141	−12.0	–	–	–

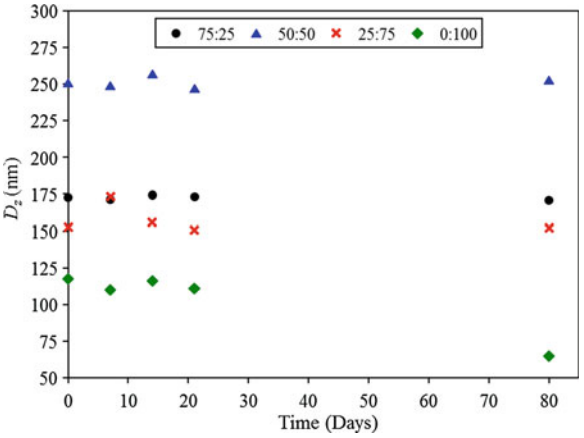

Fig. 4.33 DLS measurements of FA loaded samples over time—batch 4 from Table 4.11

Table 4.12 Stability under physiologically relevant conditions studied for **G2′:2000PEG**-pHPMA$_{100}$-EGDMA$_{0.8}$ FA loaded nanoparticles

Batch 4—Diluted to 0.25 mg/mL with 0.14 M NaCl								
G2′:2000PEG-pHPMA$_{100}$-EGDMA$_{0.8}$	Original		Day 0		Day 1		Day 7	
	D_z (nm)	PdI	D_z (nm)	PdI	D_z (nm)	PdI	D_z (nm)	PdI
75:25	173	0.041	176	0.021	176	0.032	195	0.030
50:50	250	0.073	271	0.179	245	0.048	259	0.132
25:75	153	0.090	153	0.088	150	0.073	159	0.073
0:100	117	0.141	127	0.129	122	0.087	125	0.096
Batch 4—Diluted to 0.25 mg/mL with TB								
75:25	173	0.041	177	0.020	180	0.021	221	0.065
50:50	250	0.073	256	0.100	244	0.098	252	0.060
25:75	153	0.090	151	0.095	150	0.087	186	0.233
0:100	117	0.141	129	0.166	131	0.108	133	0.159

Batch 4 was also used for studying the stability of the FA loaded nanoparticles under physiologically relevant conditions, see Table 4.12. The samples were diluted from 1 mg/mL to 0.25 mg/mL (concentration of polymer) with either 0.14 M NaCl or TB and DLS measurements were performed immediately after dilution, at 1 day and at 7 days. These time scales were chosen to check the stability of the particles at timescales appropriate for pharmacological experiments. The D_z of the particles remain quite similar with no significant differences over time. Therefore the loading of a hydrophobic molecule in these nanoparticles has improved the stability to 0.14 M NaCl solution and TB.

Batch 5 was studied via DLS over time and with the dilution in TB which gave similar results to that of batch 4; no aggregation or precipitation of particles was

observed and the D_z and PdI values remain similar over time and with the addition of TB (see Appendix, Table A.11).

Whilst preparing these materials for pharmacological assessment it was also thought that two of the previously discussed DP_{50} materials could also be prepared and studied to assess any potential pharmacological benefit. *Hyp*-polydendrons 90:10-pHPMA$_{50}$-EGDMA$_{0.8}$ and 75:25-pHPMA$_{50}$-EGDMA$_{0.8}$ were both insoluble in water and exhibited nanoprecipitation behaviour (as opposed to individual objects) and although their stability under physiologically relevant conditions was limited, they were stable for a long enough period of time to assess their transcellular permeability (a typical study is conducted over 4 h). Therefore these two materials were prepared in the same manner as the DP_{100} FA loaded samples, previously discussed, and their stability over time and in physiologically relevant conditions was investigated. Table 4.13 shows the DLS measurements for various batches, which shows that whilst the samples appear reproducible there was some variability in size. Table 4.14 shows the nanoparticles stability in physiologically relevant conditions, which shows a slight initial increase in size for the 90:10 samples, whereas the 75:25 only shows increase in size over 7 days, however, these changes in size were not considered to be significant. Table 4.15 shows the DLS measurements over time for these two FA loaded samples stored at room temperature in distilled water which showed no significant variation in size or dispersity over 11 weeks of storage. Therefore the samples chosen for further pharmacological assessment were 90:10 and 75:25 DP_{50}, 75:25, 50:50, 25:75 and 0:100 DP_{100}. A photograph of each of these samples, before and after dilution with 0.14 M NaCl is shown in Fig. 4.34.

The DLS size distribution by intensity traces for each of these samples (from batch 4) which were used for pharmacological experiments are shown in Fig. 4.35. The original samples and stability over time in TB are highlighted, showing very little change after 1 day, and a slight change after 7 days in the 50:50 DP_{100} and 25:75 DP_{100} samples to a larger diameter and slightly broader PdI values.

SEM analysis of the FA loaded particles, see Fig. 4.36, shows that the nanoparticles retain a similar morphology as observed for the unloaded particles (Fig. 4.16 for the DP_{50} and Fig. 4.30 for the DP_{100} samples). The samples imaged were from batch 5 (Tables 4.11 and 4.13) which does not include a 0:100 DP_{100} sample; due to preliminary pharmacology testing this sample was eliminated from further studies which is discussed in more detail below. The 90:10 DP_{50}, 75:25 DP_{50} and 75:25 DP_{100} FA loaded particles (Fig. 4.36a–c) all appear as individual spherical particles, with no crystallised FA observable, indicating that the FA is encapsulated within the polymeric nanoparticles. Whereas the 50:50 DP_{100} FA loaded particles (Fig. 4.36d) appear to have a different morphology, as misshapen particles, which may be due to particles drying out upon preparation for SEM imaging. The 0:100 DP_{100} FA loaded particles (Fig. 4.36e) dried in a similar manner to the unloaded particles, where they look slightly vesicle-like.

Table 4.13 DLS data for various batches of **G2′:2000PEG**-pHPMA$_{50}$-EGDMA$_{0.8}$ FA loaded nanoparticles

G2′:2000PEG-pHPMA$_{50}$-EGDMA$_{0.8}$	Batch 1		Batch 2		Batch 3		Batch 4			Batch 5		
	D_z (nm)	PdI	D_z (nm)	PdI	D_z (nm)	PdI	D_z (nm)	PdI	Zeta potential (mV)	D_z (nm)	PdI	Zeta potential (mV)
90:10	193	0.045	247	0.049	230	0.063	236	0.031	−16.0	178	0.036	−24.8
75:25	256	0.151	213	0.188	230	0.093	225	0.116	−14.5	176	0.091	−6.47

Table 4.14 Stability under physiologically relevant conditions studied for **G2′:2000PEG**-pHPMA$_{50}$-EGDMA$_{0.8}$ FA loaded nanoparticles

Batch 4—Diluted to 0.25 mg/mL with 0.14 M NaCl								
G2′:2000PEG-pHPMA$_{50}$-EGDMA$_{0.8}$	Original		Day 0		Day 1		Day 7	
	D_z (nm)	PdI	D_z (nm)	PdI	D_z (nm)	PdI	D_z (nm)	PdI
90:10	236	0.031	283	0.176	241	0.053	253	0.047
75:25	225	0.116	243	0.226	215	0.045	313	0.250
Batch 4—Diluted to 0.25 mg/mL with TB								
90:10	236	0.031	248	0.111	239	0.034	261	0.044
75:25	225	0.116	232	0.135	216	0.067	214	0.041

Table 4.15 Stability over time measured via DLS for **G2′:2000PEG**-pHPMA$_{50}$-EGDMA$_{0.8}$ FA loaded nanoparticles—from batch 4

G2′:2000PEG-pHPMA$_{50}$-EGDMA$_{0.8}$	Day 0		Day 7		Day 14		Day 21		Day 80	
	D_z (nm)	PdI	D_z (nm)	PdI	D_z (nm)	PdI	D_z (nm)	PdI	D_z (nm)	PdI
75:25	236	0.031	267	0.178	247	0.132	233	0.064	243	0.092
50:50	225	0.116	218	0.123	224	0.113	215	0.094	219	0.132

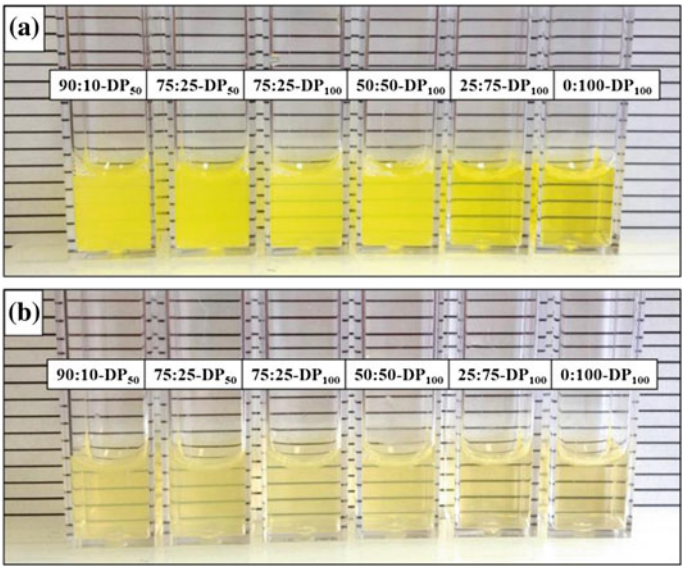

Fig. 4.34 Photograph of **a** FA loaded particles (1 mg/mL) and **b** after dilution to 0.25 mg/mL with 0.14 M NaCl

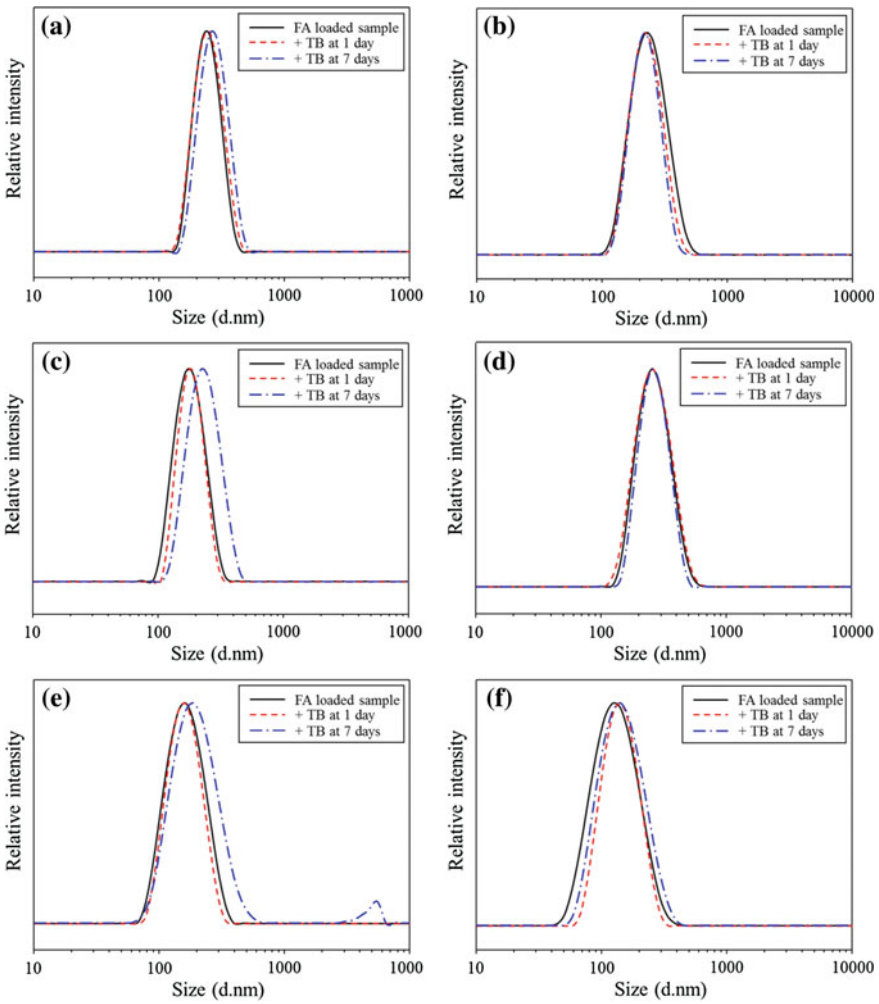

Fig. 4.35 DLS traces for FA loaded **G2′:2000PEG** *hyp*-polydendron materials; **a** 90:10-pHPMA$_{50}$-EGDMA$_{0.8}$, **b** 75:25-pHPMA$_{50}$-EGDMA$_{0.8}$, **c** 75:25-pHPMA$_{100}$-EGDMA$_{0.8}$, **d** 50:50-pHPMA$_{100}$-EGDMA$_{0.8}$, **e** 25:75-pHPMA$_{100}$-EGDMA$_{0.8}$ and **f** 0:100-pHPMA$_{100}$-EGDMA$_{0.8}$, and addition of TB at 1 and 7 days

4.4.5.1 Transcellular Permeability Assay

As discussed previously, these materials were targeting oral dosing and therefore transcellular permeability must be assessed. The relative toxicity of the materials to gut epithelial cells was also investigated to determine suitability for therapeutic delivery. To determine an appropriate lead candidate from the FA loaded *hyp*-polydendron nanoparticle preparations, the transcellular permeability of the nanoparticles was first ascertained. As previously described (Sect. 1.5.3.2), a Caco-2 cell

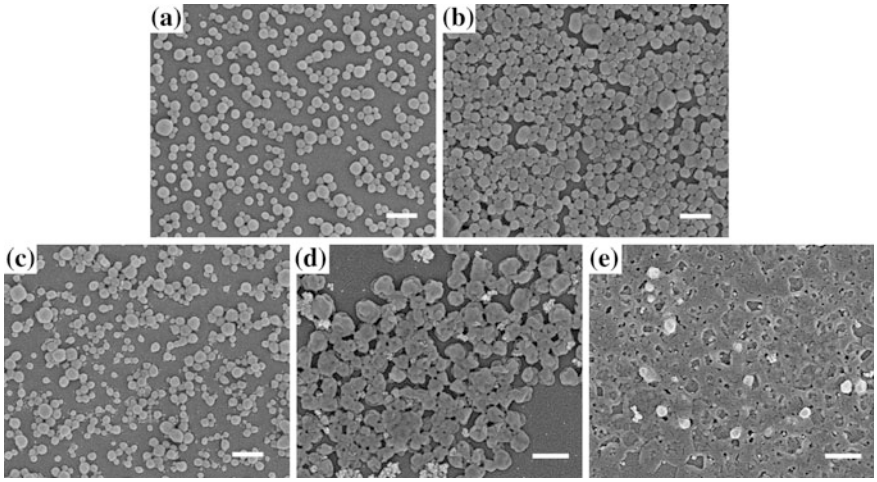

Fig. 4.36 SEM images of **G2′:2000PEG** FA loaded samples; **a** 90:10 DP_{50}, **b** 75:25 DP_{50}, **c** 75:25 DP_{100}, **d** 50:50 DP_{100} and **e** 25:75 DP_{100}. Scale bars are 400 nm

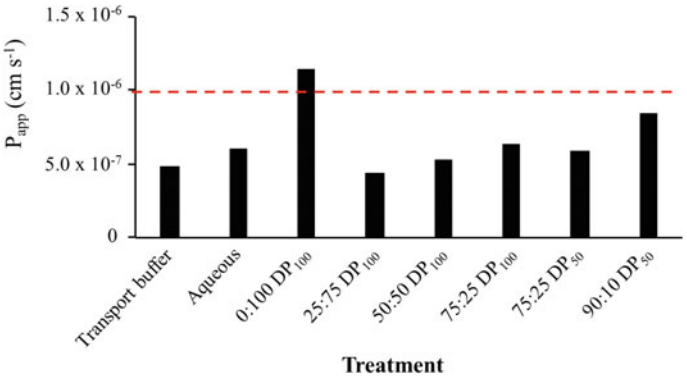

Fig. 4.37 P_{app} of ^{14}C mannitol following 1 h incubation, after monolayer was exposed to each FA treatment

monolayer was utilised in transwell plate experiments. 10 µM of FA loaded *hyp*-polydendron or 10 µM aqueous FA was added to the apical or basolateral chamber of the wells to quantify transport in both Apical > Basolateral (A > B) and Basolateral > Apical (B > A) direction and the plates were sampled 4 h after incubation. To assess monolayer integrity following incubation, 250 µl of TB containing 2 µl/mL ^{14}C mannitol was added to the apical compartment and incubated for 1 h. Scintillation fluid (4 mL) was added to 100 µl of both apical and basolateral sampled contents and quantified on the scintillation counter. Figure 4.37 shows the ^{14}C mannitol P_{app}.

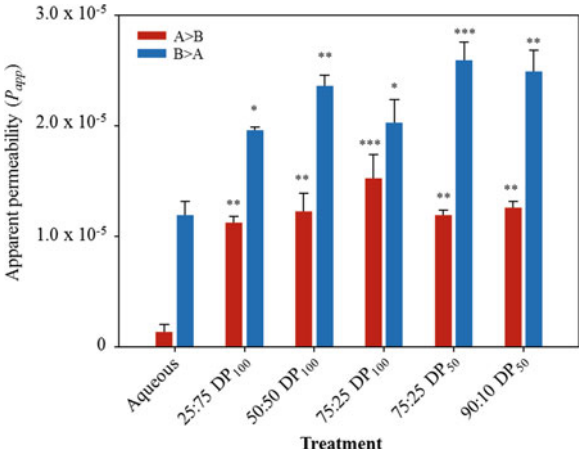

Fig. 4.38 Apparent permeability (P_{app}) of FA across the Caco-2 cell monolayer following a 4 h incubation period with aqueous and loaded *hyp*-polydendron materials. *, $P < 0.05$; **, $P < 0.01$; and ***, $P < 0.001$ (ANOVA) (n = 3)

The monolayer was considered compromised (breaks within the monolayer that would allow spurious permeation values) if the apparent permeability observed for the ^{14}C mannitol was $> 0.953 \times 10^{-6}$ cm s^{-1} [17]. Therefore the 0:100-pHPMA$_{100}$-EGDMA$_{0.8}$ material was removed from further pharmacological studies, as it appeared to compromise the integrity of the Caco-2 cell monolayer and therefore results from this experiment may not have been accurate.

The P_{app} of the FA loaded materials is shown in Fig. 4.38, with movement from the apical to basolateral compartment (A > B) shown in red and movement from basolateral to apical compartment in blue. Each FA loaded **G2′:2000PEG** material showed a statistically significant increase in both A > B and B > A movement of FA across the Caco-2 cell monolayer compared to the aqueous preparation. Therefore the encapsulation of FA into these specific *hyp*-polydendrons appears to enhance the permeation across the Caco-2 cell monolayer, suggesting that these nanoparticles are permeating the membrane.

The P_{app} ratio A > B/B > A gives an indication of the permeability of the materials from the apical to the basolateral side of the monolayer and is shown in Fig. 4.39a for these materials. All of the *hyp*-polydendron FA loaded materials show a much higher A > B/B > A ratio than the aqueous FA. Figure 4.39b shows the efflux ratio for the materials which is calculated from B > A/A > B and gives an indication of movement of material from the basolateral chamber to the apical chamber. All of the **G2′:2000PEG** FA loaded materials studied give a favourable efflux ratio when compared to the aqueous FA preparation. Therefore comparatively less FA is transported B > A when formulated with a *hyp*-polydendron. The lead candidate from the *hyp*-polydendron materials tested was chosen to be the 75:25 DP$_{100}$ sample as it showed the highest P_{app} ratio and one of the lowest efflux ratios, which suggests that this sample had the highest permeability through the Caco-2 monolayer.

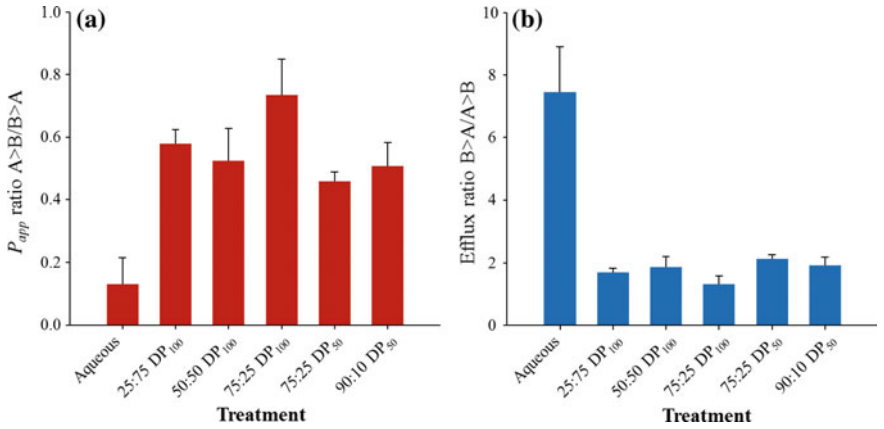

Fig. 4.39 **a** P_{app} ratio A > B/B > A and **b** efflux ratio B > A/A > B for FA loaded materials compared to the aqueous preparation of FA

4.4.5.2 Cytotoxicity Assays

Toxicity experiments were conducted to assess whether the materials were toxic to the Caco-2 cells used for the model intestinal epithelial transwell plate experiment. ATP and MTT assays were conducted with an incubation period of 1 and 5 days across a range of FA concentrations (0.1–15 μM). Figure 4.40 shows the ATP assay performed with an incubation period of 5 days, the 1 day incubation plots are shown in the Appendix (Fig. A.33). At the higher concentration of FA there appears to be some toxicity to the cells as a drop in luminescence is observed for both incubation over 1 and 5 days. A drop in luminescence indicates that cells were producing less ATP and therefore the drop in ATP production is a marker for cell death. This drop in luminescence was more prominent for the FA loaded *hyp*-polydendron particles than the aqueous preparation, however, they were not toxic at the concentration used for the Caco-2 transcellular permeation experiments which were performed at 10 μM FA.

The MTT assays conducted with an incubation period of 5 days are shown in Fig. 4.41. The corresponding 1 day incubation period data is shown in the Appendix (Fig. A.34). Again toxicity is observed for the highest concentrations studied due to a drop in the absorbance measured at 560 nm for both 1 and 5 day incubation periods. This indicates that the mitochondrial activity of cells is reduced and therefore cell death has occurred. The concentration used for the Caco-2 transcellular permeation assays did not cause toxicity here either.

Although each FA loaded *hyp*-polydendron material studied did show toxicity, they did not show toxicity at the concentration the transcellular permeation experiments were conducted.

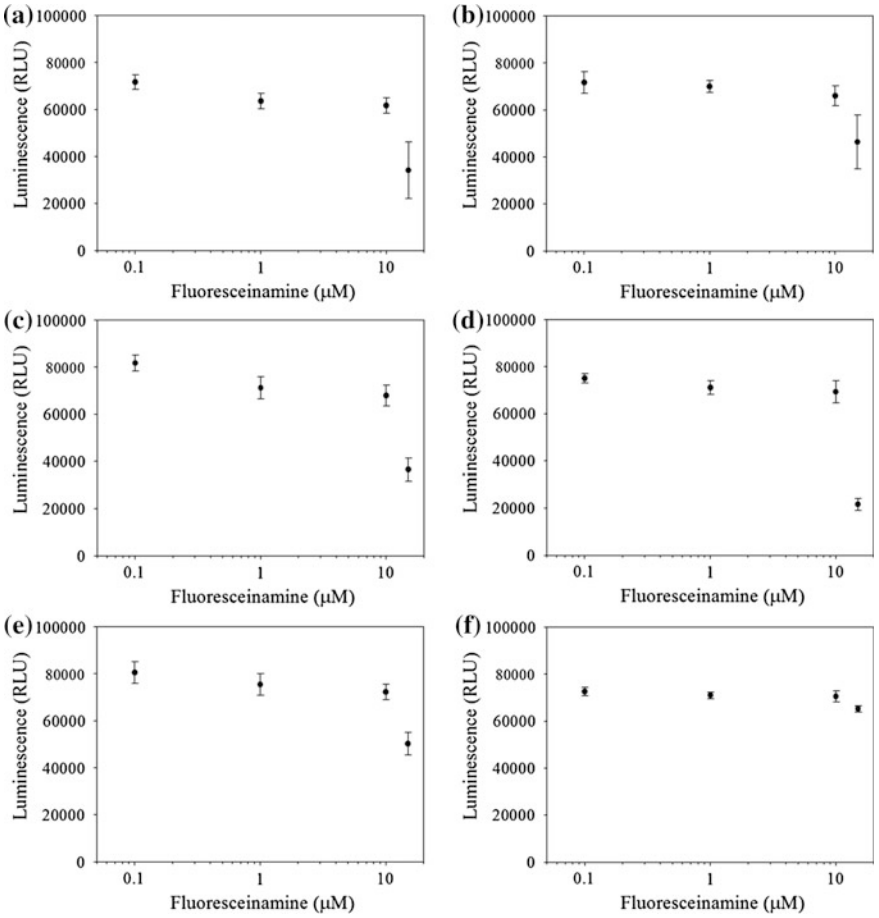

Fig. 4.40 Caco-2 cell ATP assay 5 day incubation: **a** 90:10 DP_{50}, **b** 75:25 DP_{50}, **c** 75:25 DP_{100}, **d** 50:50 DP_{100}, **e** 25:75 DP_{100}, **f** Aqueous. Error = standard deviation

Further toxicity testing was performed on the lead candidate, 75:25 DP_{100} using ATHP-1 cells (monocyte-derived macrophages), as further experiments were to be conducted to assess the accumulation of this sample in both Caco-2 and ATHP-1 cells.

The FA loaded 75:25 DP_{100} sample shows increased toxicity to ATHP-1 cells when compared with the aqueous preparation of FA when both ATP (Fig. 4.42) and MTT (Fig. 4.43) assays were conducted over a 5 day incubation period. The corresponding 1 day incubation data is shown in the Appendix (Figs. A.35 and A.36).

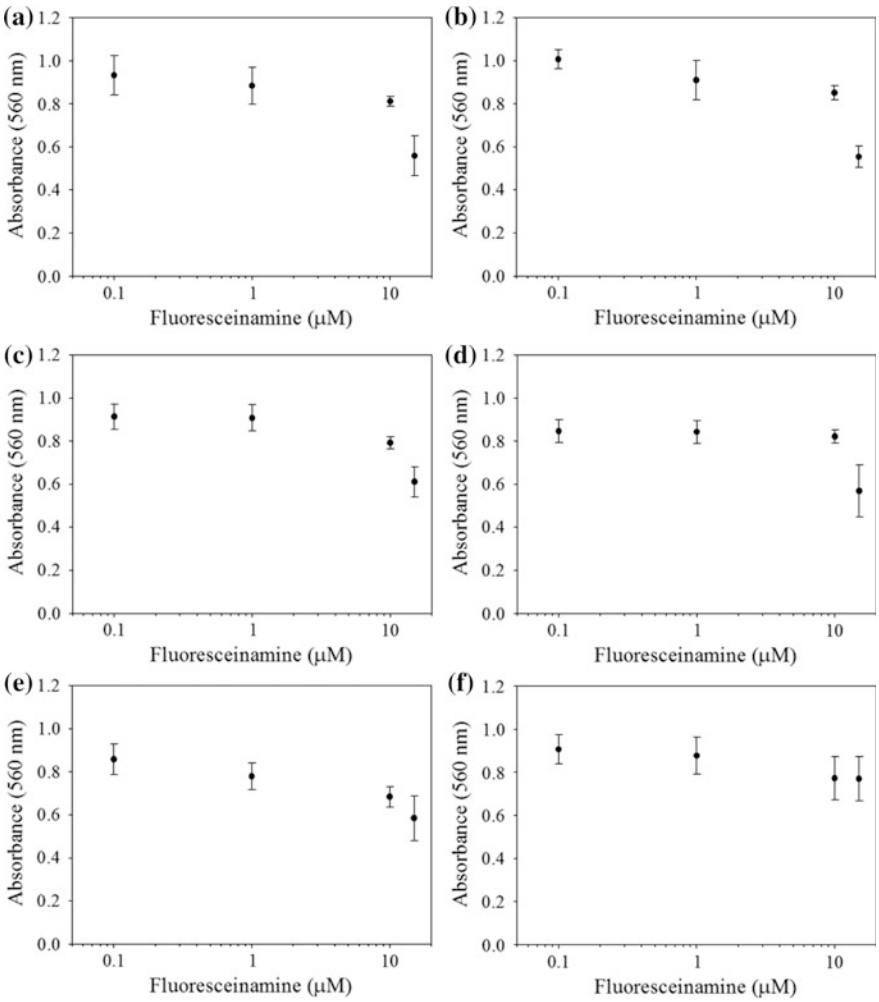

Fig. 4.41 Caco-2 cell MTT assay 5 day incubation: **a** 90:10 DP_{50}, **b** 75:25 DP_{50}, **c** 75:25 DP_{100}, **d** 50:50 DP_{100}, **e** 25:75 DP_{100}, **f** Aqueous. Error = standard deviation

4.4.5.3 Accumulation in Caco-2 and ATHP-1 Cells

The cellular accumulation ratio (CAR) for the FA loaded 75:25 DP_{100} sample in Caco-2 and ATHP-1 cells was investigated. This was conducted with the Caco-2 cell line to ascertain whether the FA loaded nanoparticles were crossing the Caco-2 monolayer via a transcellular or paracellular pathway. Transcellular permeation involves the passage of the material through the Caco-2 cell, whereas paracellular permeation is the passage of the material through the tight junctions present between cells. If material accumulates in the Caco-2 cell it is an indication that

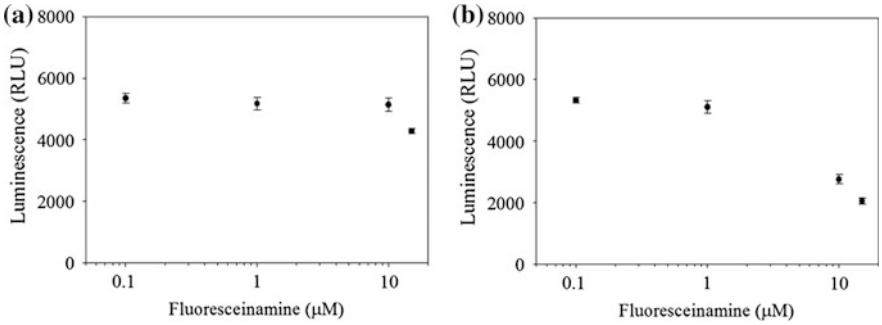

Fig. 4.42 ATHP-1 cell ATP assay 5 day incubation period; **a** aqueous preparation, **b** 75:25 DP_{100} Error = standard deviation

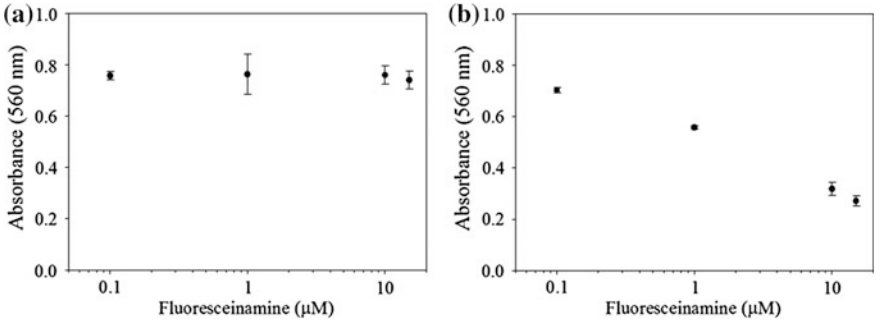

Fig. 4.43 ATHP-1 cell MTT assay 5 day incubation period; **a** aqueous preparation, **b** 75:25 DP_{100}. Error = standard deviation

permeation occurs through the cell. The CAR of the FA loaded 75:25 DP_{100} sample is shown in Fig. 4.44a with respect to the aqueous preparation. The CAR of the 75:25 DP_{100} sample was larger than that observed for the aqueous preparation, showing that by encapsulating FA in the *hyp*-polydendron nanoparticle the CAR of FA increased by approximately fourfold. This result suggests that the material is entering the Caco-2 cell when moving from the apical to the basolateral compartments in the transcellular permeation experiments with the Caco-2 cell monolayer.

The CAR was also assessed for the aqueous and the 75:25 DP_{100} *hyp*-polydendron formulated FA in ATHP-1 cells. ATHP-1 cells are monocyte derived macrophage cells which are used to ascertain the accumulation of materials in macrophages and can be indicative of phagocytic uptake mechanisms. Accumulation in macrophages can be advantageous in the treatment of certain infectious diseases such as HIV, where macrophages act as a cellular sanctuary site for the virus. The FA loaded 75:25 DP_{100} material showed a slightly increased CAR in the ATHP-1 cells when compared to the aqueous FA preparation, however, the

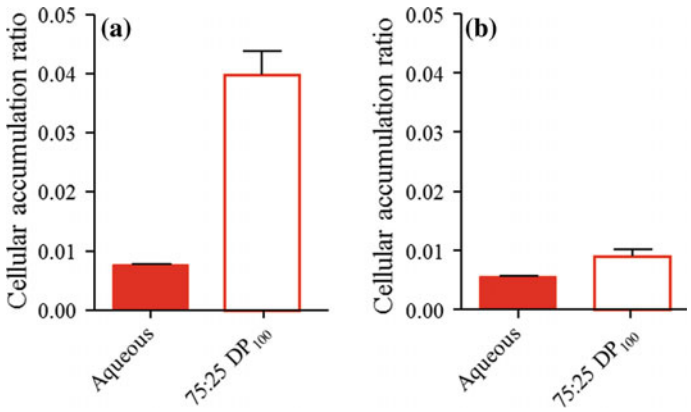

Fig. 4.44 Cellular accumulation ratios of the 75:25-pHPMA$_{100}$-EGDMA$_{0.8}$ FA formulation in **a** Caco-2 cells and **b** ATHP-1 cells

increase was not statistically significant and therefore does not suggest a selective accumulation in macrophage cells.

The FA loaded *hyp*-polydendron materials studied showed promising results in the transcellular permeation through the Caco-2 monolayer experiment in all cases, and low toxicity to the Caco-2 cells at the concentration used. This is necessary when considering oral dosing of nanoparticles. The cellular accumulation experiment using Caco-2 cells highlights that the 75:25 DP$_{100}$ sample studied does accumulate in the Caco-2 cells, indicating possible transcellular permeation as opposed to paracellular permeation. However, this material did not accumulate in macrophages at a high level which would be a desirable property in the treatment of infectious diseases such as HIV, where macrophage cells are a sanctuary site for the HIV virus.

4.4.6 Dialysis of FA Loaded Nanoparticles

The pharmacological assessment of these materials gave promising results; therefore the ability of the nanoparticles to release the encapsulated dye was investigated as an ideal drug delivery candidate must ultimately have the ability to release an encapsulated drug.

Nanoparticle formulations were taken from batch 4, and 5 mL of each sample was dialysed against distilled water (200 mL) using a dialysis membrane with a molecular weight cut off (MWCO) of 2,000 g/mol. Samples were periodically taken from the outside compartment of the membrane and measured by UV-Vis spectroscopy before being returned to the outside compartment of the dialysis to maintain a constant total volume of water of 205 mL during the dialysis experiment. Calibration curves were determined using FA dissolved in water, see Appendix

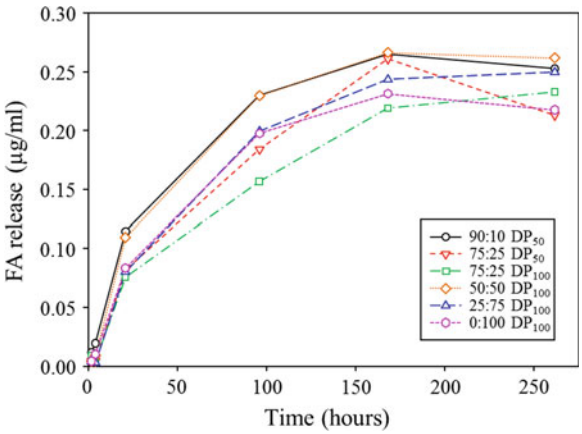

Fig. 4.45 Dialysis experiment with FA loaded nanoparticle samples—absorbance at 485 nm

Fig. A.37. The absorbance at 485 nm was used as this absorbance was the most distinguishable from the samples measured. Figure 4.45 shows the release of FA over time. As the FA concentration of each sample was 10 µg/mL and 5 mL of each sample was dialysed against 200 mL distilled water, when the FA had reached equilibrium on both sides of the dialysis membrane the concentration should have been 0.24 µg/mL. Each sample showed a plateau of FA release after 150 h and in each case the final concentration of FA reached at 168 h was between 0.22 and 0.26 µg/mL.

Therefore each FA loaded *hyp*-polydendron studied showed a release of FA over time, however, there did not appear to be any particular trend across the **G2′**:**2000PEG** content and the rate of release.

4.5 Conclusion

To conclude, an increase in the length of the hydrophilic PEG macroinitiator did lead to the formation of nanoparticles stable under physiologically relevant conditions. It was found that by varying the length of the hydrophobic pHPMA primary chain in the branched polymer core that various types of nanoparticulate objects could be formed with dramatic differences in their nanoprecipitation behaviours. Individual objects did not show any particular pharmacological benefits, however, when the hydrophobic segment of the polymers was large enough to afford nanoprecipitate particles the pharmacological data collected was much more promising. *Hyp*-polydendrons were used in the formation of nanoparticles which could permeate a well-known Caco-2 cell monolayer model experiment which mimicked the intestinal epithelial cells to predict the transcellular permeability of the materials. The permeation of FA across the Caco-2 monolayer was enhanced

when encapsulated in the *hyp*-polydendron materials studied over non-encapsulated FA. Accumulation of the lead FA loaded *hyp*-polydendron formulation (75:25-$pHPMA_{100}$-$EGDMA_{0.8}$) was also demonstrated, suggesting a transcellular pathway across the Caco-2 monolayer. Further studies are required to determine the exact method of transport across the Caco-2 cell monolayer.

References

1. R. Singh, J.W. Lillard Jr, Exp. Mol. Pathol. **86**, 215–223 (2009)
2. L. Zhang, F.X. Gu, J.M. Chan, A.Z. Wang, R.S. Langer, O.C. Farokhzad, Clin. Pharmacol. Ther. **83**, 761–769 (2008)
3. AB_2 brancher synthesis was developed by Sam Auty, a fellow PhD student in the Rannard group
4. H. Willcock, A.I. Cooper, D.J. Adams, S.P. Rannard, Chem. Commun. **2009**, 3095–3097 (2009)
5. A. Stoddart, *Synthesis, Characterisation and Properties of Novel Dendrimers* (Durham University, Durham, UK, 2002)
6. K. Jankova, X.Y. Chen, J. Kops, W. Batsberg, Macromolecules **31**, 538–541 (1998)
7. I. Bannister, N.C. Billingham, S.P. Armes, S.P. Rannard, P. Findlay, Macromolecules **39**, 7483–7492 (2006)
8. R.A. Slater, T.O. McDonald, D.J. Adams, E.R. Draper, J.V.M. Weaver, S.P. Rannard, Soft Matter **8**, 9816–9827 (2012)
9. J.M.G. Cowie, *Polymers: Chemistry and Physics of Modern Materials*, 2nd edn. (Blackie and Son Limited, UK, 1991)
10. A. Blanazs, J. Madsen, G. Battaglia, A.J. Ryan, S.P. Armes, J. Am. Chem. Soc. **133**, 16581–16587 (2011)
11. N.A. Lynd, A.J. Meuler, M.A. Hillmyer, Prog. Polym. Sci. **33**, 875–893 (2008)
12. K. Matyjaszewski, J.H. Xia, Chem. Rev. **101**, 2921–2990 (2001)
13. J.P. Rao, K.E. Geckeler, Prog. Polym. Sci. **36**, 887–913 (2011)
14. H. Fessi, F. Puisieux, J.P. Devissaguet, N. Ammoury, S. Benita, Int. J. Pharm. **55**, R1–R4 (1989)
15. G. Riess, Prog. Polym. Sci. **28**, 1107–1170 (2003)
16. H. Sun, E.C. Chow, S. Liu, Y. Du, K.S. Pang, Expert Opin. Drug Met. **4**, 395–411 (2008)
17. R. Elsby, D.D. Surry, V.N. Smith, A.J. Gray, Xenobiotica **38**, 1140–1164 (2008)

Chapter 5
Hyp-polydendrons; Studies of Nanoprecipitation Behaviour

5.1 Introduction

Various studies were performed on previously discussed materials to investigate the properties and behaviour of *hyp*-polydendron materials and the nanoparticles formed via nanoprecipitation. Compositional analysis of the **G2′**:**2000PEG** *hyp*-polydendrons and *hyp*-block copolymers is discussed in more detail, with respect to the nanoprecipitation behaviour of the materials. Other questions that arose whilst research was conducted that needed further study included; (1) whether the high molecular weight branched polymer species present in the *hyp*-polydendron materials dictated the positive nanoprecipitation behaviour observed when compared to linear materials, and (2) the ability to encapsulate more than one hydrophobic molecule within the nanoprecipitates.

5.2 Nanoprecipitation Behaviour of G2′:2000PEG Materials

Chapter 4 discussed the synthesis and characterisation of a range of mixed initiator **G2′**:**2000PEG** polymers ranging from 100:0 to 0:100, containing pHPMA primary chains with a DP_n of 20, 50 and 100 monomer units. Interestingly, across the range of *hyp*-polydendrons and *hyp*-block copolymers synthesised, different water solubilities were observed and different nanoprecipitation behaviour was observed.

F.L. Hatton, *Hyperbranched Polydendrons*,
Springer Theses, DOI 10.1007/978-3-319-18753-2_5

5.2.1 Nanoprecipitation Study of G2′:2000PEG DP_{20} Materials

As discussed previously, the nanoprecipitation behaviour of the various materials appeared to relate to the water-solubility of the branched polymers. Therefore, a water-solubility test was conducted with the materials containing a branched DP_{20} core. Figure 5.1 shows 20 mg of each material within this series before (Fig. 5.1a) and after addition of 1 mL of distilled water and overnight mixing using a roller mixer (Fig. 5.1b). In this series of **G2′**:**2000PEG** materials, the 100:0 and 90:10 polymers were insoluble in water, as expected due to the low levels of hydrophilic **2000PEG** macroinitiator, whilst all of the remaining samples were water-soluble under these conditions (75:25–0:100; $pHPMA_{20}$-$EGDMA_{0.8}$).

The nanoprecipitation behaviour of these samples was assessed at initial concentrations of 5 and 10 mg/mL with two different dilution factors (*df*). Table 5.1 shows the measurements of the resulting dispersions by DLS.

Due to the water-solubility of the majority of the polymers prepared with a chain length of 20 monomer units, many samples were unsuitable for measurement via DLS due to the insufficient light scattering. The 25:75 and 50:50 samples were suitable for measurement by DLS at the higher final concentrations, however, below 1 mg/mL no accurate measurement could be taken. Under two nanoprecipitation conditions these samples were measurable (i_{10}-f_2 and i_5-f_1); the 25:75 DP_{20} gave D_z of 62 and 63 nm with PdI values of 0.447 and 0.479 respectively whilst the 50:50 DP_{20} had a D_z of 38 nm and PdI 0.451 under the i_{10}-f_2 conditions, and with a i_5-f_1 dilution the D_z was 34 nm and PdI was 0.310. The two water-insoluble polymers were expected to nanoprecipitate in a similar manner to the previously discussed water-insoluble DP_{50} and DP_{100} polymers (Chap. 4, see

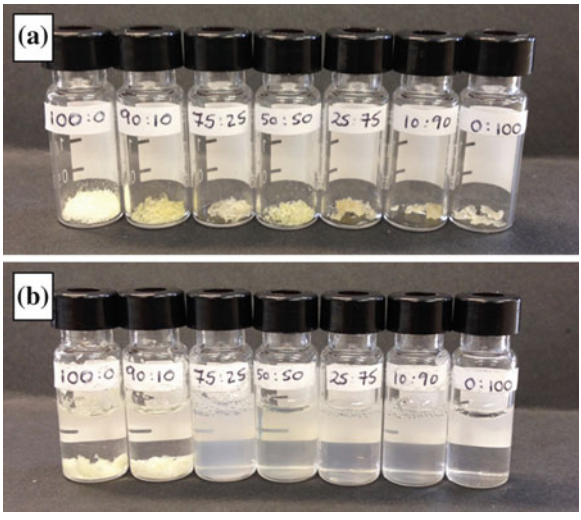

Fig. 5.1 Photograph highlighting the solubility of each **G2′**:**2000PEG**-$pHPMA_{20}$-$EGDMA_{0.8}$ sample, 20 mg in 1 mL water: **a** before and **b** after addition of water

Table 5.1 DLS D_z and PdI values for the nanoprecipitations performed using the **G2′:2000PEG**-pHPMA$_{20}$-EGDMA$_{0.8}$ *hyp*-polydendrons and *hyp*-block copolymer

G2′:2000PEG pHPMA$_{20}$-EGDMA$_{0.8}$	i_{10}-f_2		i_5-f_1		i_{10}-$f_{0.1}$		i_5-$f_{0.05}$	
	D_z (nm)	PdI	D_z (nm)	PdI	D_z (nm)	PdI	D_z (nm)	PdI
100:0	87	0.129	62	0.099	108	0.112	72	0.113
90:10	83	0.590	168	0.584	525	0.245	–[a]	–[a]
75:25	–[a]	–[a]	272	0.466	278	0.318	–[a]	–[a]
50:50	38	0.451	34	0.310	*	*	*	*
25:75	62	0.447	63	0.479	*	*	*	*
10:90	*	*	*	*	*	*	*	*
0:100	*	*	*	*	*	*	*	*

Many samples were not suitable for DLS measurement due to *lack of scattering, and [a]very high polydispersity
D_z z-average diameter

Sect. 4.4). However, only the 100:0 DP$_{20}$ *hyp*-polydendron appeared to nanoprecipitate in the same manner; D_z increased with increasing initial and final concentrations within the same *df*. This can also be seen in Fig. 5.2 where the size distribution by intensity traces for each 100:0 DP$_{20}$ nanoparticle sample prepared via nanoprecipitation are shown.

5.2.2 Hydrophilic Versus Hydrophobic Content of G2′:2000PEG Polymers

The targeted compositions of the various **G2′:2000PEG** branched polymers were compared to the composition observed by ^{1}H NMR spectroscopy. The final ^{1}H NMR spectra for each polymer was analysed and peaks could be distinguished that

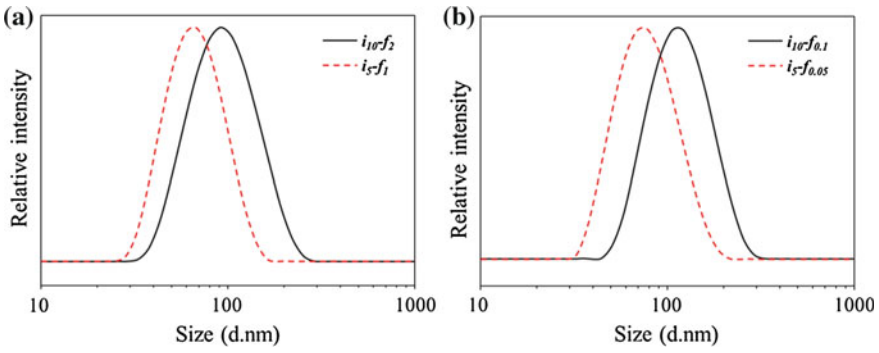

Fig. 5.2 DLS size distribution by intensity traces for each **G2′:2000PEG**-100:0-pHPMA$_{20}$-EGDMA$_{0.8}$ nanoprecipitation **a** *df* = 0.2 and **b** *df* = 0.01

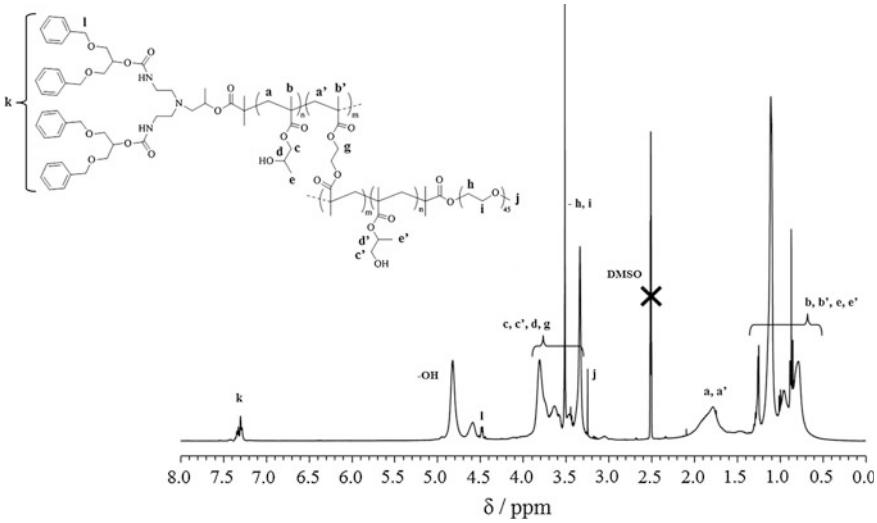

Fig. 5.3 ^{1}H NMR (d_6-DMSO, 400 MHz) spectrum of the **G2′**:**2000PEG** 50:50-pHPMA$_{50}$-EGDMA$_{0.85}$ *hyp*-polydendron with major peaks assigned

corresponded to the aromatic peaks present in the **G2′** dendron initiator at 7.3 ppm, the methyl group at the end of the PEG chain at 3.24 ppm, and the two methyl groups present in the HPMA monomer between 0.6 and 1.3 ppm. Figure 5.3 shows the ^{1}H NMR spectrum for the **G2′**:**2000PEG**-50:50-pHPMA$_{50}$-EGDMA$_{0.85}$ *hyp*-polydendron with major peaks assigned. The linear polymers synthesised were also analysed by ^{1}H NMR spectroscopy, and the spectra for each can be seen in the Appendix in Figs. A.38 and A.39.

The various series of **G2′**:**2000PEG**-pHPMA$_n$-EGDMA$_x$ polymers synthesised in Chap. 4 all contained the same chemical structures, with varying ratios of initiators and monomers. The variation in **G2′**:**2000PEG** functionality can be observed via ^{1}H NMR spectroscopy and is shown in Fig. 5.4 for the DP$_{20}$ *hyp*-polydendrons and *hyp*-polymer containing ratios of **G2′**:**2000PEG** initiators of 100:0, 75:25, 25:75 and 0:100. The aromatic peaks attributed to the **G2′** dendron initiator are easily distinguishable and can be seen decreasing as the amount of **G2′** dendron incorporation decreases.

Figure 5.5 shows the same ^{1}H NMR spectra overlays for the DP$_{50}$ series and Fig. 5.6 highlights the ^{1}H NMR spectra overlays for the DP$_{100}$ series. In each series the peaks have been normalised to the HPMA monomer peaks, 0.6–1.2 ppm, to give a true representation of the varying initiator contents. The other *hyp*-polydendrons in each DP$_n$ series not shown in Figs. 5.4, 5.5 and 5.6 are shown in the Appendix in Figs. A.40, A.41 and A.42.

Whilst the aromatic protons corresponding to the **G2′** dendron initiator are clearly distinguishable and easily integrated in the ^{1}H NMR spectra, the methyl peak at the end of the **2000PEG** chain is discernible (3.2 ppm), however, the peak

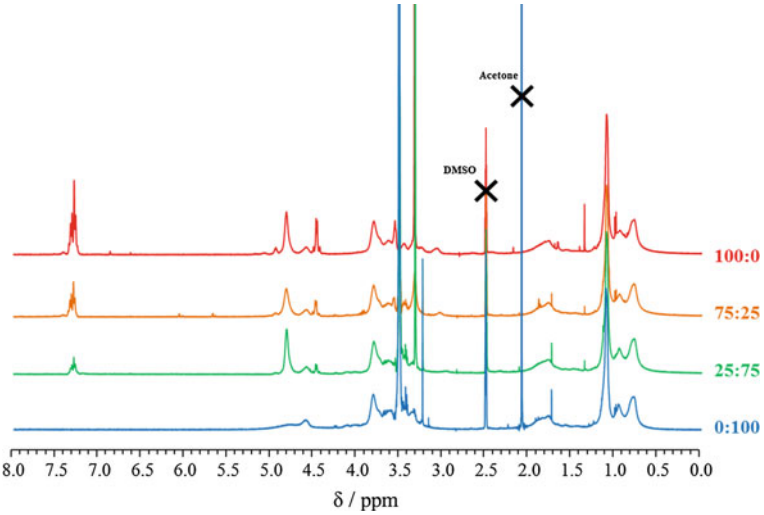

Fig. 5.4 ^{1}H NMR (d_6-DMSO, 400 MHz) spectra overlays for various **G2′:2000PEG** DP_{20} *hyp*-polydendrons

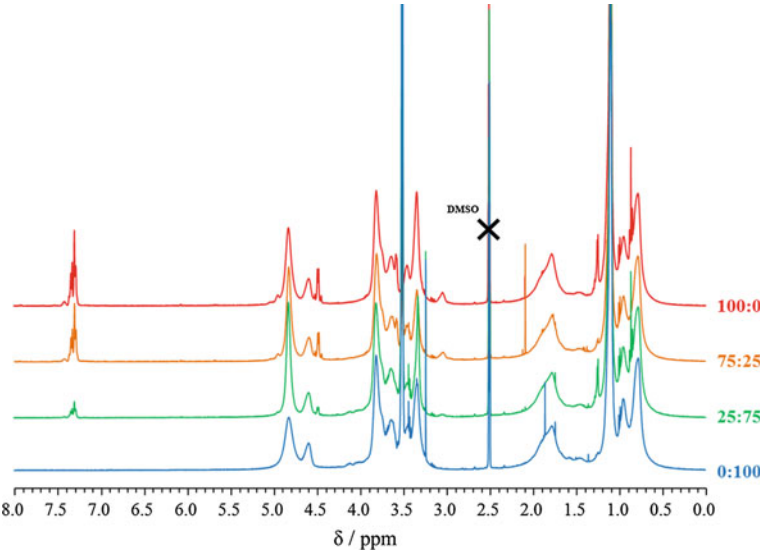

Fig. 5.5 ^{1}H NMR (d_6-DMSO, 400 MHz) spectra overlays for various **G2′:2000PEG** DP_{50} *hyp*-polydendrons

does not always reach the baseline. This is especially true for the *hyp*-polydendrons containing lower ratios of the **2000PEG** initiator. Therefore, when analysing these ^{1}H NMR spectra a certain amount of error was assumed when integrating this peak

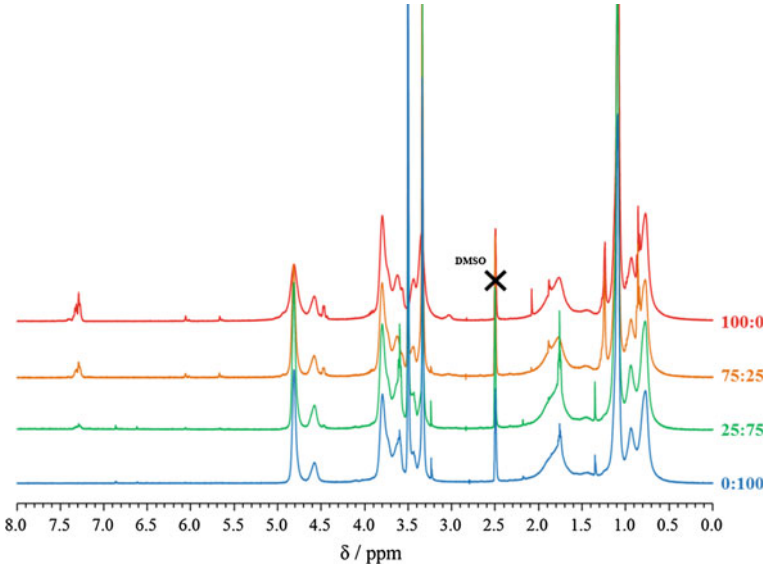

Fig. 5.6 ^{1}H NMR (d_6-DMSO, 400 MHz) spectra overlays for various **G2′**:**2000PEG** DP_{100} *hyp*-polydendrons

and it was only used to estimate the **2000PEG** content. Bearing this in mind, the ratios of **G2′** dendron and **2000PEG** initiator to the pHPMA core were calculated via ^{1}H NMR spectroscopy. Figure 5.7 shows the content of each initiator as a ratio to the HPMA monomer units, with the theoretical values targeted added as dotted lines. In each set of targeted core primary chain DP_n values, the **G2′** dendron initiator content was lower than targeted, which was probably due to a lower initiator efficiency of the **G2′** dendron initiator, as discussed in previous chapters. The **2000PEG** initiator content was generally higher than targeted by theory, which could be due to experimental errors and error when integrating ^{1}H NMR spectra.

To have a practical comparison of hydrophilic versus hydrophobic content of the polymers, the number of ethylene oxide (EO) repeat units (from the **2000PEG** macroinitiator) was compared to the hydrophobic pHPMA repeat unit content, see Fig. 5.8. This was calculated from the ^{1}H NMR spectroscopy analysis, therefore a certain error should be assumed, as previously discussed, due to errors involved with ^{1}H NMR spectra integration. However, even when taking error into consideration, the data in Fig. 5.8 could be split into two distinct sections, where the polymers were water-soluble or water-insoluble. This provides a targetable ratio of EO to HPMA that can be tuned to give *hyp*-polydendrons which are suitable for nanoprecipitation and could also be used to target those polymers which will nanoprecipitate to produce nanoparticles which are stable in physiologically relevant conditions. The lowest EO mol% of a *hyp*-polydendron that produced nanoparticles stable in physiologically relevant conditions was the 75:25 DP_{100} sample, which contained 11.5 mol% EO. To elucidate the minimum level of EO needed to

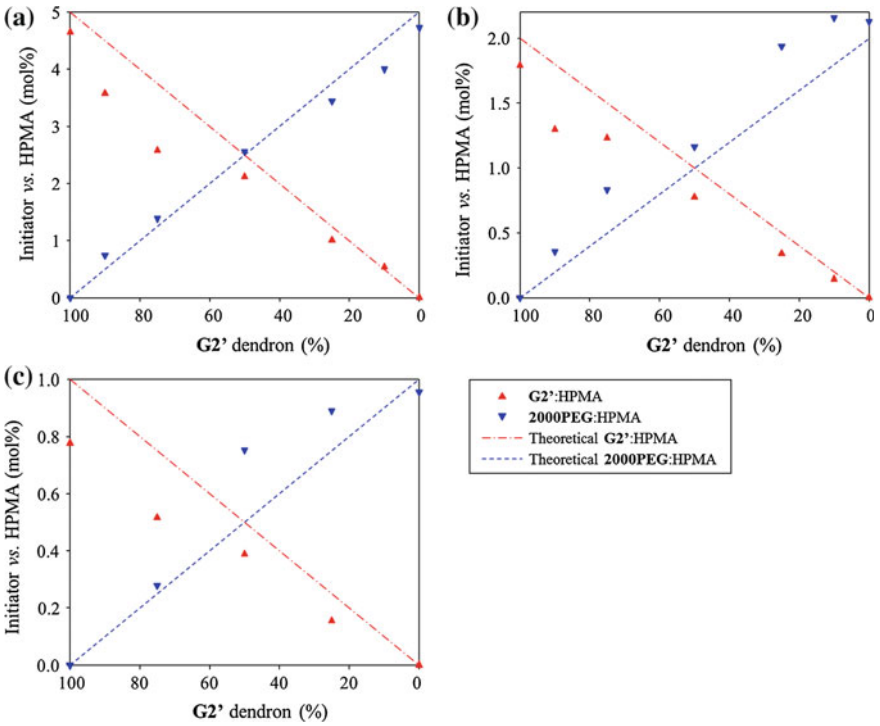

Fig. 5.7 **G2′** and **2000PEG** initiator content in **a** DP_{20}, **b** DP_{50} and **c** DP_{100} series of *hyp*-polydendrons and *hyp*-polymers calculated by ^{1}H NMR spectroscopy

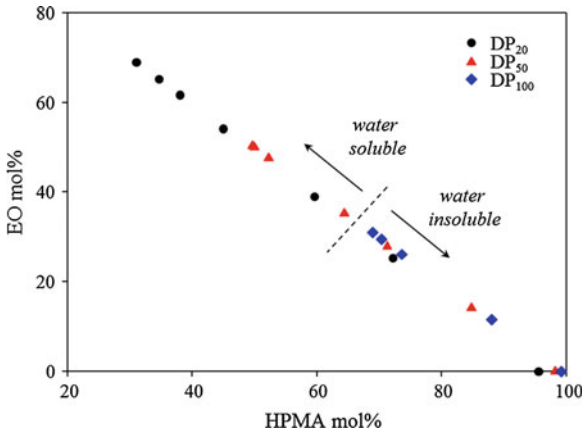

Fig. 5.8 The mol% of EO versus the HPMA mol% content of *hyp*-polydendrons and *hyp*-block copolymers from the DP_{20}, DP_{50} and DP_{100} series

introduce stability in physiologically relevant conditions more experiments would be needed in the region between 0 and 11.5 mol% EO. The values for the theoretical mol% and observed mol% via ^{1}H NMR of EO and HPMA are shown in the Appendix, Table A.12.

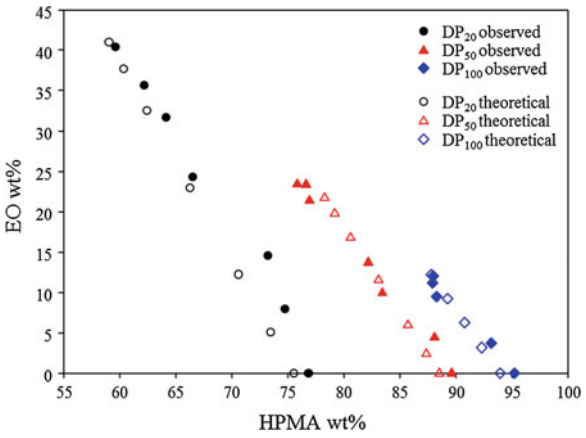

Fig. 5.9 The observed and theoretical EO wt% versus the HPMA wt% content of *hyp*-polydendrons and *hyp*-block copolymers from the DP_{20}, DP_{50} and DP_{100} series

The HPMA and EO mol% calculated via ^{1}H NMR spectroscopy analysis were used to calculate the HPMA and EO wt% present in each *hyp*-polydendron and *hyp*-block copolymer material. These observed values were compared to the theoretical values from the targeted composition. Figure 5.9 shows the observed and theoretical EO and HPMA wt% of the **G2′**:**2000PEG** materials. Some of the observed wt% values deviate from those calculated by theory somewhat. Therefore, when considering the water solubility of the materials, the observed EO and HPMA wt% and mol% values were more appropriate to understand and predict behaviour. The actual values for the theoretical wt% and observed wt% of EO and HPMA are shown in the Appendix, Table A.13.

The behaviour of the **G2′**:**2000PEG** *hyp*-polydendrons and *hyp*-block copolymers can also be described using a pseudo-phase diagram shown in Fig. 5.10, which shows the water solubility and insolubility as a function of the targeted mol% of EO monomer units versus the targeted DP_n of HPMA. The samples were classified in one of three ways; (a) being water insoluble and therefore nanoprecipitate, (b) being water soluble but measurable via DLS and (c) being water soluble but immeasurable via DLS. The dotted lines are used as this area of the plot is relatively undefined and therefore the exact placement of these lines is not known. Figure 5.11 classifies the samples in the same manner, however, showing the targeted DP_n of HPMA as a function of the **G2′** dendron initiator content highlighting how much dendron can be incorporated into the *hyp*-polydendrons to fit various criteria.

5.3 Dialysis of *Hyp*-polydendrons

To investigate the effect of various molecular weight fractions in the nanoprecipitation of *hyp*-polydendrons, fractionation was conducted using dialysis in a good solvent for the polymer. Therefore, by studying the different molecular weight fractions from dialysis, conclusions may be drawn regarding the mechanism of

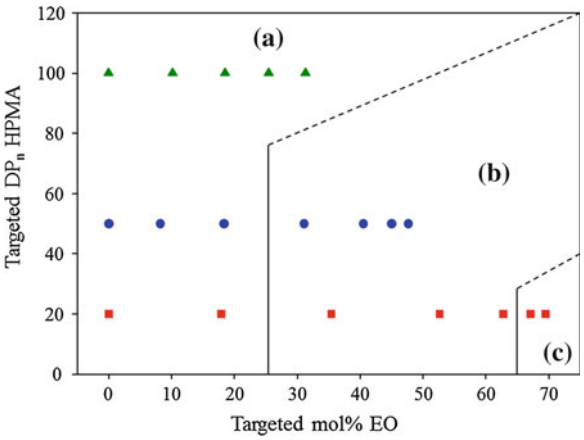

Fig. 5.10 Pseudo-phase diagram elucidated for the various **G2′**:**2000PEG** *hyp*-polydendrons and *hyp*-block copolymers, using targeted DP_n of HPMA versus targeted mol% of EO. Phase regions where the polymers are insoluble in water (**a**), water soluble but are detectable via DLS (**b**), and water soluble and undetectable via DLS (**c**)

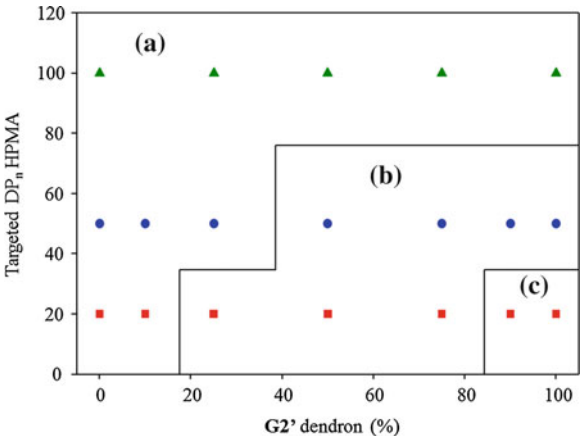

Fig. 5.11 Phase diagram elucidated for the various **G2′**:**2000PEG** *hyp*-polydendrons and *hyp*-polymers synthesised, using the targeted DP_n of HPMA versus **G2′** dendron content (%). Phase regions where the polymers are insoluble in water (**a**), water soluble but are detectable via DLS (**b**), and water soluble and undetectable via DLS (**c**)

nanoprecipitation and the role of the very high molecular weight material present within these samples. The two *hyp*-polydendron samples chosen for the dialysis experiment had already shown good nanoprecipitation behaviour and contained a broad range of molecular weight species when analysed by GPC. **G2′**-$pHPMA_{50}$-$EGDMA_{0.8}$ and **G2′**-$pHPMA_{100}$-$EGDMA_{0.8}$ (see Chap. 4, Sect. 4.3.2) were, therefore, dialysed against IPA utilising two different molecular weight cut off

Table 5.2 Molecular weights and Đ of **G2′**-pHPMA$_{50}$-EGDMA$_{0.8}$ and **G2′**-pHPMA$_{100}$-EGDMA$_{0.8}$ *hyp*-polydendrons, HMW and LMW fractions after dialysis in IPA and the equivalent linear-dendritic polymers **G2′**-pHPMA$_{50}$ and **G2′**-pHPMA$_{100}$

Sample		100 K MWCO			300 K MWCO		
		M_n (gmol^{-1})	M_w (gmol^{-1})	Đ	M_n (gmol^{-1})	M_w (gmol^{-1})	Đ
G2′-pHPMA$_{50}$	Linear	12,300	15,500	1.26	12,300	15,500	1.26
G2′-pHPMA$_{50}$-EGDMA$_{0.8}$	Original	115,700	1,538,000	13.3	115,700	1,538,000	13.3
	HMW	178,500	1,148,000	6.44	136,400	955,800	7.01
	LMW	13,300	23,400	1.75	14,000	21,700	1.55
G2′-pHPMA$_{100}$	Linear	28,500	40,400	1.42	28,500	40,400	1.42
G2′-pHPMA$_{100}$-EGDMA$_{0.8}$	Original	123,100	1,656,000	13.5	123,100	1, 656,000	13.5
	HMW	267,300	1,934,000	7.24	236,200	1,739,000	7.37
	LMW	21,700	35,600	1.64	21,600	37,900	1.75

(MWCO) dialysis membranes, 100,000 gmol^{-1} (100 K) and 300,000 gmol^{-1} (300 K). Each dialysis experiment was conducted over 3 days, with collection of the reservoir solvent at 24, 48 and 72 h which were combined. The polymer remaining inside the dialysis membrane was recovered and analysed by GPC, see Table 5.2. The dialysed polymer, within the dialysis membrane, is referred to as the high molecular weight (HMW) fraction below, and the polymer collected outside the dialysis membrane is referred to as the low molecular weight (LMW) fraction.

Perhaps somewhat surprisingly there appeared to be little to no difference in the polymer fractions collected from the 100 K MWCO membrane versus the 300 K MWCO membrane. The RI GPC overlays shown in Figs. 5.12 and 5.13 confirm this observation for the **G2′**-pHPMA$_{50}$-EGDMA$_{0.8}$ and **G2′**-pHPMA$_{100}$-EGDMA$_{0.8}$ polymers respectively. The traces observed for the 100 and 300 K HMW fractions almost overlay exactly, as do the 100 and 300 K LMW fractions. The LMW fractions were quite similar to the linear polymer equivalents reported in

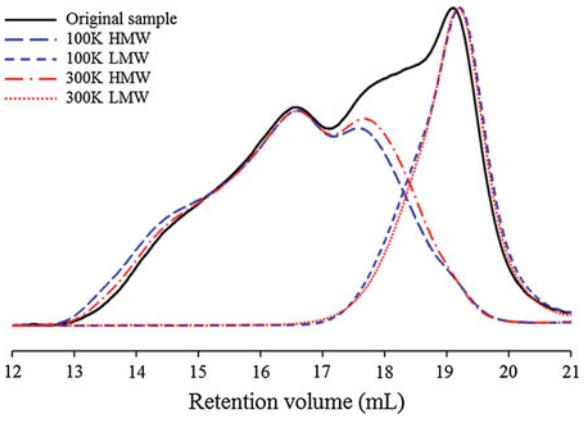

Fig. 5.12 GPC RI overlays for the **G2′**-pHPMA$_{50}$-EGDMA$_{0.8}$ *hyp*-polydendron, HMW and LMW fractions from dialysis experiments in IPA using 100 and 300 K MWCO dialysis membranes

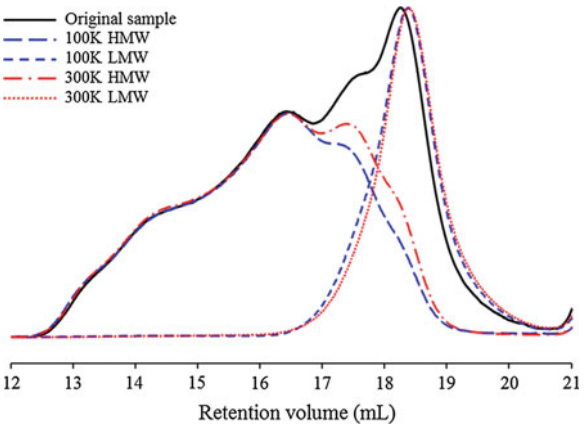

Fig. 5.13 GPC RI overlays for the **G2′**-pHPMA$_{100}$-EGDMA$_{0.8}$ *hyp*-polydendron, HMW and LMW fractions from dialysis experiments in IPA using 100 and 300 K MWCO dialysis membranes

Chap. 4 (Sect. 4.3.1), see Table 5.2. This suggests that dialysing these polymers in IPA has mainly removed the linear chains from the original samples to give a HMW fraction which contains a broad range of polymeric species with dispersities from 6.4 to 7.4. The removal of the predominantly linear species has also had a noticeable effect of the M_n and M_w values of the HMW fraction, as would be expected.

As the HMW fractions from the dialysis experiments in IPA afforded polymer fractions which were relatively similar in molecular weight to the original polymer samples a different solvent was chosen for the dialysis, to study the effect of the solvent, if any, on the resulting molecular weights of LMW and HMW fractions. **G2′**-pHPMA$_{50}$-EGDMA$_{0.8}$ was therefore dialysed against MeOH using the same 100 and 300 K MWCO dialysis membranes. Table 5.3 shows the molecular weights and dispersities for the LMW and HMW fractions form the dialysis in MeOH.

The GPC chromatogram overlays for the **G2′**-pHPMA$_{50}$-EGDMA$_{0.8}$ dialysis experiments in MeOH are shown in Fig. 5.14. Again, there was no significant difference between the 100 and 300 K MWCO dialysis membranes used, as molecular weights are similar and the GPC chromatograms overlay almost perfectly.

Evidently, when using MeOH as the dialysis solvent, higher molecular weight polymer species were able to cross the dialysis membrane, therefore the polymer

Table 5.3 Molecular weights and Đ of **G2′**-pHPMA$_{50}$-EGDMA$_{0.8}$ *hyp*-polydendron, HMW and LMW fractions after dialysis in MeOH and the equivalent linear-dendritic polymer **G2′**-pHPMA$_{50}$

Sample		100 K MWCO			300 K MWCO		
		M_n (gmol^{-1})	M_w (gmol^{-1})	Đ	M_n (gmol^{-1})	M_w (gmol^{-1})	Đ
G2′-pHPMA$_{50}$	Linear	12,300	15,500	1.26	12,300	15,500	1.26
G2′-pHPMA$_{50}$-EGDMA$_{0.8}$	Original	115,700	1,538,000	13.3	115,700	1,538,000	13.3
	HMW	761,200	2,326,000	3.06	615,800	1,990,000	3.23
	LMW	28,293	192,100	2.74	25,400	99,480	3.92

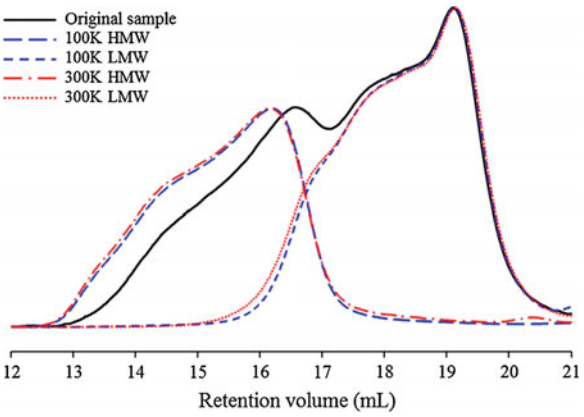

Fig. 5.14 GPC RI overlays for the **G2′**-pHPMA$_{50}$-EGDMA$_{0.8}$ *hyp*-polydendron, HMW and LMW fractions from dialysis experiments in MeOH using 100 and 300 K MWCO dialysis membranes

sample collected from the outside of the dialysis membrane in this experiment had higher molecular weights and a higher Đ than the equivalent sample when dialysed using IPA. The polymer sample collected from inside the dialysis membrane also had higher molecular weights and a much smaller Đ than the original sample. This effect may be due to either a variation in pore size within the dialysis membrane when solvated with the different solvents or a significant variation in solvated radius of the polymers in IPA and MeOH. Neither of these factors has been investigated in detail.

5.3.1 *Nanoprecipitations Using Various Molecular Weight Fractions*

The various molecular weight fractions obtained from the dialysis experiments were investigated for their behaviour under nanoprecipitation conditions (see Sects. 2.6, 3.4 and 4.4 in Chaps. 2, 3 and 4 respectively for previous nanoprecipitation experiments). Each sample collected in the dialysis experiments was nanoprecipitated using $\boldsymbol{i_5}$-$\boldsymbol{f_1}$, dissolving the polymers in THF as the volatile, good solvent and using water as the anti-solvent (see Chap. 4, Sects. 4.4.2 and 4.4.4 for previous nanoprecipitations conducted with the original polymer samples described here). Table 5.4 shows the D_z and PdI values for each as measured via DLS. In each case the HMW fractions formed nanoparticles with narrow PdIs, whereas the LMW fractions formed much larger particles with broader PdIs.

The size distribution by intensity traces for the LMW and HMW samples from the dialysis experiment conducted with the **G2′**-pHPMA$_{50}$-EGDMA$_{0.8}$ in IPA are shown in Fig. 5.15 for the 100 and 300 K MWCO dialysis membranes. Both of the HMW fractions had similar D_z (188 and 204 nm) and narrow polydispersities (0.070 and 0.095), whilst the LMW fractions gave nanoprecipitates with much larger D_z (620 and 767 nm) and broader PdIs (0.214 and 0.424).

Table 5.4 DLS measurements for the nanoprecipitations performed using the dialysed **G2′**-pHPMA$_{50}$-EGDMA$_{0.8}$ and **G2′**-pHPMA$_{100}$-EGDMA$_{0.8}$ *hyp*-polydendrons

Samples prepared (***i*$_5$-*f*$_1$**)		100 K MWCO		300 K MWCO	
		D_z (nm)	PdI	D_z (nm)	PdI
G2′-pHPMA$_{50}$	Linear	882	0.241	882	0.241
G2′-pHPMA$_{50}$-EGDMA$_{0.8}$	*Original—before dialysis*			*64*	*0.211*
	HMW$_{IPA}$	188	0.070	204	0.095
	LMW$_{IPA}$	620	0.214	767	0.424
	HMW$_{MeOH}$	158	0.041	136	0.068
	LMW$_{MeOH}$	–[a]	–[a]	–[a]	–[a]
G2′-pHPMA$_{100}$	Linear	250	0.035	250	0.035
G2′-pHPMA$_{100}$-EGDMA$_{0.8}$	*Original—before dialysis*			*329*	*0.022*
	HMW$_{IPA}$	164	0.041	166	0.047
	LMW$_{IPA}$	506	0.111	727	0.248

[a]Samples could not be measured by DLS as they had precipitated out of solution
D_z z-average diameter

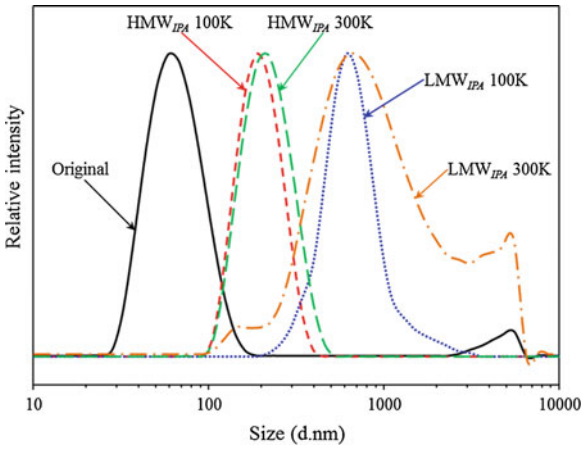

Fig. 5.15 DLS size distribution by intensity traces for the nanoprecipitations (***i*$_5$-*f*$_1$**) of the HMW and LMW fractions of **G2′**-pHPMA$_{50}$-EGDMA$_{0.8}$ dialysed in IPA with the 100 and 300 K MWCO dialysis membranes

These LMW nanoprecipitations had given D_z and PdIs that were much closer to the linear polymer equivalent when nanoprecipitated (see Sect. 4.4.1). The **G2′**-PHPMA$_{50}$ nanoprecipitation at ***i*$_5$-*f*$_1$** gave a D_z of 882 nm and PdI of 0.241.

The size distribution by intensity traces for the nanoparticle samples prepared from the dialysed fractions of **G2′**-pHPMA$_{100}$-EGDMA$_{0.8}$ in IPA are shown in Fig. 5.16. The HMW nanoprecipitates have almost identical D_z from both the 100 K (164 nm) and 300 K (166 nm) MWCO dialysis membranes, and narrow polydispersities (0.041 and 0.047). Again both of the LMW fractions gave nanoparticles that were much larger in D_z with broader polydispersities (100 K MWCO–506 nm, PdI = 0.111; 300 K MWCO–727 nm, PdI = 0.248). The linear-dendritic polymer equivalent nanoprecipitation using **G2′**-pHPMA$_{100}$ gave a D_z of 250 nm and PdI

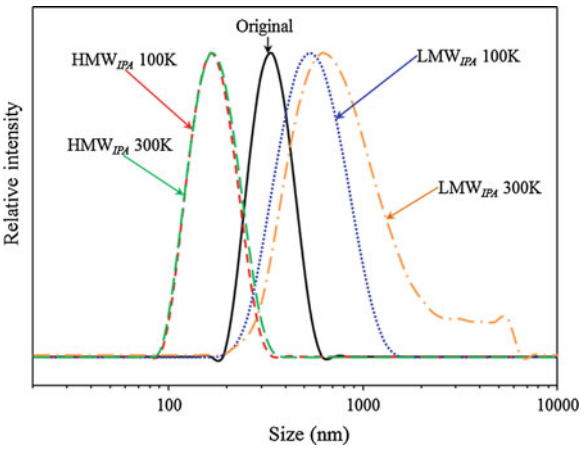

Fig. 5.16 DLS size distribution by intensity traces for the nanoprecipitations of the HMW and LMW fractions of **G2′**-pHPMA$_{100}$-EGDMA$_{0.8}$ dialysed in IPA with the 100 and 300 K MWCO dialysis membranes

of 0.035. Therefore the LMW fraction nanoprecipitations did not give as similar results with the DP$_{100}$ *hyp*-polydendron as with the DP$_{50}$.

The nanoprecipitations using the dialysed **G2′**-pHPMA$_{50}$-EGDMA$_{0.8}$ *hyp*-polydendron in MeOH also gave nanoparticles with narrow polydispersities when the HMW fractions were used. Figure 5.17 shows the size distribution by intensity traces for these samples. The 100 K MWCO HMW fraction had a D_z of 158 nm and PdI of 0.014, whilst the 300 K MWCO HMW fractions was 136 nm in diameter with a polydispersity of 0.068. When the LMW fractions were nanoprecipitated under the same conditions, they both precipitated out of solution and therefore were not suitable for measurement via DLS.

Therefore from the various nanoprecipitations conducted using different molecular weight fractions of the original *hyp*-polydendron samples, it can be proposed that the highly branched high molecular weight fractions of the samples gave better nanoparticles than when the lower molecular weight fractions were

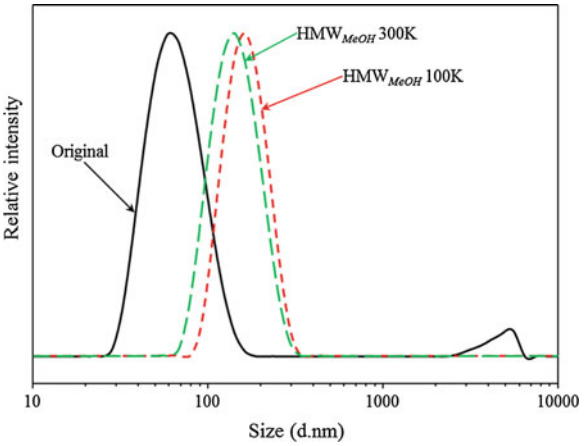

Fig. 5.17 DLS size distribution by intensity traces for the nanoprecipitations of the HMW and LMW fractions of **G2′**-pHPMA$_{50}$-EGDMA$_{0.8}$ dialysed in MeOH with the 100 and 300 K MWCO dialysis membranes

used. This suggests that the presence of the higher molecular weight polymer species could improve the nanoprecipitation of linear polymer samples, as in all the original *hyp*-polydendron samples the full range of various molecular weight species is present and the high molecular weight material may be acting as the nucleation points for successful nanoprecipitation. The ATRP branching mechanism, as discussed previously [1], does not lead to a fully branched sample and, despite the presence of linear polymers within the *hyp*-polydendron and *hyp*-polymer samples, near monodisperse and stable nanoprecipitates are formed. The material directing the nanoprecipitation mechanism is probably not the linear fraction, and is more likely to be the higher molecular weight branched polymer species within the distribution. To determine the validity of this hypothesis, an experiment was conducted where the highest molecular weight fraction from the dialysis experiments was mixed with the linear equivalent polymer in varying ratios prior to nanoprecipitation. It was hoped that this would determine the impact of the HMW polymer and the amount of such material that would be required to induce the stable nanoprecipitation observed with many of the *hyp*-polydendron and *hyp*-polymer samples discussed in this thesis.

5.3.2 Co-nanoprecipitation of Linear and High Molecular Weight Polymer Fractions

The HMW fraction chosen for blending with linear polymer samples was the HMW_{MeOH} collected from the 100 K MWCO membrane during dialysis of the **G2′**-$pHPMA_{50}$-$EGDMA_{0.8}$ *hyp*-polydendron (M_n = 761,200 $gmol^{-1}$, M_w = 2,326,000 $gmol^{-1}$, Đ = 3.06). This fraction had the highest molecular weight and was shown to nanoprecipitate to form nanoparticles with narrow polydispersities. This was mixed at various wt% values with the **G2′**-$pHPMA_{50}$ linear-dendritic polymer, utilising THF as the good solvent, which has been studied under various nanoprecipitation conditions (see Chap. 4, Sect. 4.4.1); under $\boldsymbol{i_5}$-$\boldsymbol{f_1}$ conditions nanoprecipitates with a D_z of 882 nm and PdI of 0.241 were previously seen. Addition of the mixed *hyp*-polydendron and the linear-dendritic hybrid polymers to an anti-solvent can be described as co-nanoprecipitation and Table 5.5 shows the results of the co-nanoprecipitations as measured via DLS.

There is a general trend observed from the co-nanoprecipitations; increasing the wt% of HMW polymer within the experiment led to a considerable decrease in the D_z observed, with the exception of the 95:5 Linear:HMW wt% sample. This can also be seen in Fig. 5.18 where the D_z is plotted with increasing the HMW wt% present. There does not appear to be trend in the PdI across the series, however, when HMW polymer was introduced to the linear the PdI values were lower and remained below 0.11, showing the impact of the presence of the high molecular weight material on directing and controlling the nanoprecipitation to produce near monodisperse, uniform nanoparticles.

Table 5.5 DLS measurements of samples with varying ratios of linear: HMW polymer wt% using nanoprecipitation conditions ***i*$_5$-*f*$_1$**

Linear G2′-pHPMA$_{50}$ (wt%)	**HMW$_{MeOH}$ G2′**-pHPMA$_{50}$-EGDMA$_{0.8}$ (wt%)	D_z (nm)	PdI
100	0	672	0.215
99	1	198	0.034
97.5	2.5	191	0.034
95	5	346	0.110
92.5	7.5	177	0.072
90	10	182	0.089
80	20	166	0.062
70	30	167	0.101
60	40	150	0.045
50	50	157	0.110
0	100	145	0.075

D_z z-average diameter

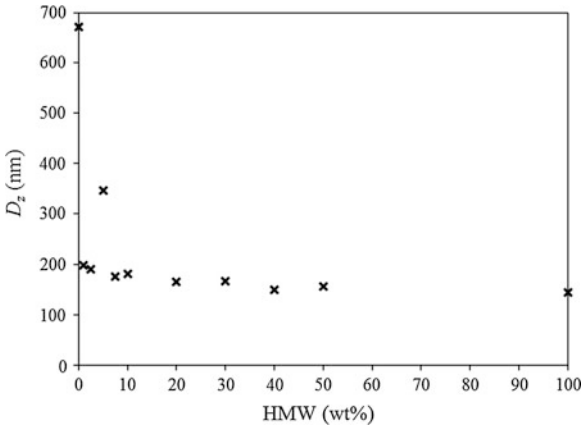

Fig. 5.18 Variation in D_z with varying the ratio of Linear:HMW polymer co-nanoprecipitations; see Table 5.5

A selection of the DLS size distribution by intensity traces for the Linear:HMW co-nanoprecipitations are shown in Fig. 5.19, showing the decrease in size with increasing HMW fraction wt%. This suggests that the HMW fraction does have an influence on the formation of nanoparticles via nanoprecipitation, even at very low concentrations. The huge difference in nanoprecipitation behaviour with the inclusion of just 1 wt% of HMW *hyp*-polydendron also supports the previous discussion about the similarity of nanoprecipitation behaviour of *hyp*-polydendrons with the same ratio of initiators but with different molecular weights (see Chap. 3, Sect. 3.4.1). It is proposed that the actual molecular weight of the polymer sample does not affect the resulting nanoprecipitate size. This may be due to a very low, but critical concentration of HMW highly branched polymer required to direct the nanoprecipitation process (<1 wt%). Therefore, even though lower molecular weight samples contain less HMW polymer, the presence of the small fraction of

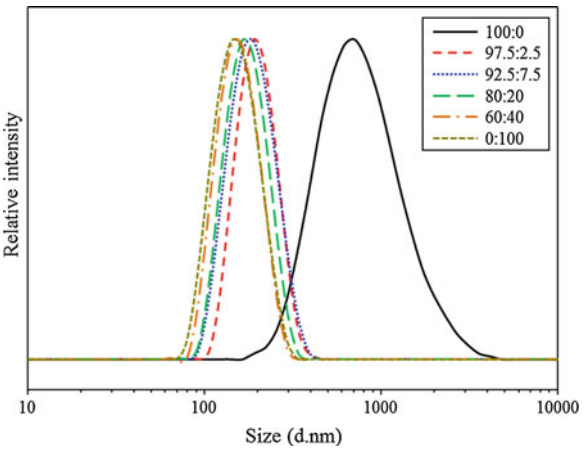

Fig. 5.19 DLS size distribution by intensity traces for various mixtures of Linear:HMW polymer co-nanoprecipitations, see Table 5.5 and Fig. 5.18

highly branched material lead to an unaffected nanoprecipitation. This is corroborated by the results discuss here, as the variation of HMW material from 1 to 100 wt% leads to D_z variations of only 198–145 nm. Therefore as long as a minimum amount is used, it would appear that the nanoparticles formed would be smaller and more monodisperse than the corresponding linear nanoprecipitations.

It was worth noting that separate dialysis experiments were conducted using a different **G2′**-pHPMA$_{100}$-EGDMA$_{0.8}$ and the mass of each molecular weight fraction collected was recorded. When IPA was used as the dialysis solvent the HMW fraction constituted 92 % of the total mass dialysed, whilst the LMW fraction was only 8 % of the total mass. When MeOH was used as the dialysis solvent the HMW fraction was 30 % of the total mass dialysed, whilst the LMW was 70 %.

5.4 Nanoprecipitation of Linear Versus Branched *Hyp*-block Copolymers

When the **2000PEG**-pHPMA$_{100}$ linear A-B block copolymer was initially synthesised the resulting molecular weights were higher than expected and the GPC chromatograms indicated that low levels of branching had occurred due to higher molecular weight species observed in the RALS chromatograms. Therefore the HPMA monomer was purified via column chromatography to remove any potential dimethacrylate impurity, and the purified monomer was used to re-synthesise the **2000PEG**-pHPMA$_{100}$ sample discussed in Chap. 4. The molecular weights (GPC) of the two **2000PEG**-pHPMA$_{100}$ polymers, synthesised with purified and unpurified monomer, are shown in Table 5.6, with the molecular weights of the corresponding **2000PEG**-pHPMA$_{100}$-EGDMA$_{0.8}$ *hyp*-block copolymer. The **2000PEG**-pHPMA$_{100}$ polymer synthesised with the purified HPMA will be described as the 'linear' sample, the **2000PEG**-pHPMA$_{100}$ synthesised using the unpurified HPMA

Table 5.6 GPC molecular weights and Đ for the **2000PEG** initiated DP_{100} linear, slightly branched and branched polymers

Sample	Name	GPC (DMF)		
		M_n ($gmol^{-1}$)	M_w ($gmol^{-1}$)	Đ
2000PEG-$pHPMA_{100}$[a]	Linear	22,400	27,800	1.24
2000PEG-$pHPMA_{100}$	Slightly branched	29,700	75,500	2.54
2000PEG-$pHPMA_{100}$-$EGDMA_{0.8}$	Branched	53,900	335,300	6.23

[a]Purified HPMA used

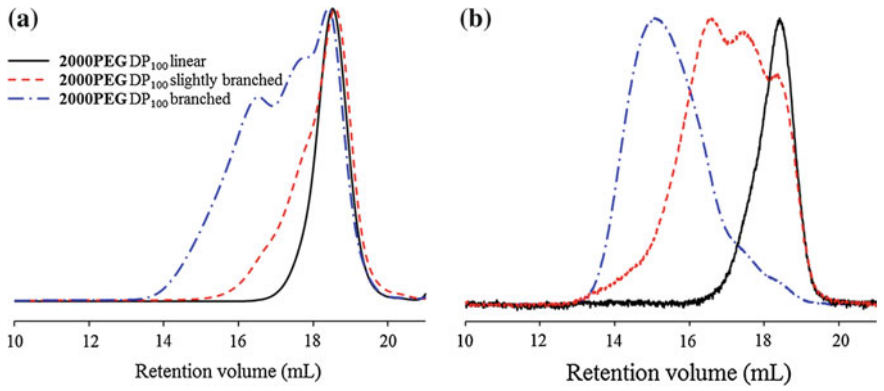

Fig. 5.20 GPC chromatogram overlays of **a** RI and **b** RALS detectors for the **2000PEG** DP_{100} linear, slightly branched and branched samples

will be described as 'slightly branched' and the **2000PEG**-$pHPMA_{100}$-$EGDMA_{0.8}$ as the 'branched' sample.

The RI and RALS GPC chromatogram overlays are shown in Fig. 5.20 for these **2000PEG** initiated DP_{100} linear, slightly branched and branched polymers. It is clear from the GPC overlays that the slightly branched sample does not just contain linear chains due to the broad peak visible on the RALS chromatogram (Fig. 5.20b).

These three samples were subjected to the same nanoprecipitation techniques described previously; by dissolving the polymers in THF, a good solvent, and adding them to an anti-solvent for the pHPMA polymer chain. As the **2000PEG** initiator is hydrophilic, any resulting nanoparticles are provided with a degree of steric stabilisation. The nanoprecipitations were performed with initial concentrations of 25, 10, 5 and 1 mg/mL and two *df*; 0.2 and 0.01; see Table 5.7 for the D_z and PdIs.

The D_z were plotted against increasing initial nanoprecipitate concentration ($\boldsymbol{i_x}$) for each *df* to study differences between each sample, see Fig. 5.21. For nanoprecipitations with a *df* of 0.2 the variation in D_z between the linear, slightly branched and branched samples is large, showing that the linear sample has larger D_z across all concentrations, whilst the slightly branched and branched samples are much

Table 5.7 DLS measurements for the nanoprecipitations of the **2000PEG** DP_{100} linear, slightly branched and branched polymers

Nanoprecipitation conditions			Linear		Slightly branched		Branched	
i_x (mg/mL)	f_y (mg/mL)	*df*	D_z (nm)	PdI	D_z (nm)	PdI	D_z (nm)	PdI
25	5	0.2	712	0.221	260	0.250	363	0.267
10	2	0.2	336	0.130	142	0.098	176	0.173
5	1	0.2	276	0.112	115	0.055	128	0.074
1	0.2	0.2	179	0.190	106	0.101	87	0.052
25	0.25	0.01	139	0.183	146	0.209	155	0.228
10	0.1	0.01	101	0.127	98	0.105	107	0.136
5	0.05	0.01	79	0.135	78	0.124	85	0.133
1	0.01	0.01	*	*	62	0.329	52	0.250

D_z z-average diameter *sample was not suitable for measurement by DLS due to a low detection of scattered light

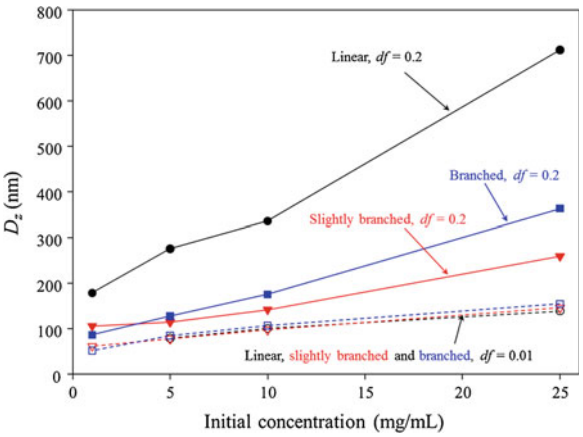

Fig. 5.21 D_z of **2000PEG** initiated DP_{100} linear, slightly branched and branched nanoprecipitation samples with varying final concentrations with *df* = 0.2; linear (*black filled circles*), slightly branched (*red filled triangles*), branched (*blue filled squares*) and *df* = 0.01; linear (*black open circles*), slightly branched (*red open triangles*), branched (*blue open squares*)

more similar in D_z. This suggests with only a low amount of branching present in the polymer sample the nanoprecipitation behaviour is similar to polymers with higher molecular weights and more branching present.

However, when comparing the **2000PEG** initiated DP_{100} linear, slightly branched and branched samples with *df* = 0.01, the resulting nanoparticle sizes observed are very similar for each of these samples. This suggests that the final concentration or *df* also has an effect on the formation of nanoparticles irrespective of polymer morphology.

5.5 FRET Experiments

The nanoprecipitations performed using the hydrophobic *hyp*-polydendrons have been shown to encapsulate various hydrophobic molecules, such as pyrene, Nile red and fluoresceinamine (see Chap. 3, Sect. 3.4.5 for pyrene and Nile red. See Chap. 4, Sect. 4.4.5 for fluoresceinamine). It was hypothesised that more than one type of molecule could be encapsulated in the nanoparticles via nanoprecipitation, therefore a fluorescence spectroscopy technique was employed to assess whether two different molecules could be encapsulated in the same nanoparticle.

Förster resonance energy transfer (FRET) is the transfer of energy from a donor fluorophore in the excited state to an acceptor fluorophore through non-radiative dipole-dipole coupling. The efficiency of the energy transfer is inversely proportional to the sixth power of the distance between the donor and the acceptor, therefore FRET is extremely sensitive to variations in distance between the fluorophores [2, 3]. This is represented graphically in Fig. 5.22, showing (A) FRET when the donor and acceptor fluorophores are within 10 nm of each other and (B) when they are more than 10 nm apart no FRET is observed [4]. When FRET is highly efficient only emission from the acceptor fluorophore is observed and no emission is observed from the donor fluorophore. One pair of FRET dyes commonly used is 3,3′-dioctadecyloxacarbocyanine perchlorate (DiO) and 1,1′-dioctadecyl-3,3,3′,3′-tetramethylindocarbocyanine perchlorate (DiI), where DiO is the

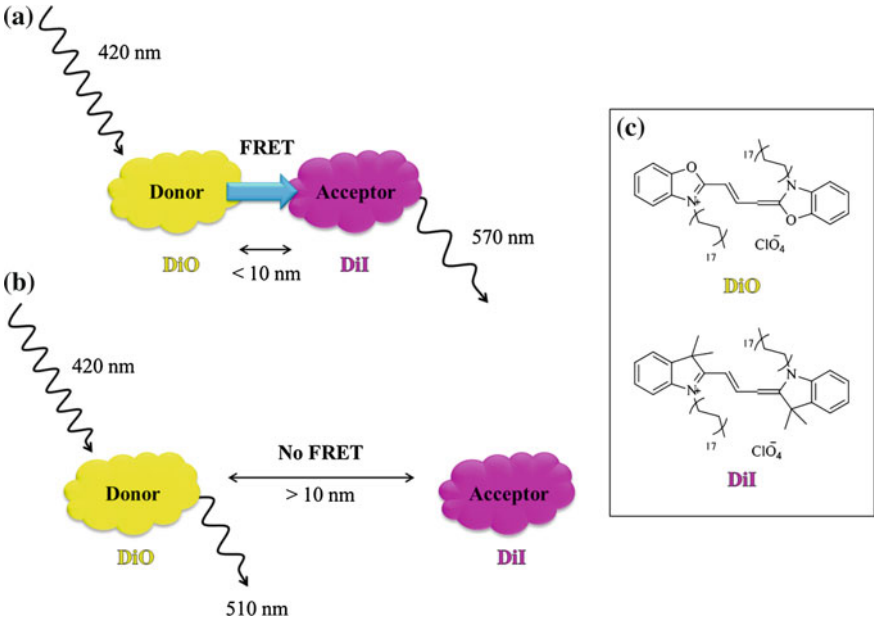

Fig. 5.22 Graphical representation of FRET, with DiO as the donor and DiI as the acceptor fluorophore showing **a** with FRET, **b** no FRET and **c** the DiO and DiI chemical structures

donor fluorophore and DiI is the acceptor fluorophore [5]. The chemical structures of these two dyes are shown in Fig. 5.22c.

FRET has wide range of applications in biological systems; it has been used to elucidate molecular interactions in membranes, to study protein structure and protein-protein interactions in solution and to investigate nucleic acids and nucleic acid-protein complexes, as well as enhancing microscopy studies [3, 4]. More recently FRET has been applied to systems involving polymeric micelles to detect the cellular uptake of the micelles and stability as the FRET signal is lost upon breakdown of the micelles [6]. FRET has also been applied in the study of multi-component organic nanoparticles to assess cellular uptake of whole particles, as a loss of FRET signal implies the dissolution or breakdown of mixed nanoparticles [5].

Here the DiO/DiI FRET pair has been used to ascertain whether more than one molecule can be loaded into the nanoparticles produced by nanoprecipitation of *hyp*-polydendrons, as FRET will be observed if the fluorophores are indeed located within the same particle. The *hyp*-polydendron chosen for this study was the **G2:750PEG**-50:50-pHPMA$_{50}$-EGDMA$_{0.8}$ (see Chap. 3) as it has previously been shown to nanoprecipitate with successful loading of both Nile red and pyrene.

The **G2:750PEG**-50:50-pHPMA$_{50}$-EGDMA$_{0.8}$ was nanoprecipitated with an initial concentration of 5 mg/mL and a final concentration of 1 mg/mL (***i*$_5$-*f*$_1$**). This was repeated with encapsulation of either DiO, DiI or a 1:1 mixture of DiO:DiI. Three different levels of loading of the dye molecules were prepared with the D_z and PdI values for these samples shown in Table 5.8. The highest loading achieved in each case was 2 w/w%, the size distribution by intensity DLS traces for each sample are shown in Fig. 5.23. Loading of the nanoparticles with DiO, DiI and a 1:1 mixture of the two dyes was achieved by dissolving the dyes in the organic solvent (THF) with the *hyp*-polydendron before nanoprecipitation into water.

Loading the samples with each dye resulted in an increase in D_z from 115 nm for the blank sample, to 193 nm for the DiO loaded, 143 nm for the DiI loaded and 156 nm for the dual loaded nanoparticles. The PdI values remained low (<0.050; blank sample PdI = 0.067) and the zeta potentials of each nanoprecipitates were very similar and negative, indicating charge stabilisation as discussed previously.

Table 5.8 D_z, PdI and zeta potential for various dye loaded nanoparticles using the **G2:750PEG**-50:50-pHPMA$_{50}$-EGDMA$_{0.8}$ *hyp*-polydendron

G2:750PEG (50:50) 1 mg/mL	1 w/w% (0.01 mg/mL)		2 w/w% (0.02 mg/mL)			5 w/w% (0.05 mg/mL)	
	D_z (nm)	PdI	D_z (nm)	PdI	Zeta Potential (mV)	D_z (nm)	PdI
Blank	115	0.067	115	0.067	−28.2	115	0.067
DiO	128	0.066	193	0.024	−48.3	476	0.101
DiI	101	0.086	143	0.048	−47.6	–	–
Dual (1:1)	109	0.077	156	0.040	−47.4	–	–

D_z z-average diameter

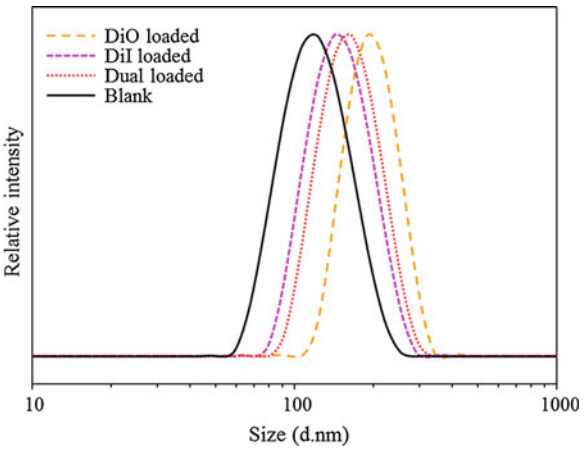

Fig. 5.23 DLS size distribution by intensity traces for the blank and DiO, DiI and dual loaded nanoparticles formulated with $\boldsymbol{i_5\text{-}f_1}$ with **G2**:**750PEG**-50:50-pHPMA$_{50}$-EGDMA$_{0.8}$ *hyp*-polydendronõ

These samples were analysed by fluorescence spectroscopy, see Fig. 5.24. The individual DiO and DiI loaded nanoparticles were excited at 420 nm, as was the dual loaded nanoparticles. Each sample was diluted with distilled water so that the final concentration of each dye was 0.005 mg/mL. The DiO loaded particles had an emission maxima at 509 nm, when excited at 420 nm, whilst the DiI loaded particles only showed very small emission maxima at 570 nm. Ideally, the excitation wavelength should only excite the donor fluorophore (DiO) and not the acceptor (DiI), allowing acceptor emission wavelength to be solely attributed to FRET. However, the most suitable excitation wavelength for this experiment was found to be 420 nm; at lower wavelengths the donor (DiO) did not show sufficient emission and higher wavelengths led to unacceptably high acceptor emission (DiI).

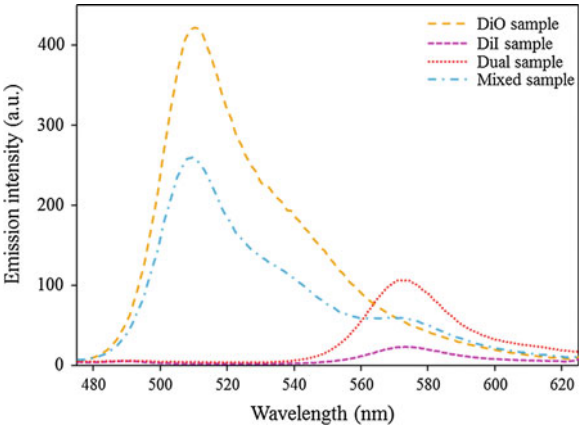

Fig. 5.24 Fluorescence spectra for the DiO, DiI and dual loaded **G2**:**750PEG**-pHPMA$_{50}$-EGDMA$_{0.8}$ nanoparticles and a 1:1 mixture of DiO and DiI loaded nanoparticles at t = 0 of mixing, diluted to a concentration of 0.005 mg/mL for each dye, exciting at 420 nm

Under these conditions, FRET is considered to occur if an increase in emission at 570 nm is seen.

The fluorescence spectrum for the nanoprecipitate sample containing both fluorophores (dual sample) clearly shows a FRET signal as no emission was observed from DiO (509 nm) and only emission at 570 nm (for the DiI) was seen. Energy transfer from the DiO in the excited state to the DiI, within the nanoprecipitates, was obviously efficient and the dyes clearly in close proximity (<10 nm). This strongly indicates that the two dye molecules were located within the same nanoparticle. A mixture of the DiO loaded and DiI loaded nanoparticles, in a ratio of 1:1 (mixed sample; 1 mL of each sample), was measured immediately after mixing, and a strong emission peak at 509 nm was observed with a smaller peak at 570 nm. This indicates that some FRET may be occurring, however, as the dyes are located in different nanoparticles the distance between them would be expected to be >10 nm on average and only a poor energy transfer was observed.

FRET can be quantified by calculating the FRET ratio, as described in Eq. (5.1) below, where I_{DiO} and I_{DiI} are the fluorescence intensities at 509 and 570 nm respectively when exciting the samples at 420 nm.

$$FRET\ ratio = \frac{I_{DiI}}{(I_{DiO} + I_{DiI})} \tag{5.1}$$

Therefore if energy transfer is 100 % efficient, the FRET ratio has a maximum value of 1; conversely, if no FRET is observed the observed FRET ratio will be 0. The FRET ratios corresponding to Fig. 5.24 for each sample were: DiO = 0.127, DiI = 0.894, the dual sample = 0.947 and mixed sample = 0.188. The DiO sample had a low FRET ratio and did not show FRET as there was only donor present and no acceptor. The DiI sample did not show FRET; the FRET ratio appears high as a consequence of the absent signal from the donor. The dual sample showed the highest FRET ratio, which was expected as the two dyes were mixed before nanoprecipitation and therefore were encapsulated inside the nanoparticles. The mixed sample had a low FRET ratio (immediately after mixing) as the two dyes are located within separate nanoparticles as they were prepared as individually loaded nanoparticles; this figure may be artificially high due to the inherent emission from DiI when excited at this wavelength.

5.5.1 Study of FRET Over Time in Mixed DiO and DiI Samples

The FRET ratio of the mixed sample was studied at ambient temperature over time to assess whether the dyes could pass between particles or whether aggregation of nanoprecipitates would lead to the induction of a FRET signal. It was predicted that as the dyes were hydrophobic and had very limited water solubility, they would remain in the nanoparticle cores and the FRET ratio would not change over time.

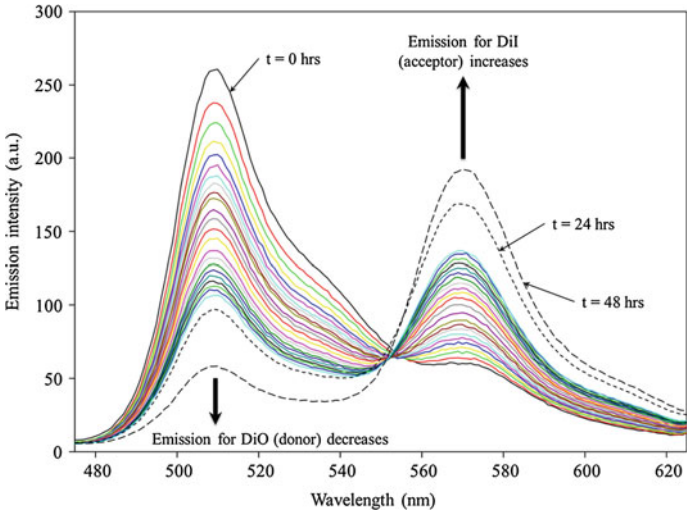

Fig. 5.25 Fluorescence spectra overlays over time after mixing equal volumes of the DiO and DiI loaded **G2**:**750PEG**-pHPMA$_{50}$-EGDMA$_{0.8}$ samples, to give a final concentration of 0.005 mg/mL of each fluorophore, exciting at 420 nm

Figure 5.25 shows the fluorescence emission spectra for this experiment; mixing the samples at t = 0 and taking measurements every 30 min for the first 4 h, then every hour for 18 h, then two further measurements were made at 24 and 48 h. The experiment did show a dramatic change in the fluorescence spectra, which was unexpected; the emission observed for the donor (DiO) at 509 nm decreased and the emission observed at 570 nm for the acceptor (DiI) increased.

This suggested that the two fluorophores were moving between nanoparticles to change the fluorescence spectra observed. The FRET ratio for each measurement was calculated and the change in the FRET ratio over time can be seen in Fig. 5.26.

The FRET ratio at t = 0 was 0.188, which increased to 0.768 after 48 h of mixing the samples. Another measurement was performed after a further 7 days, where the FRET ratio had increased to 0.931, almost as high as the dual component sample prepared by incorporating both dyes into the solution with the polymer. DLS measurements were performed on the mixed sample at various time points; t = 0, t = 48 h and t = 9 days. The DLS size distribution by intensity traces for each of these samples can be seen in Fig. 5.27. The D_z and PdI values remained extremely similar over the course of the experiment, therefore, the FRET ratio is probably not increasing due to aggregation of particles. The appearance of the sample had changed over time, see Fig. 5.28 for photographs of each sample. Figure 5.28a, b shows the DiO loaded nanoparticles and DiI loaded nanoparticles respectively, diluted to 0.005 mg/mL fluorophore concentration. Figure 5.28c shows the dual loaded sample diluted to a final concentration of 0.005 mg/mL of DiO and DiI (i.e. overall 0.01 mg/mL total concentration of fluorophores). The mixed sample at t = 0

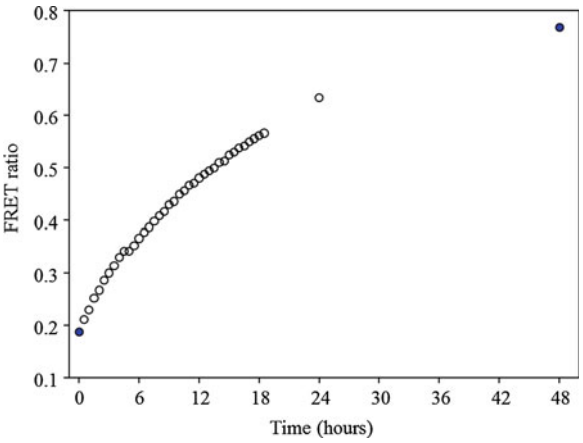

Fig. 5.26 FRET ratio over time after mixing equal volumes of the DiO and DiI loaded **G2**:**750PEG**-pHPMA$_{50}$-EGDMA$_{0.8}$ samples, to give a final concentration of 0.005 mg/mL of each fluorophore. *Filled circles* represent time points when the sample was also measured by DLS

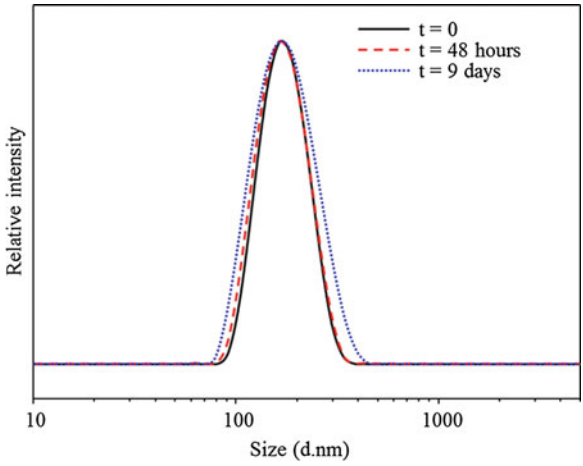

Fig. 5.27 DLS size distribution by intensity traces for the mixed DiI and DiO loaded **G2**:**750PEG**-pHPMA$_{50}$-EGDMA$_{0.8}$ samples over time

(Fig. 5.28d) and after 9 days (Fig. 5.28e) had slightly different shades of pink, perhaps indicating the movement of the fluorophores.

To rule out the possibility of movement of dye between particles by dissolution into the water, a dialysis experiment was conducted where the donor (DiO) loaded particles were placed inside the dialysis membrane and the acceptor (DiI) loaded particles were placed outside of the dialysis membrane. The dialysis membrane used had a MWCO of 2,000 gmol^{-1}, therefore it can be assumed that only small molecules would be able to cross the membrane, and not the nanoparticles. This would either confirm or deny the possibility of the dye molecules moving between

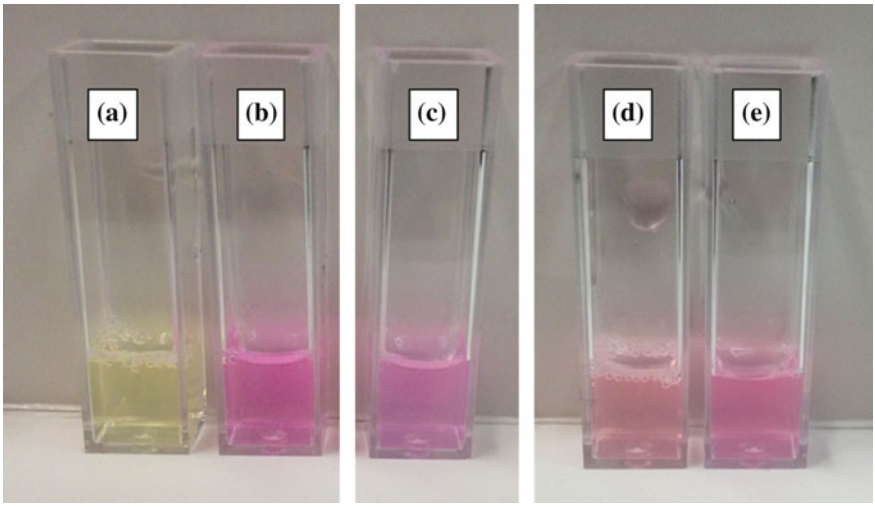

Fig. 5.28 Photographs of various DiO and DiI loaded nanoparticles; **a** DiO loaded, **b** DiI loaded, **c** dual loaded, **d** mixed sample t = 0 and **e** mixed sample at t = 9 days

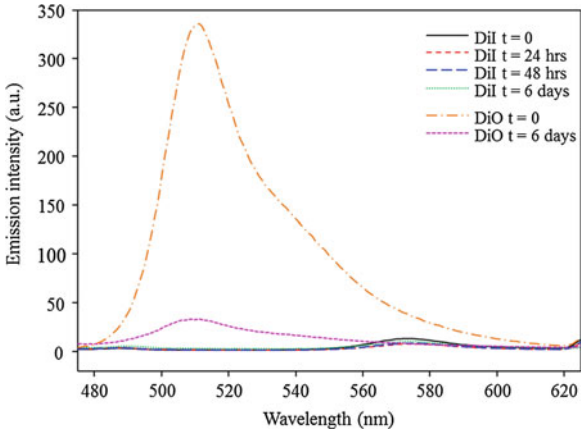

Fig. 5.29 Fluorescence spectra for DiI and DiO loaded **G2**:**750PEG**-pHPMA$_{50}$-EGDMA$_{0.8}$ samples taken over time during dialysis experiment

particles by transport through the water. Samples were taken at various time points from outside of the dialysis membrane and measured by DLS to ensure the nanoparticles were still intact and by fluorescence spectroscopy to monitor any change in the emission at 570 nm, corresponding to the DiI emission. As the emission at 570 nm was low when exciting the DiI loaded nanoparticles at 420 nm, if the DiO was diffusing out of the dialysis membrane and entering the DiI loaded particles outside of the membrane, an increase in the emission at 570 nm would be observed due to an increase in FRET.

The fluorescence spectra for the dialysis experiment are shown in Fig. 5.29. There appears to be no increase in emission at 570 nm over time, therefore suggesting that there is no movement of dye across the dialysis membrane. The decrease in intensity observed for the DiO sample after 6 days could be attributed to loss of material due to adherence of the nanoprecipitates to the dialysis tubing and therefore a loss in fluorescence emission, or the effect of bleaching of the fluorophore.

The water insolubility of the two dyes was also shown by attempting to dissolve each dye in water at the same concentration present in the nanoparticles (0.02 mg/mL). The samples were rolled for 7 days and analysed by fluorescence spectroscopy, exciting at 420 nm, and very little emission was observed due to the minimal water solubility of DiO and DiI (see Appendix Fig. A.43).

The mechanism of the dye movement between nanoparticles was not clear and requires further investigation. One possible explanation could be the movement of polymer macromolecules between nanoparticles in a dynamic manner with encapsulated dye molecules, which would therefore facilitate the movement of dye molecules from one nanoparticle to another.

5.6 Conclusions

In this chapter the varying **G2′**:**2000PEG** initiator content in the previously described series of *hyp*-polydendrons and *hyp*-block copolymers was further studied, with the samples showing defined separation when water solubility was investigated. The pseudo-phase diagrams show the three different categories of materials that have been synthesised; water-insoluble, water-soluble and detectable by DLS and water-soluble and undetectable by DLS. This would aid in future investigations of the ratio of **2000PEG** needed to introduce salt stability into the subsequently formulated particles, without introducing too much to inhibit nanoprecipitation.

The separation of various molecular weight *hyp*-polydendrons was also investigated, showing that, via a dialysis technique, the molecular weights could be tuned somewhat by using different dialysis solvents. The subsequently isolated high molecular weight *hyp*-polydendron fractions were further investigated in the production of co-nanoparticles formulated via the co-nanoprecipitation of the linear-dendritic polymer equivalent and high molecular weight branched polymers. These results suggested that the HMW fraction considerably influences the nanoprecipitation behaviour of the polymers.

The FRET experiments showed that the encapsulation of two different hydrophobic molecules was successful with an increase in FRET observed with dual loaded nanoparticles, over that observed when simply mixing the two singly loaded DiO and DiI particles. However, further study of the mixture of the two singly loaded nanoparticles showed that the FRET ratio increased over time, indicating the movement of DiO and or DiI between nanoparticles. Dialysis and water solubility

experiments ruled out the movement of dye between particles via the water the particles were dispersed in, therefore suggesting movement of dye molecules via collisions of nanoparticles.

References

1. I. Bannister, N.C. Billingham, S.P. Armes, S.P. Rannard, P. Findlay, Macromolecules **39**, 7483–7492 (2006)
2. P.G. Wu, L. Brand, Anal. Biochem. **218**, 1–13 (1994)
3. R.M. Clegg, Curr. Opin. Biotechnol. **6**, 103–110 (1995)
4. E.A. Jares-Erijman, T.M. Jovin, Nat. Biotechnol. **21**, 1387–1395 (2003)
5. T.O. McDonald, P. Martin, J.P. Patterson, D. Smith, M. Giardiello, M. Marcello, V. See, R.K. O'Reilly, A. Owen, S. Rannard, Adv. Funct. Mater. **22**, 2469–2478 (2012)
6. S.-Y. Lee, J.Y. Tyler, S. Kim, K. Park, J.-X. Cheng, Mol. Pharmaceut **10**, 3497–3506 (2013)

Chapter 6
Conclusions and Future Work

6.1 Synthesis and Characterisation of *Hyp*-polydendron Materials and Subsequent Nanoparticle Formation

Chapter 2 demonstrated the synthesis of G1 and G2 dendrons which were subsequently transformed into initiators for ATRP. These **G1** and **G2** dendron initiators and a commercially available initiator (**EBiB**) were used in the methanolic homopolymerisation of HPMA to produce linear and linear-dendritic polymers with varying degrees of polymerisation (20, 50 and 100 monomer units). The kinetic evaluation of these polymerisations (for DP_{50}) showed that the polymerisations adhered to the expected first order kinetics reported for ATRP, with a linear increase of molecular weight with increasing conversion. The incorporation of a divinyl monomer (EGDMA) into the polymerisation afforded high molecular weight branched polymers (up to $M_w = 2.3 \times 10^6$ $gmol^{-1}$), bearing the initiator functionality at one end of every chain. The initiator:EGDMA molar ratio was kept constant at 1:0.8 to prevent gelation. The branched polymers containing the **G1** or **G2** dendron moiety at the end of every chain were termed hyperbranched polydendrons (*hyp*-polydendrons) due to the hyperbranched pHPMA core, containing multiple dendron functionalities in one highly branched macromolecule. The hyperbranched polymers containing no dendron functionality (**EBiB** initiated branched polymers) were described as *hyp*-polymers. Kinetic evaluation of the branched polymerisations also revealed first order kinetics as expected, however the molecular weights increased dramatically at high conversions (>80 %) due to the intermolecular branching of chains owing to the incorporation of the divinyl monomer in the polymer chains.

The linear, linear-dendritic, *hyp*-polymers and *hyp*-polydendrons of various DP_n values were subsequently investigated for their ability to form nanoparticles via a nanoprecipitation approach. Initially, a study was conducted where the polymers were dissolved in a good solvent (acetone) and nanoparticle formation was induced by adding an anti-solvent (hexane) for the pHPMA polymer chains. The formation

F.L. Hatton, *Hyperbranched Polydendrons*,
Springer Theses, DOI 10.1007/978-3-319-18753-2_6

of nanoparticles was followed by DLS and showed a huge difference between the formation of particles from the linear and linear dendritic polymers when compared the equivalent *hyp*-polymers and *hyp*-polydendrons. The nanoparticles formed using the *hyp*-polymers and *hyp*-polydendrons were much smaller and had smaller polydispersity indices than the linear and linear-dendritic polymer analogues.

Further investigation of nanoparticle formation using these materials was conducted using water as the anti-solvent. This produced near monodisperse nanoparticles which were stable over an extended period of time (>23 months) when the *hyp*-polymer and *hyp*-polydendron materials were used. However, the linear and linear-dendritic polymer analogues were generally larger in size and polydispersity, and showed aggregation over time and ultimately precipitation. The nanoparticles were also analysed by SEM, showing discreet spherical nanoparticles, with the number average diameter calculated by SEM agreeing with the number average diameter as observed via DLS measurements.

6.2 Mixing Dendron and PEG Initiators for the Polymerisation of Branched pHPMA and Aqueous Nanoparticle Formation

The concept of introducing mixed functionality to the *hyp*-polydendrons was investigated in Chap. 3 by statistically blending two different ATRP initiators in the copolymerisation of HPMA and EGDMA. This produced highly branched macromolecules containing the two different initiator functionalities which would not be achievable via a homopolymerisation approach. The **G2** dendron synthesised in Chap. 2 was mixed with a **750PEG** macroinitiator at various ratios (100:0, 90:10, 75:25, 50:50, 25:75, 10:90 and 0:100) with a targeted DP_n of 50 monomer units to produce six *hyp*-polydendrons and one *hyp*-block copolymer. Maintaining the initiator:EGDMA molar ratio at 1:0.8 the materials produced showed a decrease in molecular weights and dispersities with increasing **750PEG** content. This indicated that the **750PEG** initiator had a higher initiator efficiency than the **G2** dendron initiator. To ensure the **750PEG** initiator was suitable for ATRP, kinetic experiments were conducted showing first order kinetics, with a linear increase in molecular weights for the homopolymerisation of HPMA and a large increase in molecular weights and dispersities when the copolymerisation of HPMA and EGDMA was studied.

Aqueous nanoprecipitation of these materials was conducted to produce a range of nanoparticles with varying **G2** dendron and **750PEG** initiator content. The mechanism of nanoprecipitation suggested that upon nucleation and aggregation of nanoparticles, the **G2** dendron and **750PEG** functionalities could reside either at the surface of the nanoparticles or inside the nanoparticles. This was ascertained by encapsulation of two different fluorescent dyes; Nile red and pyrene, which both report on the surrounding environment. Nile red exhibits an increased fluorescence

intensity in hydrophobic environments than in hydrophilic environments. The fluorescence intensity observed was higher when the Nile red was encapsulated in *hyp*-polydendron nanoparticles with a higher **G2** dendron initiator content. Pyrene has five predominant vibronic bands when excited at 335 nm, the ratio of peak 1 in the fluorescence emission spectra to the third predominant peak, peak three, gives rise to the I_1/I_3 ratio. The I_1/I_3 ratio varied across the series of *hyp*-polydendrons and *hyp*-block copolymer, from 1.42 for the 100:0 *hyp*-polydendron to 1.53 for the 0:100 *hyp*-block copolymer, indicating that with increasing **750PEG** content the polarity of the nanoparticles internal environment is increasing.

To assess the *hyp*-polydendron and *hyp*-block copolymer nanoparticles potential to act as drug delivery vehicles, preliminary pharmacological experiments were conducted. Cytotoxicity assays were performed using the Caco-2 cell line which represents the first barrier to orally dosed materials, the intestinal epithelial cells. The materials did not cause toxicity to Caco-2 cells across a range of concentrations. The transcellular permeability of the materials was also assessed, using the Caco-2 cell monolayer which is a model experiment to predict absorption of materials across the intestinal epithelial cells into the systemic circulation. These materials show at trend in the apparent permeability (P_{app}) across the membrane, where the (P_{app}) increased with increasing **G2** dendron content of the *hyp*-polydendron formulated nanoparticle samples. Whilst showing pharmacological benefits, the nanoparticles were not stable to salt or transport buffer solutions. This was due to the particles being charge stabilised, where addition of salt screens the charges on the nanoparticles' surface leading to aggregation. Therefore it was desirable to produce nanoparticles which would be sterically stabilised, rather than charge stabilised, to afford stability in physiological conditions.

6.3 Mixing Dendron and PEG Initiators for the Polymerisation of Branched pHPMA and Formation of Sterically Stabilised Nanoparticles

Following the work conducted in Chap. 3, the main aim of Chap. 4 was to produce *hyp*-polydendron nanoparticles which would be stable to salt and buffer solutions, and show potential for drug delivery. Therefore, a mixed initiator approach was once again utilised, with a longer PEG chain macroinitiator; **2000PEG**. The **G2** dendron synthesis was improved by using an AB_2 molecule developed in the research group. Therefore the structure of the **G2** dendron in Chap. 4 was slightly different to that used in Chap. 3 and was termed the **G2′** dendron initiator. The **G2′** dendron initiator and **2000PEG** macroinitiator homopolymerisations of HPMA were conducted with targeted DP_n of 20, 50 and 100 monomer units, and kinetic evaluation of selected polymerisations showed expected ATRP behaviour with a linear increase in molecular weights and low dispersities (<1.4). The initiators were also used in the copolymerisation of HPMA and EGDMA to afford high molecular

weight branched polymers, *hyp*-polydendrons for the **G2′** dendron initiated branched polymers and *hyp*-block copolymers when the **2000PEG** macroinitiator was utilised. The branched polymerisations were also assessed via kinetic experiments, again showing expected ATRP behaviour of first order kinetics, with a steep increase in molecular weight and dispersity when conversion had reached >70−80 %.

The **G2′** dendron initiator and **2000PEG** macroinitiator were subsequently mixed in a statistical manner at various ratios (**G2′**:**2000PEG**: 100:0, 90:10, 75:25, 50:50, 25:75, 10:90 and 0:100) for the copolymerisation of HPMA and EGDMA, targeting three DP_n of HPMA (20, 50 and 100 monomer units). The ratio of initiator:EGDMA utilised in the DP_{50} was varied for each ratio to find the highest level possible before gelation occurred. This showed that with increasing the **2000PEG** content, the ratio could be increased from 1:0.8, for 100:0, to 1:0.95 for 0:100 **G2′**:**2000PEG**. The DP_{20} and DP_{100} series were polymerised using an initiator:EGDMA ratio of 1:0.8, which showed a similar trend of molecular weights and dispersity as observed in Chap. 3 for the **G2**:**750PEG** branched polymer synthesis. When the **2000PEG** content was increased the molecular weights and dispersities decreased across the series, suggesting that the **2000PEG** initiator had a higher initiator efficiency than the **G2′** dendron initiator.

The subsequent *hyp*-polydendrons were investigated for their nanoprecipitation behaviour. Firstly, the DP_{50} series was subjected to nanoprecipitation conditions at various initial and final concentrations. The results, as measured via DLS, showed that at the higher level of **2000PEG** macroinitiator incorporation, the resulting nanoparticle sizes obtained were independent of the concentration of the polymers used, whilst with higher **G2′** dendron initiator content the *hyp*-polydendrons exhibited the same nanoprecipitation behaviour that had been observed for the branched polymers studied in Chaps. 2 and 3. It was found that this was due to the water-solubility of the polymers. With increasing **2000PEG** macroinitiator (from 50−100 %) the resulting *hyp*-polydendrons and *hyp*-block copolymer were actually water-soluble, therefore when being nanoprecipitated they were dissolved in a good solvent and added to another good solvent, rather than an anti-solvent. This resulted in what was described as ‘individual object’ formation, rather than nanoprecipitates as previously observed with hydrophobic polymer nanoprecipitations.

The stability of the resulting nanoparticles was assessed under physiologically relevant conditions, using salt solution (0.14 M NaCl) and transport buffer. The incorporation of even the lowest amount of **2000PEG** (10 %) afforded salt stability to the resulting nanoparticles, therefore, each sample was investigated for any pharmacological benefits as drug delivery vehicles. The pharmacological evaluation of the DP_{50} materials gave an indication that the *hyp*-polydendron and *hyp*-block copolymer materials which did not display classical nanoprecipitation behaviour (**G2′**:**2000PEG**; 50:50, 25:75, 10:90 and 0:100) whilst showing no toxicity to Caco-2 cells, showed no enhancement of transcellular permeability of the model drug encapsulated and therefore no pharmacological benefits. However, the samples showing classical nanoprecipitation behaviour and larger D_z (**G2′**:**2000PEG**; 90:10 and 75:25) were also non-toxic to Caco-2 cells and showed an enhanced

transcellular permeation of a model drug across the Caco-2 cell monolayer when compared to the aqueous model drug preparation.

Therefore a study of the DP_{100} *hyp*-polydendrons and *hyp*-block copolymer was conducted; increasing the length of the hydrophobic pHPMA primary chain length was expected to result in branched polymers that were more hydrophobic than the DP_{50} series. It was found that none of the DP_{100} materials were water-soluble and all materials demonstrated classical nanoprecipitation behaviour, identical to the hydrophobic branched polymers studied in the DP_{50} series and previous Chapters. These nanoparticles were assessed for their cytotoxicity and transcellular permeation across the Caco-2 cell monolayer. Materials which showed pharmacological benefit were the **G2′**:**2000PEG** 75:25, 50:50 and 25:75 DP_{100} *hyp*-polydendron nanoparticles, with the 75:25 material showing the highest transcellular permeation across the Caco-2 cell monolayer, therefore this sample was used for subsequent cell accumulation studies. The cellular accumulation ratio (CAR) was calculated for the 75:25 *hyp*-polydendron nanoparticles in Caco-2 cells, to elucidate whether the transport across the monolayer occurred via a transcellular or paracellular pathway. Increased accumulation in the Caco-2 cells was seen (over the free model drug), indicating a transcellular pathway for the observed permeation. Accumulation in ATHP-1 cells (monocyte derived macrophage cells) was also investigated to ascertain whether the nanoparticles could be used to target macrophages cells, which is one of many cellular sanctuary sites for the HIV virus. The 75:25 *hyp*-polydendron nanoparticles did not show any increase in accumulation in the ATHP-1 cells when compared to the free model drug and further pharmacological evaluation of the 'lead material', 75:25 DP_{100} formulated nanoparticles, are required to undertake mechanistic studies to assess the permeation pathway across the Caco-2 cell monolayer.

6.4 *Hyp*-polydendrons; Studies of Nanoprecipitation Behaviour

The water solubility and nanoprecipitation behaviour of the **G2′**:**2000PEG** DP_{20} series was discussed in Chap. 5. The 75:25, 50:50, 25:75, 10:90 *hyp*-polydendrons and 0:100 *hyp*-block copolymer were all water-soluble and therefore did not exhibit classical nanoprecipitation behaviour. The 100:0 DP_{20} *hyp*-polydendron did form nanoprecipitates that increased in size with increasing starting solution, and final dispersion, concentrations. However, although the 90:10 DP_{20} sample was not water-soluble, it did not form nanoparticles as expected.

The **G2′**:**2000PEG** DP_{20}, DP_{50} and DP_{100} series of *hyp*-polydendrons and *hyp*-block copolymers were analysed by ^{1}H NMR spectroscopy where the ratio of **G2′** dendron to the HPMA content was calculated by comparing the integrals of chemical shifts in the ^{1}H NMR spectra corresponding to protons in the **G2′** dendron and HPMA monomer residues. The observed ratio of **G2′** dendron initiator:HPMA

was lower than expected by theory and was attributed to the lower initiator efficiency of the **G2′** dendron initiator. The **2000PEG** macroinitiator:HPMA ratio was estimated by ^{1}H NMR spectroscopy, where the observed ratio was close to that calculated by theory. The integration of the peak corresponding to the **2000PEG** was not as accurate as the **G2′** dendron initiator, as the peak corresponding to the methyl group at the end of the PEG chain did not always reach the baseline, therefore the error associated with this integration was higher than with the **G2′** dendron.

The mol% content of each component (**G2′** dendron initiator, **2000PEG** macroinitiator and HPMA) was estimated using the ^{1}H NMR spectroscopy analysis. The mol% of the PEG repeat unit, ethylene oxide (EO), was calculated from the **2000PEG** mol%. The various EO mol% and HPMA mol% of the materials could be separated into two distinct domains, where the polymers were soluble or insoluble in water. This was also represented by a phase diagram of the targeted DP_n of EO and HPMA, where three distinct domains were characterised; water insoluble polymers which generally nanoprecipitated as expected, water soluble polymers which were measurable via DLS and water insoluble polymers that could not be measured via DLS due to a lack of light scattering.

To investigate the importance of the high molecular weight branched polymer fraction of the molecular weight distribution on nanoprecipitation, organic solvent dialysis experiments were conducted using the **G2′**-pHPMA$_{50}$-EGDMA$_{0.8}$ and **G2′**-pHPMA$_{100}$-EGDMA$_{0.8}$ *hyp*-polydendrons. The dialysis experiments were performed in good solvents for the *hyp*-polydendrons to separate out the low molecular weight (LMW) and high molecular weight (HMW) polymer fractions present in the *hyp*-polydendron samples. These HMW and LMW fractions were subsequently studied for their nanoprecipitation behaviours. It was found that by changing the dialysis solvent, different molecular weight polymers could be isolated. Using IPA the LMW fractions that dialysed out of the membrane for both *hyp*-polydendrons had similar molecular weights to the linear-dendritic polymer equivalents. However, when MeOH was used for the dialysis of the **G2′**-pHPMA$_{50}$-EGDMA$_{0.8}$ the LMW fraction had higher molecular weights, therefore, either the size of the pores in the dialysis membranes were affected by the solvent, or the hydrodynamic diameter of the polymer chains was different in IPA and MeOH; higher molecular weight polymer chains could diffuse through the dialysis membrane pores when using MeOH.

The nanoprecipitation of the various HMW and LMW fractions showed that in general the HMW fractions produced nanoparticles with smaller diameters and lower PdIs than the LMW fractions. The mixture of the **G2′**-pHPMA$_{50}$-EGDMA$_{0.8}$ HMW$_{MeOH}$ fraction with the linear dendritic equivalent polymer, **G2′**-pHPMA$_{50}$, showed that the size of the resulting nanoparticles and PdI was decreased with an inclusion of only 1 wt% of HMW$_{MeOH}$ *hyp*-polydendron. With increasing the wt% of the HMW$_{MeOH}$ fraction from 1−100 wt% the size of the nanoparticles decreased slightly and the PdIs remained low. This infers that incorporation of even a low amount of HMW fraction of polymer improves the nanoprecipitation when compared to the linear-dendritic polymer nanoprecipitations.

The study of the *hyp*-polydendrons was concluded by investigating the ability to encapsulate two different molecules within an individual nanoparticle by utilising FRET. It was shown that when a donor fluorophore (DiO) and an acceptor fluorophore (DiI) were formulated in separate nanoparticles FRET was not observed, however, when they were dual loaded into the nanoparticles a FRET signal was observed which was quantified using the FRET ratio. The mixture of the two singly loaded nanoparticle samples did not shown any FRET immediately after mixing, however, a study of the mixture over time showed that the FRET ratio increased, indicating that one or both of the fluorophores were moving between the nanoparticles. The movement of the fluorophores via dissolution in the water was ruled out by a dialysis experiment where the donor (DiO) nanoparticles were placed inside the membrane and the acceptor (DiI) nanoparticles were outside the membrane. The fluorescence spectra was measured from the acceptor nanoparticles outside of the membrane, which showed no increase at the acceptor (DiI) emission wavelength over time, indicating that the movement of the fluorophores between particles was not occurring. Therefore when the nanoparticles were not coming into contact with one another, there was no increase in the observed FRET ratio. This suggested that dye movement was occurring through collisions of the nanoparticles, however, further investigations would be required to elucidate the exact mechanism.

6.5 Future Work

The introduction of *hyp*-polydendrons throughout this research study has opened a new area of materials chemistry which provides opportunities across many potential fields. The materials offer new nanomedicine materials and the numerous structural and chemical options that are available for future variation, have been studied through this preliminary report. Future research directions with specific focus on nanomedicine applications include;

- Synthesis of different functional dendron initiators
  - Investigations will provide the potential for targeting of drug delivery and modification of solution behaviour.
- Fluorescent initiator incorporation
  - Bound fluorescent molecules may be used to report on the environment/location of the nanoparticles and the position of the polymer chain ends within nanoprecipitates.
- Drug encapsulation
  - The nanoprecipitates may be loaded with drug compounds to target disease (e.g. efavirenz, lopinavir and ritonavir for the treatment of HIV).

- Internal chemistry variation
  - Varying the internal hydrophobicity of the nanoparticles may be achieved through copolymerisation of different monomers into the core structures.
- Encapsulation of inorganic nanoparticles
  - Materials such as Fe_3O_4 (SPIONs) may be used to impart magnetic properties to the nanoparticles
- Thermal behaviour studies
  - The lower critical solution temperature (LCST) of the water-soluble *hyp*-polydendrons and *hyp*-block copolymers may be studied to provide useful triggers. Comparison to linear polymers will yield architectural importance
- Nanoprecipitation mechanistic studies
  - The multiple nanoprecipitation of *hyp*-polydendrons into single volumes of water would explore the nanoprecipitation mechanism and produce options for scale up
- Layer-by-layer studies
  - To sterically stabilise the charges nanoprecipitates, a layer-by-layer approach could be utilised with linear polyelectrolytes

Chapter 7
Experimental

7.1 Experimental Techniques

Two important experimental techniques used throughout this thesis were gel permeation chromatography (GPC) and dynamic light scattering (DLS), therefore, each technique is discussed in detail below.

7.1.1 Gel Permeation Chromatography (GPC)

GPC can also be referred to as size exclusion chromatography and relies upon the separation of polymeric materials by their size in an appropriate eluent. The separation of the different chain lengths within a polymer molecular weight distribution is performed by utilising columns containing porous beads with various pore sizes. Larger polymeric materials cannot enter the smaller pores and therefore have a shorter path-length through the columns, eluting at earlier retention volumes. Smaller polymeric materials, which can enter a percentage of the pores, have a long path-length through the columns and elute at later retention volumes.

Triple detection systems use refractive index (RI), differential viscometry and light scattering detectors to calculate the absolute molecular weight of the polymer. Each detector can be used to calculate different parameters which collectively elucidate the molecular weights of the different fractions within the polymer sample. Equations (7.1)−(7.3) show the calculations conducted with the data collected by each detector, where K_{RI}, K_V and K_{LS} are instrument calibration constants, *conc* is the concentration, and *dn/dc* is the change in refractive index (the refractive index increment) with the change in concentration.

$$Refractometer = K_{RI} \times \frac{dn}{dc} \times conc \tag{7.1}$$

F.L. Hatton, *Hyperbranched Polydendrons*,
Springer Theses, DOI 10.1007/978-3-319-18753-2_7

$$Viscometer = K_V \times intrinsic\ viscosity \times conc \tag{7.2}$$

$$Light\ scattering = K_{LS} \times molecular\ weight \times \left(\frac{dn}{dc}\right)^2 \times conc \tag{7.3}$$

The differential refractometer calculates the dn/dc from the concentration entered when injecting the sample, whilst the viscometer also calculates the intrinsic viscosity of the sample based on this entered concentration. The absolute molecular weight calculated by light scattering is also dependant on the concentration and the square of the dn/dc. Therefore when using triple detection it is important to determine the concentration of the sample accurately; any errors in the concentration can result in inaccurate calculation of molecular weights. Alternatively if the concentration of the sample is not known, but the dn/dc for the polymer is, a known value can be used to calculate the concentration of the sample and therefore the molecular weights and dispersity.

7.1.2 Dynamic Light Scattering (DLS)

DLS relies on the calculation of particle size using Brownian motion and the correlation between the Brownian motion of a particle suspended in a liquid and its hydrodynamic diameter. An autocorrelation function is used to assess the correlation in scattering over time which can be used to calculate the size of the particles. The correlation will be high over a very short time period as the particle has not moved very far, whilst over a long time period the correlation will be low due to the Brownian motion of the particle away from its original position. Therefore, an exponential decay of correlation function over time is observed. The method of cumulants analysis is then used to calculate the z-average diameter (D_z), which is the preferred DLS size parameter as the D_z result is insensitive to experimental noise.

The D_z is calculated from the translational diffusion coefficient by using the Stokes-Einstein equation, shown in Eq. (7.4). Where D_z is the hydrodynamic diameter, k is Boltzmann's constant, T is the absolute temperature, η is viscosity and D_t is the intensity weighted average translational diffusion coefficient calculated by the method of cumulants analysis.

$$D_z = kT/3\pi\eta D_t \tag{7.4}$$

Therefore the temperature (T) of the sample must be stable, the viscosity (η) of the dispersant medium at that temperature must be known and the refractive index of the dispersant medium is required to calculate the D_t from the cumulants method. The polydispersity index (PdI) is a measure of the width of the size distribution and is calculated using the method of cumulants.

The D_z is not the only size parameter derived from the DLS analysis. The number average and volume average may also be calculated and can give information about the particle population(s) present in a sample. The size distribution by

intensity is weighted towards larger particles, as the intensity in light scattered is proportional to the diameter to the power of 6. Therefore if an equal mixture of 5 and 50 nm particles are measured, the size distribution by number would be equal for both populations as they are present in a ratio of 1:1. The size distribution by volume would be 10^3 higher for the 50 nm compared to the 5 nm particle (the volume of a sphere is described as $4/3\pi(d/2)^3$). The size distribution by intensity will be even more weighted towards the 50 nm population as the 50 nm particles will scatter 10^6 as much light as the 5 nm particle.

This needs to be taken into consideration when multi-modal distributions are observed as even though a larger population may appear predominant in a sample, it is possible that a smaller particle size actually dominates in terms of the number of particles present.

7.2 Experimental Techniques Used Throughout This Thesis

7.2.1 Materials

All starting materials, 1,3-dibenzyloxy-2-propanol (97 %), 1,1′-carbonyldiimidazole (≥97 %), diethylenetriamine (99 %), β-butyrolactone (98 %), α-bromoisobutyryl bromide (98 %), 4-(dimethylamino)pyridine (≥99 %), triethylamine (≥99 %), hydroxypropyl methacrylate (97 %), ethylene glycol dimethacrylate (98 %) Cu(I)Cl (≥99 %), 2,2′-bipyridyl (≥99 %), poly(ethylene glycol) monomethyl ether (average M_n 750 $gmol^{-1}$), poly(ethylene glycol) monomethyl ether (average M_n 2000 $gmol^{-1}$), tert-butanol (≥99.5 %), BAPA (98 %), propylene oxide (≥99 %), Nile red (≥98 %), Pyrene (98 %) were purchased from Aldrich and used as received. 1,1′-dioctadecyl-3,3,3′,3′-tetramethylindocarbocyanine perchlorate (DiI) and 3,3′-dioctadecyloxacarbocyanine perchlorate (DiO) were purchased from Life Technologies and used as received. Anhydrous toluene and methanol, silica gel used for column chromatography, Dowex® MarathonTM MSC (hydrogen form) ion exchange resin beads and potassium hydroxide (KOH) were purchased from Aldrich and used as received. All other solvents were analytical grade and purchased from Fisher.

7.2.2 Characterisation

Molecular weights and molecular weight distributions (i.e. polydispersity index; Đ) were measured using a Malvern Viscotek instrument equipped with a GPCmax VE2001 auto-sampler, two Viscotek T6000 columns (and a guard column), a refractive index (RI) detector VE3580 and a 270 Dual Detector (light scattering and viscometer) with a mobile phase of THF at 35 °C and a flow rate of 1.0 mL min^{-1}.

NMR spectra were recorded using a Bruker DPX-400 spectrometer operating at 400 MHz for ^1H NMR and 100 MHz for ^{13}C, in $CDCl_3$, MeOD, D_2O or DMSO.

Chemical ionisation (CI) and electrospray (ES) mass spectrometry data was recorded in the Mass Spectrometry Laboratory at the University of Liverpool. The CI mass spectrometry data was obtained using a Agilent GCQTOF 7200 instrument, using methane CI gas. The ES mass spectrometry data was obtained using a MicroMass LCT mass spectrometer using electron ionisation and direct infusion syringe pump sampling. All materials were diluted with methanol.

MALDI-TOF mass spectrometry data was recorded in the EPSRC National Mass Spectrometry Facility, Swansea, using a Voyager DE-STR instrument.

Elemental analyses were obtained from a Thermo FlashEA 1112 series CHNSO elemental analyser.

Dynamic light scattering (DLS) measurements were performed using a Malvern Zetasizer Nano ZS instrument (laser wavelength; 630 nm), ran at 25 °C. Alternatively it was carried out using a Viscotek 802-100 Dynamic Light Scattering Analyzer (laser wavelength; 830 nm), ran at 20 °C.

Scanning electron microscopy (SEM) images of nanoparticles were obtained using a Hitachi S-4800 FE-SEM. Samples were dropped directly onto various SEM stub surfaces (specified in each specific chapter below) and left to dry over several hours or overnight.

Refractive indices of solvents were measured on a Refracto 30 PX on a portable refractometer at ambient temperature.

Fluorescence spectra (for Chaps. 3 and 4) were obtained on a PerkinElmer Luminescence spectrofluorophotometer LS55. Emission spectra for Nile red containing samples were recorded between 550 and 700 nm, exciting at 552 nm. The slit widths for emission and excitation were 5 and 10 nm, respectively, with a scan rate of 100 nm/min. Emission spectra for pyrene labelled samples were recorded between 330 and 500 nm, exciting at 335 nm. The slit widths for emission and excitation were 5 and 5 nm, respectively, with a scan rate of 100 nm/min.

Fluorescence spectra (for Chap. 5) were obtained on a Shimadzu RF-5301PC spectrofluorophotometer. Emission spectra for DiO and DiI containing samples were recorded between 400 and 700 nm, exciting at 420 nm. The slit widths for emission and excitation were 3 and 5 nm respectively, with a fast scan rate.

7.2.3 Linear Polymerisations via ATRP

In a typical experiment, **G2** dendron initiator (0.648 g, 0.69 mmol) and HPMA (targeted $DP_n = 50$) (5.0 g, 34.7 mmol) were weighed into a round bottom flask. The flask was equipped with magnetic stirrer bar, sealed and degassed by bubbling with N_2 for 20 min and maintained under N_2 at 30 °C. Anhydrous methanol was degassed separately and subsequently added to the monomer/initiator mixture via syringe to give a 50 vol% or 50 wt% mixture with respect to the monomer. The catalytic system; Cu(I)Cl (0.069 g, 0.69 mmol) and 2,2′-bipyridyl (bpy) (0.217 g, 1.39 mmol), were added under a positive nitrogen flow in order to initiate the reaction. The polymerisations were stopped when conversions had reached over 98 % determined

by ^{1}H NMR using the vinyl CH_2 peaks and protons of the polymer backbone. The polymerisation was stopped by diluting with a large excess of tetrahydrofuran (THF), which caused a colour change from dark brown to a bright green colour. The catalytic system was removed using Dowex® Marathon™ MSC (hydrogen form) ion exchange resin beads and basic alumina. The resulting polymer was isolated by precipitation from the minimum amount of acetone or THF into cold hexane. The [initiator]:[CuCl]:[bpy] molar ratios in all polymerizations were 1:1:2.

7.2.4 Branched Polymerisations via ATRP

The synthesis of branched polymers was conducted in the same manner as the linear polymerizations with the addition of EGDMA (e.g. 105 μL, 0.55 mmol for initiator: EGDMA 1:0.8). Various ratios of initiator: EGDMA were used; between 1:0.8 −1:0.95, each chapter describes how much was used and why.

7.2.5 Kinetic Experiments

Kinetics experiments were conducted at 30 °C. To determine the kinetic parameters of polymerisations samples ($\sim$0.1 mL) was taken at regular intervals and analysed by ^{1}H NMR and gel permeation chromatography (GPC). Approximately one third of each sample taken was diluted into 1 mL of deuterated DMSO (for ^{1}H NMR analysis) and the other two thirds was diluted into 4 mL THF (for GPC analysis). Oxidation of Cu(I) to Cu(II) was observed by a colour change from brown to turquoise in DMSO and from brown to green in THF indicating termination of the reaction. Conversion of monomer to polymer was determined by ^{1}H NMR as previously discussed. The samples diluted in THF were prepared for GPC analysis by removal of the catalytic system with Dowex® Marathon™ MSC (hydrogen form) ion exchange resin beads, transferred into a pre-weighed vial, removal of THF from the polymer solution by evaporation to give dry polymer residue of a known weight. The dry polymer residues of known weights were then diluted with HPLC grade THF to give polymer solutions with concentrations around 5.0 mg/mL. These were analysed by triple detection GPC consisting of refractive index (RI), light scattering (LS) and viscometer detectors.

7.2.6 Mixed Initiator Branched Polymerisations via ATRP

In a typical reaction, G2 dendron initiator (0.324 g, 0.35 mmol) and 2K PEG initiator (0.745 g, 0.35 mmol) (for a targeted ratio of G2 dendron: 2000PEG of

50:50 mol%) were weighed into a round bottom flask, followed by HPMA (5.0 g, 34.7 mmol, targeted DP = 50). EGDMA (112 μL, 0.59 mmol, 0.85 mol%) was added and the flask was equipped with magnetic stirrer bar, sealed and degassed by bubbling with N_2 for 20 min and maintained under N_2 at 30 °C. Anhydrous methanol was degassed separately and subsequently added to the monomer/initiator/brancher mixture via syringe to give a 50 % v/v mixture with respect to the monomer. The catalytic system; Cu(I)Cl (0.069 g, 0.69 mmol) and 2,2′-bipyridyl (bpy) (0.217 g, 1.39 mmol), were added under a positive nitrogen flow in order to initiate the reaction. The polymerisations were stopped when conversions had reached over 98 %. The polymerisations were stopped by diluting with a large excess of tetrahydrofuran (THF), which caused a colour change from dark brown to a bright green colour. The catalytic system was removed using Dowex® Marathon™ MSC (hydrogen form) ion exchange resin beads and basic alumina. The resulting polymer was isolated by precipitation from the minimum amount of THF into cold hexane. The [initiator]:[CuCl]:[bpy] molar ratios in all polymerizations were 1:1:2.

7.2.7 Aqueous Nanoparticle Formation

Polymers were dissolved in THF at various concentrations. Once fully dissolved, polymer in THF (0.1 or 1 mL, 1, 5, 10, 25 or 50 mg/mL) was added quickly to a vial of water (5 or 10 mL) stirring at ambient temperature. The solvent was allowed to evaporate overnight in a fume cupboard to give a final concentration between 0.01−10 mg/mL polymer in water. By adjusting the starting concentration and the volume of water used, the size of the corresponding nanoparticles were controlled.

7.2.8 Encapsulation of Guest Molecules in Nanoparticles

Polymers were dissolved in THF at various concentrations. The fluorescent dyes, Nile red and pyrene, were dissolved in THF to give a stock solution (0.1 mg/mL). The stock solution (50 μL, 0.1 mg/mL) was added to an empty vial and the THF was allowed to evaporate to leave 5 μg of dye. The polymer dissolved in THF (1 mL, 5 mg/mL) was added to the dry Nile red or pyrene to give a mixture containing 5 mg polymer, 5 μg dye dissolved in 1 mL of THF. This was then added quickly to a vial of water (5 mL) stirring at ambient temperature. The solvent was allowed to evaporate overnight in a fume cupboard to give a final concentration of 1 mg/mL polymer and 1 μg/mL Nile red or pyrene (0.1 w/w%) in water.

7.3 Synthesis and Characterisation of *Hyp*-polydendron Materials and Subsequent Nanoparticle Formation

For materials and characterisation see Sects. 7.2.1 *and* 7.2.2 *respectively.*

7.3.1 Initiator Synthesis

7.3.1.1 G1 Dendron Initiator (See Sect. 2.2.1)

1,3-Dibenzyloxy-2-propanol, **1** (9.80 g, 36.0 mmol) was weighed into a 2-neck round bottom flask which was equipped with magnetic stirrer and dry N_2 inlet. Dichloromethane (DCM) (100 mL) was added followed by 4-(dimethylamino) pyridine (DMAP) (0.44 g, 3.6 mmol) and triethylamine (TEA) (7.53 mL, 54.0 mmol). The reaction was cooled to 0 °C in an ice-bath and α-bromoisobutyryl bromide (5.34 mL, 43.2 mmol) was added dropwise over 20 min. After complete addition the reaction was warmed to room temperature and left stirring overnight. Reaction could be observed by the formation of a white precipitate. After 24 h the precipitate was removed by filtration, the resulting crude reaction medium was washed first with a saturated solution of $NaHCO_3$ (3 × 100 mL) followed by distilled water (3 × 100 mL). The organic layer was dried over Na_2SO_4 and concentrated in vacuo to give a pale yellow oil (81 %). Found, C, 59.55; H, 6.02 %. $C_{21}H_{25}BrO_4$ requires, C, 59.86; H, 5.98; Br, 18.96; O, 15.19 %. ^{1}H NMR (400 MHz, $CDCl_3$) δ ppm 7.35–7.20 (m, 10H), 5.26 (m, 1H), 4.55 (m, 4H), 3.69 (d, 4H), 1.93 (s, 6H). ^{13}C NMR (100 MHz, $CDCl_3$) δ ppm 171.2, 138.0, 128.4, 127.7, 127.6, 73.3, 68.5, 55.8, 30.7. *m/z* (ES MS) 443.1 $[M + Na]^+$, 461.1 $[M + K]^+$, *m/z* required 420.1 $[M]^+$ (Scheme 7.1).

7.3.1.2 G2 Dendron Initiator (See Sect. 2.2.2)

1,1′-Carbonyldiimidazole (CDI) (9.73 g, 60.0 mmol) was weighed into a 2-neck round bottom flask and equipped with magnetic stirring, condenser and dry N_2 inlet.

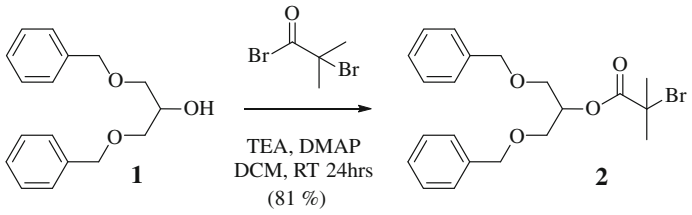

Scheme 7.1 **G1** dendron initiator synthesis

Anhydrous toluene (100 mL) was added, followed by KOH (0.34 g, 6.0 mmol) and **1** (12.35 mL, 50.0 mmol). The reaction was heated to 60 °C for 6 h. Toluene was removed in vacuo, the crude mixture was dissolved in DCM (50 mL) and washed with distilled water (3 × 50 mL). The organic layer was dried over Na_2SO_4 and concentrated in vacuo to give **3**, a pale yellow oil (97 %). Found C, 68.64; H, 6.10; N, 7.85 %. $C_{21}H_{22}N_2O_4$ requires C, 68.84; H, 6.05; N, 7.65; O, 17.47 %. ^{1}H NMR (400 MHz, $CDCl_3$) δ ppm 8.11 (s, 1H), 7.41 (s, 1H), 7.33-7.23 (m, 10H), 7.06 (s, 1H), 5.36 (qn, 1H), 4.53 (m, 4H), 3.75 (m, 4H). ^{13}C NMR (100 MHz, $CDCl_3$) δ ppm 148.3, 137.5, 137.2, 130.6, 128.4, 127.9, 127.6, 117.2, 76.1, 73.3, 68.1. *m/z* (ES MS) 367.2 $[M + H]^+$, 389.2 $[M + Na]^+$, 405.1 $[M + K]^+$, *m/z* required 366.2 $[M]^+$ (Scheme 7.2).

3 (16.84 g, 46.0 mmol) was weighed into a 2-neck round bottom flask which was equipped with magnetic stirring, condenser and dry N_2 inlet. Anhydrous toluene (120 mL) was added followed by diethylenetriamine (DETA) (2.48 mL, 23.0 mmol). The reaction was heated to 60 °C for 48 h. Toluene was removed in vacuo, the resulting crude mixture was dissolved in DCM (100 mL) and washed with distilled water (3 × 100 mL). The organic layer was dried over Na_2SO_4 and concentrated in vacuo to give **4**, a yellow oil (93 %). Found C, 68.50; H, 7.13; N, 6.00 %. $C_{40}H_{49}N_3O_8$ requires, C, 68.65; H, 7.06; N, 6.00; O, 18.29 %. ^{1}H NMR (400 MHz, $CDCl_3$) δ ppm 7.27–7.16 (m, 20H), 5.23 (s, br, NH), 5.03 (qn, 2H), 4.44 (m, 8H), 3.57 (d, 8H), 3.12 (m, 4H), 2.58 (m, 4H). ^{13}C NMR (100 MHz, $CDCl_3$) δ ppm 156.6, 138.4, 128.8, 128.1, 73.7, 72.1, 69.4, 49.0, 41.2. *m/z* (ES MS) 700.4 $[M + H]^+$, 722.3 $[M + Na]^+$, 738.3 $[M + K]^+$, *m/z* required 699.4 $[M]^+$.

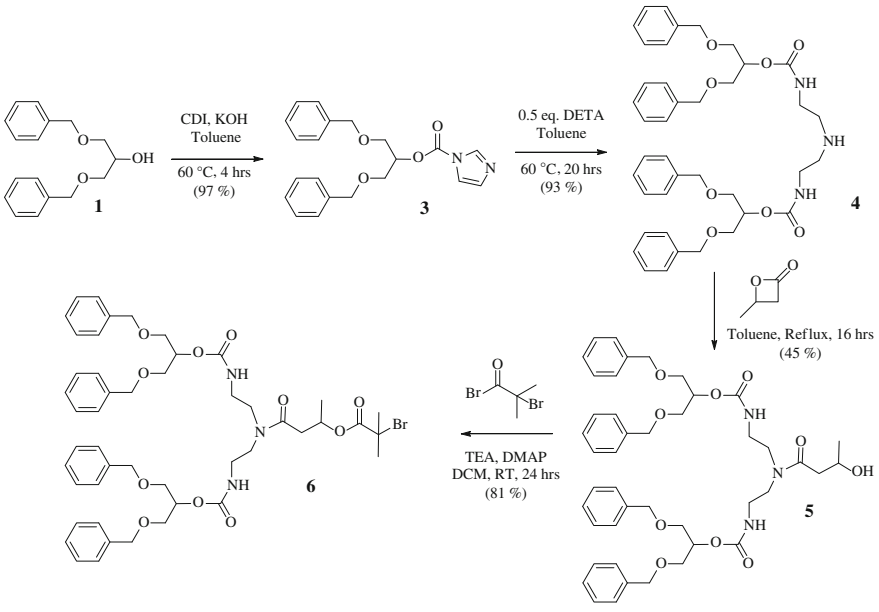

Scheme 7.2 **G2** dendron initiator synthesis

4 (15.01 g, 21.4 mmol) was weighed into a 2-neck round bottom flask, equipped with magnetic stirrer, condenser and dry N_2 inlet. Anhydrous toluene (90 mL) was added followed by dropwise addition of β-butyrolactone (2.62 mL, 32.2 mmol). The reaction was heated at reflux for 16 h. Toluene was removed in vacuo, the resulting crude mixture was dissolved in DCM (50 mL) and washed with distilled water (3 × 50 mL). The organic layer was dried over Na_2SO_4 and concentrated in vacuo to give a yellow oil. The crude product was purified by silica gel column chromatography with a mobile phase gradient of DCM:MeOH (100:0−95:5−90:10) to give **5**, a pale yellow oil (45 %). Found C, 65.35; H, 6.72; N, 5.10 %. $C_{44}H_{55}N_3O_{10}$ requires, C, 67.24; H, 7.05; N, 5.35; O, 20.36 %. ^{1}H NMR (400 MHz, $CDCl_3$) δ ppm 7.34–7.25 (m, 20H), 5.35 (br, NH), 5.31 (br, NH), 5.11 (m, 2H), 4.50 (m, 8H), 4.14 (s, 1H), 3.62 (m, 8H), 3.46-3.18 (m, br, 8H), 2.45–2.22 (m, 2H), 1.18–1.05 (m, 3H). ^{13}C NMR (100 MHz, $CDCl_3$) δ ppm 174.4, 156.8, 156.6, 138.4, 138.3, 128.8, 128.1, 128.0, 73.7, 73.6, 72.6, 72.4, 69.5, 69.3, 65.1, 48.5, 46.5, 41.2, 40.3, 39.9, 22.9. *m/z* (ES MS) 808.4 $[M + Na]^+$, *m/z* required 785.4 $[M]^+$.

5 (9.31 g, 11.85 mmol) was dissolved in DCM (100 mL) and transferred to a round bottom flask which was equipped with magnetic stirring and a dry N_2 inlet. DMAP (0.14 g, 1.19 mmol), TEA (3.30 mL, 23.7 mmol) were added and the reaction mixture was cooled to 0 °C in an ice bath followed by dropwise addition of α-bromoisobutyryl bromide (2.19 mL, 17.78 mmol). The reaction was warmed to room temperature for 24 h. A colour change from pale orange to a dark orange/brown colour was observed over time. No precipitate was observed, the crude reaction mixture was washed with a saturated $NaHCO_3$ solution (3 × 100 mL) and distilled water (3 × 100 mL). The organic layer was dried over Na_2SO_4 and concentrated in vacuo to give **6**, an orange oil (81 %). Found C, 59.50; H, 6.31; N, 4.39 %. $C_{48}H_{60}BrN_3O_{11}$ requires, C, 61.67; H, 6.47; Br, 8.55; N, 4.49; O, 18.82 %. ^{1}H NMR (400 MHz, $CDCl_3$) δ ppm 7.35–7.23 (m, 20H), 5.33 (s, br, NH), 5.10 (m, 2H), 4.52 (m, 8H), 3.71–3.53 (s, 8H), 3.52–3.12 (m, br, 8H), 2.76 (d of d, 1H), 2.47 (d of d, 1H), 1.87 (s, 6H), 1.29 (d, 3H). ^{13}C NMR (100 MHz, $CDCl_3$) δ ppm 192.5, 170.8, 156.3, 156.1, 137.9, 134.5, 128.4, 127.7, 127.6, 73.2, 73.1, 72.2, 71.8, 70.2, 69.1, 69.0, 68.8, 56.1, 48.3, 46.3, 39.6, 39.4, 38.9, 30.8, 30.7, 30.6, 19.7. *m/z* (ES MS) 958.3 $[M + Na]^+$, 974.3 $[M + K]^+$, *m/z* required 933.3 $[M]^+$.

7.3.2 Nanoparticle Formation Using Organic Solvents

Nanoparticle formation followed a nanoprecipitation method. Each polymer was dissolved in acetone at 5.0 mg/mL unless stated otherwise. 1 mL of polymer in acetone was added to a vial with magnetic stirrer bar and sealed to prevent solvent evaporation. Various volumes of hexane (0.1–4.0 mL) were added at a rate of 0.5 mL/min by a syringe pump. Throughout this paper samples are referred to by their solvent fraction of hexane, for example, 1 mL of hexane added to 1 mL of polymer in acetone leads to a solvent fraction of hexane of 0.5. The resulting samples were kept sealed to prevent solvent evaporation and were characterised within 48 h.

7.3.3 SEM Preparation

Samples in organic solvents were prepared for SEM by dropping the sample directly onto the aluminium stub which dried rapidly. These samples did not need Au sputter coating for imaging. The aqueous nanoparticle samples were dropped on a glass cover slide mounted on an aluminium stub with a carbon tab and left to dry over several hours or overnight. They were Au sputter coated at 20 mA for 2 min prior to imaging.

7.4 Mixing Dendron and PEG Initiators for the Polymerisation of Branched pHPMA and Aqueous Nanoparticle Formation

For materials and characterisation see Sects. 7.2.1 *and* 7.2.2 *respectively.*

7.4.1 750PEG Macroinitiator Synthesis (See Sect. 3.2.2)

Monomethoxy poly(ethylene glycol) (**7**, Mw ≈ 750 g/mol) (23.0 g, 30.7 mmol) was dissolved in warm THF (~40 °C), and the reaction was degassed with dry N_2. DMAP (37.5 mg, 0.3 mmol) and TEA (7.48 mL, 53.7 mmol) were added and the reaction was cooled to 0 °C in an ice bath. α-bromo isobutyryl bromide (5.69 mL, 46.0 mmol) was added dropwise over 30 min and a white precipitate appeared immediately; the $Et_3NH^+Br^-$ salt. After 24 h the precipitate was filtered, THF removed in vacuo and the resulting crude product was precipitated from acetone into petroleum ether (30−40 °C) twice to give **8** (72 %). ^{1}H NMR (400 MHz, D_2O) δ ppm 4.31 (m, 2H), 3.77 (m, 2H), 3.70–3.59 (m, 60H), 3.55 (m, 2H), 3.31 (s, 3H) and 1.89 (s, 6H). ^{13}C NMR (100 MHz, D_2O) δ ppm 174.0, 71.5, 70.4, 70.1, 70.0, 68.8, 58.6, 30.5 (Scheme 7.3).

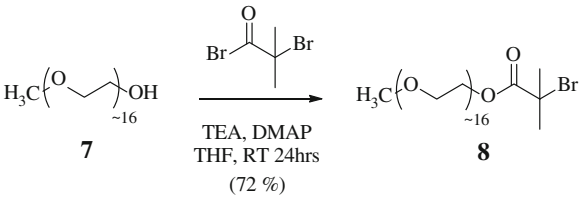

Scheme 7.3 Synthesis of 750PEG macroinitiator

7.4.2 SEM Preparation

The aqueous nanoparticle samples were dropped on a glass cover slide mounted on an aluminium stub with a carbon tab and left to dry over several hours or overnight. They were Au sputter coated at 20 mA for 2 min prior to imaging.

7.5 Mixing Dendron and PEG Initiators for the Polymerisation of Branched pHPMA and Formation of Sterically Stabilised Nanoparticles

For general materials and characterisation see Sects. 7.2.1 *and* 7.2.2 *respectively.*

7.5.1 G2′ Dendron Synthesis (See Sect. 4.2.1)

3 (14.03 g, 38.3 mmol) was added to a 2-neck round bottom flask, which was equipped with magnetic stirring, condenser and a N_2 inlet. Anhydrous toluene (100 mL) was added and the reaction was heated to 60 °C. The AB_2 brancher, **9** (3.627 g, 19.2 mmol) was dissolved in anhydrous toluene (5 mL) was added dropwise. After 18 h the reaction was stopped, the toluene removed in vacuo, the crude mixture was dissolved in dichloromethane (100 mL) and washed with water (3 × 100 mL). The organic phase was dried over Na_2SO_4 the solvent removed in vacuo and the resulting yellow oil was dried further under high vacuum to give **10**, as a pale yellow oil (94 %). ^{1}H NMR (400 MHz, $CDCl_3$) δ ppm 7.33–7.23 (m, 20H), 5.30 (s, br, NH), 5.09 (m, 2H), 4.51 (m, 8H), 3.73 (m, 1H), 3.64 (d, 8H), 3.16 (m, 4H), 2.53 (m, 2H), 2.32 (m, 2H), 2.24 (m, 2H), 1.59 (m, 4H), 1.06 (d, 3H). *m/z* (ES MS) 786.4 $[M + H]^+$, 808.4 $[M + Na]^+$, *m/z* required 785.43 $[M]^+$ (Scheme 7.4).

10 (13.381 g, 17.0 mmol) was dissolved in DCM (100 mL) and bubbled with N_2 for 20 min. 4-(Dimethylamino)pyridine (DMAP) (21 mg, 0.17 mmol) and triethylamine (TEA) (3.56 mL, 26.0 mmol) were added and the reaction vessel was cooled to 0 °C. α-Bromoisobutyryl bromide (2.53 mL, 20.0 mmol) was added dropwise, then the reaction was warmed to room temperature for 24 h. The organic phase was washed with a saturated solution of $NaHCO_3$ (3 × 150 mL) and distilled water (3 × 150 mL), dried over Na_2SO_4 and the solvent removed in vacuo to give an orange oil as the crude product. This was purified by column chromatography with a silica stationary phase and mobile phase of ethyl acetate:hexane (4:1), to give **11** a yellow oil (73 %). Found C, 63.24; H, 6.88; N, 4.44 %. $C_{49}H_{64}BrN_3O_{10}$ requires, C, 62.95; H, 6.90; N, 4.49 %. ^{1}H NMR (400 MHz, $CDCl_3$) δ ppm 7.33–7.24 (m, 20H), 5.36 (s, br, NH), 5.09 (m, 2H), 5.03 (m, 1H), 4.51 (m, 8H), 3.64 (d, 8H), 3.16 (m, 4H), 2.64–2.35 (m, 6H), 1.89 (s, 6H), 1.60 (m, 4H), 1.22 (d, 3H). ^{13}C NMR (100 MHz, $CDCl_3$) δ ppm 171.2, 156.0, 138.1, 128.3, 127.60, 127.62,

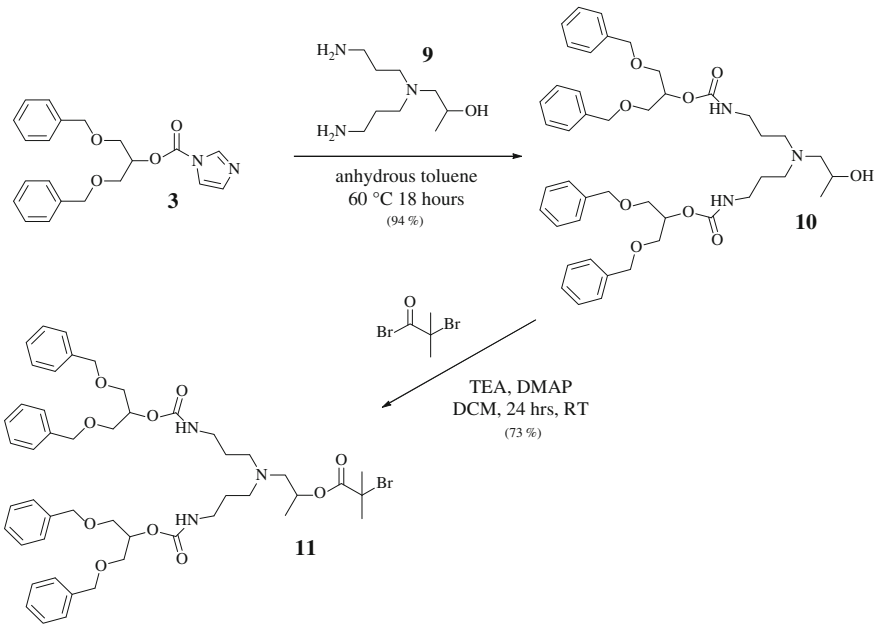

Scheme 7.4 **G2′** dendron initiator synthesis

73.2, 71.6, 70.4, 68.9, 59.1, 56.1, 52.2, 39.4, 30.6, 30.7, 27.2, 18.0. *m/z* (ES MS) 936.4 $[M + H]^+$, 959.4 $[M + Na]^+$, *m/z* required 935.4 $[M]^+$.

7.5.1.1 AB_2 Brancher Synthesis

CDI (39.137 g, 0.241 mol) was added to a 2-neck RBF fitted with a reflux condenser, magnetic stirrer and a dry N_2 inlet. Dry toluene (350 mL) was added followed by **12** (*t*-butanol) (46 mL, 0.483 mol) via syringe and the mixture was left stirring at 60 °C under nitrogen. After 6 h BAPA (17.14 mL, 0.121 mol) was added dropwise. The reaction was left stirring for a further 18 h at 60 °C then allowed to cool to room temperature. The pale yellow solution was filtered to remove any solid imidazole, and concentrated in vacuo. The remaining oil was dissolved in dichloromethane (250 mL) washed with distilled water (3 × 250 mL) and brine (150 mL). The organic layer was dried over Na_2SO_4, filtered and concentrated in vacuo to give **13** as a white waxy solid, 95 %. Found C, 57.84; H, 10.45; N, 12.91 %. $C_{16}H_{33}N_3O_4$ requires, C, 57.98; H, 10.04; N, 12.68 %. ^{1}H NMR (400 MHz, $CDCl_3$) 5.19 (s, br, NH), 3.21 (t, 4H), 2.65 (t, 4H), 1.65 (q, 4H), 1.44 (s, 18H) ^{13}C NMR (100 MHz, $CDCl_3$) 156.48, 79.34, 47.77, 39.29, 30.11, 28.79. *m/z* (ES MS) 332.3 $[M + H]^+$ (Scheme 7.5).

13 (20 g, 0.06 mol) was added to a 2-necked RBF fitted with a reflux condenser, magnetic stirrer and a dry N_2 inlet. Ethanol (200 mL) which had been dried over

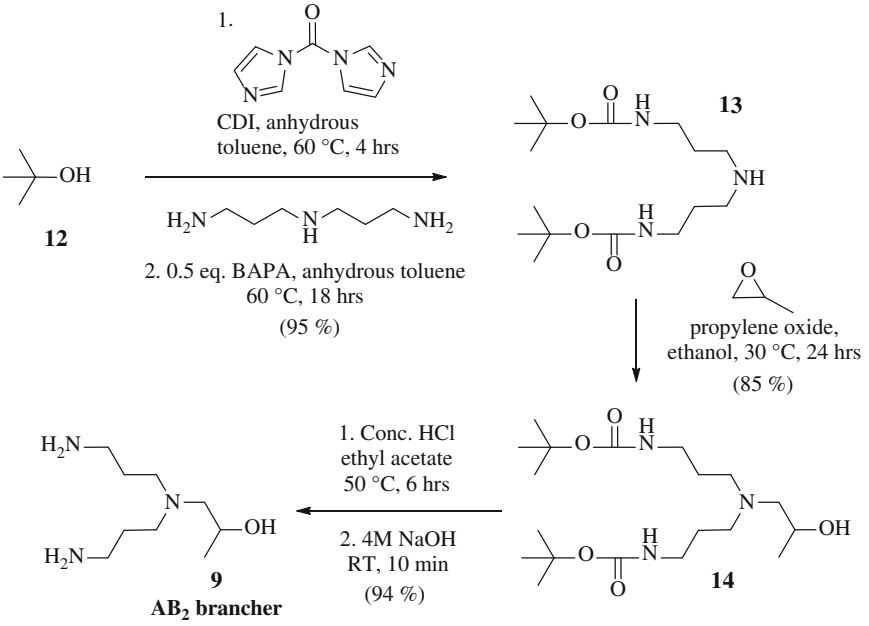

Scheme 7.5 Synthesis of the AB_2 brancher molecule, **9**

Na_2SO_4 was added and the reaction was warmed to 30 °C. Propylene oxide (11.21 mL, 0.181 mol) was added dropwise over a period of 10 min and the reaction was left stirring for 18 h. After this time, the solvent and excess propylene oxide were removed in vacuo. The crude product was purified by liquid chromatography on silica gel, eluting with EtOAc:MeOH, 4:1, the solvent was removed in vacuo to give **14** as a pale yellow viscous oil, 85 %. Found C, 58.50; H, 10.23; N, 10.82 %. $C_{19}H_{39}N_3O_5$ requires, C, 58.58; H, 10.09; N, 10.79 %. ^{1}H NMR (400 MHz, $CDCl_3$) 4.93 (s, br, NH), 3.76 (m, 1H), 3.15 (m, 4H), 2.61–2.88 (m, 6H), 1.62 (m, 4H), 1.44 (s, 18H), 1.11 (d, 3H).^{13}C NMR (100 MHz, $CDCl_3$) 156.08, 79.18, 63.45, 62.55, 51.77, 38.75, 27.48, 20.14. *m/z* (ES MS) 390.3 $[M + H]^+$

14 (33.70 g, 0.087 mol) was dissolved in ethyl acetate (300 mL) and concentrated HCl (35.03 g, 30 mL, d = 1.18 36 % active) was added very slowly. CO_2 began to evolve. The reaction vessel was left with an outlet, stirring at 50 °C for 6 h. ^{1}H NMR (D_2O) of a crude sample confirmed complete decarboxylation. The solvent was removed in vacuo and the crude oil was dissolved in 4 M NaOH (300 mL). The volume was reduced down by half (approx.) on the rotary evaporator (60 °C). Following this, the oily mixture was extracted with $CHCl_3$ (2 × 300 mL). The organic layers were then combined, dried with anhydrous Na_2SO_4, filtered and concentrated in vacuo to give the **9** the AB_2 brancher as a pale yellow oil, 94 %. Found C, 55.71; H, 12.25; N, 21.29 %. $C_9H_{23}N_3O$ requires, C, 57.10; H, 12.25; N, 22.20 %. ^{1}H NMR (400 MHz, $CDCl_3$) 3.79 (m, 1H), 2.68–2.40 (ddd, 2H), 2.31 (m, 4H), 1.89 (s, br, OH),

1.60 (m, 4H), 1.11 (d, 3H). ^{13}C NMR (100 MHz, $CDCl_3$) 63.95, 62.56, 52.10, 40.31, 30.80, 20.03. *m/z* (CI MS) 190.19 $[M+H]^+$

7.5.2 2000PEG Macroinitiator Synthesis (See Sect. 4.2.2)

Monomethoxy poly(ethylene glycol) ($M_w \approx 2000$ gmol^{-1}) (20.5 g, 10.25 mmol) was dissolved in warm THF ($\sim$40 °C), and the reaction was degassed with dry N_2. DMAP (12.5 mg, 0.1 mmol) and TEA (3.14 mL, 22.5 mmol) were added and the reaction was cooled to 0 °C in an ice bath. α-bromo isobutyryl bromide (2.53 mL, 20.5 mmol) was added dropwise over 20 min and a white precipitate appeared immediately; the $Et_3NH^+Br^-$ salt. After 24 h the precipitate was filtered, THF removed in vacuo and the resulting crude product was precipitated from acetone into petroleum ether (30−40 °C) twice (89 %). ^{1}H NMR (400 MHz, D_2O) δ ppm 4.34 (m, 2H), 3.80–3.59 (m, 186H), 3.35 (s, 3H) and 1.93 (s, 6H).

7.5.3 SEM Preparation

The aqueous nanoparticle samples were dropped on a silicon wafer mounted on an aluminium stub with a carbon tab and left to dry over several hours or overnight. They were Au sputter coated at 20 mA for 2 min prior to imaging.

7.6 Pharmacology Studies

As discussed throughout this thesis, pharmacology assessment of various *hyp*-polydendron nanoparticle materials was conducted and is described in Chaps. 3 and 4. Materials were loaded with either Nile red or fluoresceinamine (FA) and studied for their cytotoxicity to Caco-2 cells, permeation through Caco-2 cell monolayers and cellular accumulation. Table 7.1 gives a summary of all the materials studied, their concentrations and which assay have been performed with each sample.

7.6.1 Materials

Dulbecco's Modified Eagles Medium (DMEM), Hanks buffered saline solution (HBSS), Trypsin-EDTA, bovine serum albumin (BSA), Nile red, 3-(4,5-Dimethylthiazol-2-yl)-2,5—diphenyltetrazolium bromide (MTT reagent), acetonitrile

Table 7.1 Summary of all materials which had been studied for any pharmacological benefits

Formulation	Polymer (mg/mL)	Nile red (μg/mL)	FA (μg/mL)	Cytotoxicity assays (Caco-2 cells)	Caco-2 permeation assay
G2:750PEG (Chap. 3)					
100:0-pHPMA$_{50}$-EGDMA$_{0.8}$	1	1	–	✓	✓
90:10-pHPMA$_{50}$-EGDMA$_{0.8}$	1	1	–	✓	✓
75:25-pHPMA$_{50}$-EGDMA$_{0.8}$	1	1	–	✓	✓
50:50-pHPMA$_{50}$-EGDMA$_{0.8}$	1	1	–	✓	✓
25:75-pHPMA$_{50}$-EGDMA$_{0.8}$	1	1	–	✓	✓
10:90-pHPMA$_{50}$-EGDMA$_{0.8}$	1	1	–	✓	✓
0:100-pHPMA$_{50}$-EGDMA$_{0.8}$	1	1	–	✓	✓
G2′:2000PEG (Chap. 4)					
50:50-pHPMA$_{50}$-EGDMA$_{0.85}$	10	20	–	✓	✓
25:75-pHPMA$_{50}$-EGDMA$_{0.95}$	10	20	–	✓	✓
10:90-pHPMA$_{50}$-EGDMA$_{0.95}$	10	20	–	✓	✓
0:100-pHPMA$_{50}$-EGDMA$_{0.95}$	10	20	–	✓	✓
75:25-pHPMA$_{50}$-EGDMA$_{0.8}$	1	–	10	✓	✓
50:50-pHPMA$_{50}$-EGDMA$_{0.8}$	1	–	10	✓	✓
75:25-pHPMA$_{100}$-EGDMA$^{a}_{0.8}$	1	–	10	✓	✓
50:50-pHPMA$_{100}$-EGDMA$_{0.8}$	1	–	10	✓	✓
25:75-pHPMA$_{100}$-EGDMA$_{0.8}$	1	–	10	✓	✓
0:100-pHPMA$_{100}$-EGDMA$_{0.8}$	1	–	10	✗	✓

[a]Cellular accumulation studies in Caco-2 and ATHP-1 cells were also conducted using this material

(ACN) and all general laboratory reagents were purchased from Sigma (Poole, UK). Foetal bovine serum (FBS) was purchased from Gibco (Paisley, UK). The CellTiter-Glo® Luminescent Cell Viability Assay kit was from Promega (UK). The 24-well HTS transwell plates were obtained from Corning (New York, USA). The 96-well black walled, flat bottomed plates were from Sterilin (Newport, UK).

7.6.2 Characterisation

Cell count and viability was determined using a Countess automated cell counter (Invitrogen).

Absorbance was read using a Tecan Genosis plate reader at 560 nm (Tecan Magellan, Austria).

Luminescence was then measured using a Tecan Genios plate reader (Tecan Magellan, Austria).

Fluoresceinamine loaded samples were run on a Dionex HPLC using a Fortis C18 column (100 mm × 4.6 mm i.d., 3 μm). The mobile phase consisted of: (A) 95 % H_2O; 5 % ACN; 5 mM NH_4FA (B) 95 % ACN; 5 % H_2O; 5 mM NH_4FA. Elution peaks were monitored with a fluorescence detector at; 490 (ex), 530 (em) (Thermo Spectrasystem FL3000) and subsequently analysed using Chromeleon v.6.8. software.

7.6.3 Routine Cell Culture/Cell Maintenance

Caco-2 cells were purchased from American Type Culture Collection (ATCC, USA) and maintained in Dulbecco's Modified Eagles Medium (DMEM) supplemented with 15 % filtered sterile foetal bovine serum. Cells were incubated at 37 °C and 5 % CO_2 and were routinely sub-cultured every 4 days when 90 % confluent. Cell count and viability was determined using a Countess automated cell counter (Invitrogen).

7.6.4 Cytotoxicity Studies (Nile Red)

Caco-2 cells were seeded at a density of 1.0×10^4 cells/100 μL in DMEM supplemented with 15 % FBS into each well of a 96 well plate (Nunclon, Denmark) and incubated at 37 °C and 5 % CO_2. Cells from 4 separate flasks of biological replicates of each cell type were used (N1-4) to improve statistical power. Media was then aspirated from column 1 and replaced with media containing each *hyp*-polydendron or aqueous Nile red solution at an equivalent 1 μM Nile red concentration then diluted 1:1 in media across the plate up to column 11. Column 12

served as a negative control and consisted of media and untreated cells. Following *hyp*-polydendron addition, the plates were incubated for 24 or 120 h at 37 °C, 5 % CO_2 prior to assessment of cytotoxicity.

MTT assay—Following incubation of treated plates for 24 or 120 h, 20 μL of 5 mg/mL MTT reagent was added to each well and incubated for 2 h. Subsequently, 100 μL MTT lysis buffer (50 % N-N-Dimethylformamide in water containing 20 % SDS, 2.5 % glacial acetic acid and 2.5 % hydrochloric acid, pH 4.7) was added to each well to lyse overnight at 37 °C, 5 % CO_2. Following incubation the absorbance of each well was read using a Tecan Genosis plate reader at 560 nm (Tecan Magellan, Austria).

ATP assay—Following incubation of treated plates for 24 or 120 h, cells were equilibrated to room temperature for approximately 30 min. All but 20 μL of media was removed from each well and 20 μL CellTiter-Glo® (Promega, UK) reagent was added. All reagents were made fresh and in accordance with the manufacturer's instructions. Plates were put on an orbital shaker for 10 min to mix contents and allow for stabilisation of luminescence signal. Luminescence was then measured using a Tecan Genios plate reader (Tecan Magellan, Austria).

7.6.5 Caco-2 Permeation Studies (Nile Red)

Transwells were seeded with 3.5×10^4 cells per well and propagated to a monolayer over a 21 day period, during which media in the apical and basolateral wells was changed every other day. Trans-epithelial electrical resistance (TEER) values were monitored until they were >800 Ω. 1 μM of Nile red *hyp*-polydendron or 1 μM aqueous Nile red was added to the apical chamber of 4 wells and the basolateral chamber of 4 wells to quantify transport in both Apical to Basolateral (A > B) and Basolateral to Apical (B > A) direction and sampled on an hourly basis over a 4 h time period. Apparent permeability coefficient (P_{app}) was then determined by the amount of compound transported over time using Eq. (7.5) below.

$$P_{app} = (\mathrm{dQ/dt})\ (1/\mathrm{AC_0}) \tag{7.5}$$

where (dQ/dt) is the amount per time (nmol/sec), A is the surface area of the filter and C_0 is the starting concentration of the donor chamber (1 μM).

7.6.6 Aqueous Nile Red Solution for Cellular Studies

An aqueous Nile red solution was prepared in dimethyl sulfoxide (DMSO) at 1 mg/mL final concentration and used to spike either complete growth media or transport buffer. The resulting 1 μM final concentration Nile red solution was subsequently used in cytotoxicity assays or for transcellular permeability assessment respectively.

Transport buffer consisted of; Hanks buffered Saline Solution (HBSS), 25 mM 4-(2-hydroxyethyl)-1-piperazineethanesulfonic acid (HEPES), and 1 mg/mL Bovine Serum Albumin (BSA), adjusted to pH 7.4.

7.6.7 Extraction and Quantification of Nile Red

100 µL of each collected sample was mixed with 900 µL acetone, vortexed, sonicated for 6 min and centrifuged at 13,300 rpm for 3 min. The supernatant was completely dried in a vacuum centrifuge at 30 °C until the dry solid sample was left. This was reconstituted in 150 µL acetonitrile, transferred to a 96-well black walled, flat bottomed plate and measured for fluorescence intensity excitation wavelength 480 nm, emission wavelength 560 nm using a Tecan Genios plate reader (Tecan Magellan, Austria).

7.6.8 Cytotoxicity Studies (Fluoresceinamine)

Caco-2 cells were seeded at a density of 1.0×10^4 cells/100 µL in DMEM supplemented with 15 % FBS into each well of a 96 well plate (Nunclon, Denmark) and incubated at 37 °C and 5 % CO_2. Cells from 4 separate flasks of biological replicates of each cell type were used (N1-4) to improve statistical power. Media was then aspirated from column 1 and replaced with media containing each *hyp*-polydendron or aqueous FA solution at an equivalent 10 µM FA concentration then diluted 1:1 in media across the plate up to column 11. Column 12 served as a negative control and consisted of media and untreated cells. Following *hyp*-polydendron addition, the plates were incubated for 24 or 120 h at 37 °C, 5 % CO_2 prior to assessment of cytotoxicity.

MTT assay—same as the MTT assay experimental described in Sect. 7.6.4.

ATP assay—same as the ATP assay experimental described as Sect. 7.6.4.

7.6.9 Caco-2 Permeation Studies (Fluoresceinamine)

Transwells were set up and propagated to a monolayer over a 21 day period as previously described. Only wells with TEER values > 800 Ω were used.

10 µM of fluoresceinamine *hyp*-polydendron or 10 µM aqueous fluoresceinamine (transport buffer spiked with DMSO dissolved fluoresceinamine, DMSO final volume < 1 % of total volume), was added to the apical or basolateral compartment of the wells to quantify transport in both Apical > Basolateral (A > B) and Basolateral > Apical (B > A) directions (n = 3).

Plates were sampled following 4 h incubation at 37 °C, 5 % CO_2, apical and basolateral contents were stored at −30 °C prior to analysis.

To assess monolayer integrity following incubation, 250 μL of transport buffer containing 2 μL mL^{-1} ^{14}C mannitol was added to the apical compartment and incubated for 1 h. 4 mL of scintillation fluid was added to 100 μL of the sampled contents and quantified on the scintillation counter (Packard 3100 TR).

7.6.10 Aqueous Fluoresceinamine Solution for Cellular Studies

An aqueous FA solution was prepared in dimethyl sulfoxide (DMSO) at 1 mg/mL final concentration and used to spike either complete growth media or transport buffer. The resulting 1 μM final concentration FA solution was subsequently used in cytotoxicity assays or for transcellular permeability assessment respectively. Transport buffer consisted of; Hanks buffered Saline Solution (HBSS), 25 mM 4-(2-hydroxyethyl)-1-piperazineethanesulfonic acid (HEPES), and 1 mg/mL Bovine Serum Albumin (BSA), adjusted to pH 7.4.

7.6.11 Extraction and Quantification of Fluoresceinamine

150 μL of sample and prepared calibration for each *hyp*-polydendron material, were extracted using 9 volumes of acetone, sonicated for 6 min and centrifuged for 3 min prior to drying at 30 °C on a vacuum centrifuge. Each sample was reconstituted using 150 μL of 25 % DMSO.

Samples were run on a Dionex HPLC using a Fortis C18 column (100 mm × 4.6 mm i.d., 3 μm). The mobile phase consisted of: (A) 95 % H_2O; 5 % ACN; 5 mM NH_4FA (B) 95 % ACN; 5 % H_2O; 5 mM NH_4FA. Elution peaks were monitored with a fluorescence detector at; 490 (ex), 530 (em) (Thermo Spectrasystem FL3000) and subsequently analysed using Chromeleon v.6.8. software.

7.6.12 Cellular Accumulation of Fluoresceinamine in Caco-2 and ATHP-1 Cells

Caco-2 cells were seeded into 6 well plates (Nunclon^{TM}) at a density of 4×10^6 per well and incubated at 37 °C 5 % CO_2 for 24 h. THP-1 cells were seeded at a density of 4×10^6 cells per well in a 6 well plate and allowed to differentiate to ATHP-1 cells for 7 days in 10 nM PMA supplemented RPMI-1640 10 % FBS prior to use. Following incubation, the media was aspirated and cells washed twice with HBSS

(37 °C) and subsequently replaced with pre-warmed (37 °C) Transport Buffer containing either 10 μM (final concentration) aqueous fluoresceinamine or 10 μM (final concentration) *hyp*-polydendron formulated fluoresceinamine. Following 24 h incubation at 37 °C 5 % CO_2, 150 μL of the extracellular media was sampled. The remaining media was aspirated and cells were washed twice with ice cold HBSS. The ice cold HBSS was aspirated and replaced with 500 μL of a 50 % acetone 50 % water solution and incubated for 24 h at −20 °C, 150 μL of the lysate was subsequently sampled. Finally, 9 volumes of acetone was added to each intracellular and extracellular sample to extract fluoresceinamine for quantification on the HPLC as previously described, see Sect. 7.6.11. Average cell volumes were previously determined using a Scepter 2.0 Automated Cell Counter (Millipore) and used to calculate Cellular Accumulation Ratios (CAR); (Intracellular concentration/Volume)/(Extracellular concentration/Volume).

Appendix

Chapter 2

See Figs. A.1, A.2, A.3, A.4, A.5, A.6, A.7, A.8, A.9, A.10, A.11, A.12, A.13 and Tables A.1, A.2 and A.3.

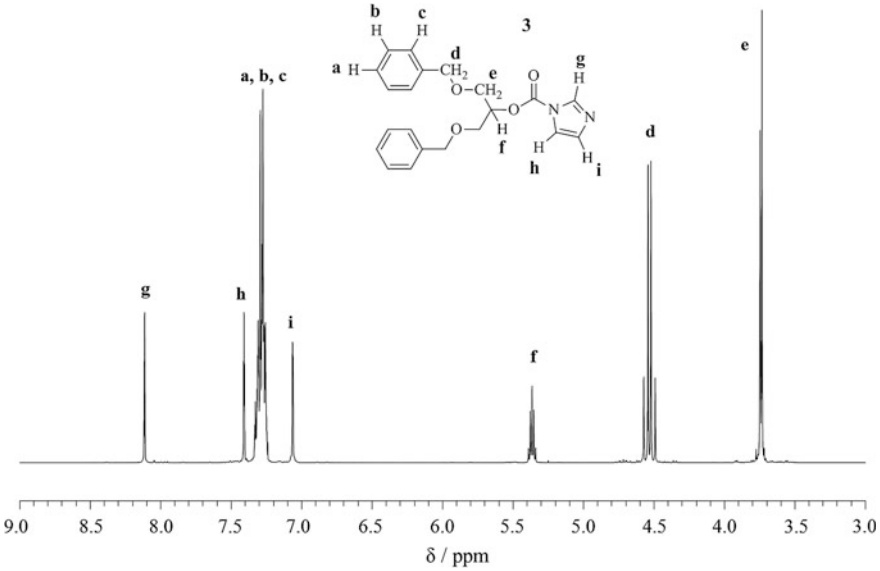

Fig. A.1 ^{1}H NMR ($CDCl_3$, 400 MHz) of G1 DBOP carboxy ester imidazole, **3**

F.L. Hatton, *Hyperbranched Polydendrons*,
Springer Theses, DOI 10.1007/978-3-319-18753-2

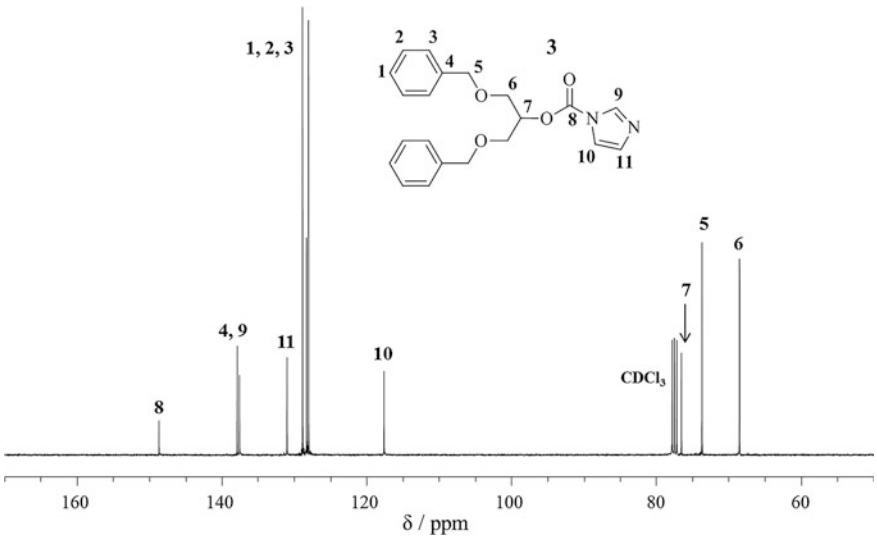

Fig. A.2 ^{13}C NMR ($CDCl_3$, 125 MHz) of G1 DBOP carboxy ester imidazole, **3**

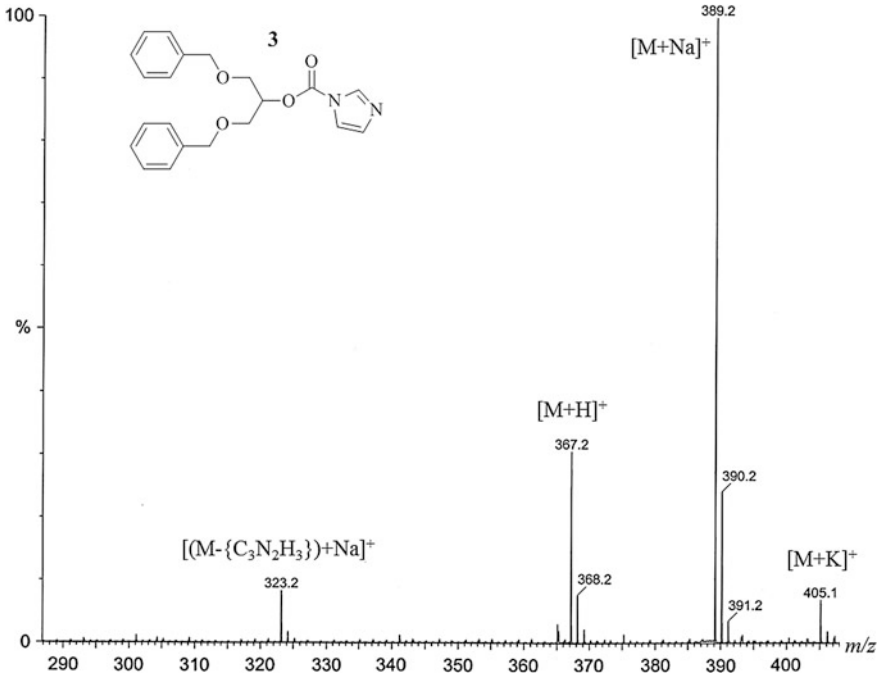

Fig. A.3 Mass spectrum (ES-MS) of G1 DBOP CI, **3**

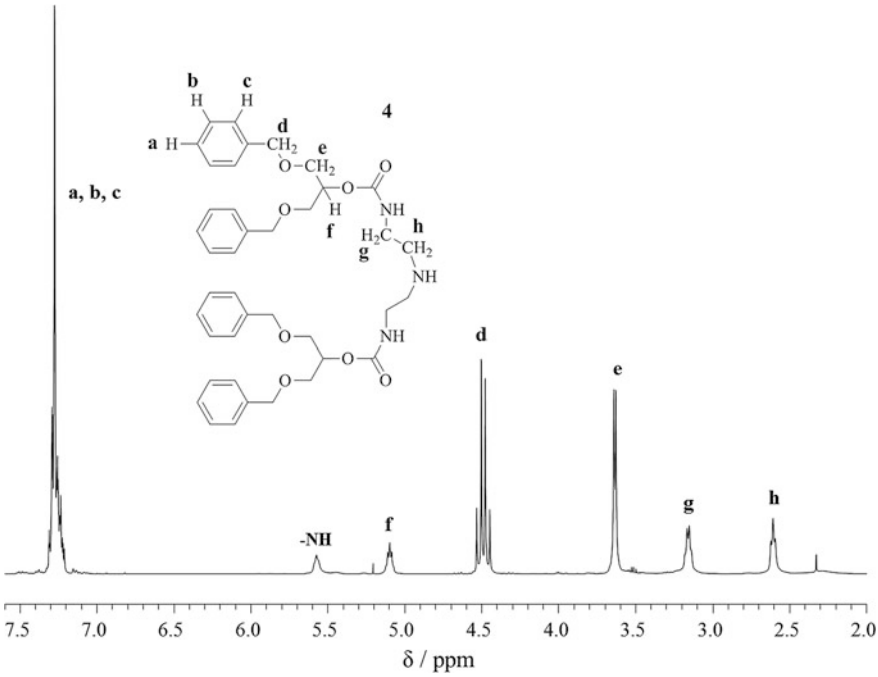

Fig. A.4 ^{1}H NMR ($CDCl_3$, 400 MHz) of G2 DBOP NH, **4**

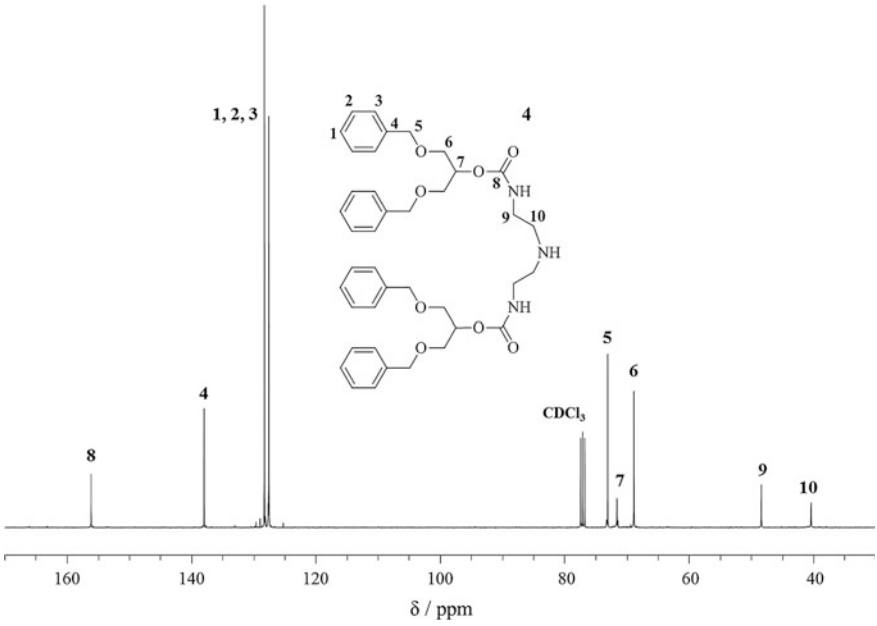

Fig. A.5 ^{13}C NMR ($CDCl_3$, 100 MHz) of G2 DBOP NH, **4**

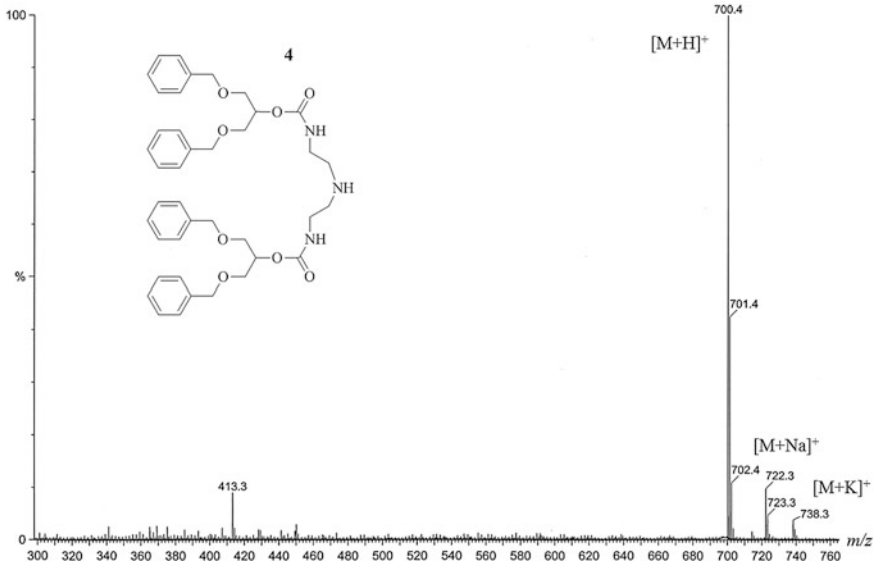

Fig. A.6 Mass spectrum (ES-MS) of G2 DBOP NH, **4**

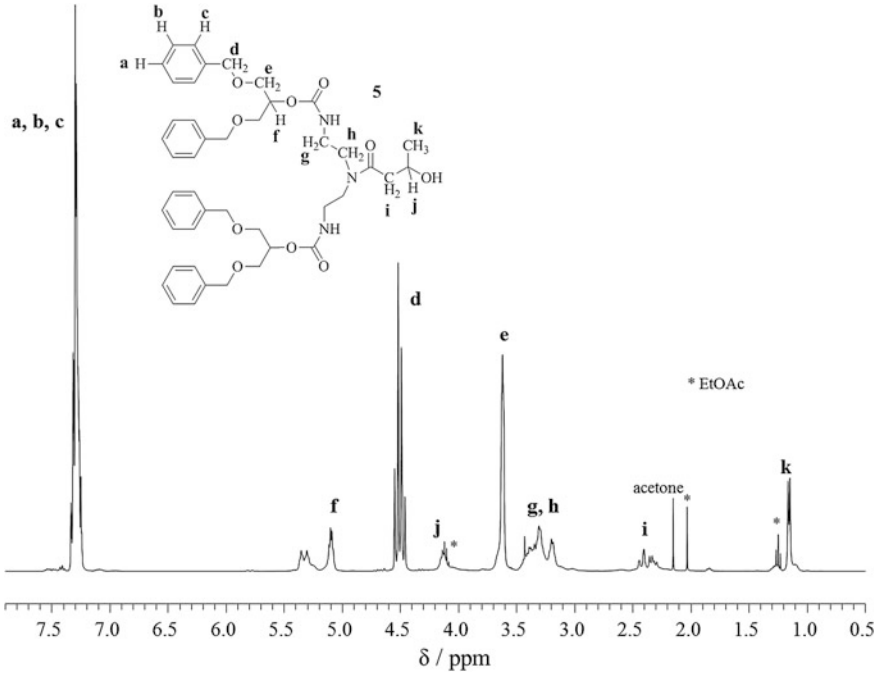

Fig. A.7 ^{1}H NMR ($CDCl_3$, 400 MHz) of G2 DBOP OH, **5**

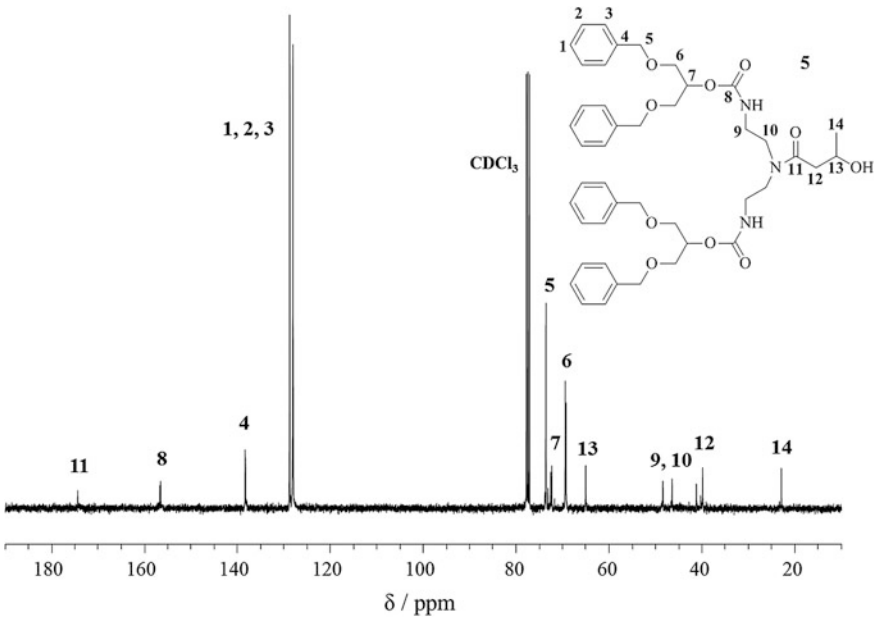

Fig. A.8 ^{13}C NMR ($CDCl_3$, 100 MHz) of G2 DBOP OH, **5**

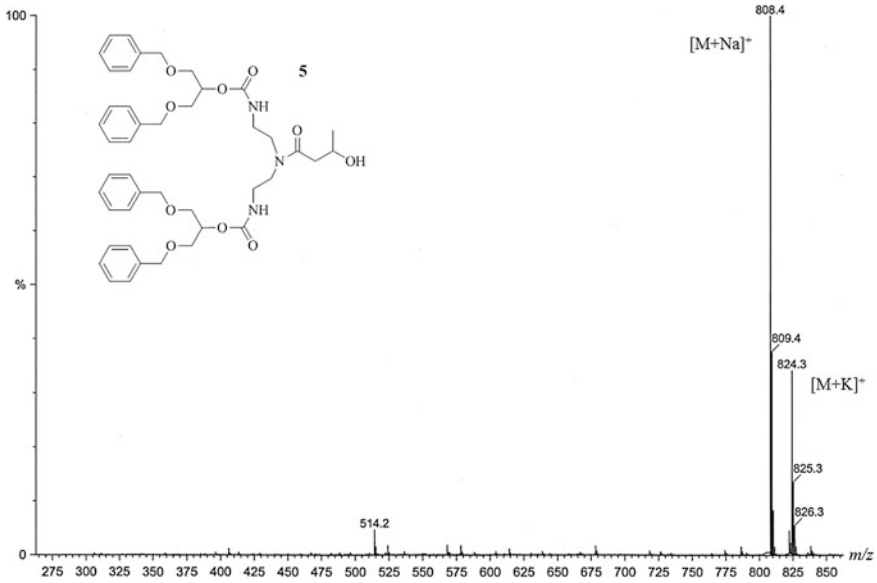

Fig. A.9 Mass spectrum (ES-MS) of G2 DBOP OH, **5**

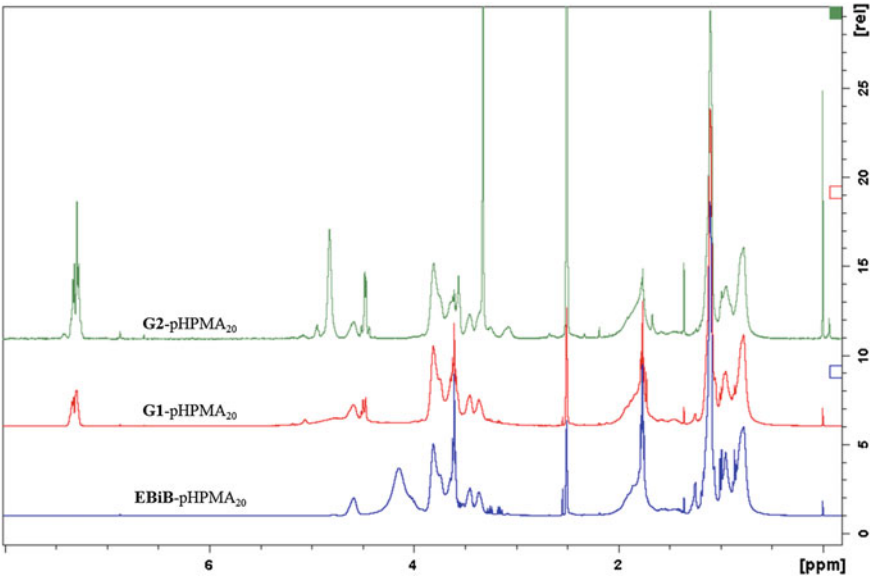

Fig. A.10 ^{1}H NMR (d_6-DMSO, 400 MHz) spectra overlay for **EBiB**-pHPMA$_{20}$, **G1**-pHPMA$_{20}$ and **G2**-pHPMA$_{20}$

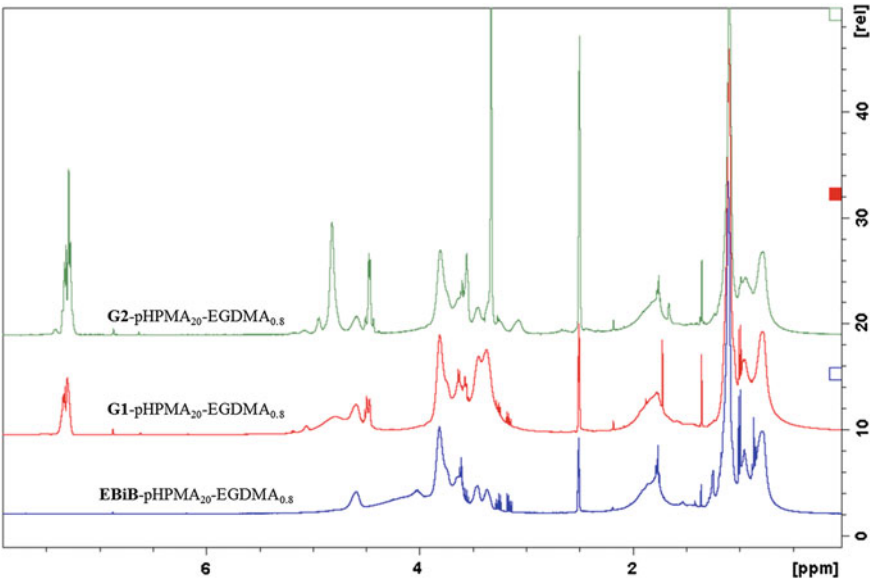

Fig. A.11 ^{1}H NMR (d_6-DMSO, 400 MHz) spectra overlay for **EBiB**-pHPMA$_{20}$-EGDMA$_{0.8}$, **G1**-pHPMA$_{20}$-EGDMA$_{0.8}$ and **G2**-pHPMA$_{20}$-EGDMA$_{0.8}$

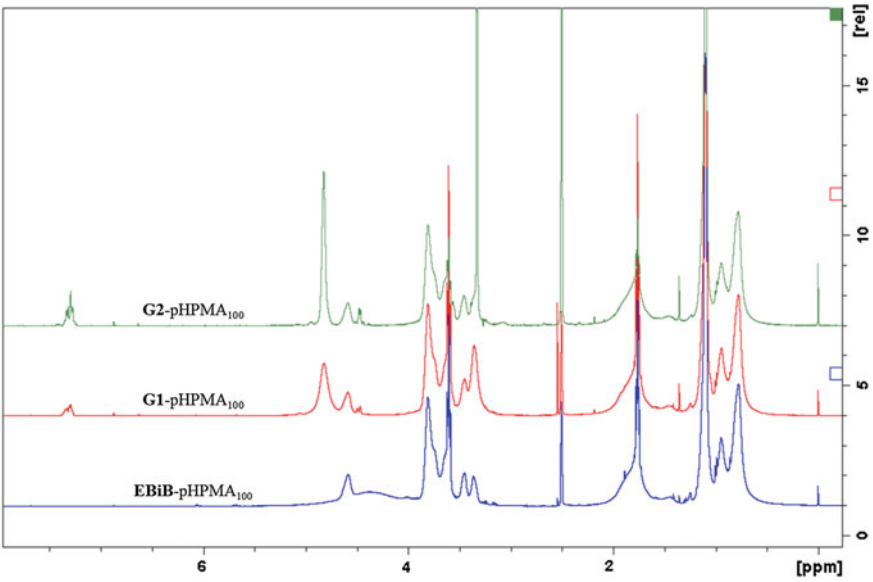

Fig. A.12 ^{1}H NMR (d_6-DMSO, 400 MHz) spectra overlay for **EBiB**-pHPMA$_{100}$, **G1**-pHPMA$_{100}$ and **G2**-pHPMA$_{100}$

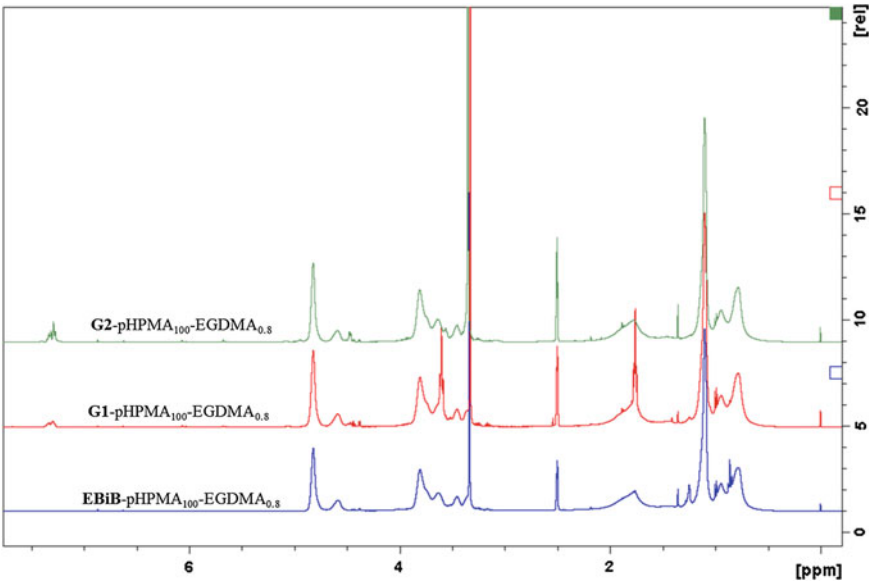

Fig. A.13 ^{1}H NMR (d_6-DMSO, 400 MHz) spectra overlay for **EBiB**-pHPMA$_{100}$-EGDMA$_{0.8}$, **G1**-pHPMA$_{100}$-EGDMA$_{0.8}$ and **G2**-pHPMA$_{100}$-EGDMA$_{0.8}$

Table A.1 Different initial concentrations used in the formation of nanoparticles with **G1**-pHPMA$_{50}$-EGDMA$_{0.8}$ (see Fig. 2.25)

G1-pHPMA$_{50}$-EGDMA$_{0.8}$						
Initial concentration	20 (mg/mL)		5 (mg/mL)		0.5 (mg/mL)	
Fraction of hexane added (Φ_{hex})	D_z (nm)	PdI	D_z (nm)	PdI	D_z (nm)	PdI
0	–	–	46	0.369	58	0.342
0.09	–	–	42	0.361	–	–
0.17	27	0.268	40	0.325	–	–
0.23	396	0.288	162	0.021	156	0.339
0.29	294	0.164	141	0.027	84	0.217
0.33	313	0.137	149	0.075	90	0.144
0.43	230	0.106	140	0.056	92	0.142
0.5	217	0.094	136	0.072	84	0.115
0.67	247	0.173	133	0.06	85	0.067
0.75	–	–	161	0.033	94	0.027
0.8	–	–	201	0.013	117	0.004

Table A.2 DLS values for the formation and dilution with acetone of **G1**-pHPMA$_{50}$-EGDMA$_{0.8}$ with Φ_{hex} = 0.67 and an initial concentration of 5 mg/ml (see Fig. 2.26)

Fraction of hexane added (Φ_{hex})	Formation of sample		Dilution of sample with Acetone	
	D_z (nm)	PdI	D_z (nm)	PdI
0.09	42	0.361	51	0.297
0.17	40	0.325	44	0.275
0.23	162	0.021	125	0.116
0.29	141	0.027	151	0.080
0.33	149	0.075	157	0.073
0.43	140	0.056	161	0.066
0.5	136	0.072	165	0.082
0.67	133	0.06	157	0.064

Table A.3 DLS values for the dilution of a **G1**-pHPMA$_{50}$-EGDMA$_{0.8}$ sample at Φ_{hex} = 0.80, and concentration of 1 mg/ml with the same solvent system; Φ_{hex} = 0.80 and Φ_{ace} = 0.20 (see Fig. 2.27)

Concentration (mg/ml)	D_z (nm)	PdI
1	398	0.077
0.5	372	0.023
0.25	369	0.060
0.125	375	0.058
0.0625	341	0.082

Chapter 3

See Figs. A.14, A.15, A.16, A.17, A.18, A.19, A.20, A.21, A.22, and Tables A.4, A.5, A.6 and A.7.

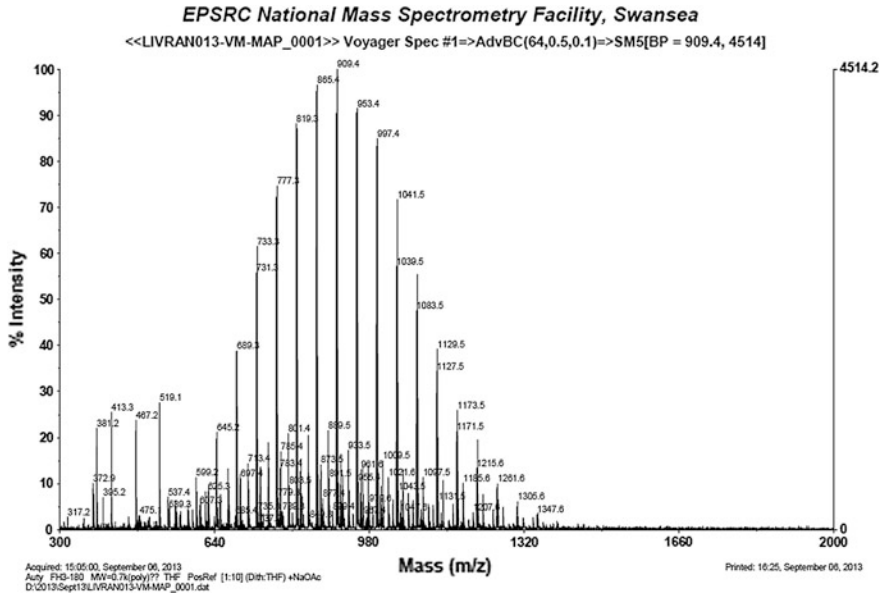

Fig. A.14 Mass spectrometry analysis of **750PEG** initiator (MALDI-TOF)

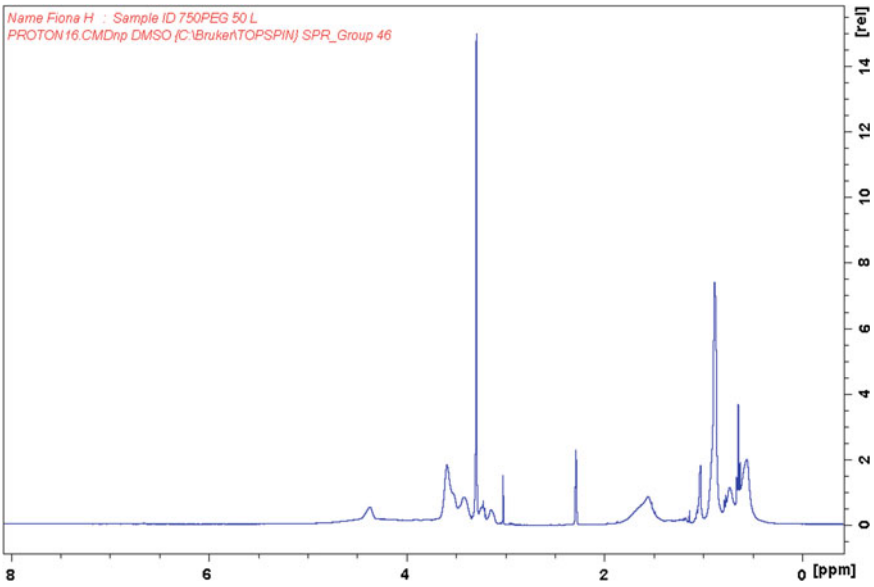

Fig. A.15 ^{1}H NMR (d_6-DMSO, 400 MHz) spectrum for the **750PEG**-pHPMA$_{50}$ linear block copolymer

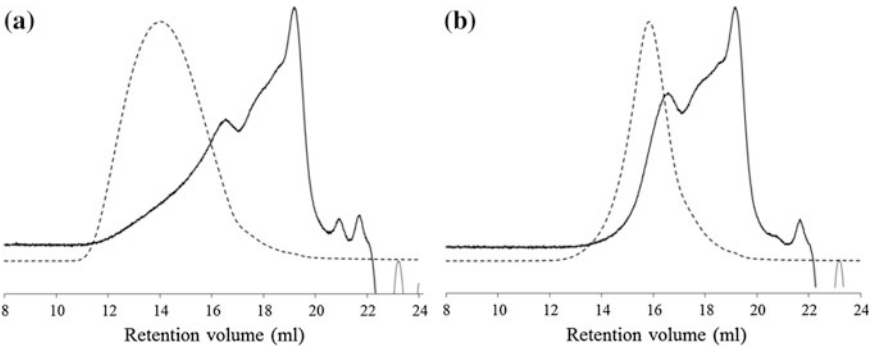

Fig. A.16 GPC chromatogram overlays of **a G2**:**750PEG**-50:50-pHPMA$_{50}$-EGMDA$_{0.95}$ and **b 750PEG**-pHPMA$_{50}$-EGDMA$_{0.95}$ with refractive index (RI) traces (*solid line*) and right angle light scattering (RALS) traces (*dashed line*)

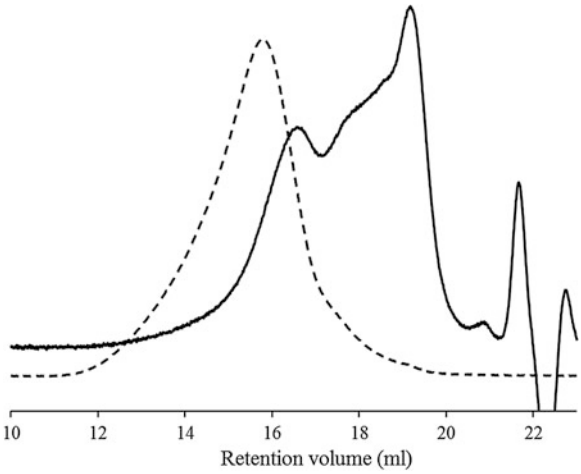

Fig. A.17 GPC chromatogram overlay of **G2:750PEG** 25:75-pHPMA$_{50}$-EGMDA$_{0.9}$ with refractive index (RI) trace (*solid line*) and right angle light scattering (RALS) trace (*dashed line*)

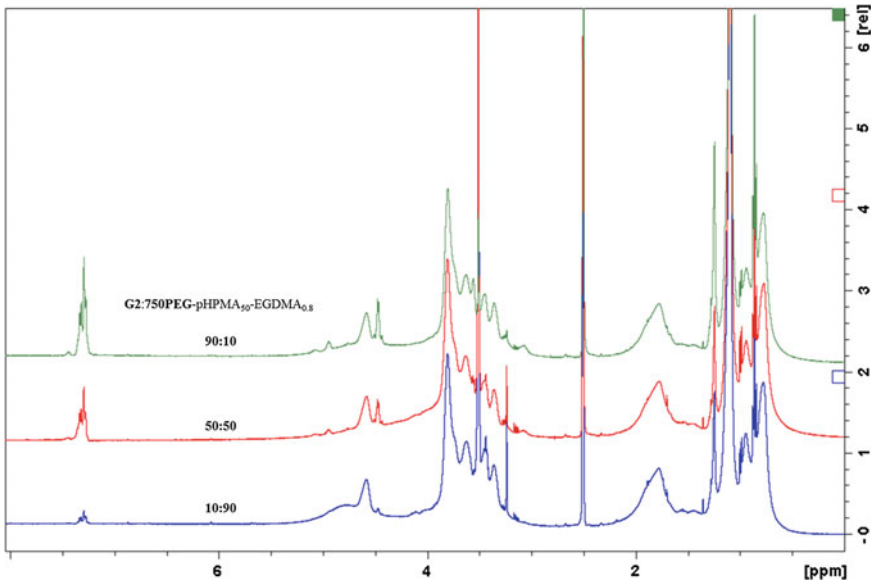

Fig. A.18 ^{1}H NMR (d$_6$-DMSO, 400 MHz) spectra overlay for **G2:750PEG** 90:10, 50:50 and 10:90-pHPMA$_{50}$-EGDMA$_{0.8}$

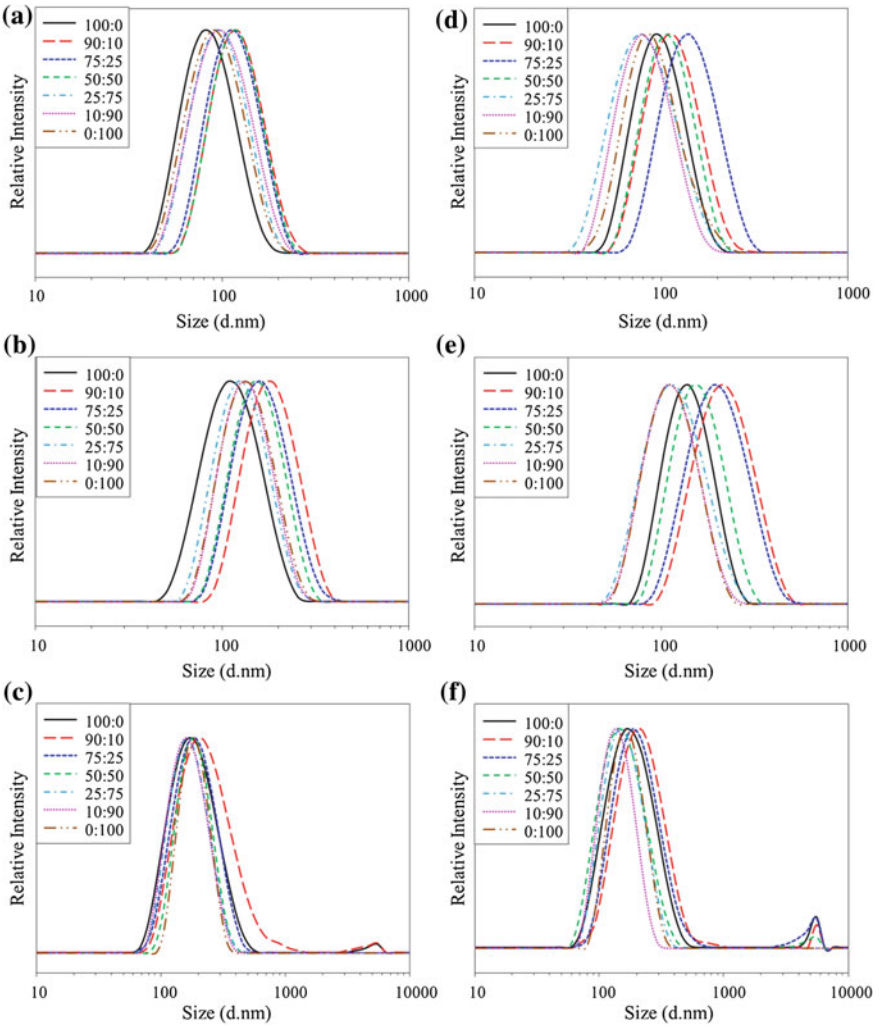

Fig. A.19 DLS size distribution by intensity traces for the **G2**:**750PEG**-pHPMA$_{50}$-EGDMA$_{0.8}$ nanoprecipitations; **a** i_5-f_1, **b** i_{10}-f_2, **c** i_{25}-f_5, **d** i_5-$f_{0.05}$, **e** i_{10}-$f_{0.1}$ and **f** i_{25}-$f_{0.25}$

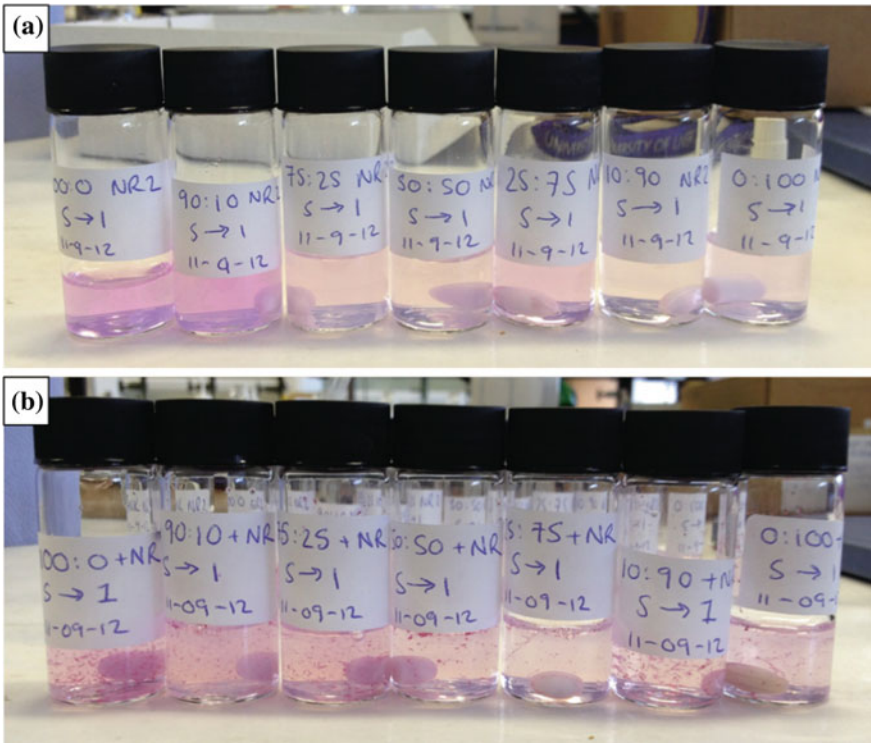

Fig. A.20 Photographs of Nile Red loaded nanoparticles using G2:750PEG-pHPMA50-EGDMA0.8 series from 100:0 (*left*) to 0:100 (*right*) with **a** 0.1 w/w% and **b** 1 w/w% Nile red with respect to the mass of polymer

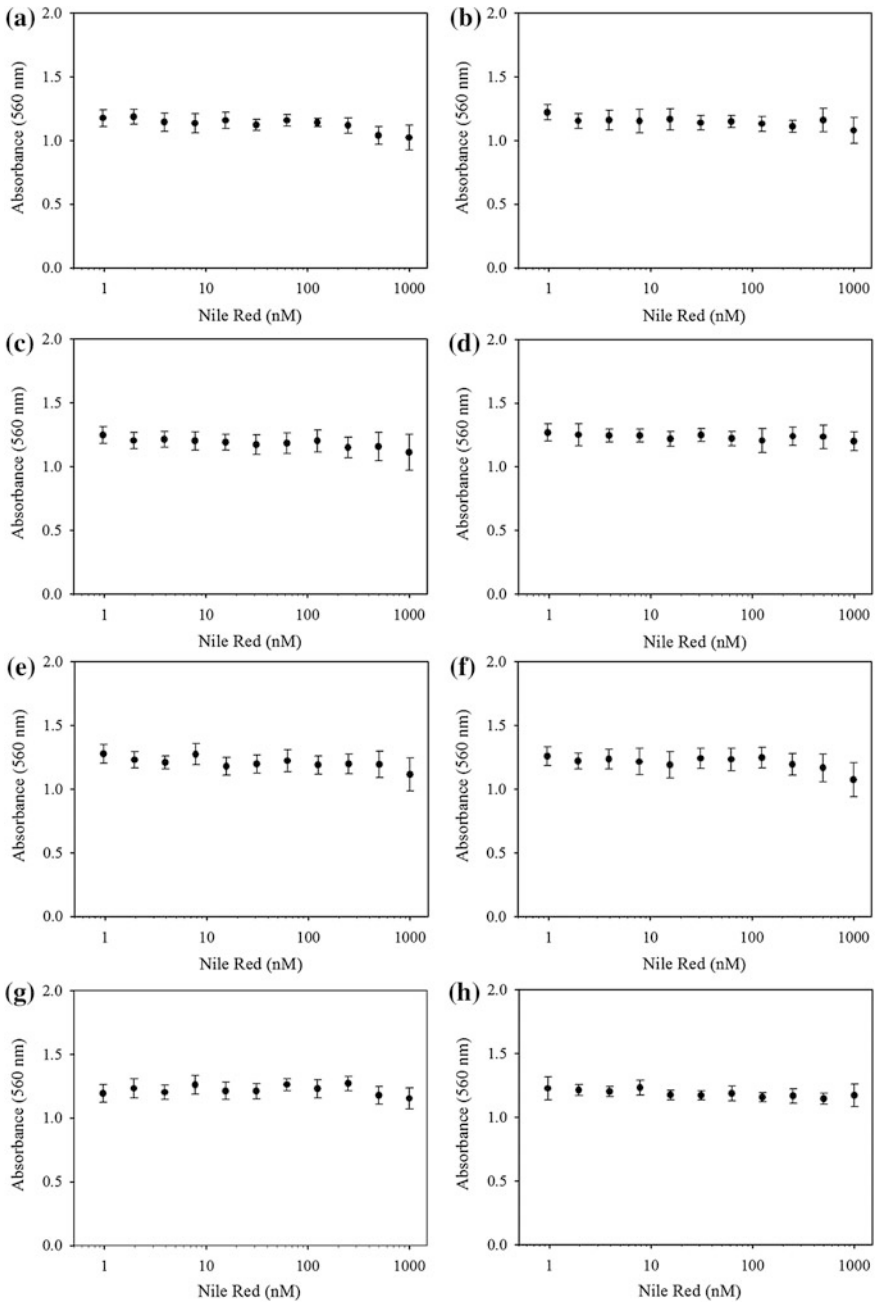

Fig. A.21 MTT assay of Caco-2 cells following 1 day incubation with aqueous Nile Red and each *hyp*-polydendron. **a** 100:0. **b** 90:10. **c** 75:25. **d** 50:50. **e** 25:75. **f** 10:90. **g** 0:100. **h** Aqueous. Error = standard deviation

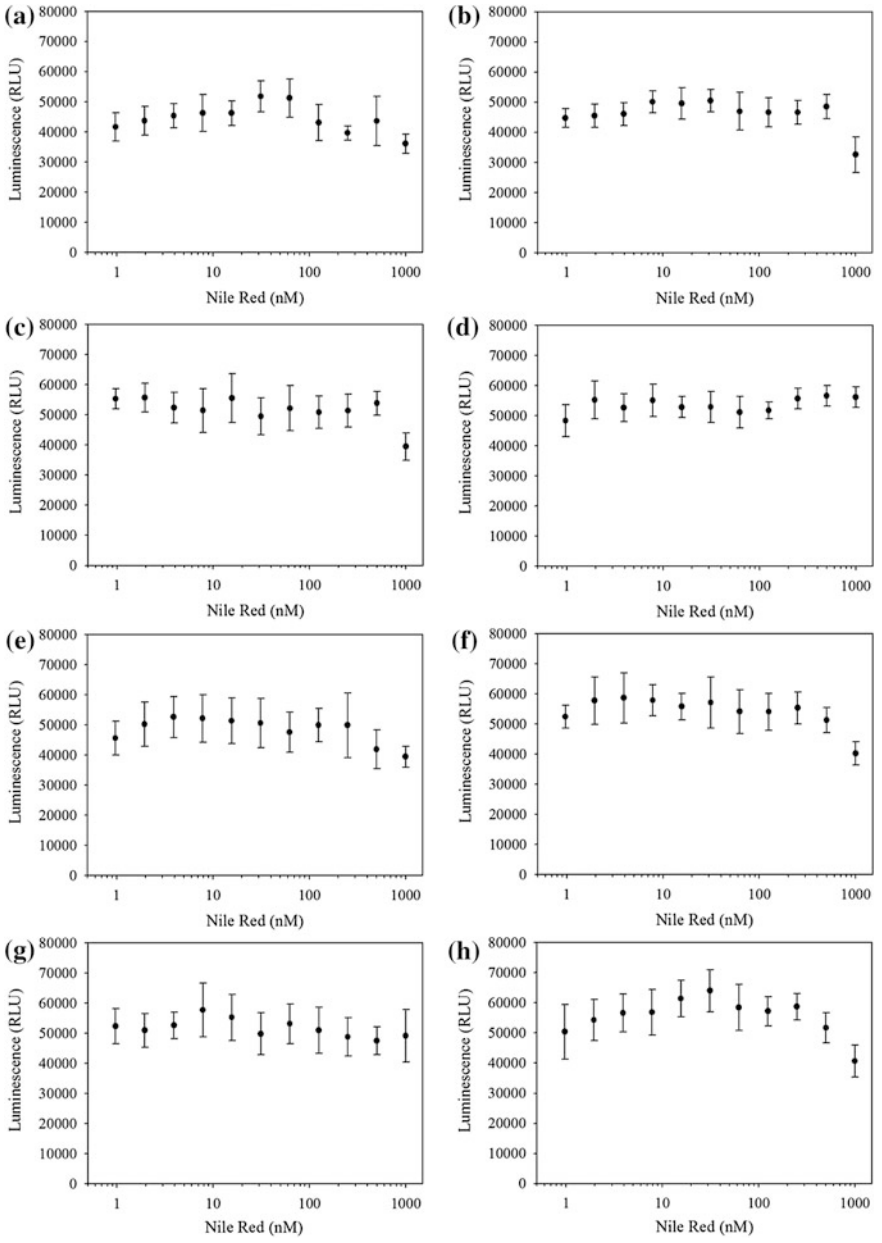

Fig. A.22 ATP assay of Caco-2 cells following 1 day incubation with aqueous Nile Red and each *hyp*-polydendron. **a** 100:0. **b** 90:10. **c** 75:25. **d** 50:50. **e** 25:75. **f** 10:90. **g** 0:100. **h** Aqueous. Error = standard deviation

Table A.4 DLS measurements for the dilution experiment conducted with the **G2:750PEG**-50:50-pHPMA$_{50}$-EGDMA$_{0.8}$ *hyp*-polydendron formulated using i_5-f_1

Concentration (mg/mL)	**G2:750PEG**-50:50-pHPMA$_{50}$-EGDMA$_{0.8}$	
	Z-Ave diameter (nm)	PdI
1.0	75	0.064
0.5	74	0.056
0.25	72	0.066
0.125	73	0.057
0.0625	72	0.063
0.0313	72	0.081
0.0156	72	0.074

Table A.5 DLS measurements of the swelling experiment conducted with the **G2:750PEG**-50:50-pHPMA$_{50}$-EGDMA$_{0.8}$ *hyp*-polydendron formulated using i_5-f_1 adding various volumes of THF, with the refractive index of the dispersant media for each sample

Volume of THF added (μL)	**G2:750PEG**-50:50-pHPMA$_{50}$-EGDMA$_{0.8}$		Refractive index of dispersant media
	Z-Ave diameter (nm)	PdI	
0	74	0.082	1.3334
13	77	0.069	1.3338
40	84	0.078	1.3359
80	92	0.105	1.3380
133	106	0.092	1.3418
200	126	0.076	1.3463
333	168	0.186	1.3538
466	162	0.062	1.3597
600	211	0.071	1.3648

Table A.6 DLS data of blank, nile red and pyrene loaded nanoparticle samples (i_5-f_1) 0.1 w/w% dye with respect to the mass of polymer

Hyp-polydendron **G2:750PEG**	Blank samples		Nile Red loaded		Pyrene loaded	
	Z-Ave diameter (nm)	PdI	Z-Ave Diameter (nm)	PdI	Z-Ave Diameter (nm)	PdI
100:0	81	0.083	76	0.109	69	0.061
90:10	116	0.069	119	0.061	134	0.046
75:25	110	0.073	108	0.067	98	0.067
50:50	115	0.067	98	0.069	97	0.060
25:75	93	0.078	93	0.081	83	0.079
10:90	94	0.091	101	0.075	88	0.074
0:100	88	0.076	97	0.095	90	0.074

Table A.7 Apparent permeability (*P*app) of Nile Red polydendrons and aqueous Nile Red across Caco2 cell monolayers following 1 h incubation

*P*app (cm s^{-1})			
Polydendron formulation (G2:750PEG ratio)	Apical > Basolateral	Basolateral > Apical	A > B/ B > A ratio
1.00:0.00	1.763×10^{-5}	1.538×10^{-6}	11.4605
0.75:0.25	2.613×10^{-5}	2.056×10^{-6}	12.7123
0.50:0.50	5.271×10^{-5}	5.555×10^{-6}	9.4872
0.25:0.75	4.135×10^{-5}	4.684×10^{-6}	8.8279
0.10:0.90	4.042×10^{-4}	4.580×10^{-5}	8.8255
0.00:1.00	2.060×10^{-5}	3.188×10^{-6}	6.4626
Aqueous Nile Red	2.371×10^{-5}	6.384×10^{-6}	3.7140

Data are given as the mean of experiments conducted in biological triplicate

Chapter 4

AB_2 Brancher Synthesis

The AB_2 brancher synthesis was developed in the research group and the reaction scheme is shown in Scheme 4.2 (Scheme A.1).

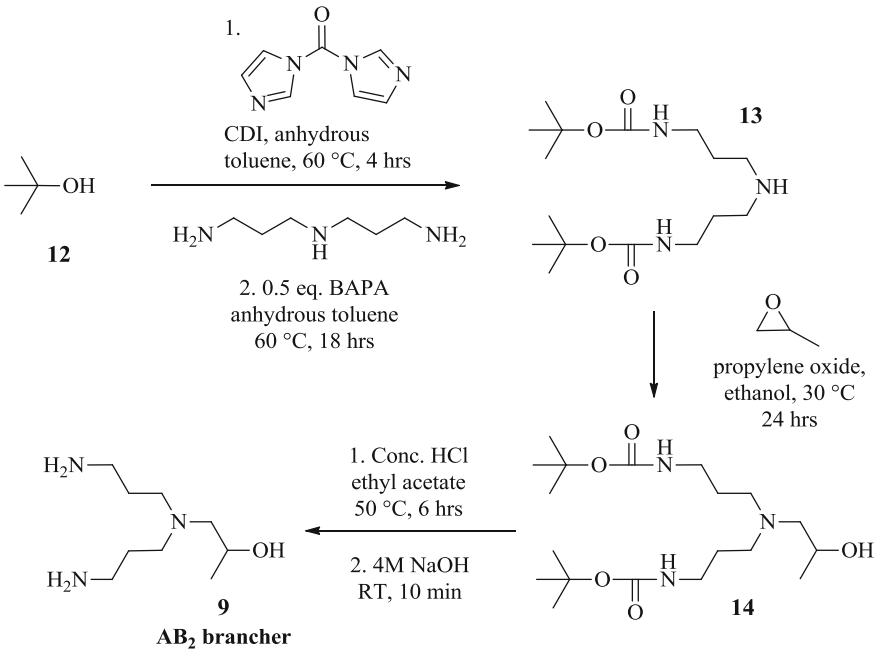

Scheme A.1 AB_2 Brancher synthesis

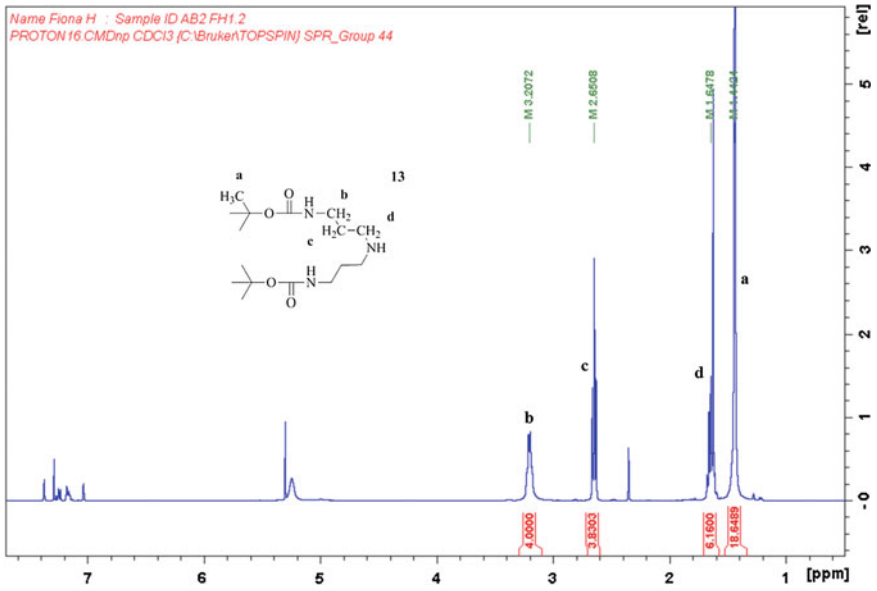

Fig. A.23 ^{1}H NMR ($CDCl_3$, 400 MHz) of **13**, intermediate in the AB_2 synthesis

tert-Butanol was reacted with CDI to give an imidazole carboxylic ester intermediate in situ with subsequent reaction with bis(3-aminopropyl)amine (BAPA), where the primary amines selectively react with the in situ intermediate to give **13**, see Appendix Fig. A.25 for ^{1}H NMR spectrum of **13**. This reaction has been previously reported[4] and the selectivity of the reaction allows coupling of molecules whilst retaining the functionality of the secondary amine for further reaction. The secondary amine was utilised for the ring opening reaction with propylene oxide to give **14**, see Appendix Fig. A.26 for the ^{1}H NMR spectrum of **14**. The conditions for the propylene oxide ring opening were tuned to ensure the product was the ring opened adduct which gave a secondary alcohol rather than a primary alcohol.[5] Deprotection of **14** afforded **9**, the AB_2 brancher and was achieved by reaction with conc. HCl before addition of 4 M NaOH, which was used to break the intermediary salt which is formed after deprotection, to give the two free primary amines. The ^{1}H NMR spectrum of **9** is shown in Fig. 4.4 (Figs. A.25, A.26, A.27, A.28, A.29, A.30, A.31, A.32, A.33, A.34, A.35, A.36, A.37 and Tables A.8, A.9, A.10, A.11).

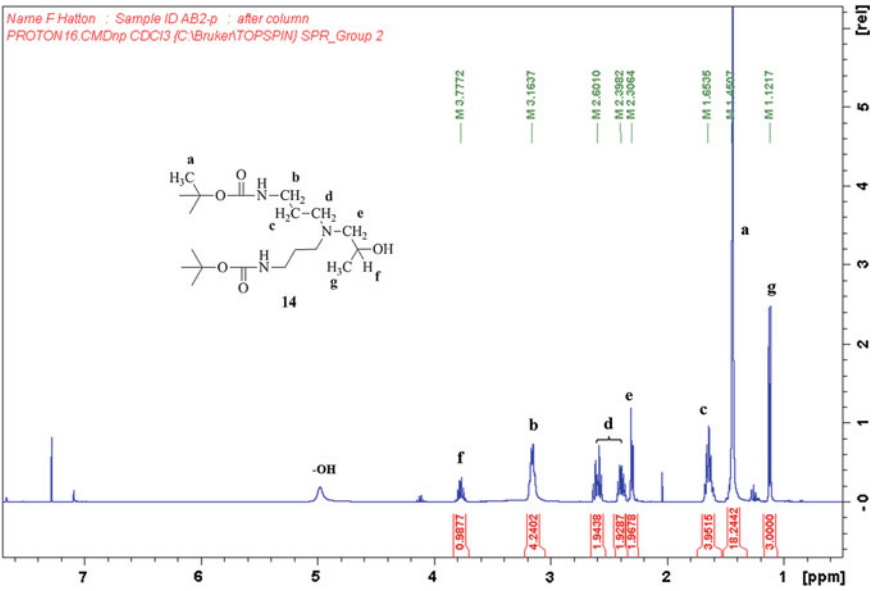

Fig. A.24 ^{1}H NMR ($CDCl_3$, 400 MHz) of **14**, intermediate in the AB_2 synthesis

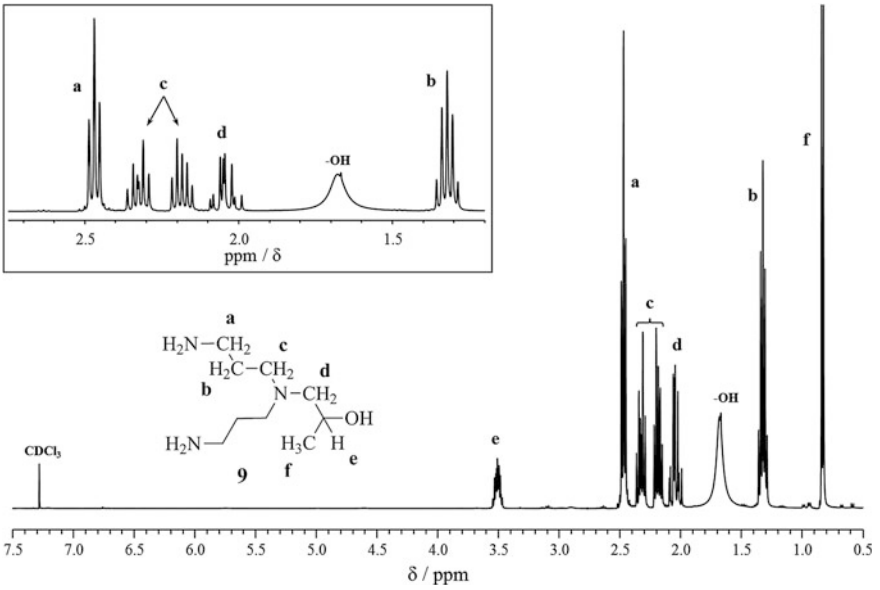

Fig. A.25 ^{1}H NMR (400 MHz $CDCl_3$) spectrum for the AB_2 brancher, **9**

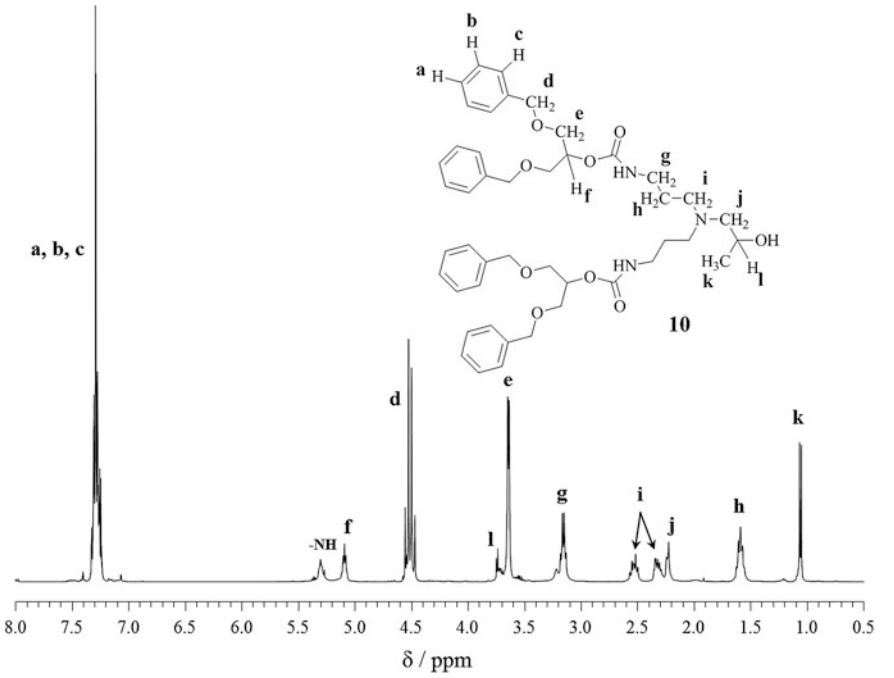

Fig. A.26 ^{1}H NMR ($CDCl_3$, 400 MHz) of G2 dendron, **10**

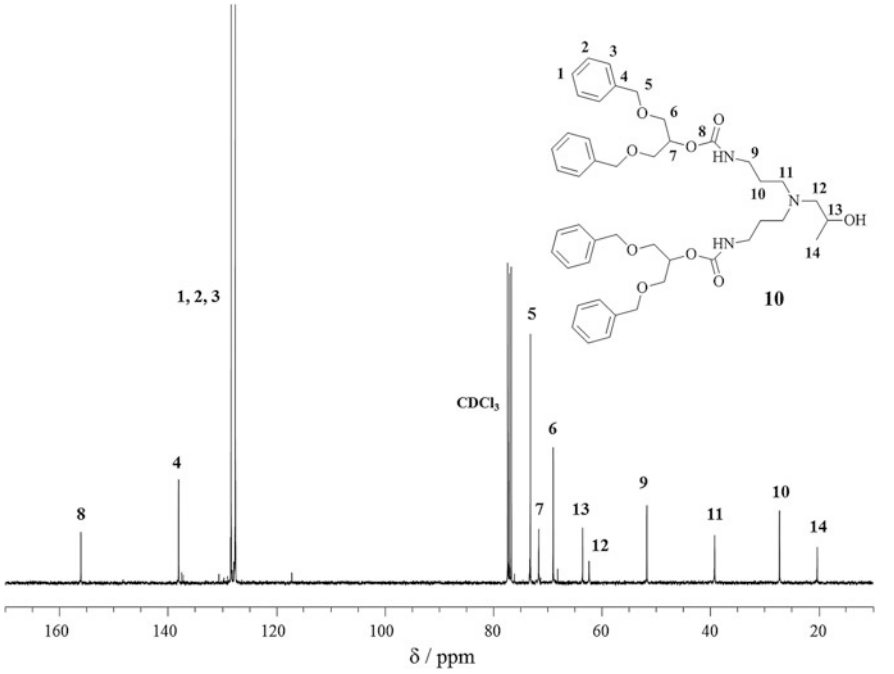

Fig. A.27 ^{13}C NMR ($CDCl_3$, 100 MHz) of G2 dendron, **10**

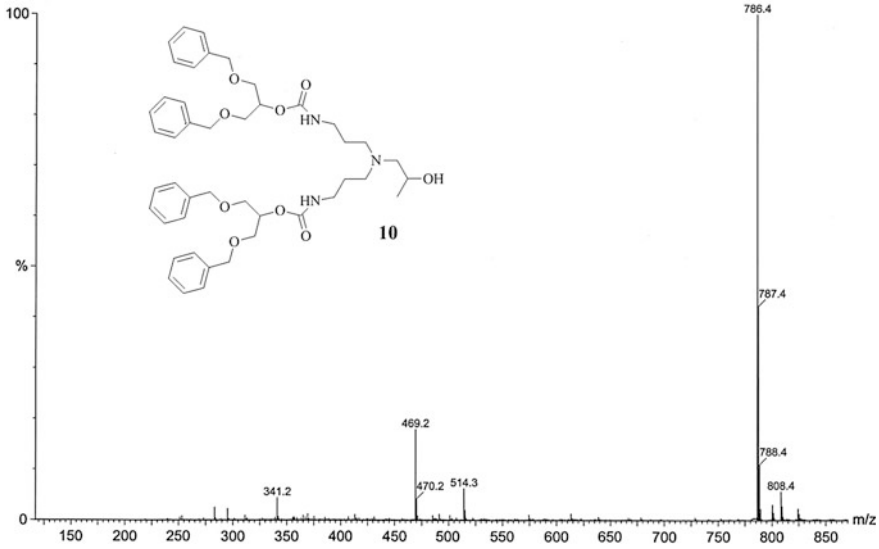

Fig. A.28 Mass spectrum (ES-MS) of G2 dendron, **10**

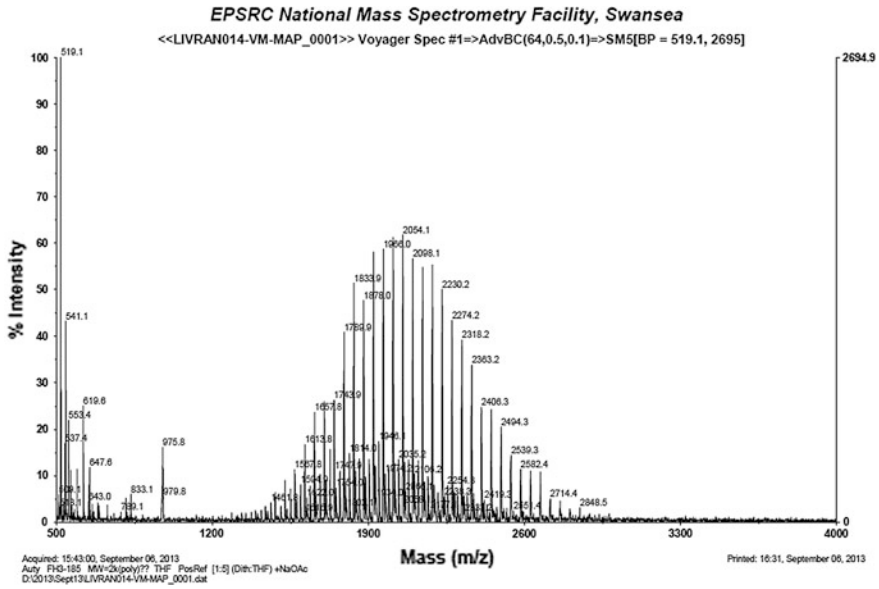

Fig. A.29 MALDI-TOF for **2000PEG** initiator

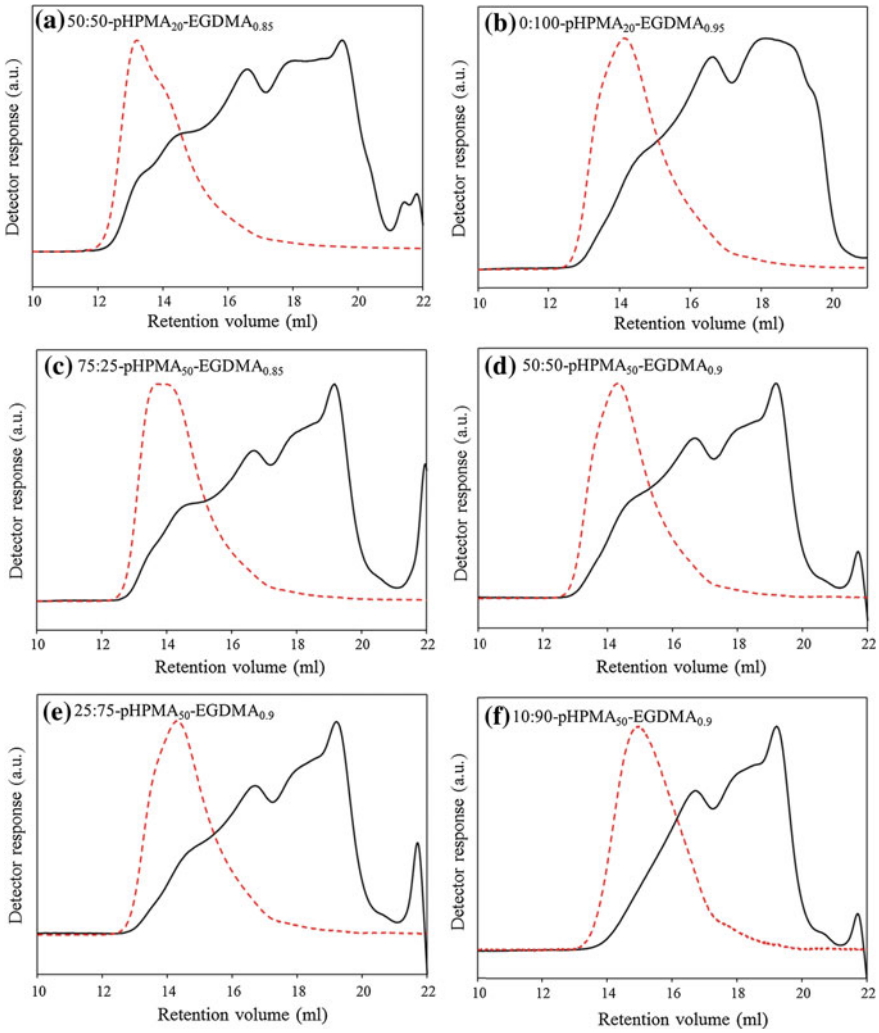

Fig. A.30 GPC chromatogram overlays for **G2′:2000PEG** initiated polymers; RI chromatogram (*black solid lines*), RALS chromatogram (*red dotted lines*)

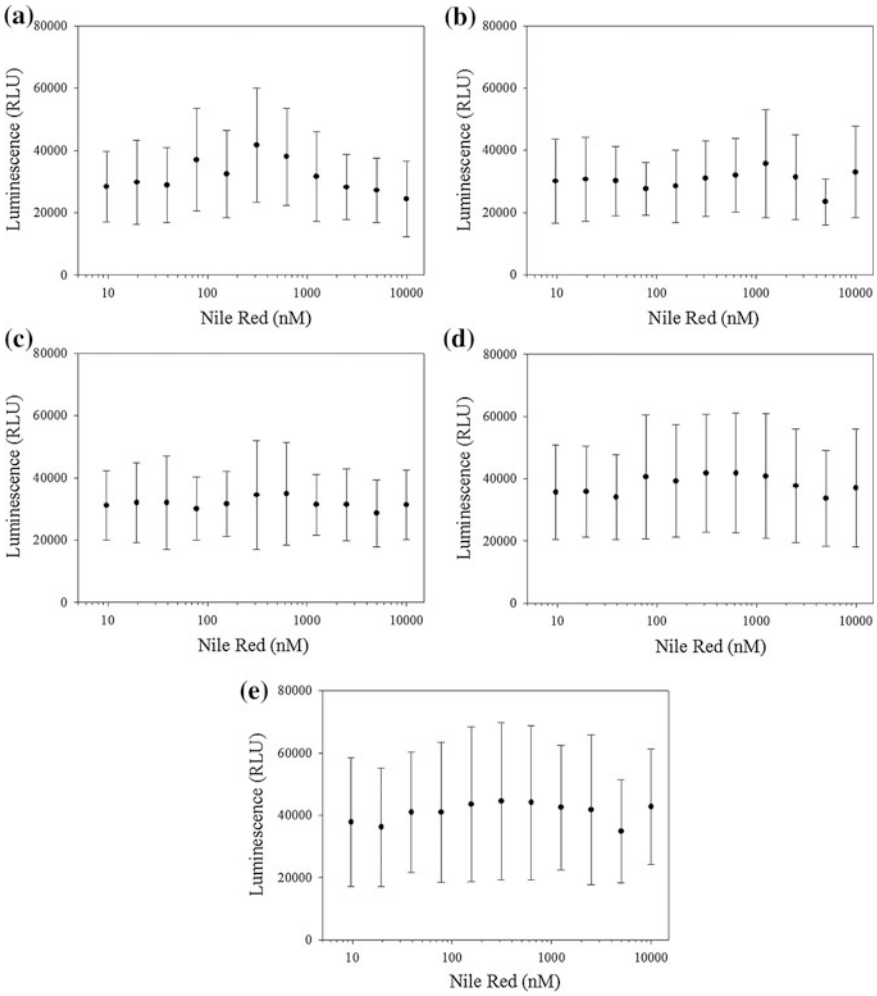

Fig. A.31 ATP assay of Caco-2 cells following 24 h incubation with aqueous Nile Red and each polydendron. **a** Aqueous Nile Red. **b** 50:50. **c** 25:75. **d** 10:90. **e** 0:100. Error calculated using the standard deviation

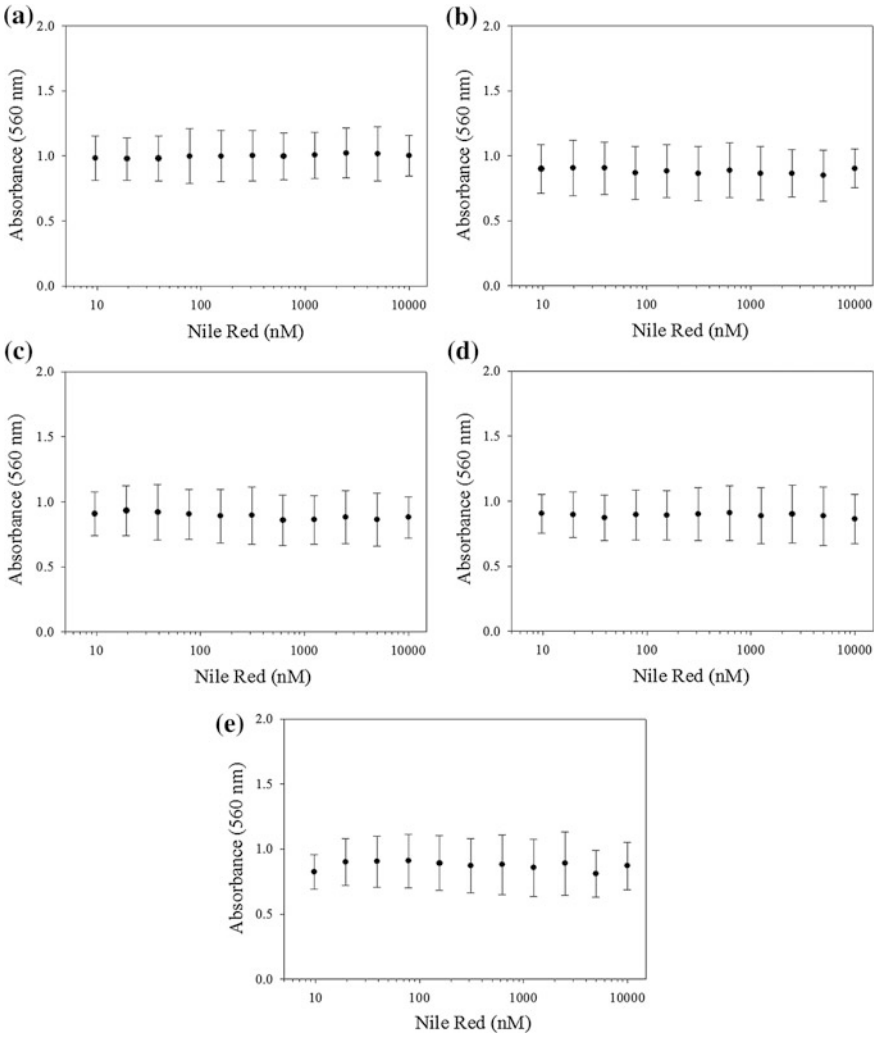

Fig. A.32 MTT assay of Caco-2 cells following 24 h incubation with aqueous Nile Red and each polydendron. **a** Aqueous Nile Red. **b** 50:50. **c** 25:75. **d** 10:90. **e** 0:100. Error calculated using the standard deviation

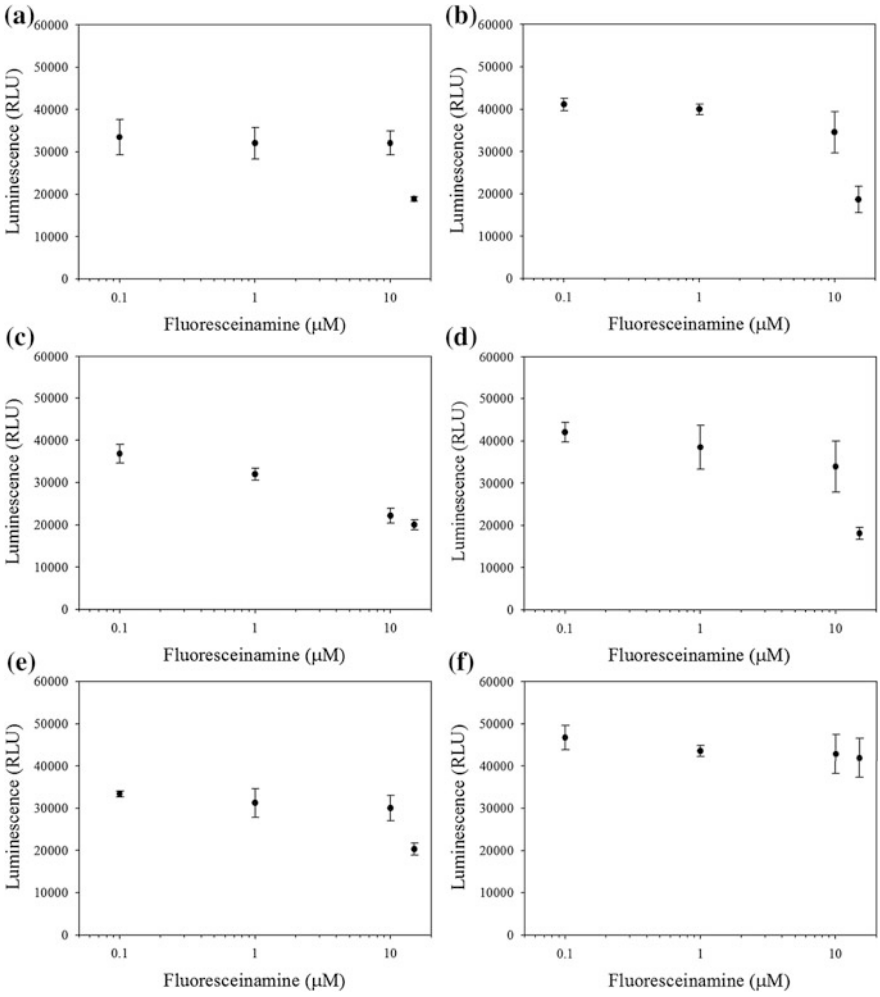

Fig. A.33 Caco-2 cell ATP assay 1 day incubation: **a** 90:10 50 B, **b** 75:25 50 B, **c** 75:25 100 B, **d** 50:50 100 B, **e** 25:75 100 B, **f** aqueous. Error bars from standard deviation

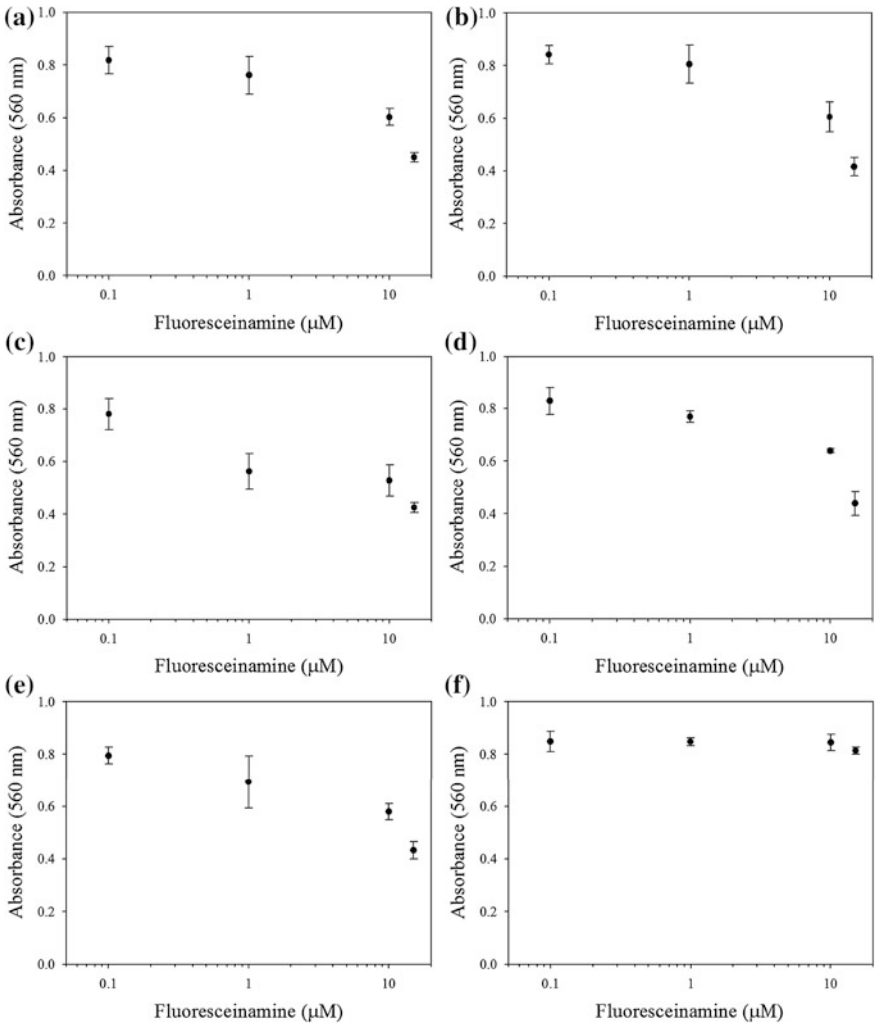

Fig. A.34 Caco-2 cell MTT assay 1 day incubation: **a** 90:10 50 B, **b** 75:25 50 B, **c** 75:25 100 B, **d** 50:50 100 B, **e** 25:75 100 B, **f** aqueous. Error bars from standard deviation

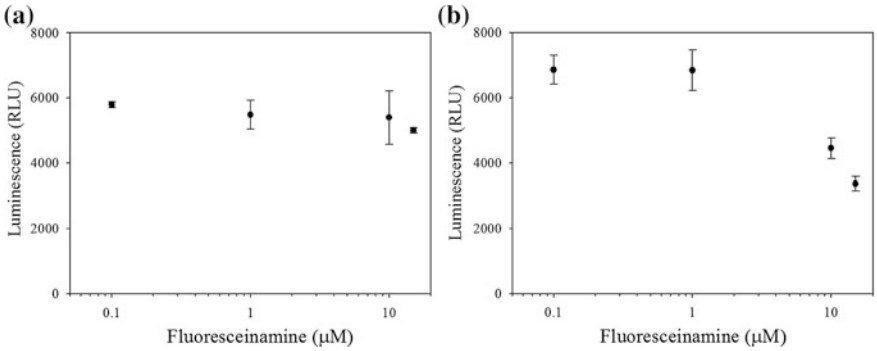

Fig. A.35 ATHP-1 cell ATP assay 1 day incubation period—**a** aqueous preparation, **b** 75:25 DP_{100} Error = standard deviation

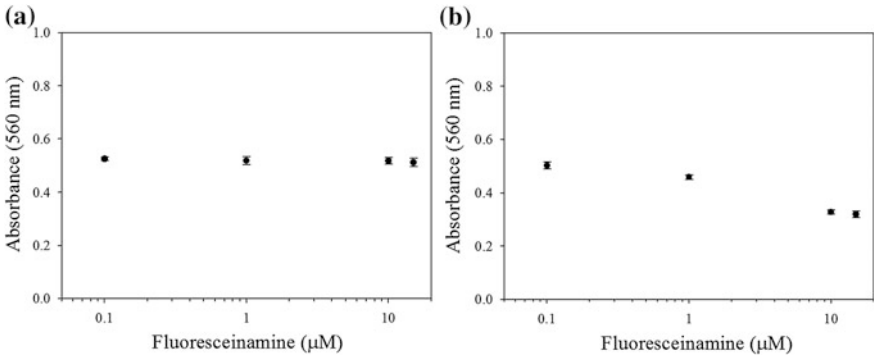

Fig. A.36 ATHP-1 cell MTT assay 1 day incubation period—**a** aqueous preparation, **b** 75:25 DP_{100} Error = standard deviation

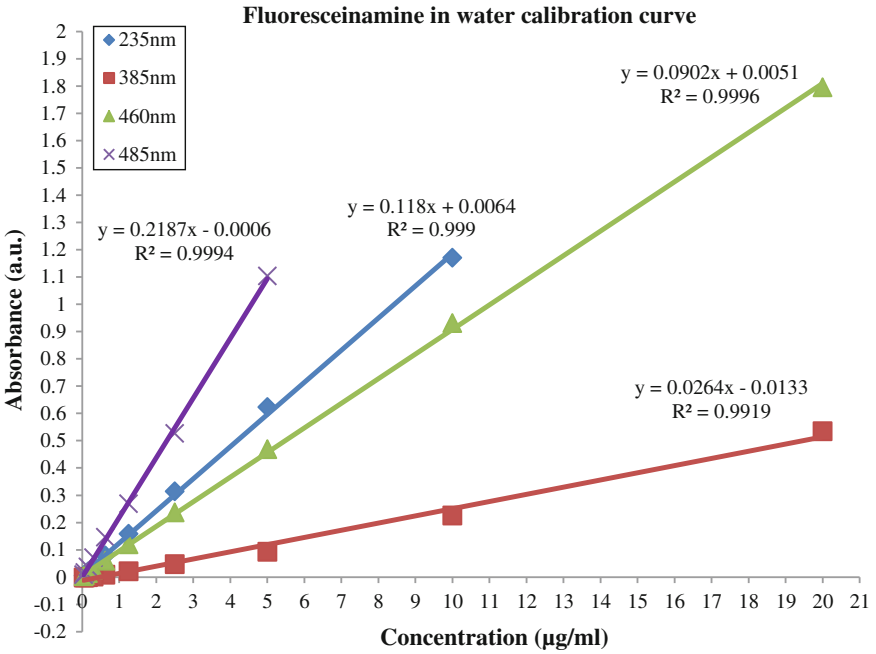

Fig. A.37 UV-Vis spectroscopy calibration curves for fluoresceinamine in water

Table A.8 DLS data for the i_5-f_1 nanoprecipitations performed using **G2′:2KPEG**-pHPMA$_{50}$-EGDMA$_x$ using THF and acetone as a good solvent

G2′:2KPEG-pHPMA$_{50}$-EGDMA$_x$	THF		Acetone	
	D_z (nm)	PdI	D_z (nm)	PdI
100:0	68	0.386	–	–
90:10	176	0.034	258	0.192
75:25	215	0.085	261	0.137
50:50	116	0.038	170	0.224
25:75	53	0.238	54	0.240
10:90	35	0.178	36	0.248
0:100	33	0.304	39	0.462

Table A.9 DLS data for the i_5-f_1 nanoprecipitations performed using **G2′:2KPEG**-pHPMA$_{100}$-EGDMA$_{0.8}$ using THF and acetone as a good solvent

G2′:2KPEG-pHPMA$_{100}$-EGDMA$_{0.8}$	THF		Acetone	
	D_z	PdI	D_z	PdI
100:0	329	0.022	438	0.255
75:25	143	0.073	289	0.146
50:50	160	0.034	168	0.065
25:75	137	0.047	139	0.044
0:100	128	0.074	143	0.179

Table A.10 DLS measurements of FA loaded **G2′:2KPEG**-pHPMA$_{100}$-EGDMA$_{0.8}$ nanoparticles 1 mg/mL polymer and 0.01 mg/mL FA over time (batch 4)

G2′:2KPEG-pHPMA$_{100}$-EGDMA$_{0.8}$	Day 0		Day 7		Day 14		Day 21		Day 80	
	D_z	PdI	D_z	PdI	D_z	PdI	D_z	PdI	D_z	PdI
75:25	173	0.041	171	0.028	174	0.022	173	0.045	171	0.041
50:50	250	0.073	248	0.077	256	0.052	246	0.05	252	0.064
25:75	153	0.09	173	0.21	156	0.072	151	0.06	152	0.079
0:100	117	0.141	110	0.093	116	0.058	111	0.072	65	0.093

Table A.11 FA loaded **G2′:2000PEG**-pHPMA$_{100}$-EGDMA$_{0.8}$ nanoparticles 1 mg/mL polymer and 0.01 mg/mL FA (batch 5) DLS measurements over time and diluted with transport buffer

G2′:2KPEG-pHPMA$_{100}$-EGDMA$_{0.8}$	Day 0		Day 21		Day 42		After dilution with transport buffer to 0.25 mg/mL	
	D_z	PdI	D_z	PdI	D_z	PdI	D_z	PdI
75:25	160	0.032	153	0.043	156	0.037	158	0.050
50:50	212	0.034	210	0.019	212	0.028	209	0.020
25:75	192	0.135	194	0.196	193	0.166	211	0.260

Chapter 5

See Figs. A.38, A.39, A.40, A.41, A.42, A.43 and Tables A.12, A.13.

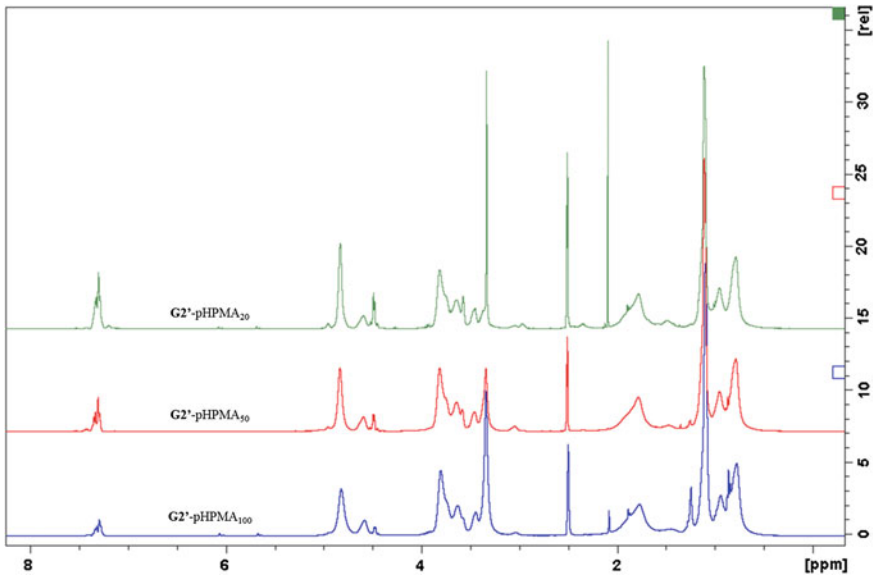

Fig. A.38 ^{1}H NMR (d_6-DMSO, 400 MHz) spectra overlay for **G2′-**pHPMA$_{20}$, **G2′-**pHPMA$_{50}$ and **G2′-**pHPMA$_{100}$

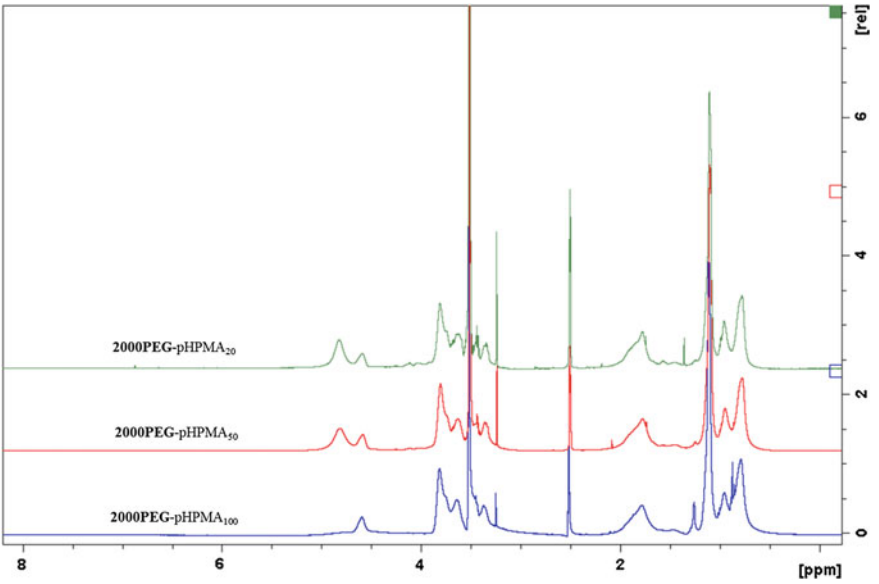

Fig. A.39 ^{1}H NMR (d_6-DMSO, 400 MHz) spectra overlay for **2000PEG-**pHPMA$_{20}$, **2000PEG-**pHPMA$_{50}$ and **2000PEG-**pHPMA$_{100}$

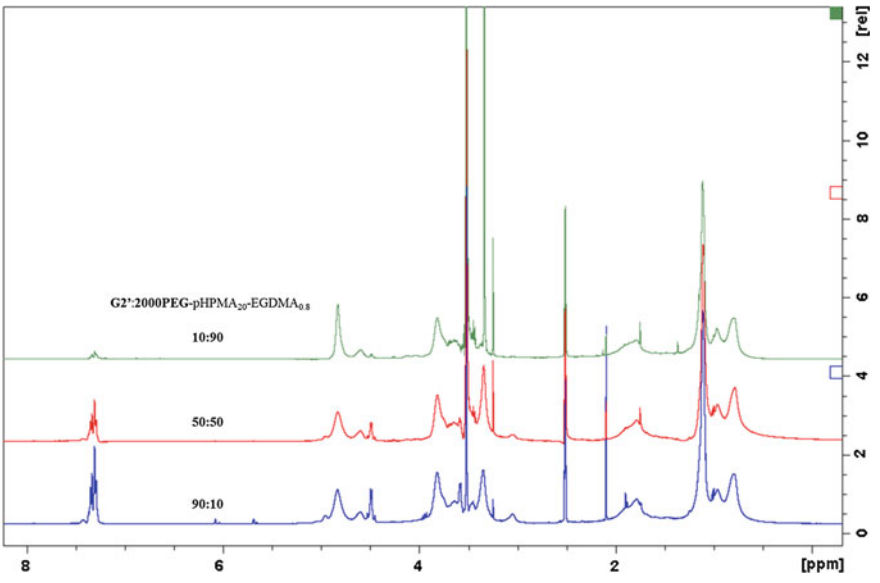

Fig. A.40 ^{1}H NMR (d_6-DMSO, 400 MHz) spectra overlay for **G2′:2000PEG** 10:90-pHPMA$_{20}$-EGDMA$_{0.8}$, 50:50-pHPMA$_{20}$-EGDMA$_{0.8}$ and 90:10-pHPMA$_{20}$-EGDMA$_{0.8}$

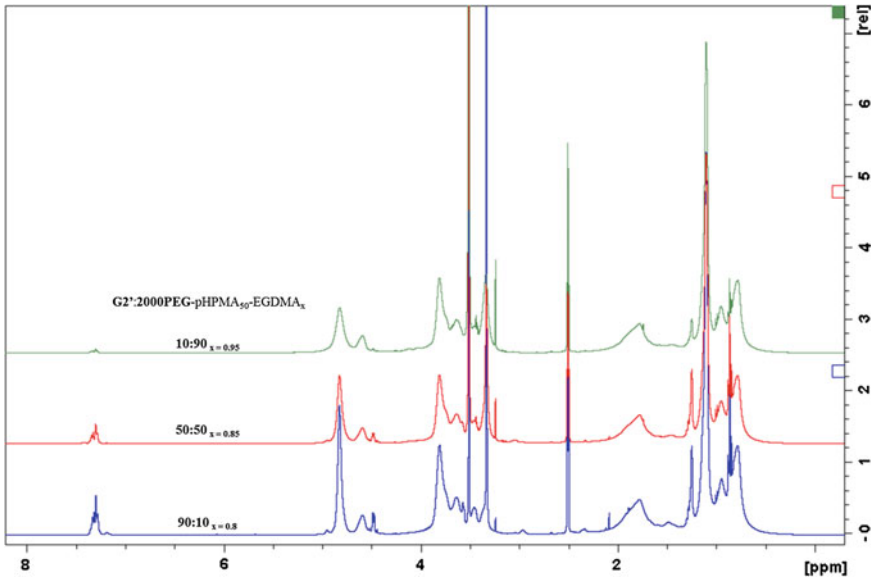

Fig. A.41 ^{1}H NMR (d_6-DMSO, 400 MHz) spectra overlay for **G2′:2000PEG** 10:90-pHPMA$_{50}$-EGDMA$_{0.95}$, 50:50-pHPMA$_{50}$-EGDMA$_{0.85}$ and 90:10-pHPMA$_{50}$-EGDMA$_{0.8}$

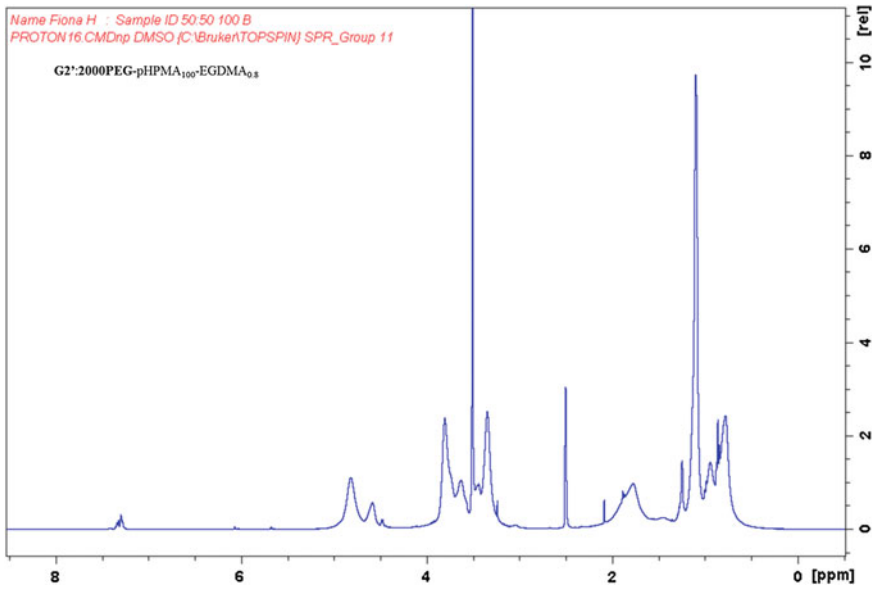

Fig. A.42 ^{1}H NMR (d_6-DMSO, 400 MHz) spectra overlay for **G2′:2000PEG** 50:50-pHPMA$_{100}$-EGDMA$_{0.8}$

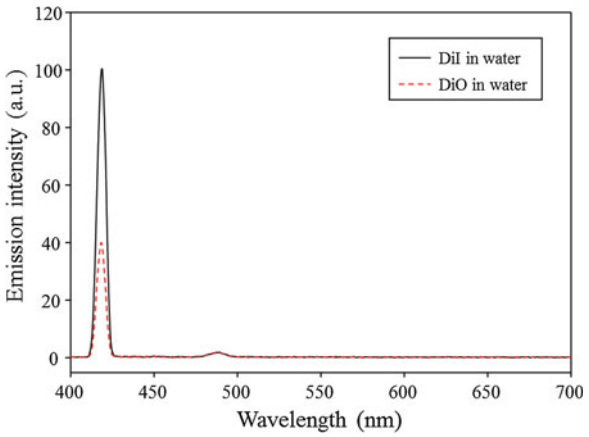

Fig. A.43 Fluorescence spectra from DiI and DiO in water

Table A.12 Theoretical mol% and calculated mol% via ^{1}H NMR spectroscopy of the **G2′**dendron initiator, EO repeat unit in the **2000PEG** initiator and HPMA repeat unit along the pHPMA chain for each **G2′**:**2000PEG** branched polymer synthesised

G2 dendron (%)	2000PEG (%)	pHPMA targeted	Theoretical (mol%)			Calculated (mol%)		
			G2	EO	HPMA	G2	EO	HPMA
100	0	20	4.76	0.00	95.24	4.44	0.00	95.56
90	10	20	3.54	17.88	78.59	2.58	25.19	72.22
75	25	20	2.33	35.41	62.26	1.54	38.87	59.59
50	50	20	1.16	52.60	46.24	0.95	54.04	45.01
25	75	20	0.46	62.76	36.78	0.38	61.58	38.04
10	90	20	0.16	67.08	32.76	0.19	65.16	34.65
0	100	20	0.00	69.47	30.53	0.00	68.95	31.05
100	0	50	1.96	0.00	98.04	1.76	0.00	98.24
90	10	50	1.62	8.21	90.17	1.10	14.13	84.77
75	25	50	1.21	18.31	80.48	0.88	27.84	71.28
50	50	50	0.68	31.06	68.26	0.50	35.14	64.36
25	75	50	0.30	40.44	59.26	0.18	47.55	52.27
10	90	50	0.11	44.98	54.91	0.07	50.29	49.64
0	100	50	0.00	47.64	52.36	0.00	49.98	50.02
100	0	100	0.99	0.00	99.01	0.77	0.00	99.23
75	25	100	0.67	10.14	89.19	0.45	11.54	88.01
50	50	100	0.41	18.46	81.14	0.29	26.08	73.64
25	75	100	0.19	25.40	74.42	0.11	29.48	70.41
0	100	100	0.00	31.27	68.73	0.00	31.02	68.98

Table A.13 Theoretical wt% and calculated wt% via ^{1}H NMR spectroscopy of the **G2′**dendron initiator, EO repeat unit in the **2000PEG** initiator and HPMA repeat unit along the pHPMA chain for each **G2′**:**2000PEG** branched polymer synthesised

G2 dendron (%)	2000PEG (%)	pHPMA targeted	Theoretical wt%			Calculated wt%		
			G2	EO	HPMA	G2	EO	HPMA
100	0	20	24.48	0.00	75.52	23.17	0.00	76.83
90	10	20	21.44	5.10	73.46	17.33	7.95	74.72
75	25	20	17.16	12.25	70.59	12.24	14.57	73.19
50	50	20	10.74	23.00	66.26	9.12	24.37	66.51
25	75	20	5.06	32.51	62.43	4.19	31.68	64.13
10	90	20	1.96	37.70	60.34	2.18	35.66	62.15
0	100	20	0.00	40.97	59.03	0.00	40.39	59.61
100	0	50	11.48	0.00	88.52	10.38	0.00	89.62
90	10	50	10.20	2.43	87.38	7.41	4.48	88.11
75	25	50	8.34	5.95	85.71	6.64	9.94	83.41
50	50	50	5.39	11.53	83.08	4.13	13.69	82.18
25	75	50	2.61	16.79	80.60	1.70	21.35	76.94
10	90	50	1.03	19.79	79.18	0.71	23.45	75.85
0	100	50	0.00	21.73	78.27	0.00	23.37	76.63
100	0	100	6.09	0.00	93.91	4.80	0.00	95.20
75	25	100	4.49	3.20	92.31	3.12	3.73	93.15
50	50	100	2.94	6.30	90.76	2.22	9.53	88.24
25	75	100	1.45	9.29	89.26	0.88	11.23	87.89
0	100	100	0.00	12.19	87.81	0.00	12.07	87.93